Modelling and Simulation in Engineering

Computational Fluid Dynamics and Its Applications 2012

Guest Editors: Guan Heng Yeoh, Chaoqun Liu, Jiyuan Tu, and Victoria Timchenko

Computational Fluid Dynamics and Its Applications 2012

Modelling and Simulation in Engineering

Computational Fluid Dynamics and Its Applications 2012

Guest Editors: Guan Heng Yeoh, Chaoqun Liu, Jiyuan Tu, and Victoria Timchenko

Editorial Board

Contents

Computational Fluid Dynamics and Its Applications 2012, Guan Heng Yeoh, Chaoqun Liu, Jiyuan Tu, and Victoria Timchenko
Volume 2012, Article ID 610610, 2 pages

New Theories on Boundary Layer Transition and Turbulence Formation, Chaoqun Liu, Ping Lu, Lin Chen, and Yonghua Yan
Volume 2012, Article ID 619419, 22 pages

Numerical Model for Cavitational Flow in Hydraulic Poppet Valves, Sandor I. Bernad and Romeo Susan-Resiga
Volume 2012, Article ID 742162, 10 pages

Determination of Flow Conditions in Coronary Bifurcation Lesions in the Context of the Medina Classification, Marjan Molavi Zarandi, Rosaire Mongrain, and Olivier F. Bertrand
Volume 2012, Article ID 419087, 10 pages

A CFD Simulation on How the Different Sizes of Silica Gel Will Affect the Adsorption Performance of Silica Gel, John White
Volume 2012, Article ID 651434, 12 pages

A Study of the Location of the Entrance of a Fishway in a Regulated River with CFD and ADCP, Anders G. Andersson, Dan-Erik Lindberg, Elianne M. Lindmark, Kjell Leonardsson, Patrik Andreasson, Hans Lundqvist, and T. Staffan Lundström
Volume 2012, Article ID 327929, 12 pages

Simulating the Effects of Structural Parameters on the Hydraulic Performances of Venturi Tube, Yanqi Sun and Wenquan Niu
Volume 2012, Article ID 458368, 7 pages

Landing Gear Aerodynamic Noise Prediction Using Building-Cube Method, Daisuke Sasaki, Deguchi Akihito, Hiroshi Onda, and Kazuhiro Nakahashi
Volume 2012, Article ID 632387, 16 pages

Detailed CFD Modelling of Open Refrigerated Display Cabinets, Pedro Dinis Gaspar, L. C. Carrilho Gonalves, and R. A. Pitarma
Volume 2012, Article ID 973601, 17 pages

The Role of Mesh Generation, Adaptation, and Refinement on the Computation of Flows Featuring Strong Shocks, Aldo Bonfiglioli, Renato Paciorri, and Andrea Di Mascio
Volume 2012, Article ID 631276, 15 pages

Computational Fluid Dynamics Modelling and Experimental Study on a Single Silica Gel Type B, John White
Volume 2012, Article ID 598479, 9 pages

Turbulent and Transitional Modeling of Drag on Oceanographic Measurement Devices, Abraham, J. M. Gorman, F. Reseghetti, E. M. Sparrow, and W. J. Minkowycz
Volume 2012, Article ID 567864, 8 pages

Hindawi Publishing Corporation
Modelling and Simulation in Engineering
Volume 2012, Article ID 610610, 2 pages
doi:10.1155/2012/610610

Editorial
Computational Fluid Dynamics and Its Applications 2012

Guan Heng Yeoh,[1,2] Chaoqun Liu,[3] Jiyuan Tu,[4] and Victoria Timchenko[2]

[1] *Australian Nuclear Science Technology Organisation (ANSTO), Locked Bag 2001, Kirrawee, NSW 2233, Australia*
[2] *School of Mechanical and Manufacturing Engineering, University of New South Wales, Sydney, NSW 2052, Australia*
[3] *Centre for Numerical Simulation and Modeling, Department of Mathematics, University of Texas at Arlington, Arlington, TX 76019-0408, USA*
[4] *School of Aerospace, Mechanical and Manufacturing Engineering, RMIT University, P.O. Box 71, Bundoora, VIC 3083, Australia*

Correspondence should be addressed to Guan Heng Yeoh, guan.yeoh@ansto.gov.au

Received 9 September 2012; Accepted 9 September 2012

The launch of this annual focus/special issue in this year has been built upon the success of the special issue that was introduced last year in the published special issue of Modeling and Simulation in Engineering. There is no doubt that there is an increasing resurgence of computer simulation technology changing or reshaping the landscape on how computational fluid dynamics, better known by its acronym CFD, is currently being applied in many fields of engineering research and application. For this particular issue, we have managed to collate a range of topics and papers that pertinently encapsulate the many advances and applications of CFD which we have the great pleasure of sharing with the wider community. We certainly would like to thank the numerous authors for their excellent contributions and patience in assisting us. More importantly, we would like to warmly acknowledge the tiresome work of all referees in reviewing these papers.

This annual focus/special issue contains eleven papers. The advances and wide applications of CFD in each of the papers are detailed in the following.

"*New theories on boundary layer transition and turbulence formation*" by C. Liu et al. presents a short review on the investigation of late boundary layer transition and turbulence via direct numerical simulation (DNS). A new theory has been proposed which comprises receptivity, linear instability, large vortex structure formation, small-length-scale generation, loss of symmetry, and randomization to turbulence. A new theory on turbulence is also proposed which comprises all small length scales generated by *shear linear instability* rather than *vortex breakdown* through multiple-level ejections and sweeps and consequent multiple-level positive and negative spikes. Through their DNS observation, energy is transferred from large to small vortices by multiple-level sweeps which are in contrast to Kolmogorov's theory where the cascading of energy occurs from large to small vortices through vortex stretch and breakdown.

"*The role of mesh generation, adaptation, and refinement on the computation of flows featuring strong shocks*" by A. Bonfiglioli et al. presents some recent advances in computational approaches to better capture shock waves. There is a strong relationship between the development and application of mesh adaption/refinement/generation techniques and the computation of high-quality solutions of flows featuring strong shocks. Mesh adaption/refinement/generation techniques that can adapt to the shock front have been found to be a key ingredient in achieving accurate solutions for this kind of flow fields. Nevertheless, more relevant and conclusive enhancements in terms of solution quality can be obtained by means of a shock-fitting technique for unstructured grids. Indeed, the use of this newly developed technique completely removes the capturing process which has been the source of most of the problems that have plagued current shock-capturing schemes.

"*Landing gear aerodynamic noise prediction using building-cube method*" by D. Sasaki et al. presents the application of a building-cube method to solve the fluid flow around a JAXA landing gear. The building-cube method is a multiblock-structured Cartesian mesh solver. Here, the computational domain can be decomposed of assembly

of various sizes of building blocks where smaller blocks are employed to capture the fine details of the fluid flow. The airframe noise is predicted through the coupling of incompressible Navier-Stokes flow solver and the aeroacoustic analogy-based Curle's equation to predict the acoustic sound generated from the object in the fluid flow. Good agreement is achieved between the experimental data and numerical predictions. The results also show that the torque link position highly affects the flow acceleration at the axle region between two wheels, which causes the change in sound pressure level at the observation point.

"*Turbulent and transitional modeling of drag on oceanographic measurement devices*" by J. P. Abraham et al. presents the use of CFD in determining the drag on oceanographic devices (bathythermographs). Such devices are employed to monitor changes in ocean heat content. Fall-rate equation is reasonably accurate for ocean environments that match the experiments from the correlations developed. In order to better improve drag calculations which can significantly impact the estimation of ocean heating associated with global warming, a CFD approach has been undertaken to provide drag coefficients which can be used to predict depths independent of a fall-rate equation.

"*A Study of the location of the entrance of a fishway in a regulated river with CFD and ADCP*" by A. G. Andersson et al. presents the application of CFD to determine the flow downstream of a hydropower plant with regards to upstream migrating fish. Field measurements via an Acoustic Doppler Current Profiler (ADCP) were utilised to purposefully validate the CFD simulations. Various configurations were investigated in order to assess the flows at the fishway entrance and further downstream, where the flow from the turbine meets the old river bed, which represent the current fish passage for upstream migrating fish.

"*Numerical model for cavitational flow in hydraulic poppet valves*" by S. I. Bernad and R. Susan-Resiga presents the CFD investigation of two-phase flow inside a poppet valve. A mixture model is applied to predict pressure and density distributions of the flow inside the cavity. Cavitation model that utilizes the modified Rayleigh-Plesset equations for bubble dynamics is adopted. The cavitating flow pressure distribution displays a constant value inside the vapour-filled cavity, with a slow increase as the mixture density increases. The investigation of the liquid-gas mixture density shows a smooth and continuous transition from vapour to liquid. This transition takes place over a relatively large region.

"*Simulating the effects of structural parameters on the hydraulic performances of venturi tube*" by Y. Sun and W. Niu presents a parametric CFD investigation to assess the effects of structural parameters (such as throat taper, throat contraction ratio, and throat length) on the hydraulic performance (such as outlet faceted average velocity, minimum pressure, and critical pressure) of a Venturi tube under different inlet pressures and pressure differences between inlet and outlet. The throat contraction ratio is found to be the contributing factor to the Venturi injector performance.

"*Computational fluid dynamics modelling and experimental study on a single silica gel type B*" by J. White presents the application of CFD in in the area of porous media and adsorption cooling system. CFD can be a useful tool to predict the water vapour flow pattern, temperature, heat transfer, flow velocity and adsorption rate. By obtaining useful experimental data from thermogravimetric measurements, CFD predictions are found to be comparable with the measured data. This implies that CFD could provide useful information for the design of adsorption cooling systems and better predict the system performance.

"*A CFD simulation on how the different sizes of silica gel will affect the adsorption performance of silica gel*" by J. White presents a review on the application of CFD in simulating the adsorption of water vapour on silica gel granules and to study the effect of granule sizes indicating that reducing the granule size increases the adsorption. CFD has been found to be a promising tool in evaluating the heat transfer behaviour in an adsorption bed. Further CFD studies are required for evaluating the adsorption performance with a larger silica gel and porous media.

"*Determination of flow conditions in coronary bifurcation lesions in the context of the medina classification*" by M. M. Zarandi et al. presents the use of CFD in understanding the flow condition and wall shear stress distributions in various bifurcation lesion types in a coronary artery bifurcation. The flow ratio and time-dependence patterns of WSS resulting from the numerical simulation of pulsating hemodynamic flows are investigated in healthy and stenosed coronary artery bifurcations. Various stenoses configurations are considered in the context of Medina lesion classification, and a detailed numerical result for time-dependent wall shear stress distributions that may be involved in lesion initiation and progression is presented. The results indicated that in the bifurcation lesion types, the flow condition and wall shear stress distribution in side branch are influenced by the lesion morphologies which cannot be fully assessed by quantitative coronary angiographic parameters.

"*Detailed CFD modelling of open refrigerated display cabinets*" by P. D. Gaspar et al. presents a comprehensive CFD modelling of air flow and heat transfer in an open refrigerated display cabinet (ORDC). The physical-mathematical model considers the flow through the internal ducts, across fans and evaporator, and includes the thermal response of food products. Air humidity effect and thermal radiation heat transfer between surfaces are accounted in the model. Experimental tests are performed to characterize the phenomena near physical extremities and to validate the numerical predictions. The agreement between numerical predictions and experimental results is found to be satisfactory and adequate for these types of engineering problems. Such predictive capabilities of the computational model could be used to promote a range of geometrical and functional parametric studies that could better improve the thermal performance of the ORDC and consequently food safety.

Guan Heng Yeoh
Chaoqun Liu
Jiyuan Tu
Victoria Timchenko

Hindawi Publishing Corporation
Modelling and Simulation in Engineering
Volume 2012, Article ID 619419, 22 pages
doi:10.1155/2012/619419

Research Article

New Theories on Boundary Layer Transition and Turbulence Formation

Chaoqun Liu, Ping Lu, Lin Chen, and Yonghua Yan

Department of Mathematics, The University of Texas at Arlington, Arlington, TX 76019, USA

Correspondence should be addressed to Chaoqun Liu, cliu@uta.edu

Received 26 January 2012; Accepted 25 March 2012

Academic Editor: Guan Heng Yeoh

This paper is a short review of our recent DNS work on physics of late boundary layer transition and turbulence. Based on our DNS observation, we propose a new theory on boundary layer transition, which has five steps, that is, receptivity, linear instability, large vortex structure formation, small length scale generation, loss of symmetry and randomization to turbulence. For turbulence generation and sustenance, the classical theory, described with Richardson's energy cascade and Kolmogorov length scale, is not observed by our DNS. We proposed a new theory on turbulence generation that all small length scales are generated by "shear layer instability" through multiple level ejections and sweeps and consequent multiple level positive and negative spikes, but not by "vortex breakdown." We believe "shear layer instability" is the "mother of turbulence." The energy transferring from large vortices to small vortices is carried out by multiple level sweeps, but does not follow Kolmogorov's theory that large vortices pass energy to small ones through vortex stretch and breakdown. The loss of symmetry starts from the second level ring cycle in the middle of the flow field and spreads to the bottom of the boundary layer and then the whole flow field.

1. Introduction

These comments clearly show that the mechanism of turbulence formation and sustenance is still a mystery for research. Note that both Heisenberg and Lamb were not optimistic for the turbulence study.

1.1. Turbulence Is a Mystery. Turbulence is still covered by a mystical veil in nature after over a century of intensive study. Following comments are made by Wikipedia web page at http://en.wikipedia.org/wiki/Turbulence "Nobel Laureate Richard Feynman described turbulence as "the most important unsolved problem of classical physics" (USA Today 2006). According to an apocryphal story, Werner Heisenberg (another Nobel Prize winner) was asked what he would ask God, given the opportunity. His reply was "When I meet God, I am going to ask him two questions: Why relativity? And why turbulence? I really believe he will have an answer for the first." [1]. Horace Lamb was quoted as saying in a speech to the British Association for the Advancement of Science, "I am an old man now, and when I die and go to heaven there are two matters on which I hope for enlightenment. One is quantum electrodynamics, and the other is the turbulent motion of fluids. And about the former I am rather optimistic" [2, 3].

1.2. Richardson's Vortex and Energy Cascade Theory (1928). Richardson believed that a turbulent flow is composed by "eddies" of different sizes. The large eddies will be stretching, unstable, and breaking up to smaller eddies. These smaller eddies undergo the same process, giving rise to even smaller eddies. This process will continue until reaching a sufficiently small length scale such that the viscosity of the fluid can effectively dissipate the kinetic energy into internal energy. During the process of vortex breakdown, the kinetic energy of the initial large eddy is divided into the smaller eddies.

1.3. Kolmogorov Assumption (1941). The classical theory on turbulence was given by Kolmogorov, a famous Russian mathematician. In general, the large scales of a flow are not isotropic, because they are determined by the particular boundary conditions. Agreeing with Richardson, Kolmogorov assumed that in Richardson's energy cascade, this geometrical and directional information is lost while the

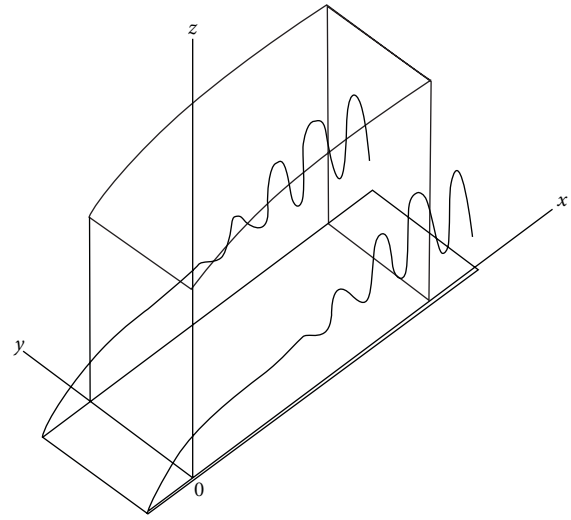

Figure 1: Computation domain.

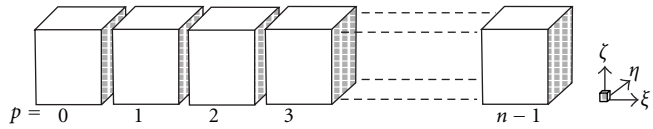

Figure 2: Domain decomposition along the streamwise direction in the computational space.

scale is reduced so that the statistics of the small scales have a universal character—they are statistically isotropic for all turbulent flows when the Reynolds number is sufficiently high. It was assumed that there is no dissipation during the energy transfer from large vortex to small vortex through "vortex breakdown."

1.4. Kolmogorvo's First and Second Hypotheses (1941). Based on his assumption, Kolmogorov [6, 7] further gave very famous theories on the smallest length scale, which is later called Kolmogorov scale (first hypothesis), and turbulence energy spectrum (second hypothesis):

$$\eta = \left(\frac{\nu^3}{\varepsilon}\right)^{1/4},$$

$$E(k) = C\varepsilon^{2/3}k^{-5/3},$$

$$\varepsilon = \nu\left\{2\overline{\left(\frac{\partial u_1}{\partial x_1}\right)^2} + 2\overline{\left(\frac{\partial u_2}{\partial x_2}\right)^2} + 2\overline{\left(\frac{\partial u_3}{\partial x_3}\right)^2} + \overline{\left(\frac{\partial u_2}{\partial x_1} + \frac{\partial u_1}{\partial x_2}\right)^2} + \overline{\left(\frac{\partial u_3}{\partial x_2} + \frac{\partial u_2}{\partial x_3}\right)^2} + \overline{\left(\frac{\partial u_1}{\partial x_3} + \frac{\partial u_3}{\partial x_1}\right)^2}\right\}, \quad (1)$$

where, η is Kolmogorov scale, ν is kinematic viscosity, ε is the rate of turbulence dissipation, E is the energy spectrum function, C is a constant and κ is the wave number. These formulas were obtained by Kolmogorov's hypotheses that the small length scales are determined by ν and ε, and E is related to κ and ε. These formulas are unique according to the dimensional analysis [8].

If all small vortices are generated by "shear layer instability" but not "vortex breakdown", Kolmogorov's first hypothesis will lose the background. The smallest length scales will be related to stability of the weakest unstable "shear layer". This will require a deep study of "shear layer instability" not only "dimensional analysis".

1.5. A Short Review of Study on Late Boundary Layer Transition. The transition process from laminar to turbulent flow in boundary layers is a basic scientific problem in modern fluid mechanics. After over a hundred years of study on flow transition, the linear and weakly non-linear stages of flow transition are pretty well understood [10, 11]. However, for late non-linear transition stages, there are still many questions remaining for research [4, 12–16]. Adrian [17] described hairpin vortex organization in wall turbulence, but did not discuss the sweep and ejection events and the role of the shear layer instability. Wu and Moin [18] reported a new DNS for flow transition on a flat plate. They did obtain fully developed turbulent flow with structure of forest of ring-like vortices by flow transition at zero pressure gradients. However, they did not give the mechanism of the late flow transition. The important mechanism of boundary layer transition such as sweeps, ejections, and positive spikes cannot be found from that paper. Recently, Guo et al. [19] conducted an experimental study for late boundary layer

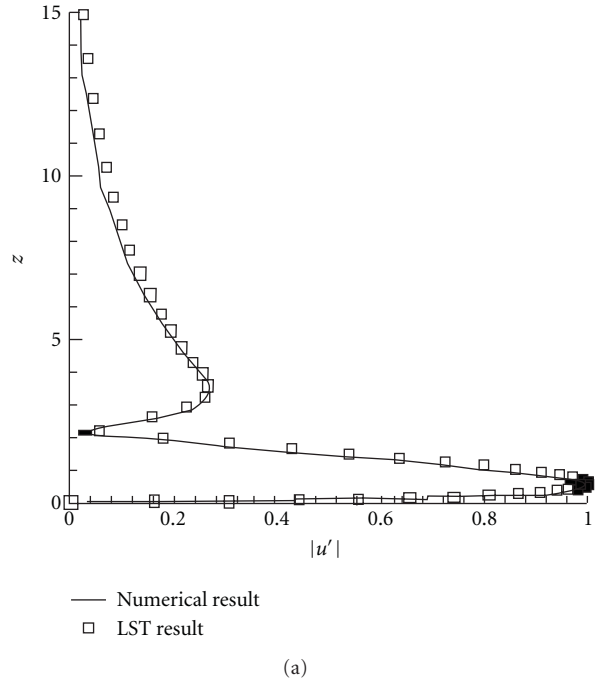

(a)

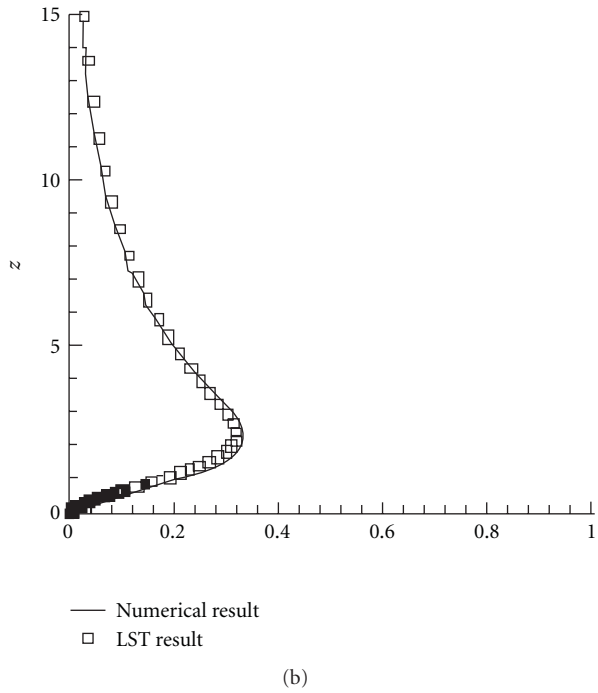

(b)

Figure 3: Comparison of the numerical and LST velocity profiles at Rex = 394300.

transition in more details. They concluded that the U-shaped vortex is a barrel-shaped head wave, secondary vortex, and is induced by second sweeps and positive spikes.

In order to get deep understanding the mechanism of the late flow transition in a boundary layer and physics of turbulence, we recently conducted a high order direct numerical simulation (DNS) with 1920 × 241 × 128 gird points and about 600,000 time steps to study the mechanism of the

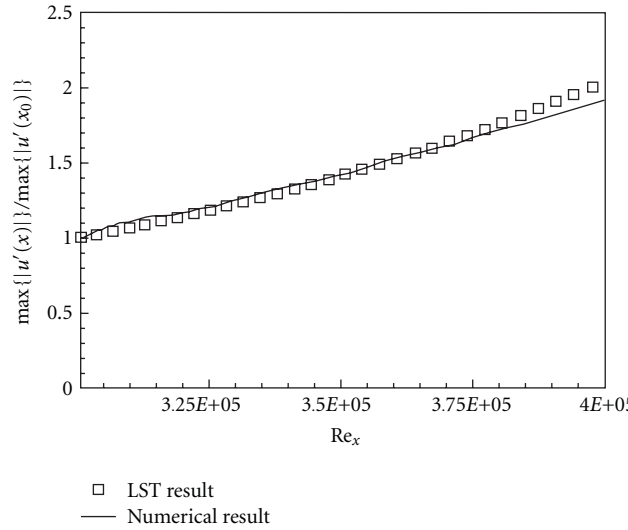

Figure 4: Comparison of the perturbation amplification rate between DNS and LST.

late stages of flow transition in a boundary layer at a free stream Mach number 0.5 [20–32]. The work was supported by AFOSR, UTA, TACC and NSF Teragrid. A number of new observations are made and new mechanisms are revealed in late boundary layer transition (LBLT) including:

(i) mechanism on secondary and tertiary vortex formation;

(ii) mechanism on first ring-like vortex formation;

(iii) mechanism on second sweep formation;

(iv) mechanism on high share layer formation;

(v) mechanism on positive spike formation;

(vi) mechanism on multiple ring formation;

(vii) mechanism on U-shaped vortex formation;

(viii) mechanism on small length vortices generation;

(ix) mechanism on multiple level high shear layer formation;

(x) mechanism of energy transfer paths;

(xi) mechanism on symmetry loss or so called "flow randomization;"

(xii) mechanism on thickening of turbulence boundary layer;

(xiii) mechanism of high surface friction of turbulent flow.

A λ_2 technology developed by Jeong and Hussain [33] is used for visualization.

1.6. Different Physics Observed by Our High-Order DNS. According to our recent DNS, "vortex breakdown" is not observed [24, 29, 30]. Liu gave a new theory that "turbulence is not generated by vortex breakdown but shear layer instability" [24, 30, 32]. Liu believes that "shear layer instability" is the "mother of turbulence."

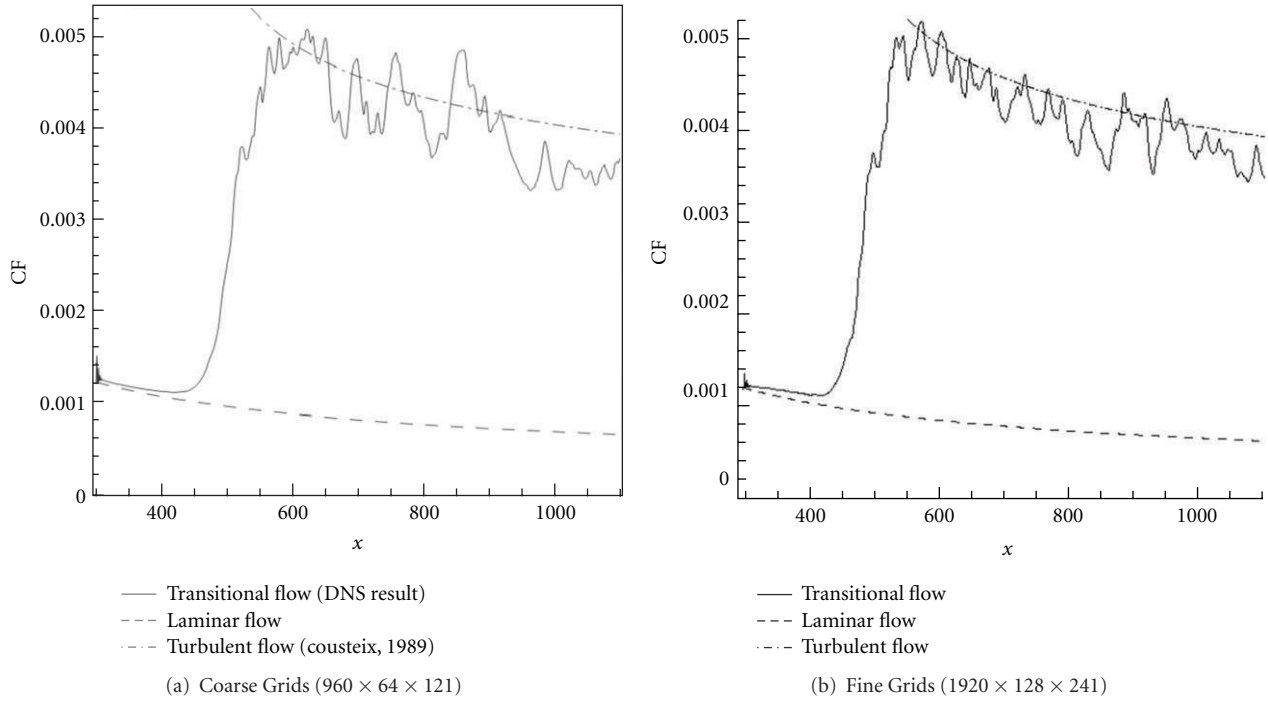

(a) Coarse Grids (960 × 64 × 121)

(b) Fine Grids (1920 × 128 × 241)

Figure 5: Streamwise evolutions of the time- and spanwise-averaged skin-friction coefficient.

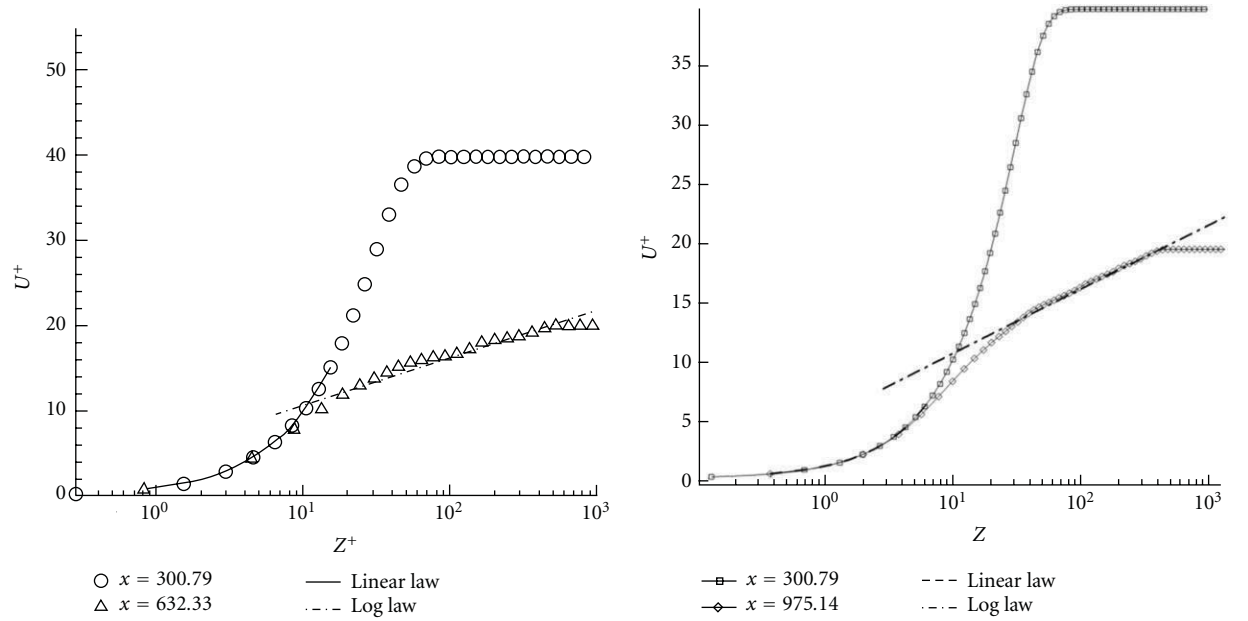

(a) Coarse Grids (960 × 64 × 121)

(b) Fine Grids (1920 × 128 × 241)

Figure 6: Log-linear plots of the time- and spanwise-averaged velocity profile in wall unit.

As Richardson's energy cascade and Kolmogorov's assumption about "vortex breakdown" are challenged, Kolmogorov's assumption that the smallest vortices are statistically isotropic becomes questionable. Since the smallest vortices are generated by the "shear layer instability," which is closely related to the shape of body configuration, they cannot be isotropic.

1.7. Questions to Classical Theory on Boundary Layer Transition. The classical theory, which considers "vortex breakdown" as the last stage of boundary layer transition on a flat plate, is challenged and the phenomenon of "hairpin vortex breakdown to smaller structures" is not observed by our new DNS [24, 27, 28]. The so-called "spikes" are actually a process of multibridge or multiring formation, which is

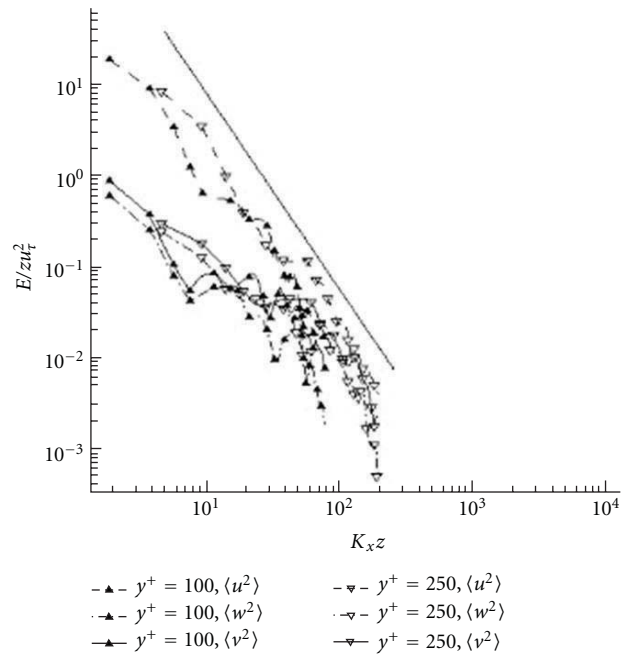

(a)

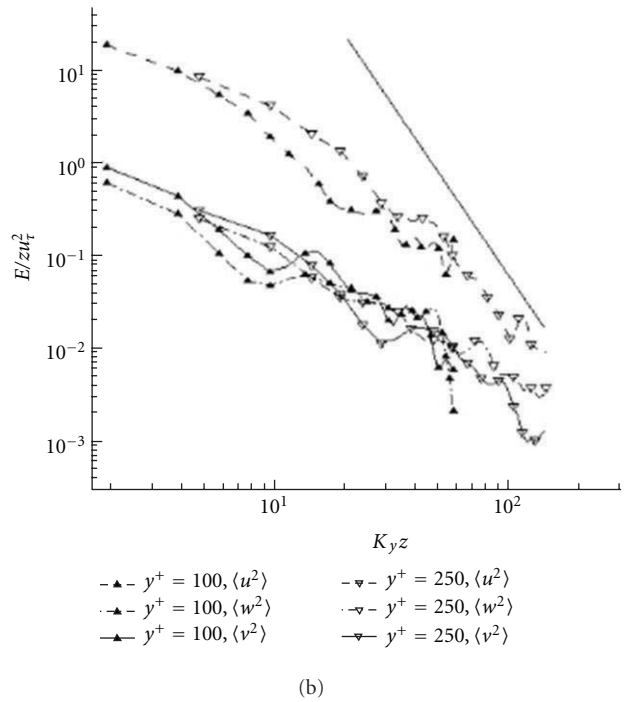

(b)

Figure 7: (a) Spectra in x-direction (b) Spectra in y-direction.

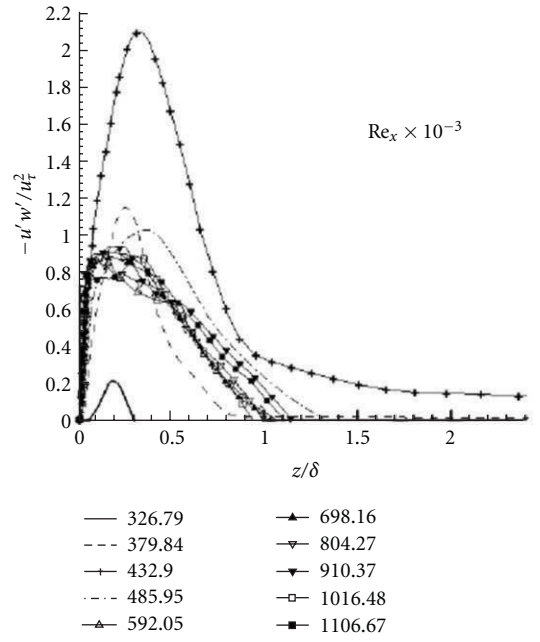

Figure 8: Reynolds stress.

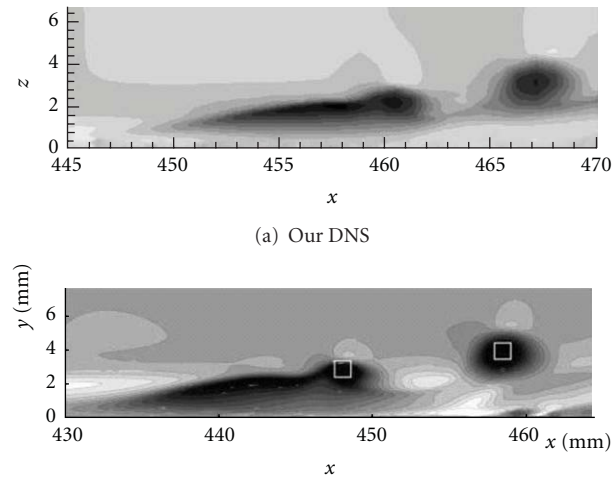

(a) Our DNS

(b) Borodulin et al. [4]

Figure 9: Qualitative comparison of contours of streamwise velocity disturbance u in the (x, z)-plane (light shades of gray correspond to high values).

a rather stable large vortex structure and can travel for a long distance.

As experiment is quite expensive and has very limited power in date acquisition, direct numerical simulation (DNS) becomes a more and more important tool to discover physics. The purpose of this work is to find physics of turbulence by direct numerical simulation. The paper is organized as follows: Section 1 is a background review; Section 2 shows the case set up and code validation; Section 3 is our observation and analysis; Section 4 is a summary of our new finding; Section 5 is the conclusions which are made based on our recent DNS.

1.8. New Theory on Boundary Layer Transition Given by Liu. Classical theory on boundary layer transition can be described four stages: (1) boundary layer receptivity; (2) linear instability; (3) non-linear growth; (4) vortex breakdown to turbulence. Apparently, we disagree with the classical

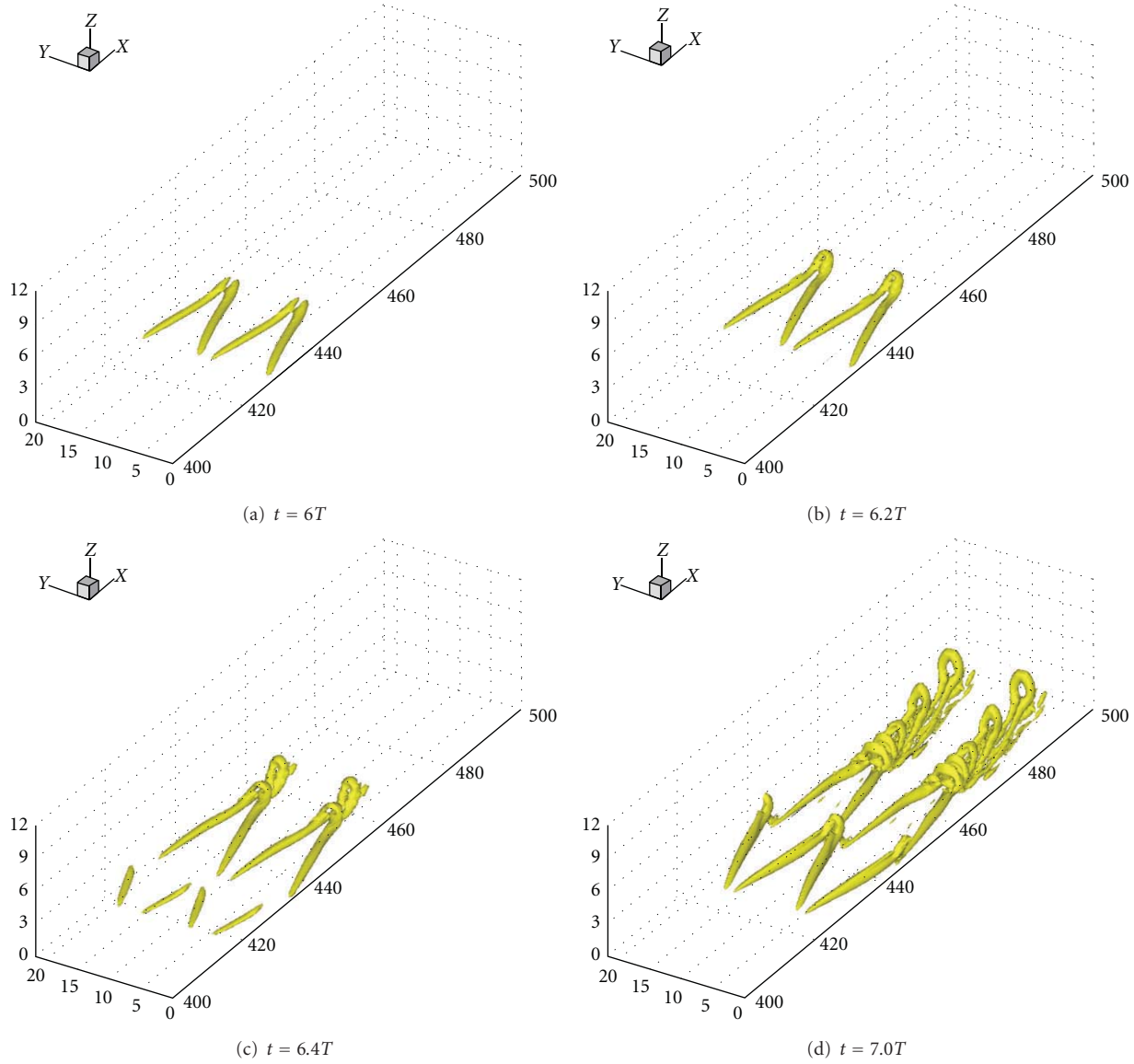

(a) $t = 6T$ (b) $t = 6.2T$

(c) $t = 6.4T$ (d) $t = 7.0T$

Figure 10: Evolution of vortex structure at the late-stage of transition (where T is the period of T-S wave).

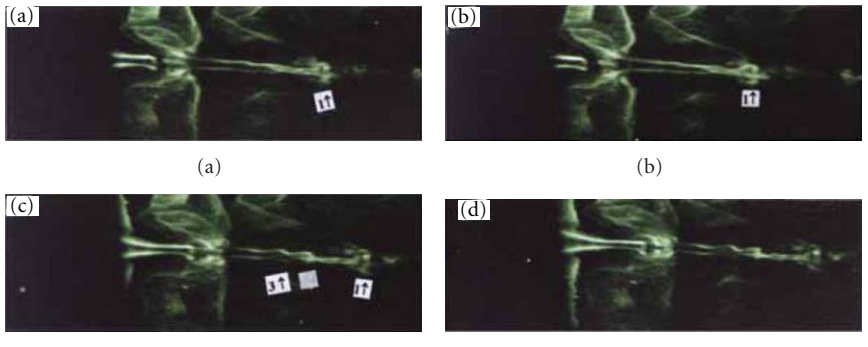

(a) (b)

(c) (d)

Figure 11: Evolution of the ring-like vortex chain by experiment [5].

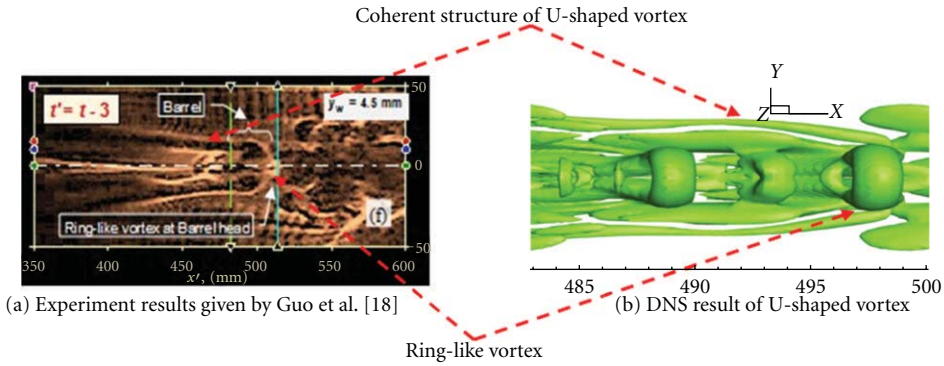

(a) Experiment results given by Guo et al. [18] (b) DNS result of U-shaped vortex

Figure 12: Qualitative vortex structure comparison with experiment.

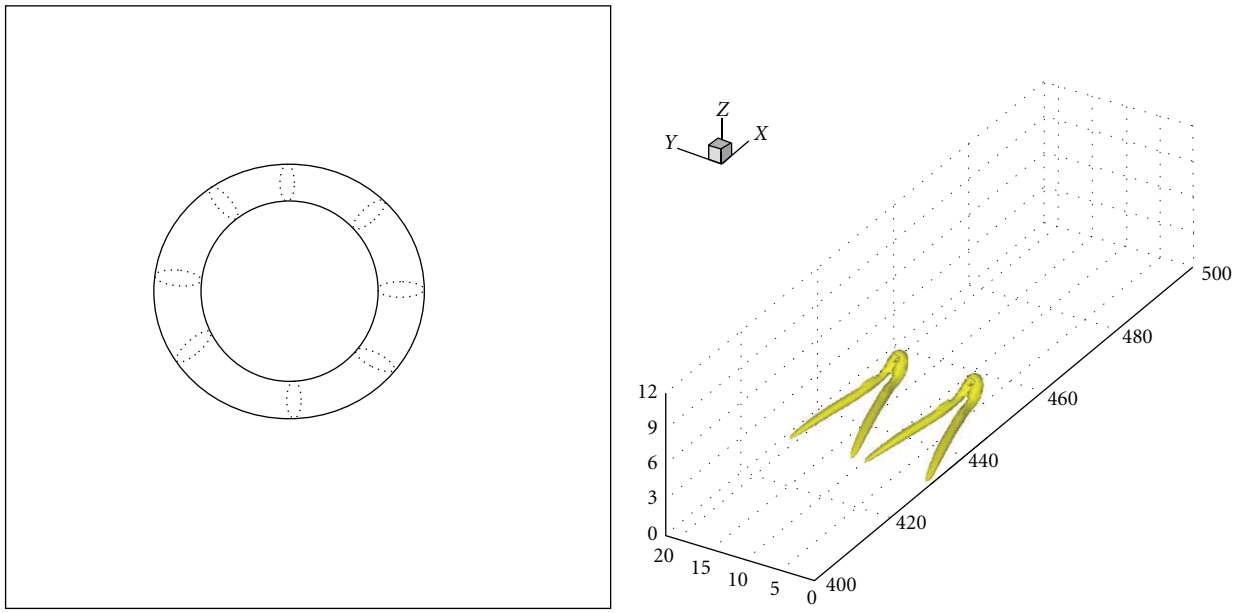

(a) Vortex ring without legs (b) Vortex ring with legs

Figure 13: Vortex rings with or without legs.

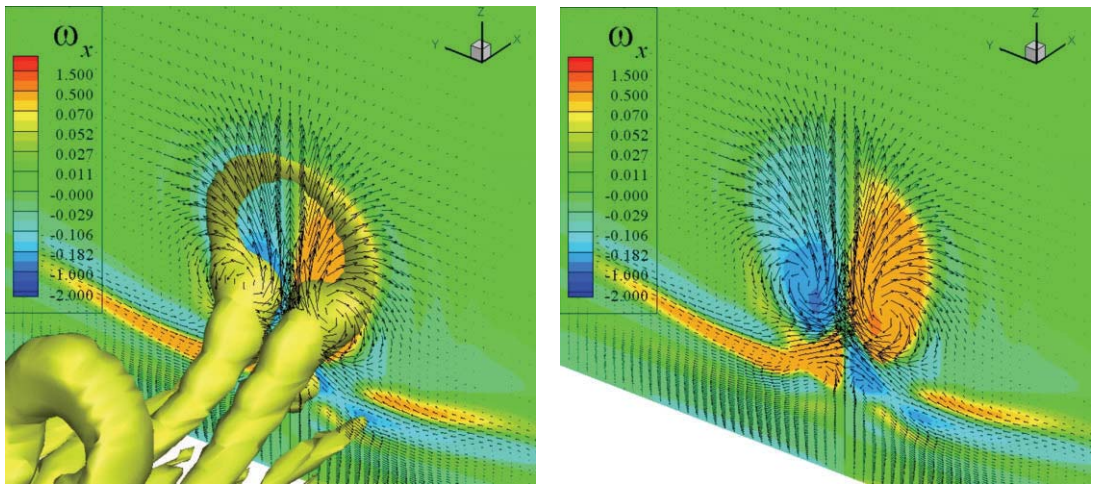

(a) (b)

Figure 14: Formation processes of first ring-like vortex.

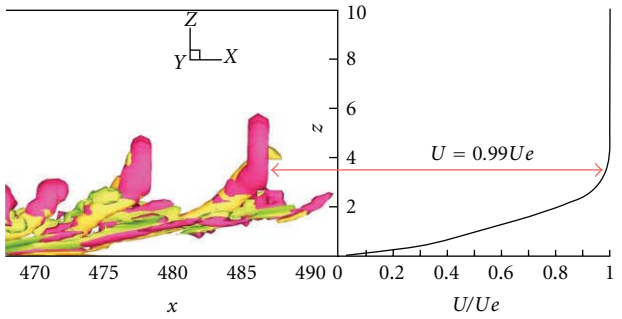

FIGURE 15: The shape and position of ring-like vortices in boundary layer ($z = 3.56, U = 0.99Ue$).

theory on "vortex breakdown to turbulence." The new theory of boundary layer transition can be described by five stages: (1) boundary layer receptivity; (2) linear instability; (3) large vortex structure formation; (4) small vortices generation; (5) symmetry loss and turbulence formation. By the way, the vortex cascade in turbulence given by Richardson, Kolmogorov and others is not observed.

1.9. New Theory on Turbulence Generation and Sustenance Given by Liu. The new theory on turbulence formation and sustenance can be described as follows. All small length scales (turbulence) are generated by shear layer instability which is produced by large vortex structure with multiple level vortex rings, multiple level sweeps and ejections, and multiple level negative and positive spikes near the laminar sublayers. Therefore, "turbulence" is not generated by "vortex breakdown" but rather positive and negative spikes and consequent high shear layers. "Shear layer instability" is considered as the "mother of turbulence." This new theory may give a universal mechanism for turbulence generation and sustenance—the energy is brought by large vortex structure through multiple level sweeps in a boundary layer.

2. Case Setup and Code Validation

2.1. Case Setup. The computational domain is displayed in Figure 1. The grid level is $1920 \times 128 \times 241$, representing the number of grids in streamwise (x), spanwise (y), and wall normal (z) directions. The grid is stretched in the normal direction and uniform in the streamwise and spanwise directions. The length of the first grid interval in the normal direction at the entrance is found to be 0.43 in wall units ($Y^+ = 0.43$). The parallel computation is accomplished through the message passing interface (MPI) together with domain decomposition in the streamwise direction (Figure 2). The flow parameters, including Mach number and Reynolds number are listed in Table 1. Here, x_{in} represents the distance between leading edge and inlet, Lx, Ly, Lz_{in} are the lengths of the computational domain in x-, y-, and z-directions, respectively, and T_w is the wall temperature.

2.2. Code Validation. The DNS code—"DNSUTA" has been validated by NASA Langley and UTA researchers [24, 32, 34] carefully to make sure the DNS results are correct.

TABLE 1: Flow parameters.

M_∞	Re	x_{in}	Lx	Ly	Lz_{in}	T_w	T_∞
0.5	1000	$300.79\,\delta_{\text{in}}$	$798.03\,\delta_{\text{in}}$	$22\,\delta_{\text{in}}$	$40\,\delta_{\text{in}}$	273.15 K	273.15 K

2.2.1. Comparison with Linear Theory. Figure 3 compares the velocity profile of the T-S wave given by our DNS results to linear theory. Figure 4 is a comparison of the perturbation amplification rate between DNS and LST. The agreement between linear theory and our numerical results is quite good.

2.2.2. Grid Convergence. The skin friction coefficient calculated from the time-averaged and spanwise-averaged profile on a coarse and fine grid is displayed in Figure 5. The spatial evolution of skin friction coefficients of laminar flow is also plotted out for comparison. It is observed from these figures that the sharp growth of the skin-friction coefficient occurs after $x \approx 450\delta_{\text{in}}$, which is defined as the "onset point." The skin friction coefficient after transition is in good agreement with the flat-plate theory of turbulent boundary layer by Cousteix in 1989 [35]. Figures 5(a) and 5(b) also show that we get grid convergence in skin friction coefficients.

2.2.3. Comparison with Log Law. Time-averaged and spanwise-averaged streamwise velocity profiles for various streamwise locations in two different grid levels are shown in Figure 6. The inflow velocity profiles at $x = 300.79\delta_{\text{in}}$ is a typical laminar flow velocity profile. At $x = 632.33\delta_{\text{in}}$, the mean velocity profile approaches a turbulent flow velocity profile (log law). This comparison shows that the velocity profile from the DNS results is a turbulent flow velocity profile and the grid convergence has been realized.

2.2.4. Spectra and Reynolds Stress (Velocity) Statistics. Figure 7 shows the spectra in x- and y-directions. The spectra are normalized by z at location of $\text{Re}_x = 1.07 \times 10^6$ and $y^+ = 100.250$. In general, the turbulent region is approximately defined by $y^+ > 100$ and $y/\delta < 0.15$. In our case, The location of $y/\delta = 0.15$ for $\text{Re}_x = 1.07 \times 10^6$ is corresponding to $y^+ \approx 350$, so the points at $y^+ = 100$ and 250 should be in the turbulent region. A straight line with slope of $-3/5$ is also shown for comparison. The spectra tend to tangent to the $k^{-5/3}$ law.

Figure 8 shows Reynolds shear stress profiles at various streamwise locations, normalized by square of wall shear velocity. There are 10 streamwise locations which are selected starting from leading edge to trailing edge. As expected, close to the inlet at $\text{Re}_x = 326.8 \times 10^3$ where the flow is laminar, the values of the Reynolds stress is much smaller than those in the turbulent region. The peak value increases with the increase of x. At around $\text{Re}_x = 432.9 \times 10^3$, a big jump is observed, which indicates the flow is in transition. After $\text{Re}_x = 485.9 \times 10^3$, the Reynolds stress profile becomes close to each other in the turbulent region. So for this case, we can consider that the flow transition starts after $\text{Re}_x = 490 \times 10^3$.

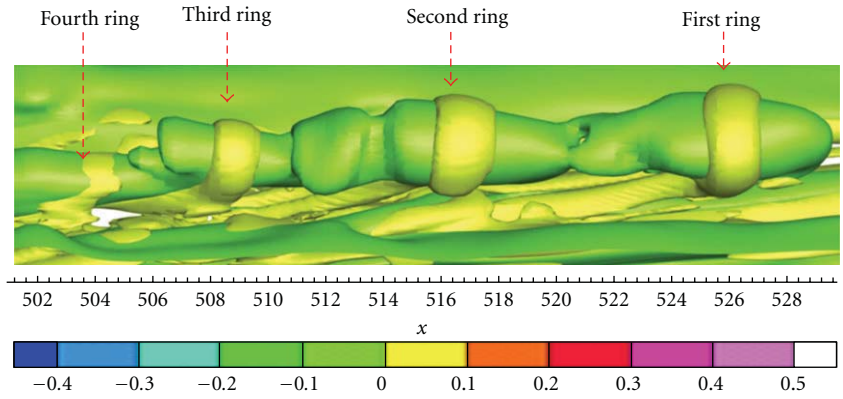

Figure 16: Three-dimensional momentum deficit and multiple ring-like vortex formation.

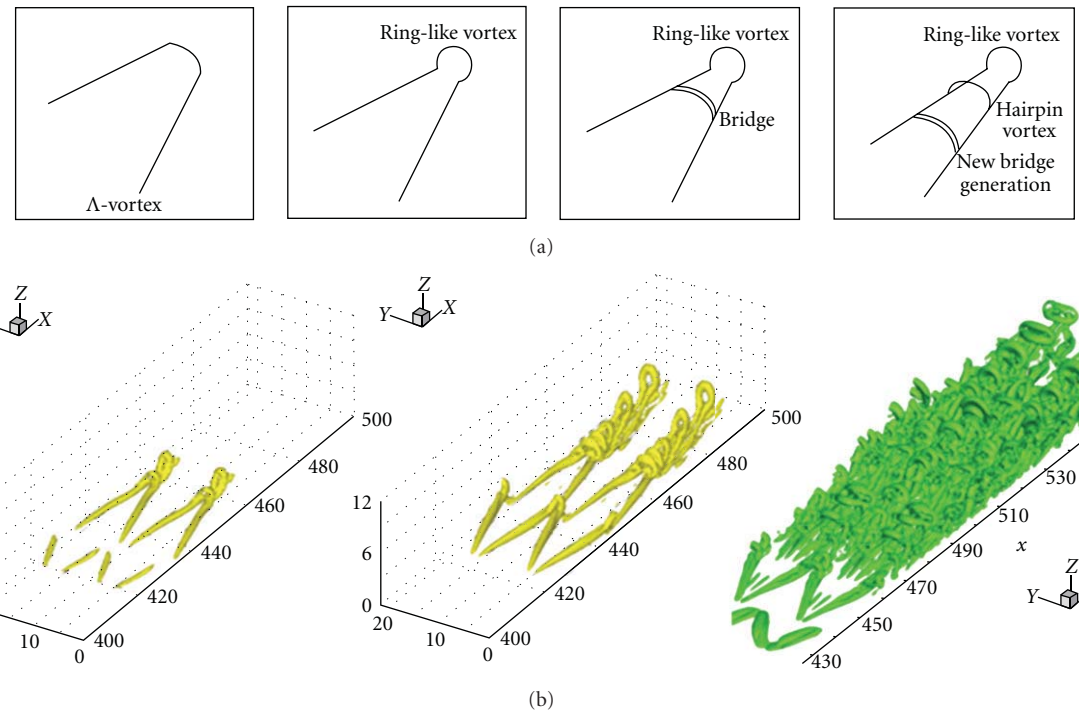

Figure 17: (a) Sketch for mechanism of multiring generation, (b) multiple ring formation.

2.2.5. Comparison with Other DNS. Although we cannot compare our DNS results with those given by Borodulin et al. [4] quantitatively, we still can find that the shear layer structure are very similar in two DNS computations in Figure 9.

2.2.6. Comparison with Experiment. By this λ_2-eigenvalue visualization method, the vortex structures shaped by the nonlinear evolution of *T-S* waves in the transition process are shown in Figure 10. The evolution details are briefly studied in our previous paper [20] and the formation of ring-like vortices chains is consistent with the experimental work ([5], Figure 11) and previous numerical simulation by Bake and his coauthors [15].

2.2.7. U-Shaped Vortex in Comparison with Experimental Results. Figure 12(a) [19] represents an experimental investigation of the vortex structure including ring-like vortex and barrel-shaped head (U-shaped vortex). The vortex structures of the nonlinear evolution of *T-S* waves in the transition process are given by DNS in Figure 12(b). By careful comparison between the experimental work and DNS, we note that the experiment and DNS agree with each other in a detailed flow structure comparison. This cannot be obtained by accident, but provides the following clues: (1) both DNS and experiment are correct, (2) disregarding the differences in inflow boundary conditions (random noises versus enforced *T-S* waves) and spanwise boundary conditions (nonperiodic versus periodic) between experiment and DNS, the vortex

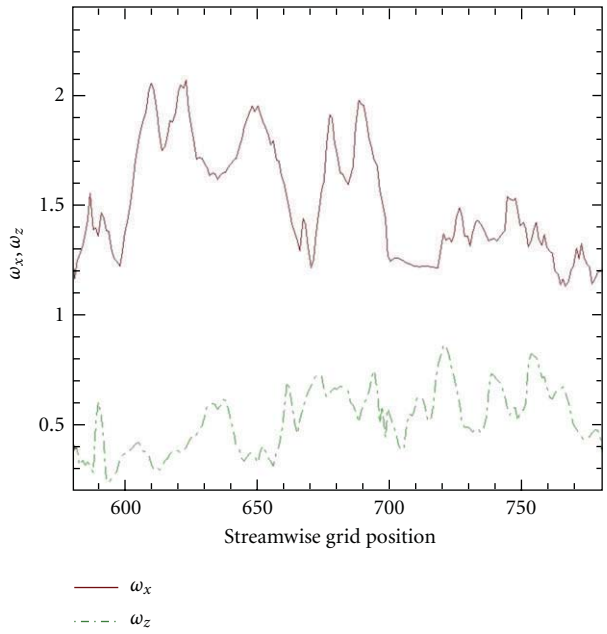

FIGURE 18: Maximum streamwise and spanwise vorticity along x-coordinate (Helmoholtz vorticity conservation).

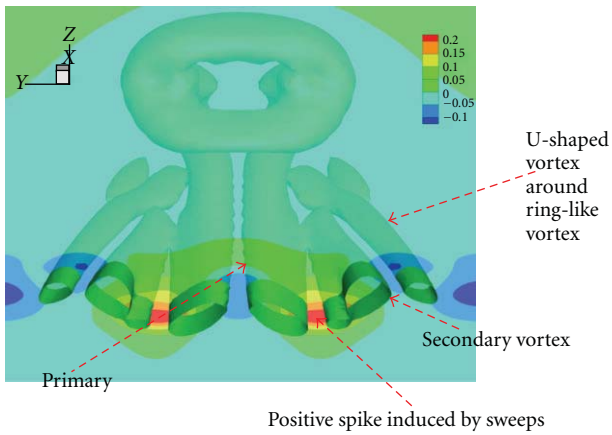

FIGURE 19: U-shaped vortex with streamwise velocity perturbation contour.

structures are same, (3) no matter K-, H- or other types of transition, the final vortex structures are same, (4) there is a universal structure for late boundary layer transition; (5) turbulence has certain coherent structures (CS) for generation and sustenance.

All these verifications and validations above show that our code is correct and our DNS results are reliable.

3. Observation and Analysis done by Our DNS

Following observations have been made and reported by our previous publications [20–28, 30–32, 36, 37].

3.1. Mechanism of Large Coherent Vortex Structure. Late boundary transition starts from the formation of the first vortex ring.

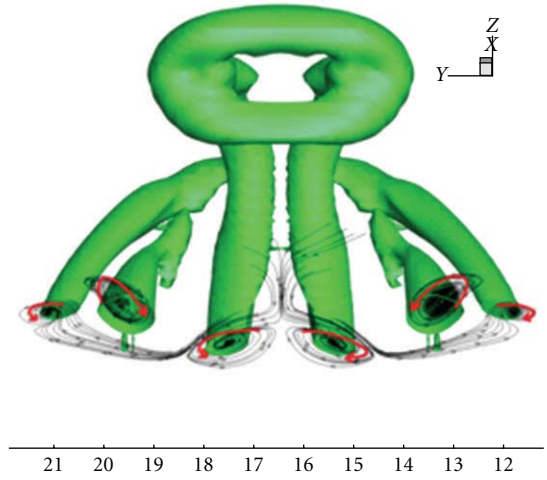

FIGURE 20: Isosurface of λ_2 and stream trace at $x = 530.348\delta_{in}$.

3.1.1. Vortex Rings in Flow Field [23]. According to Helmholtz vorticity conservation law, the vortex tube cannot have ends inside the flow field. The only form of vortex tube existing inside the flow filed must be ring with or without legs (Figure 13).

3.1.2. Mechanism of First Ring-Like Vortex Formation [23]. The ring shape of first ring-like vortex is caused by the interaction between the prime streamwise vortices and secondary streamwise vortices (Figure 14), which is quite different from the one given by Moin et al. [38]. The ring-like vortex is located at the edge of the boundary layer or in other words located in the inviscid zone ($z = 3.56, U = 0.99Ue$). The vortex ring is perpendicularly standing and the shape of the ring is almost perfectly circular, which will generate the strongest downwash sweeps (Figures 14 and 15). More important, no vortex "pinch off" is observed.

3.1.3. Mechanism of Multiple Ring Formation [37]. The ejection by rotation of the primary vortex legs brings low speed flow from lower boundary layer up and forms a cylinder-like momentum deficit zone in the middle of the two legs (green in Figure 16). The momentum deficit zone is also located above the legs and forms shear layers due to the stream-wise velocity difference between surrounding high-speed flow and low-speed flow in the deficit zone. These shear layers are not stable and multiple ring-like vortices (yellow in Figure 16) are generated by the shear layers one by one (Figure 17). This process must satisfy the Helmholtz vorticity conservation and the primary streamwise vorticity must be reduced when a new spanwise-oriented ring is formed (Figure 18). Different from Borodulin et al. [4], neither "vortex breakdown and reconnection" nor "Crow theory" is observed by our new DNS.

3.1.4. Primary, Secondary, and U-Shaped Vortices [31]. U-shaped vortex is part of large coherent vortex structure and is generated by secondary vortices which are induced by the

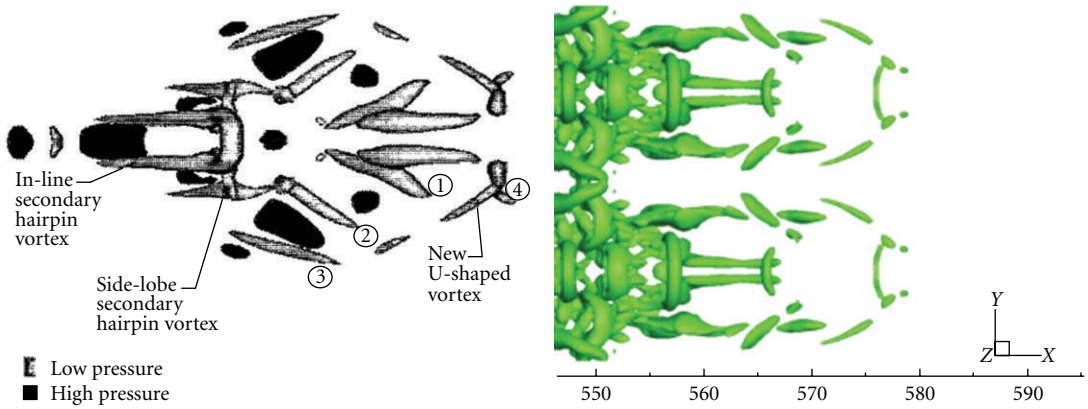

Figure 21: (a) U-shaped vortex [9], (b) DNS with a different λ-value (fake).

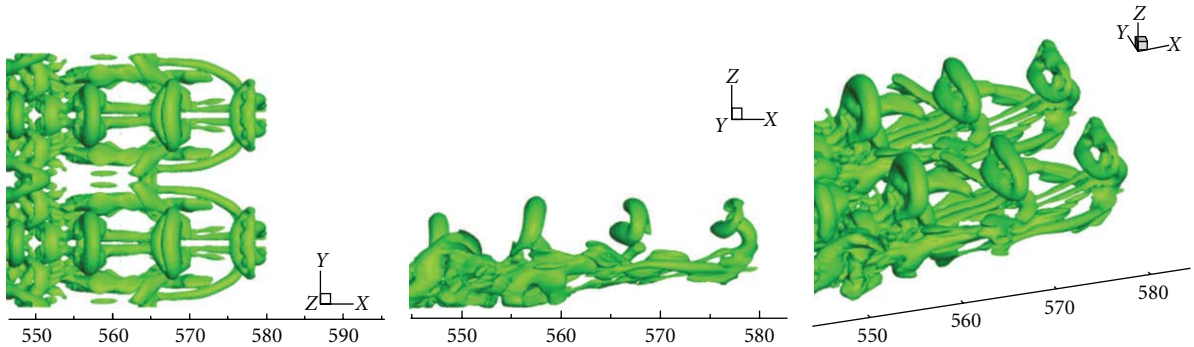

Figure 22: View of young turbulence spot head from different directions ($t = 8.8T$).

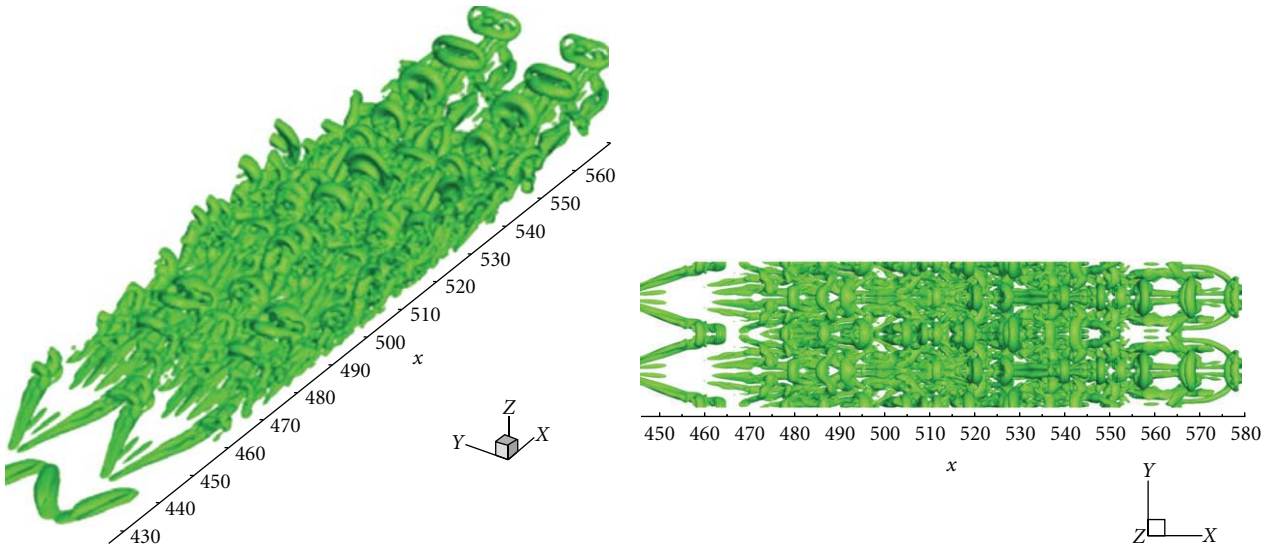

Figure 23: 3D angle view and 2D top view of the young turbulence spot ($t = 8.8T$).

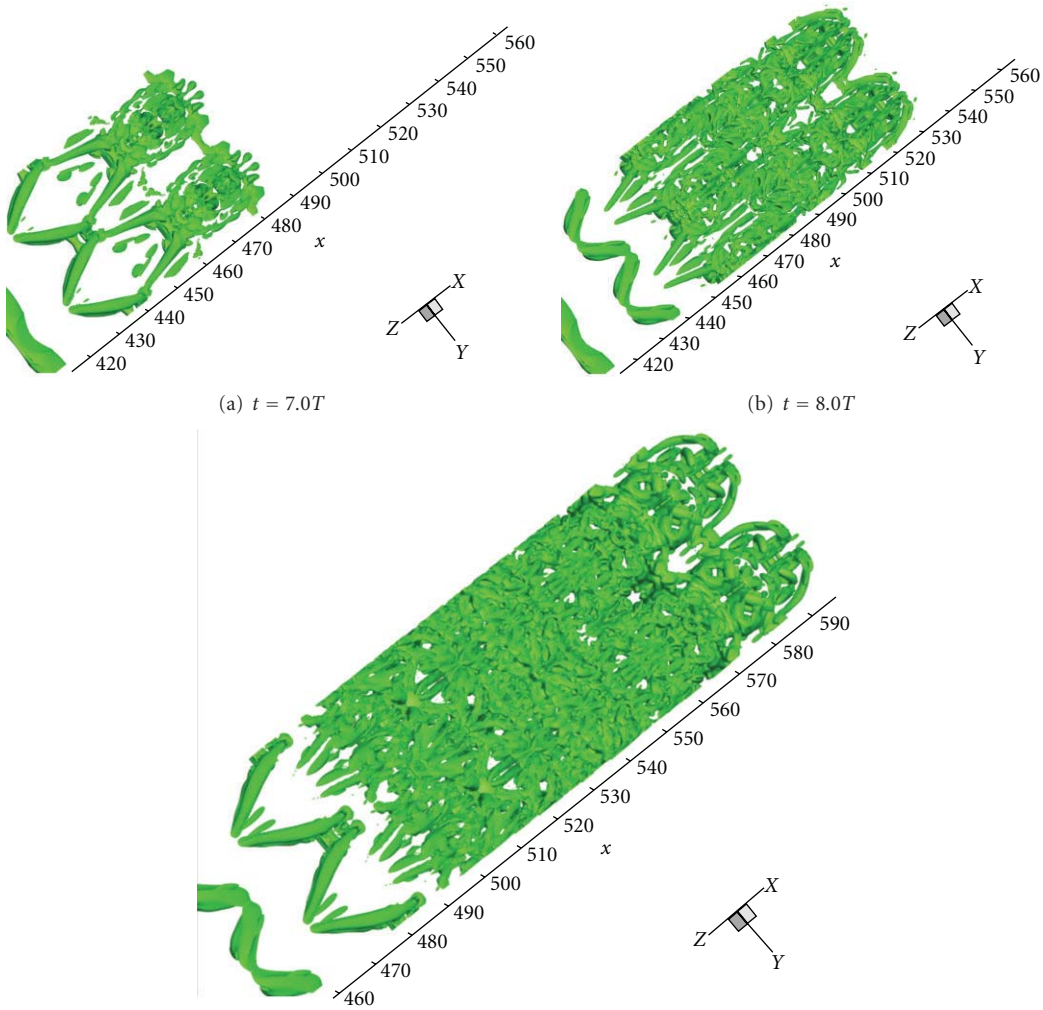

(a) $t = 7.0T$ (b) $t = 8.0T$

(c) $t = 8.8T$

FIGURE 24: Small length scale vortex generation at different time steps (view up from bottom): small length scale vortices are generated by the solid wall near the ring necks from the beginning to the end.

primary vortex. Being different from Guo et el. [19], the U-shaped vortex is not a wave and is not induced by second sweeps and positive spikes. Actually, the U-shaped vortex is a tertiary (not secondary) vortex with same vorticity sign as the original ring legs (Figures 19 and 20). In addition, the U-shaped vortices serve as additional channels to supply vorticity to the multiple ring structure [32].

3.2. Mechanism of Small Length Vortices Generation. Turbulence has two futures: (1) small length vortices; (2) nonsymmetric structure (Randomization).

3.2.1. "Vortex Breakdown to Turbulence" is Challenged [29, 30]. In the new DNS [27, 28], it has been observed that the multiple vortex structure is a quite stable structure and never breaks down. Previously reported "vortex breakdown" is either based on 2-D visualization or made by using low pressure center as the vortex center (Figure 21(a)). We can use a different λ_2 value to get similar "vortex breakdown" (Figure 21(b)), which is faked. Here, we define vortex as a tube with a rotated core and isosurfaces of constant vorticity flux. However, there is no evidence that the vortex breaks down. Let us look at the head of the so-called "turbulence spot" from different directions of view (Figure 22). Due to the increase of the ring (bridge) number and vorticity conservation, the leading rings will become weaker and weaker until they cannot be detected, but they never break down (see Figure 23).

3.2.2. Mechanism of Small-Length Scale (Turbulence) Generation—by "Shear Layers" [30, 32]. The question will be raised that where do the small length scales come from if the small vortices are not generated by "vortex breakdown"? Since we believe that the small vortices are generated by shear layers near the wall surface, we take snap shots in the direction of view from the bottom to top (Figure 24). The evidence provided by our new DNS confirms that the small length scale vortices are generated near the bottom of the

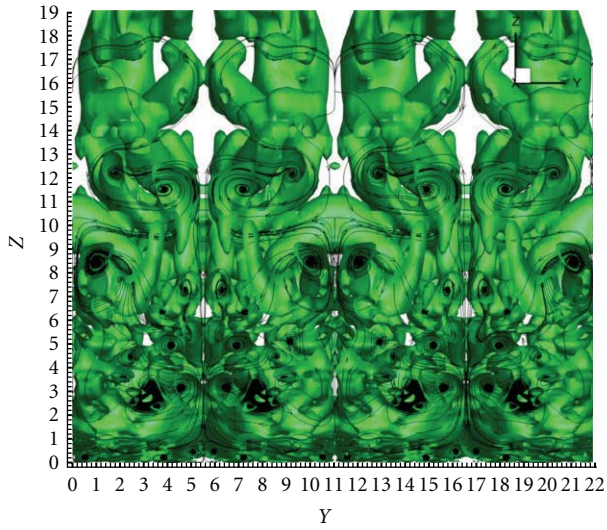

(a) λ_2 isosurfaces

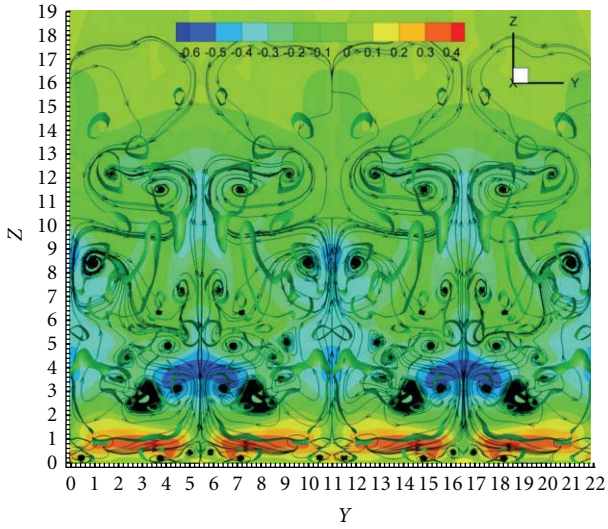

(b) Contour of velocity perturbation

FIGURE 25: Visualization of isosurface λ_2 and velocity perturbation at $x = 508.633$ for (Y, Z)-Plane $t = 15T$.

boundary layer. Being different from classical theory which believes turbulence is generated by "vortex breakdown", our new DNS found that all small length scales (turbulence) are generated by high-shear layers (HS) near the bottom of the boundary layers. There is no exception. When we look at the later stage of flow transition at $t = 15T$, we can see that all small length scales are located around the high-shear layers, especially at those near the wall surface (Figures 25 and 26).

3.2.3. High-Shear Layer Formation by Sweeps [30]. Experiment and our numerical results have confirmed that there is a second sweep excited by every ring-like vortex (Figure 27). Combined with the first sweep generated by the original λ vortex legs, it forms strong positive spikes which generate strong high shears at the bottom of the boundary layer (red in Figure 28). Figures 29 and 30 are contours of isosurface of λ_2 and velocity perturbation at $x = 508.66$. The second sweep movement induced by ring-like vortices working together with first sweep will lead to huge energy and momentum transformation from high-energy inviscid zones to low-energy zones near the bottom of the boundary layers and we can observe that all small length scales are generated around high shear layers between the positive spike (momentum increment) and solid wall surface.

3.2.4. Multiple-Level Sweeps and Multiple-Level Negative and Positive Spikes [32]. The positive spikes (momentum increment) could generate new ring-like vortices. The new ring-like vortices can further generate new sweeps and form new positive spikes (Figure 31) at the location which are very close to the bottom of the boundary layer (laminar sublayer). The new positive spike could induce new smaller vortex rings by unstable shear layers. These multilevel sweeps and multilevel negative and positive spikes provide channels for energy transfer from the inviscid area (high energy area) down to the bottom (low energy area). This is the mechanism why turbulence can be generated and sustained. This mechanism can be interpreted as a universal mechanism for both transitional and turbulent flow in a boundary layer.

3.2.5. Energy Transfer Paths and Universal Turbulence Spot Structure [32]. Figures 32 and 33 are sketches describing energy transfer and likely universal turbulence structure.

3.2.6. Surface Friction. Figure 34 is a time and spanwise averaged surface friction coefficient (CF). From the figure, it is clearly seen that there is a jump starting at $x = 430$ which indicates an onset of flow transition and reach a maximum value at $x = 508.663$. It is conventionally believed that the CF is large in the turbulent area and small in the laminar area due to the strong mixing in turbulent flow. That is the reason why most turbulence models are formulated based on change of turbulent viscosity. However, from Figure 34, it is easy to find that the CF reaches maximum in a laminar area and is not directly related to mixing. Further analysis found the viscosity is not changed for incompressible flow, but the shear layer is changed sharply when the first and second sweeps caused positive spikes (momentum increment), HS layers and consequent small vortices generations. The velocity gradients suddenly jump to a very large level in the laminar sub-layer and then the CF becomes very large. Therefore, the CF jump is not caused by mixing or viscosity coefficients increase, but is, pretty much, caused by velocity gradient jump due to small vortices formation.

3.3. Loss of Symmetry (Randomization). The existing theory [41] believes that the flow randomization in DNS is caused by the background noises and removal of periodic boundary conditions. They believe that randomization starts from loss of symmetry, which is caused by background noise. According to their theory, the ring tip is affected first, which rapidly influences the small length scale structure. This will

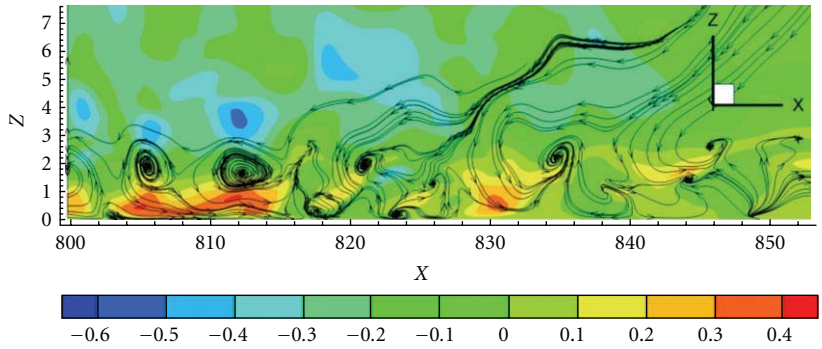

Figure 26: Visualization of isosurface λ_2 and velocity perturbation at $y = 4$ for (X, Z)-Plane $t = 15T$.

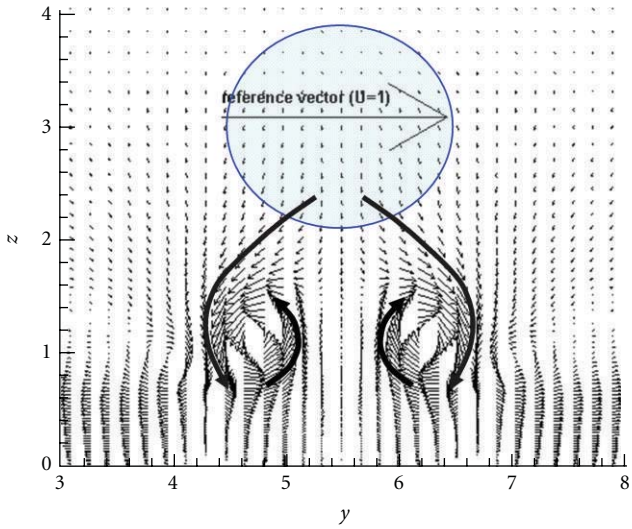

Figure 27: Velocity vector field.

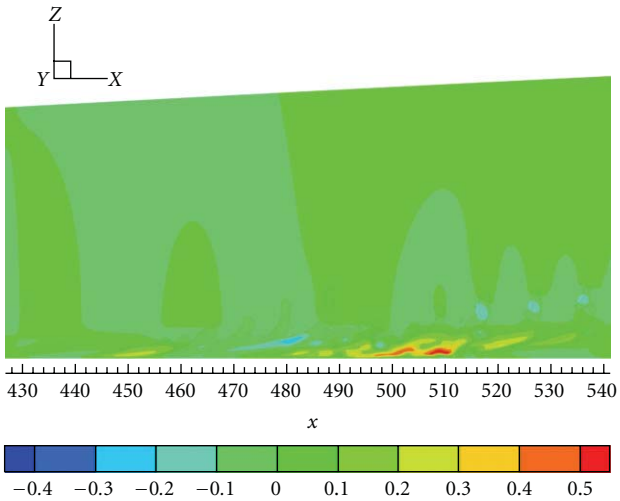

Figure 28: Vorticity distribution at $x = 508.633$.

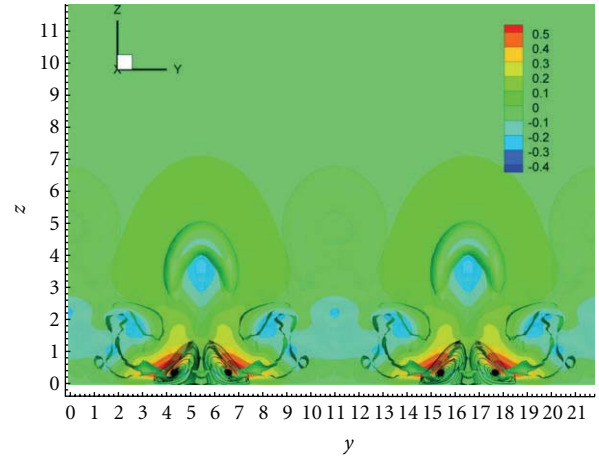

Figure 29: :Isosurface of λ_2 and velocity at $x = 508.66$.

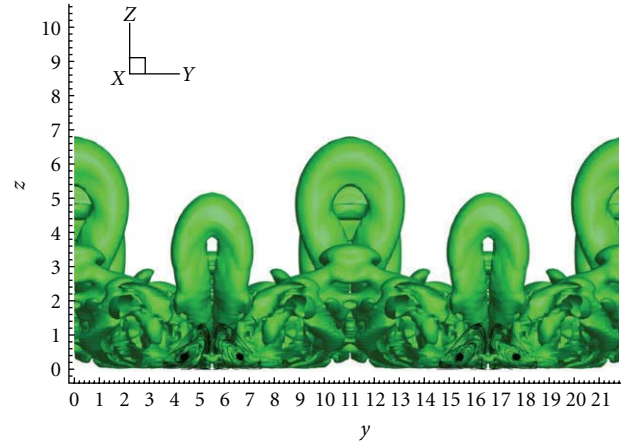

Figure 30: Isosurface of λ_2 and stream traces at $x = 508.66$.

lead to loss of symmetry and randomization for the whole flow field quickly.

However, what we observed in our new DNS is that the loss of symmetry starts from second level rings (Figure 35) while the top and bottom rings are still symmetric

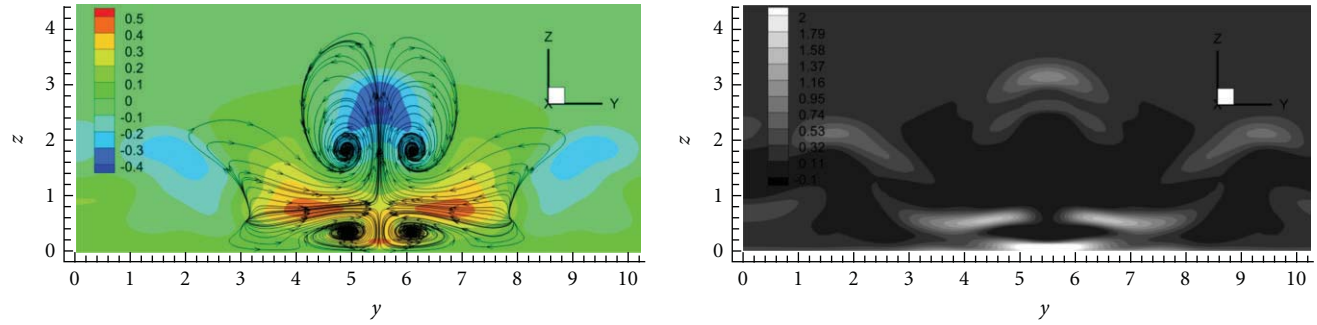

(a) Streamwise velocity perturbation and stream trace

(b) Spanwise vorticity distribution

Figure 31: (a) Multilevel sweeps; (b) multilevel positive spikes.

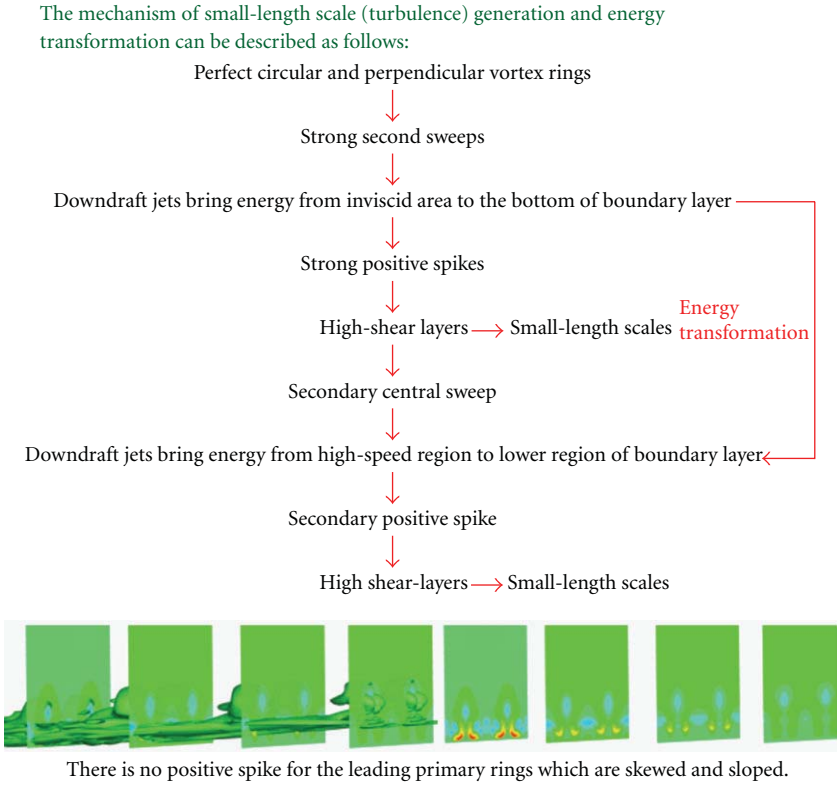

Figure 32: Energy transfer paths and universal structure for turbulence.

(Figure 36). The nonsymmetric structure of second level rings will influence the small length scale at the bottom quickly. The change of symmetry in the bottom of the boundary layer is quickly spread to the up level through ejections. This will lead to randomization of the whole flow field. Therefore, the internal instability of multiple level ring spot overlapping structure, especially the middle ring cycles, is a critical reason for flow randomization, but mainly not the background noise. In addition, the loss of symmetry starts in the middle of the flow domain, not the inflow and not the outflow (Figure 37(a)). As mentioned, we did not change the periodic boundary conditions and the solution is still periodic in the spanwise direction (period = 2π is enforced). In addition, we did not add any additional background noise or inflow perturbation. However, we found that the flow lost symmetry first and then was randomized step by step (see Figures 38(a)–38(d)). The flow was first periodic (period = π) and symmetric in the spanwise direction, $\sum_{k=0}^{n} a_k \cos(2ky)$, but then lost symmetry in some areas, and finally everywhere. It was periodic with a period of π, same as the inflow, but changed with a period of 2π. The flow is still periodic because we enforced the periodic boundary condition in the spanwise direction with a period of 2π. This means the flow does not only have $\sum_{k=0}^{n} a_k \cos(2ky)$ but also has $\sum_{k=0}^{n} b_k \sin(2ky)$ which is newly generated. Meanwhile, flow lost periodicity with period = π, but has to be periodic with period = 2π (Figures 38(c) and 38(d)), which we enforced. Since the DNS study is focused on the mechanism

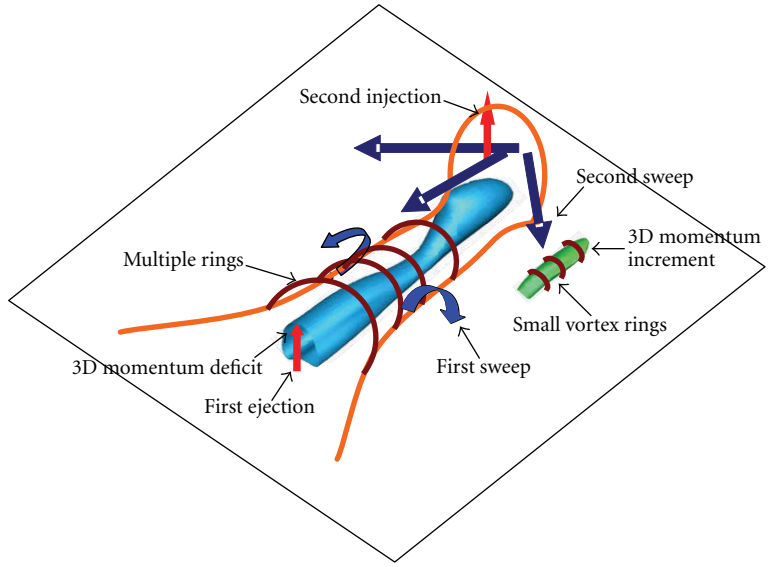

Figure 33: Sketch of mechanism of multiple rings formation and small vortices formation.

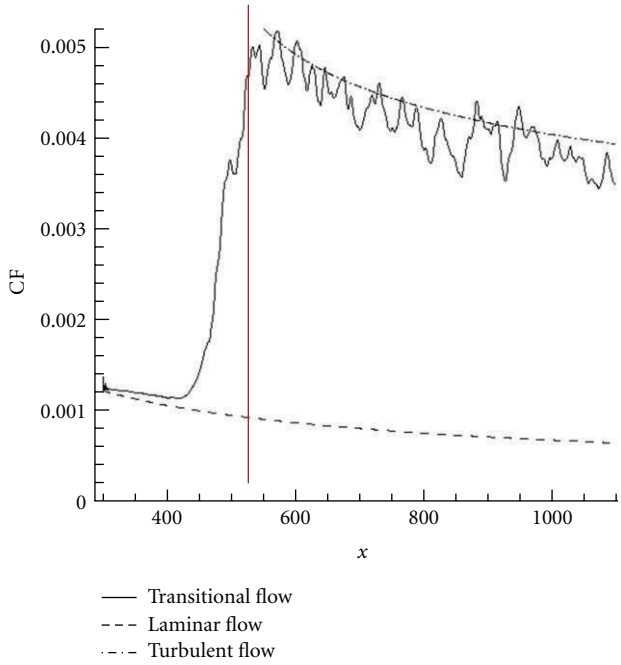

Figure 34: Maximum CF at $x = 508.633$ (Laminar).

of randomization and the DNS computation only allows use of two periods in the spanwise direction, we consider that the flow is randomized when the symmetry is lost and period is changed from π to 2π (Figures 38(a) and 38(b)):

$$f(y) = \sum_{k=0}^{n} a_k \cos(2ky) + \sum_{k=1}^{n-1} b_k \sin(2ky) + \sum_{k=0}^{n-1} c_k \cos(2ky + y) + \sum_{k=0}^{n-1} d_k \sin(2ky + y). \quad (2)$$

In real flow, there is no such a restriction of periodic boundary condition in the spanwise direction. A more detailed discussion about the mechanism of flow randomization will be given by another AIAA 2012 paper [36].

4. Summary of Our DNS Findings

4.1. Our New Observations. Since turbulence generation and sustenance are one of the top secret in nature, this research will bring significant impact on fundamental fluid mechanics as the classical theory and dominant concepts on late flow transition and turbulence structure are challenged. Table 2 gives a comparison of classical theory and currently dominant conclusions with the observation by our DNS.

4.2. New Theory on Turbulence Formation and Sustenance by Liu

4.2.1. Classical Theory on Turbulence. A turbulent flow is characterized by a hierarchy of scales through which the energy cascade takes place. According to Richardson, turbulence is random interactions of "eddies" as "big whorls have little whorls, little whorls have smaller whorls, that feed on their velocity, and so on to viscosity" (Figure 39 by [39]). On the other hand, vortex stretching is the core mechanism on which the turbulence energy cascade relies to establish the structure function. According to Richardson (1928) and Kolmogorov [6, 7], the radial length scale of the vortices decreases and the larger flow structures breakdown into smaller structures (Figure 40 by [40]). The process continues until the small-scale structures are small enough to the extent where their kinetic energy is overwhelmed by the fluid's molecular viscosity and dissipated into heat.

Richardson's energy cascade theory has several important points of view which can be summarized as follows:

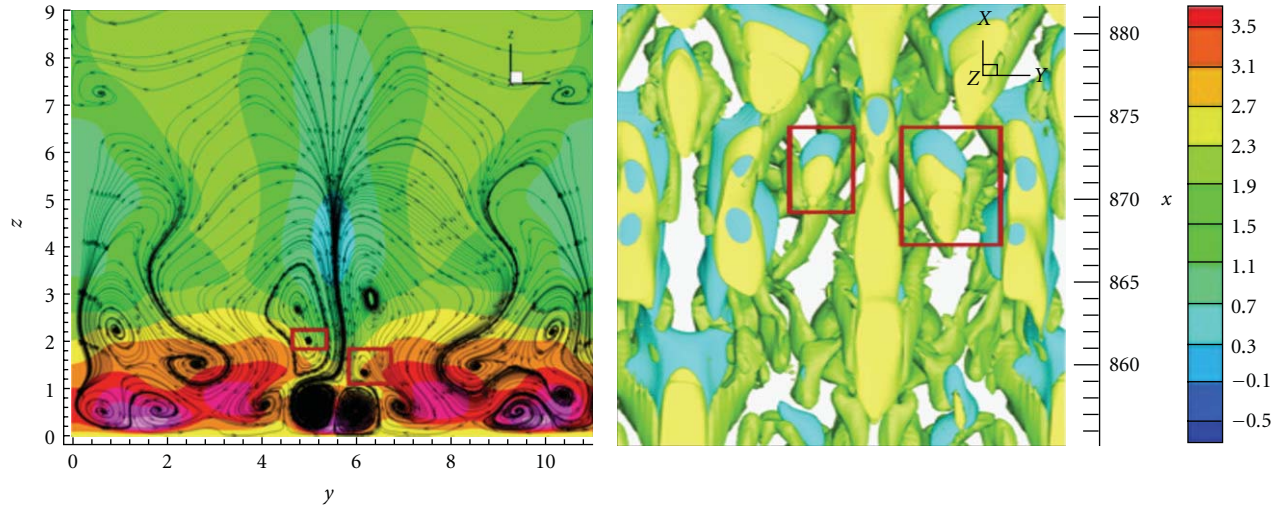

(a) Section view in y-z plane

(b) Bottom view of positive spike

FIGURE 35: The flow lost symmetry in second level rings and bottom structure at $t = 15.0T$.

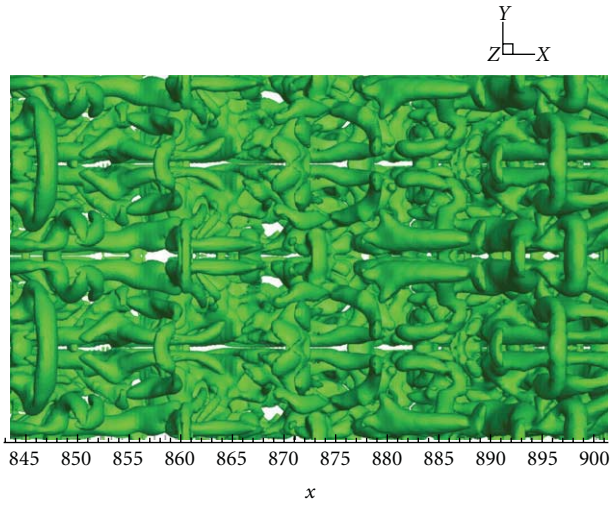

FIGURE 36: The top ring structure is still symmetric at $t = 15.0T$.

(1) stremwise vortex is stretching;

(2) vortex must break down to smaller structure due to the stretching;

(3) energy transfers from large vortex to smaller one through "vortex breakdown;"

(4) these smaller vortices continue the same process until the smallest one appears (Kolmgorov's length scale) in which viscosity is dominant;

(5) the micro-scale η (Kolmogorov scale) is several order smaller than the macro-scale L (main flowscale) and the middle length scales r ($\eta \ll r \ll L$) are basically inertial.

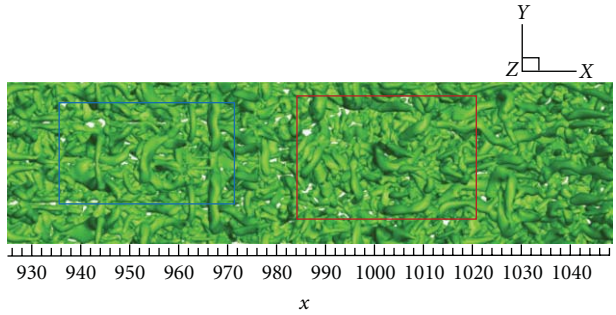

(a) Top ring structure lost symmetry (blue area is symmetric but red area is not)

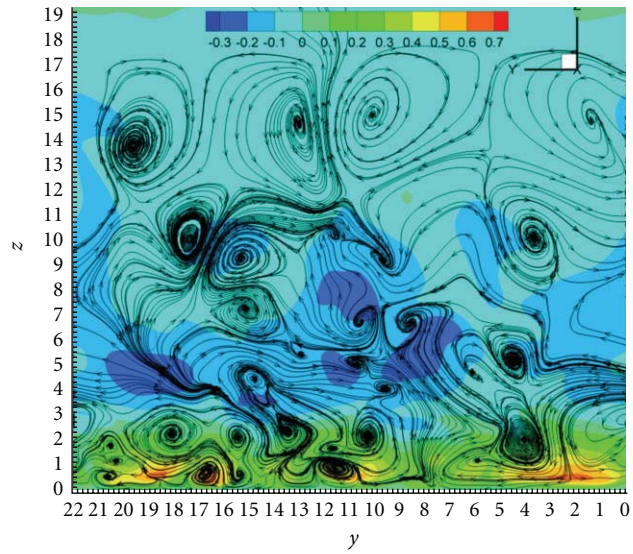

(b) Symmetry loss in the whole section of y-z plane

FIGURE 37: The whole flow field lost symmetry at $t = 21.25T$.

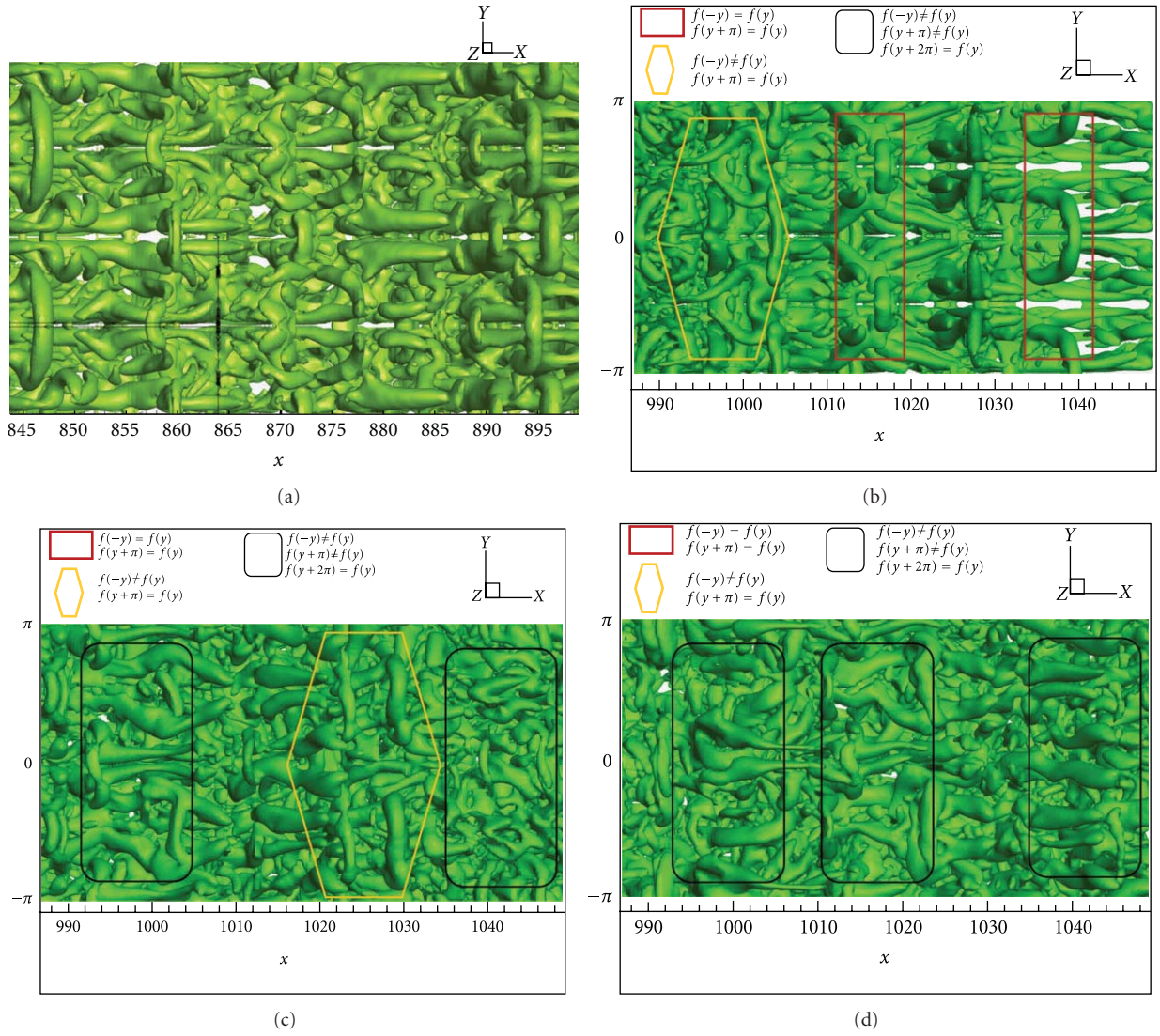

Figure 38: (a) Whole domain is symmetric and periodic —$a \times \cos 2y$ (the period = π; spanwise domain is $-\pi < y < \pi$), (b) symmetric and asymmetric—redrectangular: periodic and symmetric at $y = -\pi/2, 0, \pi/2$, that is, $f(-\pi/2 - y) = f(-\pi/2 + y)$, $f(-y) = f(y)$, $f(\pi/2 - y) = f(\pi/2 + y)$; yellow diamond: periodic, $f(y + \pi) = f(y)$, period = π; but asymmetric $f(-y) \neq f(y)$; the spanwise domain is $-\pi < y < \pi$, (c) periodic but asymmetric—yellow diamond: periodic, period = π; black box: periodic but period = 2π; the spanwise domain is $-\pi < y < \pi$. (d) Periodic but asymmetric—all black boxes: periodic but asymmetric (period = 2π); the spanwise domain is $-\pi < y < \pi$.

4.2.2. New Observations and Analyses. On the other hand, our new observations can be described as follows:

(1) stremwise vortex is stretched but never breaks down;

(2) vortex has strong rotation which causes strong mixing;

(3) in the middle of two vortex legs, there is a low-speed zone formed by ejection from boundary layer bottom to bring momentum deficit up to this area. This momentum deficit forms a long-shear layer;

(4) this shear layer in the middle of two legs is unstable and multiple rings with spanwise vorticity will form one by one to generate multiple rings near the inviscid region due to the shear layer instability especially near the narrowed vortex neck where rotation is very strong and the low speed momentum deficit is large. In this process, Helmholtz vorticity conservation must be satisfied;

(5) in the two sides of the vortex legs, high-speed zones are formed by sweeps which bring high energy (energy increment) from inviscid area to the near wall region. The energy increment will form shear layers near the wall;

(6) the momentum increment shear layers near the wall are unstable (shear layer instability) and will form multiple smaller ring-like vortices;

(7) these newly generated large and smaller vortices will continue a similar process to generate smaller ring-like vortices until the vortex size is too small and

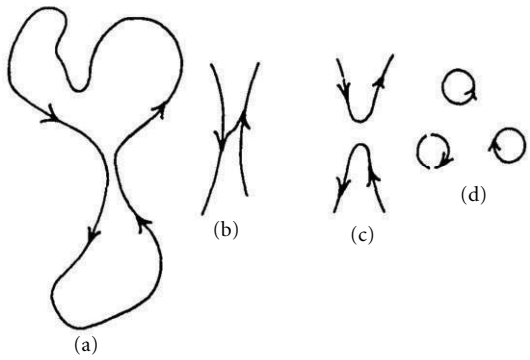

Figure 39: Sketch of vortex breakdown [39] (Tsubota et al, 2009). A vortex ring (a) can break up into smaller rigs if the transition between states (b) and (c) allowed when the separation of vortex lines becomes of atomic dimensions. The eventual small rings (d) may be identical to rotons.

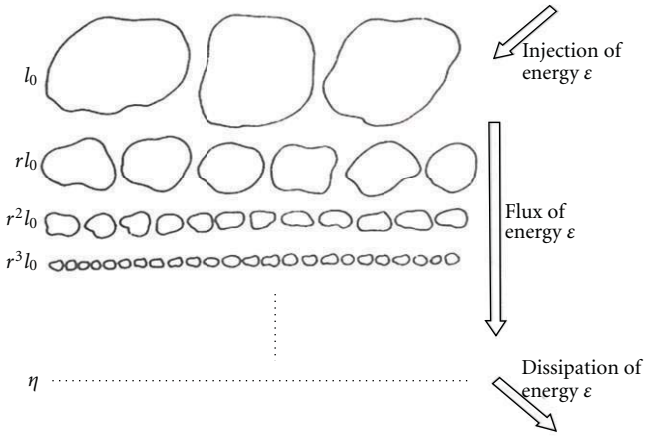

Figure 40: Sketch of Richardson cascade process [40].

the new shear layer becomes stable. The shear layer stability analysis should be further studied;

(8) energy is transferred from the large size vortices to small size vortices through multiple level sweeps. Dissipation is inevitable during the energy transfer;

(9) all smaller vortices are newly generated by shear layer instability, but not by original vortex "breakdown;"

(10) smallest length scales are all generated near the wall surface which must be related to the surface configuration and cannot be "isotropic;"

(11) surface drag is determined by small length scale generation, which must be closely related to turbulence modeling;

(12) "shear layer" control is the key issue for flow transition control, turbulent flow control, and drag reduction.

4.3. Possible Impact on Fluid Mechanics

4.3.1. Impact on Fundamental Fluid Mechanics. Since turbulence generation and sustenance are one of the top mysteries in nature, this research will bring significant impact on fundamental fluid mechanics as the classical theories on late flow transition and turbulence structure are challenged. LBLT classical theory, Richardson eddy cascade, Kolmogorov first and second hypotheses should be all revisited.

4.3.2. Impact on DNS and LES. As shown by the new DNS, it is not observed that "Kolmogorov scale" is the smallest turbulence scale but is found that the smallest length scale is determined by "shear layer instability". The estimate of energy containing scale, $\eta_{\min}/\eta_{\text{ref}} = (1/\text{Re})^{3/4}$, is too conservative. For example, an engineering hydrodynamics problem has commonly a Reynolds number, $\text{Re} = 10^8$. Considering 3D in space and 1D in time, the requirement for computation would be $Q = \text{Re}^{4\times 3/4} = (10^8)^3 = 10^{24}$. This is apparently impossible for any currently available computer or any near future computers. However, researchers in US National Research Labs and many others around the world do "implicit LES" which is really "coarse grid DNS". They do DNS, but are afraid to call DNS but "ILES". The reason is that they are afraid of "Kolmogorov scale." Since we could not find that energy is transformed from large vortices to small vortices by "vortex breakdown", "Kolmogorov scale" would lose solid scientific foundation and must be revisited. This will provide guidance to DNS which is supposed to resolve all energy-contained small length scales and LES which is expected to resolve the large eddies and model the subgird scales.

4.3.3. Impact on Turbulence Modeling. The eddy viscosity turbulence model is mainly based on "Boussinesq Assumption" (1872) that the nonlinear perturbation terms can be modeled by resolved mean scales with new turbulent coefficients of viscosity. However, most turbulence models are still empirical and case-related. The right turbulence models can be developed with deep understanding of turbulence generation and sustenance. As shown by our DNS, the perturbation and small length scales are not isotropic but configuration related. Yes, Prandtl may be right that the turbulence can be described by "mixing lengths" which represent the length of different size vortices. Although Prandtl's "mixing length" model is an old concept [42], turbulence is really generated by mixing of variety of different size vortices and the "mixing length" concept coincides with physics. The serious question is how to find the right size of "mixing length". We should develop a new "mixing length" model based on DNS data and "shear layer stability" analysis.

4.3.4. Impact on Flow Control of Flow Transition and Turbulence. Flow transition and turbulence control should be based on right understanding on flow transition and turbulence structure. Based on our observation, it is proposed to cut the energy transfer channels for high shear layer generation to stop or delay turbulence generation. It is also found that the "shear layer instability" is the "mother of turbulence." Apparently, control of shear layer formation and structure is the key issue to the control of the

Table 2: Comparison of classical theory and our DNS observation.

Topic	Classical or existing theory	Observation of our DNS
Turbulence generation	By "vortex breakdown"	Not by "vortex breakdown" but by shear layer instability
First-ring generation	Self-induced, deformed, inclined, and pinched-off	By counter-rotated vortices interaction, circular, perpendicular, no pinch-off
Multiple-ring structure	"Crow theory" or breakdown and then reconnected	No breakdown, not "Crow theory" but momentum deficit caused by ejection, vorticity conservation
Multiple-level high shears	No report	By multiple-level sweeps and ejections
Energy transfer channel, turbulence sustenance	Energy transfers from larger vortices to smaller one through "vortex breakdown" without dissipation until viscosity	From inviscid flow down to bottom by multilevel sweeps
U-shaped vortex	Head wave, secondary vortex, by second sweep, newly formed, breakdown	Not head wave, tertiary vortex, by secondary vortex, existing from beginning, never breakdown
Randomization	Background noise, starting from the top ring and then going down to the bottom	Internal property, starting from second level rings in the middle, affects bottom and then up to affect top rings. Loss of symmetry maybe caused by C-K shift
Coefficients of friction	Turbulent flow has large friction due to strong boundary layer mixing	Depending only on velocity profile changes in laminar sublayer, no matter turbulent or laminar
Richardson eddy cascade	Classical theory	Not observed
Vortex breakdown	Classical theory	Not observed
Kolmogorov scale	Classical theory	Smallest length scale should be determined by minimum shear layer instability

transitional flow and fully developed turbulent flow. It is also an important way for drag production of turbulent flow, for example, why oscillating wall and rough wall with riblets can reduce the surface drag.

5. Conclusions

In our recent DNS work [20–32, 36, 37] we have made a number of new findings on late flow transition in a boundary layer including the mechanism of large vortex structure formation, small-length scale generation and flow randomization (loss of symmetry).

New theory on flow transition and turbulence generation and sustenance has been given by Liu. Instead of four steps, that is, receptivity, linear instability, non-linear growth, vortex breakdown to turbulence, described by classical theory, Liu proposed a new theory with five steps, that is, receptivity, linear instability, large vortex formation, small length scale generation, loss of symmetry and randomization to turbulence. For turbulence generation and sustenance, the classical theory, described with Richardson's energy cascade and Kolmogorov length scale, is not observed by our DNS. Liu proposed a new theory on turbulence generation that all small length scales are generated by "shear layer instability" through multiple level ejections and sweeps and consequent multiple level positive and negative spikes, but not by "vortex breakdown" which can never happen. We believe "shear layer instability" is the "mother of turbulence." Flow randomization is caused by the internal property of instability of the structure of multiple vortex-ring-spot overlapping.

Nomenclature

M_∞: Mach number
Re: Reynolds number
δ_{in}: Inflow displacement thickness
T_w: Wall temperature
T_∞: Free stream temperature
Lz_{in}: Height at inflow boundary
Lz_{out}: Height at outflow boundary
Lx: Length of computational domain along
Ly: Length of computational domain along y direction
x_{in}: Distance between leading edge of flat plate and upstream boundary of computational domain
A_{2d}: Amplitude of 2D inlet disturbance
A_{3d}: Amplitude of 3D inlet disturbance
ω: Frequency of inlet disturbance
α_{2d},α_{3d}: Two and three dimensional streamwise wave number of inlet disturbance
β: Spanwise wave number of inlet disturbance
R: Ideal gas constant
γ: Ratio of specific heats
μ_∞: Viscosity.

Acknowledgments

This work was supported by AFOSR Grant FA9550-08-1-0201 supervised by Dr. John Schmisseur and the Department of Mathematics at University of Texas at Arlington.

The authors are grateful to Texas Advanced Computing Center (TACC) for providing computation hours. This work is accomplished by using Code DNSUTA, which was released by Dr. Chaoqun Liu at University of Texas at Arlington in 2009.

References

[1] A. Marshak, *3D Radiative Transfer in Cloudy Atmospheres*, Springer, New York, NY, USA, 2005.

[2] T. Mullin, "Turbulent times for fluids," *New Scientist*, vol. 124, no. 1690, pp. 52–55, 1989.

[3] P. A. Davidson, *Turbulence: An Introduction for Scientists and Engineers*, Oxford University Press, 2004.

[4] V. I. Borodulin, V. R. Gaponenko, Y. S. Kachanov et al., "Late-stage transitional boundary-layer structures. Direct numerical simulation and experiment," *Theoretical and Computational Fluid Dynamics*, vol. 15, no. 5, pp. 317–337, 2002.

[5] C. Lee and R. Li, "Dominant structure for turbulent production in a transitional boundary layer," *Journal of Turbulence*, vol. 8, pp. 1–34, 2007, N55.

[6] A. N. Kolmogorov, "The local structure of turbulence in incompressible viscous fluid for very large Reynolds numbers," in *Proceedings of the USSR Academy of Sciences*, vol. 30, pp. 299–303, 1941.

[7] A. N. Kolmogorov, "The local structure of turbulence in incompressible viscous fluid for very large Reynolds numbers," *Proceedings of the Royal Society of London A*, vol. 434, pp. 9–13, 1991.

[8] U. Frisch, *Turbulence: The Legacy of A. N. Kolmogorov*, Cambridge University Press, New York, NY, USA, 1995.

[9] B. Singer and R. Joslin, "Metamorphosis of a hairpin vortex into a young turbulent spot," *Physics of Fluids*, vol. 6, no. 11, pp. 3724–3736, 1994.

[10] T. Herbert, "Secondary Instability of Boundary Layer," *Annual Review of Fluid Mechanics*, vol. 20, pp. 487–526, 1988.

[11] Y. S. Kachanov, "Physical mechanisms of laminar-boundary-layer transition," *Annual Review of Fluid Mechanics*, vol. 26, no. 1, pp. 411–482, 1994.

[12] L. Kleiser and T. A. Zang, "Numerical simulation of transition in wall-bounded shear flows," *Annual Review of Fluid Mechanics*, vol. 23, no. 1, pp. 495–537, 1991.

[13] D. Sandham and L. Kleiser, "The late stages of transition in channel flow," *Journal of Fluid Mechanics*, vol. 245, pp. 319–348, 1992.

[14] U. Rist and Y. S. Kachanov, "Numerical and experimental investigation of the K-regime of boundary-layer transition," in *Laminar-Turbulent Transition*, R. Kobayashi, Ed., pp. 405–412, Springer, Berlin, Germany, 1995.

[15] S. Bake, D. G. W. Meyer, and U. Rist, "Turbulence mechanism in Klebanoff transition: a quantitative comparison of experiment and direct numerical simulation," *Journal of Fluid Mechanics*, vol. 459, pp. 217–243, 2002.

[16] Y. S. Kachanov, "On a universal mechanism of turbulence production in wall shear flows," in *Notes on Numerical Fluid Mechanics and Multidisciplinary Design*, vol. 86 of *Recent Results in Laminar-Turbulent Transition*, pp. 1–12, Springer, Berlin, Germany, 2003.

[17] R. J. Adrian, "Hairpin vortex organization in wall turbulencea," *Physics of Fluids*, vol. 19, no. 4, Article ID 041301, 2007.

[18] X. Wu and P. Moin, "Direct numerical simulation of turbulence in a nominally zero-pressure-gradient flat-plate boundary layer," *Journal of Fluid Mechanics*, vol. 630, pp. 5–41, 2009.

[19] H. Guo, V. I. Borodulin, Y. S. Kachanov et al., "Nature of sweep and ejection events in transitional and turbulent boundary layers," *Journal of Turbulence*, vol. 11, pp. 1–9, 2010.

[20] L. Chen, X. Liu, M. Oliveira, D. Tang, and C. Liu, "Vortical structure, sweep and ejection events in transitional boundary layer," *Science China Physics, Mechanics and Astronomy*, vol. 39, no. 10, pp. 1520–1526, 2009.

[21] L. Chen, X. Liu, M. Oliveira, and C. Liu, "DNS for ring-like vortices formation and roles in positive spikes formation," AIAA Paper 2010-1471, Orlando, Fla, USA, 2010.

[22] L. Chen, D. Tang, P. Lu, and C. Liu, "Evolution of the vortex structures and turbulent spots at the late-stage of transitional boundary layers," *Science China*, vol. 54, no. 5, pp. 986–990, 2011.

[23] L. Chen and C. Liu, "Numerical study on mechanisms of second sweep and positive spikes in transitional flow on a flat plate," *Computers and Fluids*, vol. 40, no. 1, pp. 28–41, 2011.

[24] X. Liu, L. Chen, M. Oliveira, D. Tang, and C. Liu, "DNS for late stage structure of flow transition on a flat-plate boundary layer," AIAA Paper 2010-1470, Orlando, Fla, USA, 2010.

[25] C. Liu and L. Chen, "Study of mechanism of ring-like vortex formation in late flow transition," AIAA Paper 2010-1456, Orlando, Fla, USA, 2010.

[26] X. Liu, Z. Chen, and C. Liu, "Late-stage vortical structures and eddy motions in transitional boundary layer status," *Chinese Physics Letters*, vol. 27, no. 2, 2010.

[27] C. Liu, L. Chen, and P. Lu, "New findings by high-order DNS for late flow transition in a boundary layer," *Modelling and Simulation in Engineering*, vol. 2011, Article ID 721487, 2011.

[28] C. Liu and L. Chen, "Parallel DNS for vortex structure of late stages of flow transition," *Computers and Fluids*, vol. 45, no. 1, pp. 129–137, 2011.

[29] C. Liu, "Numerical and theoretical study on "Vortex Breakdown"," *International Journal of Computer Mathematics*, vol. 88, no. 17, pp. 3702–3708, 2011.

[30] C. Liu, L. Chen, P. Lu, and P. Liu, "Study on multiple ring-like vortex formation and small vortex generation in late flow transition on a flat plate," 2011, *Theoretical and Numerical Fluid Dynamics*. In press.

[31] P. Lu and C. Liu, "Numerical study of mechanism of u-shaped vortex formation," *Journal of Computers and Fluids*, pp. 36–47, 2012, AIAA Paper 2011-0286.

[32] P. Lu and C. Liu, "DNS study on mechanism of small length scale generation in late boundary layer transition," *Journal of Physica D*, vol. 241, no. 2012, pp. 11–24, 2011.

[33] J. Jeong and F. Hussain, "On the identification of a vortex," *Journal of Fluid Mechanics*, vol. 285, pp. 69–94, 1995.

[34] L. Jiang, C. L. Chang, M. Choudhari, and C. Liu, "Cross-validation of DNS and PSE results for instability-wave propagation," in *Proceedings of the 16th American Institute of Aeronautics and Astronautics Computational Fluid Dynamics Conference (AIAA '03)*, Orlando, Fla, USA, June 2003, AIAA Paper #2003-3555.

[35] F. Ducros, P. Comte, and M. Lesieur, "Large-eddy simulation of transition to turbulence in a boundary layer developing spatially over a flat plate," *Journal of Fluid Mechanics*, vol. 326, pp. 1–36, 1996.

[36] P. Lu, M. Thampa, and C. Liu, "Numerical study on randomization in late boundary layer transition," in *American Institute*

of Aeronautics and Astronautics Scientific Meeting (AIAA '12), Nashville, Tenn, USA, January 2012, AIAA Paper 2012-0747.

[37] P. Lu and C. Liu, "Numerical study on mechanism of multiple ring formation," AIAA Paper 2012-0747, Nashville, Tenn, USA, 2012.

[38] P. Moin, A. Leonard, and J. Kim, "Evolution of a curved vortex filament into a vortex ring," *Physics of Fluids*, vol. 29, no. 4, pp. 955–963, 1986.

[39] R. F. Feynman, "Application of quantum mechanics to liquid helium," in *Progress in Low Temperature Physics*, C. J. Gorter, Ed., vol. 1, chapter 2, North Holland, Amsterdam, The Netherlands, 1955.

[40] U. Frisch, P. L. Sulem, and M. Nelkin, "A simple dynamical model of intermittent fully developed turbulence," *Journal of Fluid Mechanics*, vol. 87, no. 4, pp. 719–736, 1978.

[41] D. G. W. Meyer, U. Rist, and M. J. Kloker, "Investigation of the flow randomization process in a transitional boundary layer," in *High Performance Computing in Science and Engineering '03*, E. Krause and W. Jäger, Eds., pp. 239–253, Springer, New York, NY, USA, 2003.

[42] L. Prandtl, "Bericht uber Untersuchungen zur ausgebildeten Turbulenz," *Zeitschrift für Angewandte Mathematik und Mechanik, Band*, vol. 5, pp. 136–139, 1925.

Hindawi Publishing Corporation
Modelling and Simulation in Engineering
Volume 2012, Article ID 742162, 10 pages
doi:10.1155/2012/742162

Research Article

Numerical Model for Cavitational Flow in Hydraulic Poppet Valves

Sandor I. Bernad[1] and Romeo Susan-Resiga[2]

[1] *Center of Advanced Research in Engineering Sciences, Romanian Academy, Timisoara Branch, 300223 Timisoara, Romania*
[2] *Department of Hydraulic Machinery, Politehnica University of Timisoara, 300222 Timisoara, Romania*

Correspondence should be addressed to Sandor I. Bernad, sbernad@mh.mec.upt.ro

Received 9 January 2012; Accepted 10 April 2012

Academic Editor: Guan Heng Yeoh

The paper presents a numerical simulation and analysis of the flow inside a poppet valve. First, the single-phase (liquid) flow is investigated, and an original model is introduced for quantitatively describing the vortex flow. Since an atmospheric outlet pressure produces large negative absolute pressure regions, a two-phase (cavitating) flow analysis is also performed. Both pressure and density distributions inside the cavity are presented, and a comparison with the liquid flow results is performed. It is found that if one defines the cavity radius such that up to this radius the pressure is no larger than the vaporization pressure, then both liquid and cavitating flow models predict the cavity extent. The current effort is based on the application of the recently developed full cavitation model that utilizes the modified Rayleigh-Plesset equations for bubble dynamics.

1. Introduction

In hydraulic power systems, cavitation most frequently occurs in system valves, pumps, and actuators. Large differences in pressure are a frequent cause of small-scale cavitation in chambers of four-way spool valves, while high-frequency motion of a valve-controlled actuator can lead to large-scale cavitation in the cylinder. Another source of cavitation in hydraulic power systems is the improper filling of the pistons on an axial-piston pump. Either during transient loading or under steady-state operation, cavitation can occur in the return chamber of directional control valves because of the large pressure drop across the orifice. It is of interest to know the potential cavitation damage, as well as any effect of cavitation on system performance under both steady and unsteady flow conditions.

The flow inside the poppet valve is a complex process that is strongly dependent on the details of the valve geometry, the fluid properties, and the operating conditions. Separation and reattachment of jets can have a profound effect on the flow pressure and force characteristics as well as influencing the susceptibility to cavitations.

Hydraulic valves differ from process control valves in application and design. Hydraulic valves are typically used for controlling pressures and, therefore, are of the quick opening type of characteristics. Quick opening valves utilize plugs shaped in the form of a truncated cone with relatively large clearances between the plug and the seat. Or sometimes these valves utilize a disc for a poppet plug. Process control valves on the other hand are used for precise control of the fluid flow rate due to the linear or equal percentage characteristics. These type of valves usually have small clearances between the plug and the seat. Despite these differences, many of the flow phenomena in the hydraulic valve such as recirculation and jet separation and reattachment also occur in the process control valve.

A poppet valve is a seating-type valve. For this kind of valve the moving element (the poppet), usually can have a spherical or conical shape. Always, the poppet moves in a perpendicular direction to the seat. Because of the several advantages that are associated with poppet valves such as ease of manufacture, minimum leakage, and insensibility to clogging by dirt particles, poppets have been used for as pressure regulators and relief valves. The operation

of this type of valve is quite simple. The fluid pressure counterbalances the spring force and allows fluid escape through the annular passage way between the poppet and the seat.

Separating interior flows are of the utmost importance for the performance of wide variety of technical applications [1–5]. Many industrial designs today have to compromise between the hydrodynamical function and other competing functions, for example, size or mechanical function. In such compromised designs undesired separation is more likely to occur, this drastically decreases the performance of the design. In such cases, active or passive devices that increase their near-wall momentum can be used to remove or reduce the separation [2, 3, 6].

The presence of flow separation in the valve passage and the occurrence of different flow patterns have previously been identified in a number of investigations of different valve geometries. In the extensive work carried out by Tanaka in 1929 [7], it was observed that discontinuities in the flow occurred when investigating the flow quantity across the valve for different valve lifts.

The experimental work of hydraulic valves extends back over many years. Johnston et al. [8] studied forces on the valve plug as well as the pressure-flow characteristics for several different plug and seat arrangements. Schrenk [9] published work on the pressure-flow characteristics of poppet and disk valves. Stone [10] studied the characteristics of poppet valves with sharp-edged seats, small openings, and low Reynolds number. McCloy and McGuigan [11] studied the effects of the downstream chamber size in a two-dimensional model of a poppet. Some researchers have attempted to analytically predict flow through poppet valves. Von Mises [5] predicted the contraction coefficient for flow through an orifice using potential flow. Fluid forces on the plug are often estimated using simple concepts of fluid momentum change through the valve [3, 10]. Recently CFD has been combined with experimental work to analyze hydraulic valves. Vaughan and Johnston [12] modeled the valve reported experimentally by Johnston et al. [8].

Weclas et al. [13] presented a comprehensive investigation into flow separation in the inlet valve passage using measurement techniques such as discharge coefficient measurements, surface flow visualization using an oil streak technique, and detailed flow measurements using LDA. The detailed flow measurements at the valve exit plane and the surface flow visualization showed the flow separation in the valve passage and identified its distribution around the valve periphery for generic inlet port geometries.

A successful design of poppet valves requires a through analysis of both velocity and pressure fields, with the aim of improving the poppet/seat geometry. Technological considerations lead to sharp corners, which in conjunction with very narrow passages produce regions of extremely high gradients in the flow field. As pointed in [14–16], the poppet flow is not easily suited to classical mathematical analysis.

The relative simple geometry (Figure 1), produces a very complicated viscous flow field (Figure 2), which can be realistically investigated only by using computational fluid mechanics. Powerful numerical tools, such as FLUENT software [17], are now available for investigating flows through arbitrary geometries.

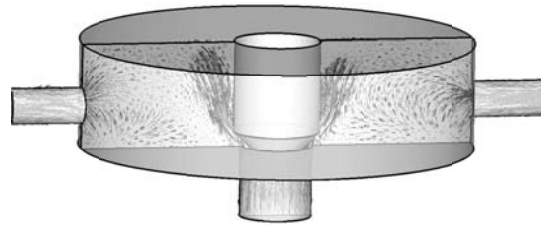

Figure 1: Velocity vector field and streamlines in meridional section plane.

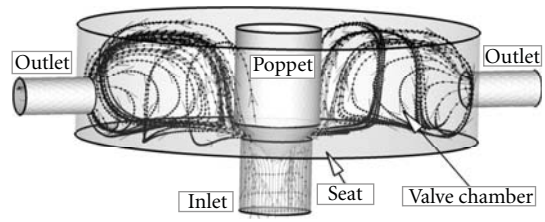

Figure 2: Flow field representation using selected streamlines inside the poppet valve.

Figure 1 shows the velocity vector field in meridional section plane overlaid with selected streamlines in the 3D computational domain. Velocity vector field in section plane shows the large recirculation region confirming the very strong nature of the helical vortex flow in this poppet valve geometry (Figure 2). The vortex evolution is clearly influenced by the position of the valve outlet section position.

As shown in our previous work [18], the cavitation region is relatively large in a poppet valve chamber; thus we expect a significant change of the flow field compared with the single-phase flow. One of the main goals of this paper is to explore the cavitating flow by using a two-phase flow model.

Section 2 presents a simple cavitating flow model employed by the commercial code FLUENT, and results obtained by using this model are presented in Section 5. The main question addressed in this paper is whether or not the single-phase flow simulation correctly predicts the vapor cavity radius and location. In addition, we also examine the differences between single-phase and two-phase models in terms of the flow rate and streamline pattern.

2. Cavitating Flow Modeling

Cavitating flows are very sensitive to the formation and transport of vapour bubbles, the turbulent fluctuations of pressure and velocity, and the magnitude of noncondensable gases, which are dissolved or ingested in the operating liquid [5, 10].

Numerical simulation of two-phase cavitating flows is an ongoing research effort with the ambitious goal to compute the unsteady evolution for cavities growth and collapse. The CFD community has developed so far a set of mature

techniques for simulating single-phase viscous flows, and the past half century of accumulated experience may very well serve to shape the numerical cavitating flow research. Early studies rely on the potential flow theory [19]. This approach is now able to correctly describe partially cavitating two-dimensional hydrofoils, including the reentrant jet cavity closure model [20]. However, extension to 3D problems and other types of cavitating flows seems to be out of reach for the potential flow model.

Although basic cavitation theoretical studies deal with bubble (or bubble clouds) dynamics by solving for the vapour-liquid interface, most of the practical cavitating flows are approached using a homogeneous flow theory. The main idea is to consider a single variable density fluid, without explicit phase interfaces. This model has emerged after carefully examining available experimental investigations, as well as by evaluating the computational costs involved in cavitating flows modelling. A review of cavitating flows numerical studies over the past decade can be found in [21], where various Reynolds Averaged Navier-Stokes (RANS) solvers have been modified to account for the secondary-phase (vapour and gas) dynamics.

The mixture model is used in the current work for the numerical simulation of cavitating flows with the FLUENT expert code [17]. In this model, the flow is assumed to be in thermal and dynamic equilibrium at the interface where the flow velocity is assumed to be continuous.

The *mixture* is a hypothetical fluid with variable density,

$$\rho_m = \alpha\rho_v + (1-\alpha)\rho_l, \tag{1}$$

ranging from liquid density for $\alpha = 0$ to vapour density ρ_v for $\alpha = 1$. The vapour volume fraction,

$$\alpha = \frac{\mathrm{Vol}_{\mathrm{vapor}}}{\mathrm{Vol}_{\mathrm{liquid}} + \mathrm{Vol}_{\mathrm{vapor}}}, \tag{2}$$

is an additional unknown of the problem. The mixture will of course satisfy the continuity equation

$$\frac{d\rho_m}{dt} + \rho_m \nabla \cdot u_m = 0, \tag{3}$$

where d/dt denotes the material derivative. Next, one has to consider a momentum equation for the mixture. A simple choice would be to neglect the viscous effects and use the Euler equation. The system of equations can be then closed with a density-pressure relationship (equation of state). This approach can take advantage of a reach legacy of inviscid compressible solvers [22]. However, when considering a barotropic mixture, that is, the density depends solely on the pressure, some physics is lost. This can be easily seen when writing the vorticity transport equation

$$\frac{\partial \boldsymbol{\omega}}{\partial t} + \mathbf{u}\cdot\nabla\boldsymbol{\omega} = \boldsymbol{\omega}\cdot\nabla\mathbf{u} + \frac{1}{\rho^2}\nabla\rho\times\nabla p + \text{viscous terms}. \tag{4}$$

The second term in the right-hand side, which accounts for the baroclinic vorticity generation, vanishes when $\rho = \rho(p)$. As a result, an important vorticity source is lost, especially in the cavity closure region [23].

Practical computations of industrial flows are using RANS equations with various turbulence modelling capabilities. This approach is embedded in most commercial codes currently available, for example, FLUENT [17]. As a result, it seems natural to build a cavitating flow model on top of such computational infrastructure.

An alternative to the equation of state is to derive a transport equation for the vapour volume fraction. The continuity equation (3), together with (1), gives the velocity divergence as

$$\nabla \cdot u_m = -\frac{1}{\rho_m}\frac{d\rho_m}{dt} = \frac{\rho_l - \rho_v}{\rho_m}\frac{d\alpha}{dt}. \tag{5}$$

Using (5), the conservative form of the transport equation for α can be easily written:

$$\frac{\partial\alpha}{\partial t} + \nabla\cdot(\alpha u_m) = \frac{1}{\rho_v}\left[\frac{\rho_v\,\rho_l}{\rho_m}\frac{d\alpha}{dt}\right]. \tag{6}$$

Equation (6) can be also written for the liquid volume fraction, $1-\alpha$:

$$\frac{\partial(1-\alpha)}{\partial t} + \nabla\cdot[(1-\alpha)\,u_m] = \frac{1}{\rho_l}\left[-\frac{\rho_v\rho_l}{\rho_m}\frac{d\alpha}{dt}\right]. \tag{7}$$

The factor in square brackets in the r.h.s. of (6) and (7) is the interphase mass flow rate per unit volume:

$$\dot{m} = \frac{\rho_v\rho_l}{\rho_m}\frac{d\alpha}{dt}. \tag{8}$$

If we add term by term (6) and (7), we end up with an inhomogeneous continuity equation of the form

$$\nabla\cdot u_m = \dot{m}\left(\frac{1}{\rho_v} - \frac{1}{\rho_l}\right), \tag{9}$$

which is used in [24] to replace the homogeneous equation (3).

Finally, the vapour volume fraction transport equation is written as

$$\frac{\partial\alpha}{\partial t} + \nabla\cdot(\alpha u_m) = \frac{1}{\rho_v}\,\dot{m}. \tag{10}$$

This is the equation for the additional variable α to be solved together with the continuity and momentum equations.

Most of the efforts in cavitation modelling are focused on correctly evaluating $\dot{m}$. One approach has been proposed by Merkle et al. [25], by modelling the phase transition process similar to the chemically reacting flows. This model was successfully employed by Kunz et al. [26] in a variety of cavitating flows. However, the model constants are chosen somehow arbitrary, and this choice ranges several orders of magnitude from one problem to another. Senocak and Shyy attempt a derivation of an empiricism-free cavitation model [23] in order to avoid the evaporation/condensation parameters introduced by Merkle.

A different approach is proposed by Schnerr and Sauer [27], who consider the vapour-liquid mixture as containing a large number of spherical bubbles. As a result, the vapour volume fraction can be written as

$$\alpha = \frac{n_b(4/3)\pi R^3}{1 + n_b(4/3)\pi R^3}, \tag{11}$$

where the number of bubbles per volume of liquid, n_b, is a parameter of the model.

From (11) we can easily get

$$\frac{d\alpha}{dt} = \alpha(1-\alpha)\frac{3\dot{R}}{R}, \tag{12}$$

where $\dot{R}$ is the bubble vapour-liquid interface velocity. A simplified Rayleigh equation can be used to compute

$$\dot{R} \equiv \frac{dR}{dt} = \operatorname{sgn}(p_v - p)\sqrt{\frac{2}{3}\frac{|p_v - p|}{\rho_l}}. \tag{13}$$

Of course the bubble grows if the mixture pressure is less than the vaporization pressure, $p < p_v$, and collapses when $p > p_v$. The bubble collapse, as modelled by the Rayleigh second-order differential equation, is much more rapid than the bubble growth. However, the above model seems to make no such difference between growth and collapse.

The present paper employs the mixture model, as implemented in the FLUENT commercial code, with the cavitation model described by (8), (12), and (13).

Physically, the cavitation process is governed by thermodynamics and kinetics of the phase change process. The liquid-vapor conversion associated with the cavitation process is modeled through two terms, which represents, respectively, condensation and evaporation. The particular form of these phase transformation rates forms the basis of the cavitation model.

3. The Numerical Approach

To simulate the cavitating flow the numerical code FLUENT [17] was used. The code uses a control-volume-based technique to convert the governing equations in algebraic equations that can be solved numerically. This control volume technique consists of integrating the governing equations at each control volume, yielding discrete equations that conserve each quantity on a control-volume basis. The governing integral equations for the conservation of mass and momentum and (when appropriate) for energy and other scalars, such as turbulence and chemical species, are solved sequentially. With the governing equations being nonlinear (and coupled), several iterations of the solution loop must be performed before a converged solution is obtained. The flow solution procedure is the SIMPLE routine [17]. This solution method is designed for incompressible flows, thus being implicit. The full Navier-Stokes equations are solved. The flow was assumed to be steady, and isothermal. In these calculations turbulence effects were considered using turbulence models, as the k-ε RNG models, with the modification of the turbulent viscosity for multiphase flow. To model the flow close to the wall, the standard wall-function approach was used, and then the enhanced wall-function approach has been used to model the near-wall region (i.e., laminar sublayer, buffer region, and fully-turbulent outer region). For this model, the used numerical scheme of the flow equations was the segregated implicit solver. For the model discretization, the SIMPLE scheme was employed for pressure-velocity coupling, second-order upwind for the momentum equations, and first-order upwind for other transport equations (e.g., vapor transport and turbulence modeling equations). Computational domain is discretized using the GAMBIT preprocessor [17]. The flow close to the body surface is of particular importance in the current study, the mesh structure in the computational domain deliberately reflects this concern by heavily clustering the mesh close to the solid surface of the body so that the boundary layer mesh is used enclosing the body surface.

4. Validation of the Cavitating Flow Model

Before any attempt of computing cavitating hydrofoil flows, we have tested the model described in Section 2 on a benchmark problem. In a previous paper [28] we have computed the cavitating flow over a blunt body, where our numerical solutions are in a good agreement with experimental data obtained by Rouse [29]. In this paper we analyse the case of a hemispherical cavitator. The flow with and without cavitation computed for the axi-symmetric cavitator with blunt fore-body and numerical results is compared with experimental data. For this particular axisymmetric body, Rouse and McNown [29] have provided the pressure coefficient distribution along the body.

In this paper we used the volume of fluid method (since it is essentially based on the transport of the local volume fraction of the liquid) implemented in FLUENT code to capture the interface between fluid and vapour.

The volume of fluid methods belong to the group of Eulerian techniques. The basic idea of the VOF method is to consider a color function, defined as the volume fraction of one of the fluids within each cell, to capture the interface. This function will be unity if the cell is filled with the gas phase, zero if the cell is filled with the liquid phase, and between zero and one if the cell contains the interface. Interfaces are then generally reconstructed using a piecewise linear interpolation. The main strength of the volume of fluid method is that it conserves mass exactly as it works directly with the volume fraction. In general, a VOF algorithm solves the problem of updating the volume fraction field given the fixed grid, the velocity field, and the volume fraction field at the previous step.

Figure 4 shows the distribution of α around a hemispherical fore-body, for a cavitation number

$$\sigma = \frac{p_\infty - p_v}{(1/2)\rho_l U_\infty^2} = 0.3. \tag{14}$$

Most of the computational domain constrains only liquid, $\alpha = 0$, but within the region with $p < p_v$ the vapour phase is formed with $0 < \alpha < 1$.

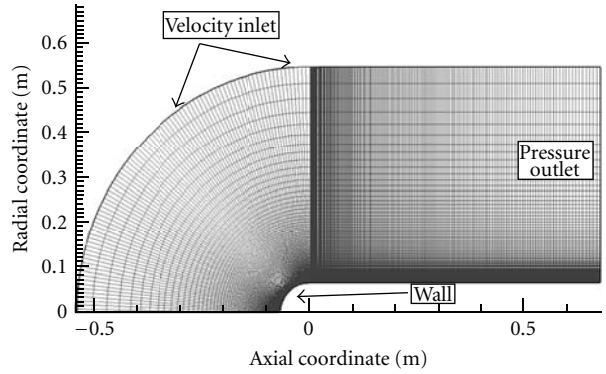

Figure 3: Computational domain and boundary conditions for hemispherical fore-body.

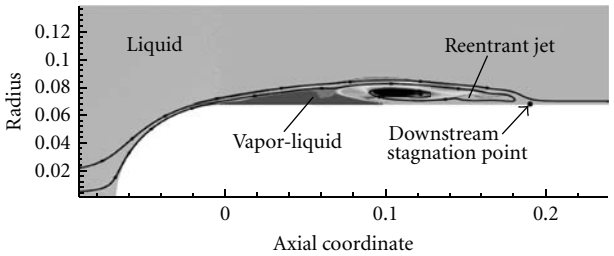

Figure 4: Vapour volume fraction and selected streamlines for cavitating flow around a hemispherical fore-body for $\sigma = 0.3$.

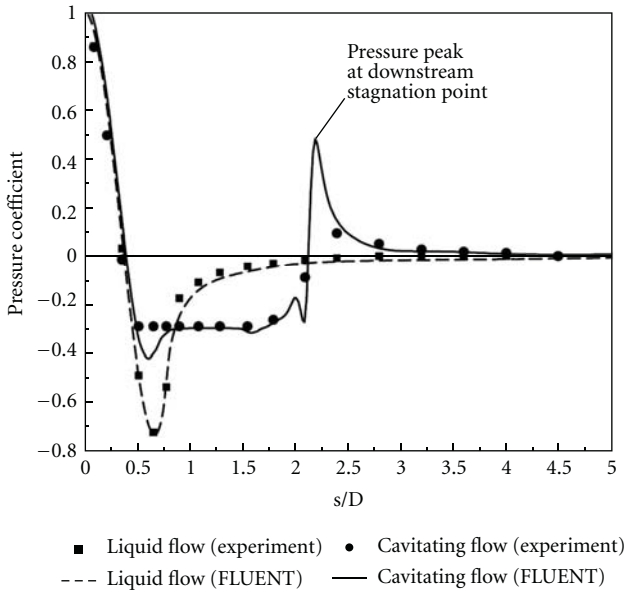

Figure 5: Pressure coefficient distribution on the hemispherical fore-body. The curves correspond to the present computations, while the points are experimental data of Rouse and McNown [29].

Cavitation occurs as a result of the flow acceleration over the body surface resulting in regions with pressures lower than the vapor pressure (Figures 3 and 4). Then, the water transforms to vapor in these regions, thereby forming vapor-filled cavities. These cavities collapse when the local pressure becomes larger than the vapor pressure, with a reentrant water jet, and the flow generally becomes unsteady. Thus, an irregular cyclic process of bubble formation and growth occurs, followed by the filling and finally breaking off of the bubble. Due to cavitation, large-density and viscosity gradients arise at the interfaces between nearly incompressible fluids.

Within the cavity there are regions practically filled with gas (the first half) and regions with a gas-liquid mixture corresponding to the reentrant jet dispersion and vaporisation. The present simulation considers a steady flow, corresponding to a stable attached cavitation. However, when the reentrant jet crosses the cavity boundary, a large part of the cavity detaches and is transported downstream, while the remaining part starts growing again.

The qualitative analysis above is completed with a quantitative comparison shown in Figure 5. The pressure coefficient is plotted against the dimensionless curvilinear abscissa along the body, originating at the axis,

$$c_p = \frac{p - p_\infty}{(1/2)\rho_l U_\infty^2}. \tag{15}$$

The numerical results correspond to the dashed line and agree very well with the experimental data [29]. In the cavitation model the vaporization pressure is adjusted to obtain the cavitation number $\sigma = 0.3$. As a result, the negative values of pressure coefficient are limited within the cavity at $-\sigma$. However, at cavitation inception (upstream and of the cavity) the pressure coefficient still drops below $-\sigma$ as the bubbles are transported faster than they can grow. At the end of the cavity there is a sharp increase in c_p, corresponding to the exact location of the downstream stagnation point from Figure 5.

5. Cavitating Flow Simulation and Analysis

Flow inside the poppet valve has been investigated considering a typical computational domain presented in Figure 6(a). Pressure conditions were considered both on the inlet and outlet sections of the axisymmetric domain, and the rest of the boundary is considered a solid wall (Figure 6(b)). In order to perform a quantitative analysis of the complicated streamline pattern inside the poppet valve chamber, an original theoretical vortex model has been proposed [16], thus allowing a parametric study of the poppet valve flow evolution in the whole range of poppet displacement.

A typical streamline pattern for the liquid flow through the poppet valve is presented in Figure 7. Three main vortices are developed in the poppet valve chamber. The first two vortices, V1 and V2, are rotating counterclockwise and clockwise, respectively, and are generated on the left-hand side and right-hand side, respectively, of the liquid jet issued from the poppet-seat opening. The third vortex, V3, is generated beyond the valve chamber, in the outflow channel. Such a qualitative analysis of the flow field has been performed also by Dietze [15], who used flow visualization to validate the numerical results, that is, the streamline pattern.

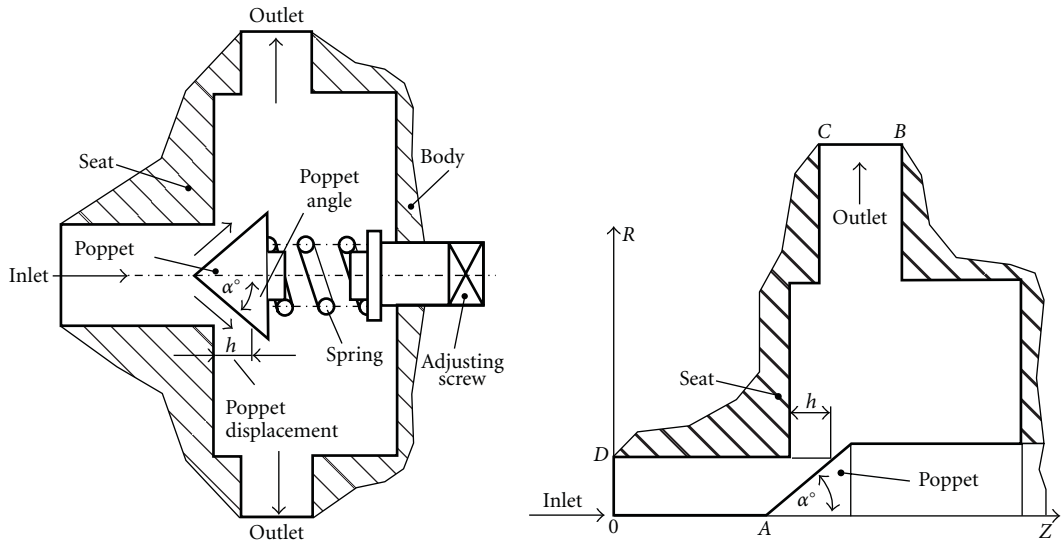

Figure 6: Cross-sectional view of a typical poppet valve and the corresponding computational domain in a meridian half-plane.

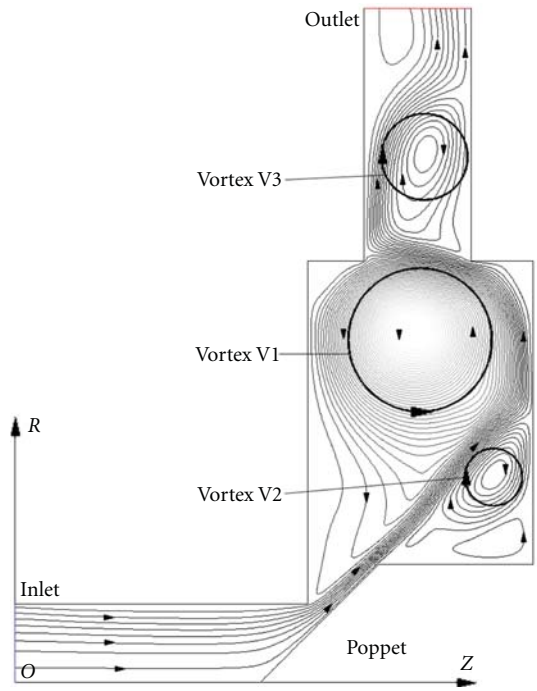

Figure 7: Streamline pattern in the meridian half-plane for a poppet valve with 28 mm inlet diameter, 45° poppet cone angle, and 5,6 mm poppet displacement, operating at inlet/outlet pressure of 61 bar/1 bar.

However, Dietze does not provide a quantitative description of the velocity and pressure fields details.

In order to carry out the mesh sensitivity analysis, numerical simulations were carried out by varying the number of mesh elements in the computational domain. Initially, the domain was discretized into 26,500 elements. The accuracy of the simulation results was then improved by employing a finer mesh that contained 60,700 elements. This number was further increased to 67,850 but resulted in no significant improvement in the results. Thus to maintain a balance between the computational cost and the numerical accuracy, we concluded (based on the mesh independence test) that the appropriate number of elements for our study is 41,970.

The presence of flow separation in the valve passage (Figure 8) and the occurrence of different flow patterns have previously been identified in a number of investigations of different valve geometries. Bulloungh and Chin [1] performed the static pressure measurements along the valve cone and seat wall for different poppet displacements. Visualization of the valve passage flow in a transparent model was investigated for different poppet valve configurations by Johnston et al. [8]. Dietze [15] in his Ph.D. thesis presented a comprehensive investigation into flow separation in the valve passage using measurement techniques and flow visualization to validate the numerical results, that is, the streamline pattern.

As mentioned in Section 3, after obtaining a steady single-phase (liquid) flow solution, the FLUENT code allows turning on the cavitation model. As a result, vapor formation is enabled where the absolute pressure is smaller than the vaporization pressure. In order to obtain correct results the so-called operating pressure p_{op} must be set to zero (it is set to the atmospheric pressure by default); therefore the gauge pressure p_{gauge} will equal the absolute pressure p_{abs},

$$p_{abs} = p_{op} + p_{gauge}. \tag{16}$$

This is particularly important for obtaining only positive absolute pressure values.

As shown in Figure 9, when the cavitating flow model is used the pressure inside the cavity becomes constant

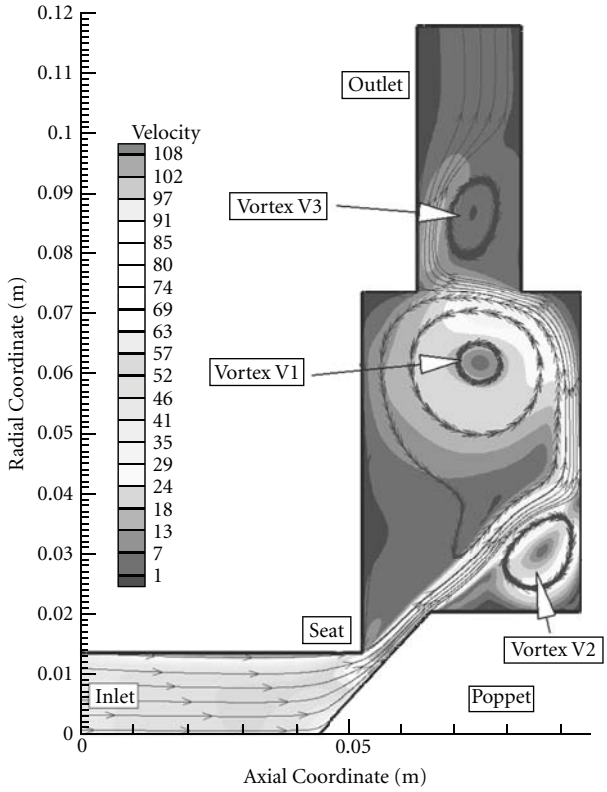

Figure 8: Streamline pattern and pressure field in the meridian half-plane of the poppet valve.

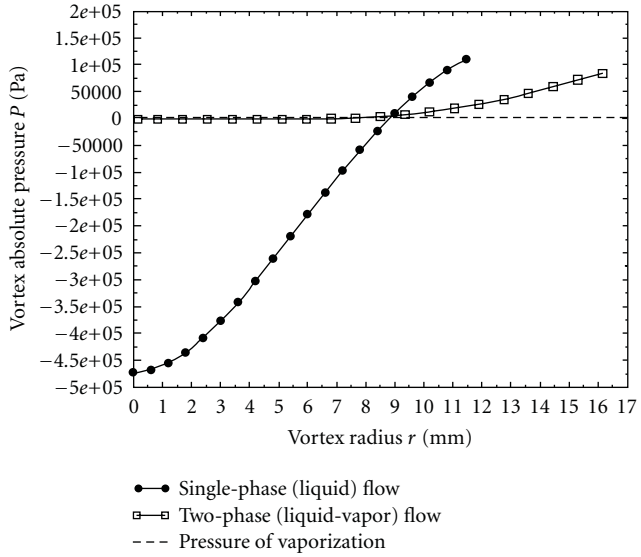

Figure 9: Radial pressure distribution inside the main vortex V1, computed for liquid flow (filled circles, see Figure 7) and liquid-vapor flow (squares).

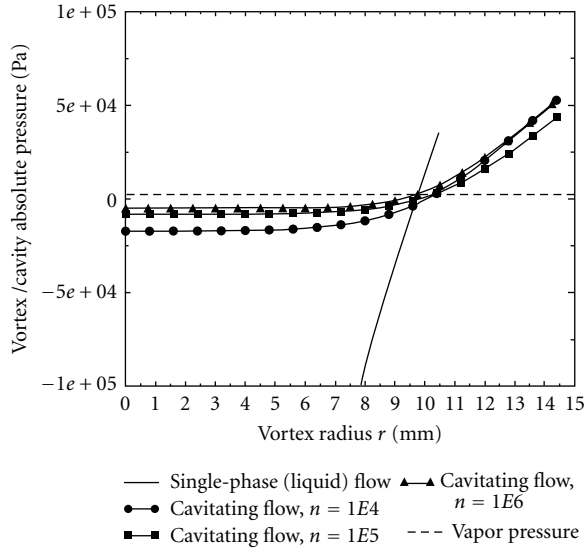

Figure 10: Influence of the bubble density number n on the pressure distribution inside the cavity.

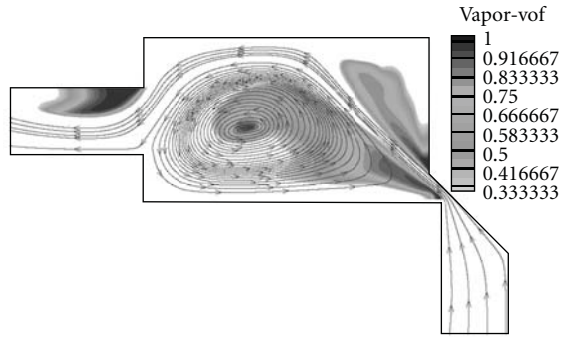

Figure 11: Radial distribution for the liquid-vapor mixture density inside the main vortex (cavity).

and equals the vaporization pressure, in concordance with cavitation physics. On the other hand, Figure 10 reveals that the pressure exceeds the vaporization pressure at the same radius of approximately 9 mm for both single-phase and two-phase models. However, one cannot say that the cavity radius is 9 mm since a continuous transition from vapor to liquid takes place.

If the cavity radius is defined such that inside the cavity the pressure does not exceed the vaporization pressure, then Figure 9 shows that both single-phase and cavitating flow models predict the same cavity extent. However, the above conclusion might be valid only for a particular value of the bubble density number n (see (11)). As a result, we have performed the numerical simulation for three values for n, namely, 10^4, 10^5, and 10^6, within the range recommended by Kubota et al. [20]. The results are presented in Figure 10, with a zoom for the pressure range around zero. We can conclude that when a steady cavitating flow configuration is computed, the bubble density number has no significant influence on the results. This is particularly important since there is no need for additional information to choose the appropriate value for n.

Figure 11 shows the liquid-vapor mixture density, starting with the vapor region inside the cavity and ending with pure liquid. One can see that there is a large region containing a mixture of liquid and vapor, as it actually happens for industrial cavitation.

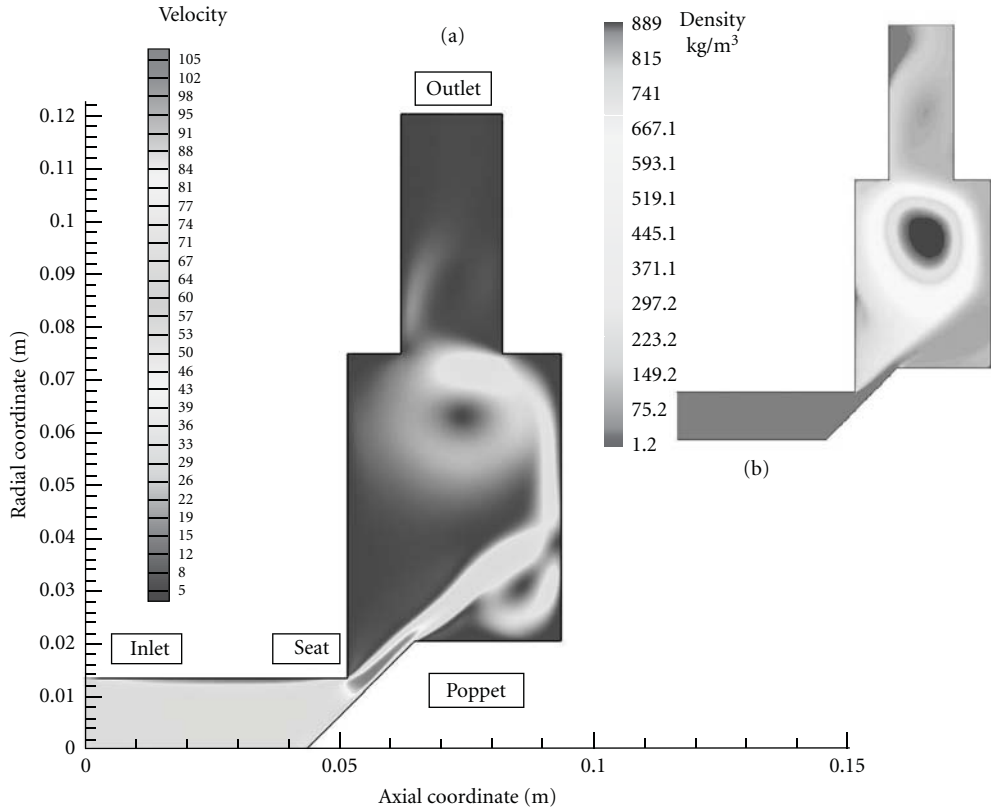

Figure 12: Velocity field and corresponding liquid-vapor mixture density distribution for cavitating flow.

A control valve creates a pressure drop in the fluid as it controls the flow rate. The profile of the fluid pressure, as it flows through the valve, is shown in Figure 11. The fluid accelerates as it takes a pressure drop through the valve trim. It reaches its highest velocity just past the throttle point, at a point called the vena contracta. The fluid is at its lowest pressure and highest velocity at the vena contracta. Past the vena contracta the fluid decelerates and some of the pressure drop is recovered as the pressure increases. The pressure in the vena contracta is not of importance until it is lower than the fluid vapor pressure. Then the fluid will quickly form vapor bubbles and, if the pressure increases above the vapor pressure, the vapor bubbles instantly collapse back to liquid (Figure 11).

The liquid flow rate will increase as the pressure drop increases. However, when cavitation vapor bubbles form in the vena contracta, the vapor bubbles will increasingly restrict the flow of liquid until the flow is fully choked with vapor. This condition is known as "choked flow" or "critical flow." When the flow is fully choked, the flow rate does not increase when the pressure drop is increased.

Cavitation will begin at the point of "incipient cavitation" and increase in intensity to the point of choked flow. Cavitation at point of "incipient cavitation" is not damaging and is almost undetectable. At some point between incipient and choked, the cavitation may damage most trim styles. The location of the "damage" point varies with trim style and material.

The radial distribution of the density inside the main vortex is presented in Figure 12. One can say that the vapour-filled cavity has a radius of 5 mm, but since we have a smooth transition from the vapor region to the liquid region other conventional cavity radii might be defined.

The cavitating flow streamline pattern is not significantly altered in comparison with the one presented in Figure 7. However, one can notice that the main vortex is slightly shifted toward the axis of symmetry and the secondary vortex V2 becomes smaller.

Figure 12 shows the liquid-vapor mixture density, starting with the vapor region inside the cavity and ending with pure liquid. One can see that there is a large region containing a mixture of liquid and vapor, as it actually happens for industrial cavitation [30]. The radial distribution of the density inside the main vortex is presented in Figure 13. One can say that the vapour-filled cavity has a radius of 5 mm, but since we have a smooth transition from the vapor region to the liquid region the above definition for the cavity radius in terms of pressure seems to be more appropriate.

As far as the flow rate is concerned, the liquid flow value is practically the same for cavitating flows. Further investigations are needed to elucidate this issue.

6. Conclusions

The paper presents a numerical investigation of cavitating flows using the mixture model implemented in the FLUENT

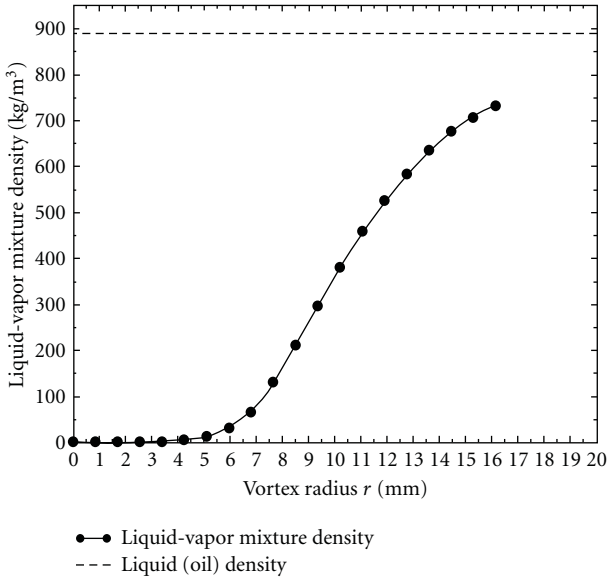

FIGURE 13: Radial distribution for the liquid-vapor mixture density inside the main vortex (cavity).

commercial code. The interphase mass flow rate is modelled with a simplified Rayleigh equation applied to bubbles uniformly distributed in computing cells, resulting in an expression for the interphase mass transfer. This is the source term for the vapor phase transport equation. As a result, the density of the liquid-vapor mixture is allowed to vary from the vapor density up to the liquid density.

The cavitation model is validated for the flow around a hemispherical body cavitator. The numerical results agree very well both qualitatively and quantitatively with the experiments. As a result we include that the present cavitational model is able to capture the major dynamics of the cavitating flows inside the hydraulic power equipment.

Cavitation damage problems are more likely to occur with water flow as water has a well-defined vapor pressure and the vapor bubble collapse is instantaneous. Hydrocarbon fluids have a less precise vapor pressure and are often a compound with several vapor pressures [31, 32]. Cavitation damage with hydrocarbon fluids is usually less severe than water, as the bubble collapse is not as sudden and can be cushioned by other vapors. However, the vibration and flow noise problems remain [3, 10].

The fluid inlet pressure is proportional to the amount of energy available to cause cavitation damage. Higher inlet pressures will produce more intense and more damaging cavitation.

The generation and implosion of the vapor bubbles will cause vibration to the valve poppet that may cause wear between the poppet and the seat.

The generation and implosion of the vapor bubbles will cause significantly elevated flow noise in addition to vibration. The cavitation bubbles will form a vapor plume in the liquid. The larger the plume, the noisier the flow and the more likely it is to cause erosion damage. The size of the plume is dependent on trim style and severity of cavitation.

The cavitating flow pressure distribution displays a constant value inside the vapor filled cavity, with a slow increase as the mixture density increases. The investigation of the liquid-gas mixture density shows a smooth and continuous transition from vapor to liquid. This transition takes place over a relatively large region. The results obtained for a steady cavitating flow does not depend on the bubble number density. This conclusion might not be true when time-dependent evolutions are investigated.

As the authors proceed with this research, they focus on several areas including: (1) improved physical model for mass transfer and (2) extended application and validation for steady two-dimensional flows.

Nomenclature

h:	Poppet displacement [m]
n_b:	Number of bubbles per unit volume of liquid [1/m^3]
p:	Mixture pressure [Pa]
p_v:	Vaporization pressure [Pa]
p_{abs}:	Absolute pressure [Pa]
p_{gauge}:	Gauge pressure [Pa]
p_{op}:	Operating pressure [Pa]
R:	Bubble radius [m]
$\dot{R}$:	Bubble vapor-liquid interface velocity [m/s]
α:	Vapour volume fraction [—]
ρ_m:	Liquid-vapor mixture density [kg/m^3]
ρ_v:	Vapor volume fraction density [kg/m^3]
σ:	Cavitation number [—]
u_m:	Liquid-vapor mixture velocity [m/s]
$\mathbf{u}$:	Absolute velocity [m/s]
$\boldsymbol{\omega} = \nabla \times \mathbf{u}$:	Vorticity [1/s]
t:	Time [s].

Acknowledgment

This work has been supported by the Romanian Academy annual program.

References

[1] W. A. Bullough and S. B. Chin, "A numerical study of the effects of poppet valve geometry on its flow characteristics," in *Proceedings of the 9th International Symposium on Transport Phenomena in Thermal-Fluids Engineering*, pp. 579–584, Singapore, June 1996.

[2] J. A. Davis and M. Stewart, "Predicting globe control valve performance—part I: CFD modeling," *Journal of Fluids Engineering*, vol. 124, no. 3, pp. 772–777, 2002.

[3] H. L. Sorensen, "Numerical and experimental analyses of flow and flow force characteristics for hydraulic seat valves with difference in shape," in *Proceedings of the Bath Workshop on Power Transmission & Motion Control*, University of Bath, 1999.

[4] A. Maier, T. H. Sheldrake, and D. Wilcock, "Geometric parameters influencing flow in an axisymmetric IC engine inlet port assembly: part I—valve flow characteristics," *Journal of Fluids Engineering*, vol. 122, no. 4, pp. 650–657, 2000.

[5] R. von Mises, "The calculation of flow coefficient for nozzle and orifice," *VDA*, vol. 61, pp. 21–23, 1916.

[6] A. Maier, T. H. Sheldrake, and D. Wilcock, "Geometric parameters influencing flow in an axisymmetric IC engine inlet port assembly: part II—parametric variation of valve geometry," *Journal of Fluids Engineering*, vol. 122, no. 4, pp. 658–665, 2000.

[7] K. Tanaka, "Airflow through suction valve of conical seat," Aeronautical Research Institute Report, Tokyo Imperial University, part 1, p. 262, part 2, p. 361, 1929.

[8] D. N. Johnston, K. A. Edge, and N. D. Vaughan, "Experimental investigation of flow and force characteristics of hydraulic poppet and disc valves," *Proceedings of the Institution of Mechanical Engineers A*, vol. 205, no. 3, pp. 161–171, 1991.

[9] E. Schrenk, *Disc Valves, Flow Patterns, Resistance, and Loading*, vol. T547, BHRA Publications, 1957.

[10] J. A. Stone, "Discharge coefficients and steady state flow forces for hydraulic poppet valves," *Transactions of the ASME D*, vol. 82, no. 1, pp. 144–154, 1960.

[11] D. McCloy and R. H. McGuigan, "Some static and dynamic characteristics of poppet valves," *Proceedings of the Institution of Mechanical Engineers*, vol. 179, no. 3, pp. 199–213, 1964.

[12] N. D. Vaughan and D. N. Johnston, "Numerical simulation of fluid flow in poppet valves," *Proceedings of the Institution of Mechanical Engineers*, vol. 206, no. 23, pp. 119–127, 1991.

[13] M. Weclas, A. Melling, and F. Durst, "Flow separation in the inlet valve gap of piston engines," *Progress in Energy and Combustion Science*, vol. 24, no. 3, pp. 165–195, 1998.

[14] S. Bernad, R. Susan-Resiga, I. Anton, and V. Ancusa, "Vortex flow modeling inside the poppet valve chamber—part 2," in *Proceedings of the Bath Workshop on Power Transmission & Motion Control (PTMC '01)*, pp. 161–176, Bath, UK, September 2001.

[15] M. Dietze, *Messung und Berechnung der Innenströmung in hydraulischen Sitzventilen*, Ph.D. thesis, Technische Universität Darmstadt, Düsseldorf, Geramny, 1996.

[16] R. Susan-Resiga, S. I. Bernad, and I. Anton, "Vortex flow modeling inside the poppet valve chamber," in *Proceedings of the 7th Scandinavian International Conference on Fluid Power (SICFP '01)*, Linkoping, Sweden, May 2001.

[17] *FLUENT 6.3 User's Guide*, Ansys Fluent, 2006.

[18] S. Bernad, R. Susan-Resiga, S. Muntean, and I. Anton, "Cavitation phenomena in hydraulic valves. Numerical modelling," *Proceedings of the Romanian Academy A*, vol. 8, no. 2, pp. 151–160, 2007.

[19] C. S. Martin, H. Medlarz, D. C. Wiggert, and C. Brennen, "Cavitation inception in spool valves," *Journal of Fluids Engineering*, vol. 103, no. 4, pp. 564–576, 1981.

[20] A. Kubota, H. Kato, and H. Yamaguchi, "A new modelling of cavitating flows: a numerical study of unsteady cavitation on a hydrofoil section," *Journal of Fluid Mechanics*, vol. 240, pp. 59–96, 1992.

[21] G. Wang, I. Senocak, W. Shyy, T. Ikohagi, and S. Cao, "Dynamics of attached turbulent cavitating flows," *Progress in Aerospace Sciences*, vol. 37, no. 6, pp. 551–581, 2001.

[22] D. R. van der Heul, C. Vuik, and P. Wesseling, "Efficient computation of flow with cavitation by compressible pressure correction," in *Proceedings of the European Congress on Computational Methods in Applied Sciences and Engineering (ECCOMAS '00)*, Barcelona, Spain, September 2000.

[23] I. Senocak and W. Shyy, "Evaluation of cavitation models for Navier-Stokes computations," in *Proceedings of the 2002 ASME Fluids Engineering Division Summer Meeting*, Paper FEDSM2002-31011, pp. 395–401, July 2002.

[24] J. L. Kueny, *Cavitation Modeling*, Lecture Series: Spacecraft Propulsion, Von Karman, Institute for Fluid Dynamics, 1993.

[25] C. L. Merkle, J. Z. Feng, and P. E. O. Buelow, "Computational modeling of the dynamics of sheet cavitation," in *Proceedings of the 3rd International Symposium on Cavitation*, pp. 307–311, 1998.

[26] R. F. Kunz, D. A. Boger, T. S. Chyczewski, D. R. Stinebring, and H. J. Gibeling, "Multi-phase CFD analysis of natural and ventilated cavitation about submerged bodies," *Proceedings of the 3rd ASME/JSME Joint Fluids Engineering Conference (FEDSM '99)*, 1999.

[27] G. H. Schnerr and J. Sauer, "Physical and numerical modeling of unsteady cavitation dynamics," in *Proceedings of the 4th International Conference on Multiphase Flow*, New Orleans, La, USA, 2001.

[28] S. Bernad, S. Muntean, R. Resiga, and I. Anton, "Numerical analysis of the cavitating flows," *Proceedings of the Romanian Academy A*, vol. 7, no. 1, pp. 33–45, 2006.

[29] H. Rouse and J. S. McNown, *Cavitation and Pressure Distribution, Head Forms at Zero Angle of Yaw*, vol. 32 of *Studies in Engineering Bulletin*, State University of Iowa, 1948.

[30] R. E. A. Arndt, "Cavitation in fluid machinery and hydraulic structures," *Annual Review of Fluid Mechanics*, vol. 13, pp. 273–328, 1981.

[31] E. Urata, "Thrust of poppet valve," *Bulletin of The Japan Society of Mechanical Engineers*, vol. 12, no. 53, pp. 1099–1109, 1969.

[32] E. Urata, "Cavitation erosion in various fluids," in *Proceedings of the Bath Workshop on Pover Transmission & Motion Control*, University of Bath, September 1999.

Hindawi Publishing Corporation
Modelling and Simulation in Engineering
Volume 2012, Article ID 419087, 10 pages
doi:10.1155/2012/419087

Research Article

Determination of Flow Conditions in Coronary Bifurcation Lesions in the Context of the Medina Classification

Marjan Molavi Zarandi,[1] Rosaire Mongrain,[1,2] and Olivier F. Bertrand[3,4]

[1] *Department of Mechanical Engineering, McGill University, Montreal, QC, Canada H3A 0C3*
[2] *Department of Cardiovascular Surgery, Montreal Heart Institute, Montreal, QC, Canada H1T 1C8*
[3] *Quebec Heart-Lung Institute, Laval Hospital, Quebec City, QC, Canada G1V 4G5*
[4] *Faculty of Medicine, Laval University, Quebec City, QC, Canada G1V 0A6*

Correspondence should be addressed to Rosaire Mongrain, rosaire.mongrain@mcgill.ca

Received 10 January 2012; Accepted 3 March 2012

Academic Editor: Guan Heng Yeoh

Coronary artery bifurcation lesions are complex and several classifications are presented to describe them. Recently, the Medina classification has been proposed. This classification uses binary values for characterization of stenosis. Flow conditions according to Medina classification have not been described. In this paper, bifurcation lesions corresponding to anatomical Medina lesion classification are compared on the basis of flow and Wall Shear Stress (WSS). Computational models of healthy and stenosed coronary artery bifurcations ((1, 1, 1), (0, 1, 1) and (1, 0, 1)) with moderate and severe stenoses of 50% and 75% diameter were analyzed. The results showed that, flow conditions vary in bifurcation lesion types according to the clinically-oriented Medina classification. The flow in SB of bifurcation was dependent of the Medina lesion type and was more affected in lesion type (1, 0, 1). The magnitudes of WSS on the inner and outer walls of SB of bifurcation lesion (1, 0, 1) in post-stenotic region and along the arterial wall were smaller than bifurcations lesions (0, 1, 1) and (1, 1, 1) respectively. Our results suggest that SB of bifurcation lesion (1, 0, 1) is more prone to atherosclerosis progression compared to types (0, 1, 1) and (1, 1, 1).

1. Introduction

From clinical practice, it is known that coronary artery bifurcations are regions where the flow is strongly perturbed, and is prone to the development of atherosclerotic lesions. As a definition, bifurcation lesion is a coronary artery narrowing that may involve the proximal main vessel, the distal main vessel, and the side branch [1]. Bifurcation lesions have always represented a major challenge for percutaneous treatment [2–5]. Part of this challenge is related to the variety of coronary lesions located at a bifurcation which present wide range of anatomical morphologies. Currently, there are seven coronary bifurcation lesion classification schemes in the literature [6–13]. These classifications are based on the presence or absence of significant angiographic stenosis within the three vessels of the bifurcation. All the published classifications are very similar in describing a given bifurcation lesion. Different lesion types are named using numbers or letters. Most of the classifications are difficult to remember [6–11]. The first attempt to overcome some of the limitations of previous classifications and simplify these classifications was successfully made by Medina et al. [12]. The classification by Medina is simple and does not need to be memorized even though it provides all the information contained in the other classifications. In this classification, the bifurcation is divided into three segments: the main branch proximal (MBP), the main branch distal (MBD), and the side branch (SB). Any narrowing with critical stenosis of 50% and above in any segment receives the binary value 1; otherwise, a binary value 0 is assigned starting from left to right. The three suffixes are separated by commas. In that context, the Medina classification is essentially an anatomical classification.

Pathologic examination of coronary arteries reveals that atherosclerosis lesions are likely to prevail at places where the vessel is curved, bifurcates, has a junction, a side branch, or

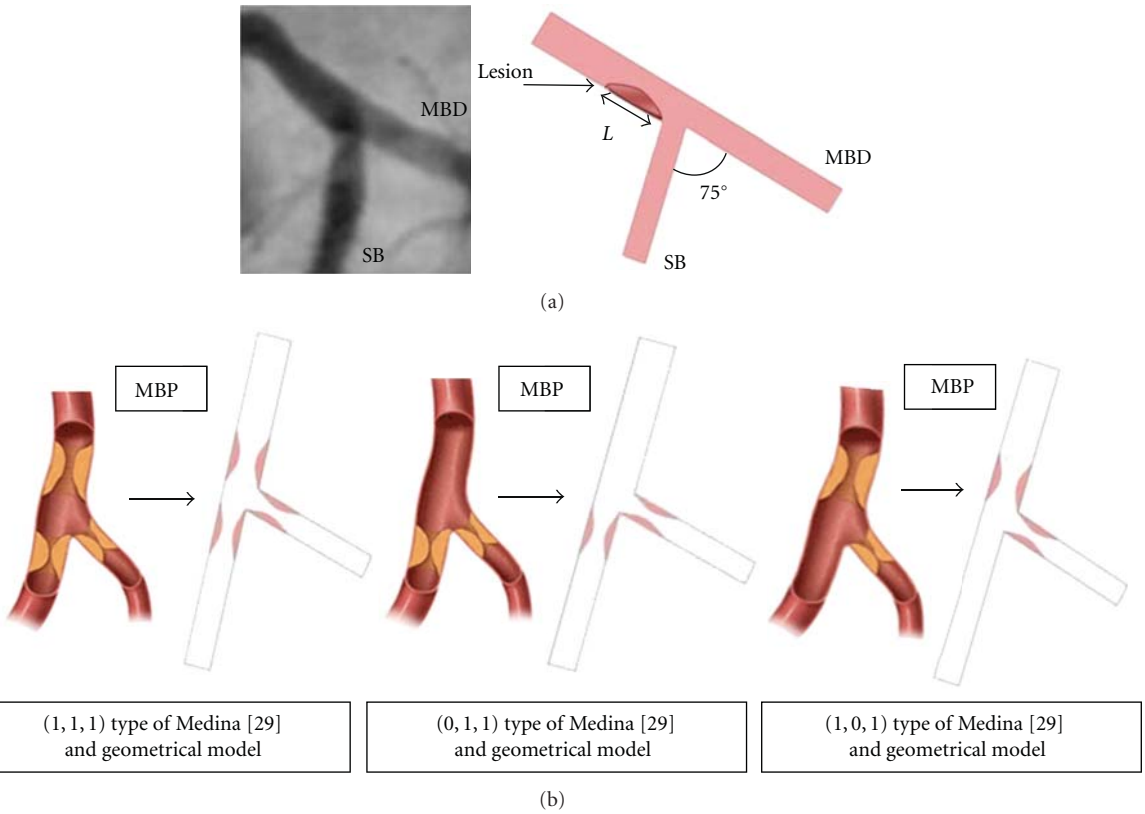

Figure 1: Angiogram of coronary artery bifurcation [26, 29] and corresponding geometrical model (a) and associated Medina lesion classification of coronary artery bifurcation (b).

other sudden change in flow geometry, and when the flow is unsteady [13–16]. Hemodynamic factors play a major role in the initiation and progression of atherosclerosis [17–19]. Studies show that arterial regions exposed to low and nonuniform shear stress are more prone to atherosclerotic lesions development [20–23].

To date, there has been no report studying flow conditions in bifurcation lesions associated with the Medina lesion classification. Using computational fluid dynamics (CFD) analysis, we studied (1) flow conditions in MBP, MBD, and SB, and (2) Wall Shear Stress (WSS) distributions in bifurcations lesions (1, 1, 1), (0, 1, 1), and (1, 0, 1).

2. Material and Methods

Hemodynamic analyses were carried out to study the flow conditions and quantify the WSS in coronary artery bifurcation which is of the most important sites of atherosclerotic plaque accumulation [24–26]. The simulation was conducted using COMSOL 3.5 which is dedicated for multiphysics and engineering applications. This software uses the finite-element method to solve the equations that govern blood flow in the computational domain. The computational domain was meshed and the combination of both momentum and continuity equations for transient, Newtonian model of the blood flow is analyzed.

A geometrical model of coronary artery bifurcation was considered to simulate the bifurcation between left main coronary artery (LMCA) and left anterior descending artery (LAD) [26]. Figure 1 shows the geometrical model of two-dimensional angiographic projections of the bifurcation (main branch proximal (MBP), main branch distal (MBD), and side branch (SB)) as well as the bifurcation lesions associated with the Medina lesion classification [3]. In our model, the dimensions of MBP, MBD, and SB are 4 mm, 3.4 mm, and SB 2.7 mm which are selected based on coronary arteriography data [27]. To have a fully developed flow at the inlet and downstream the stenoses, we considered a branch length $15D_{MBP}$ as a total branch length. The branch lengths for MBD and SB are calculated from the centre of the bifurcation to their end, equal to $12D_{MBD}$ and 11_{DSB}, respectively. A lesion length (L) of 6 mm is located at the carina in the considered bifurcation lesions. The angle between the centerline LMCA and LAD as well as the angle between the centerline MBD and SB (75°) corresponds to physiological anatomical range [28].

A similar two-dimensional model was recently presented for one stenotic bifurcation case [30].

In the stenosed bifurcation, the word "true" bifurcation lesion is used when stenosis in the proximal and/or distal segment of the main vessel and the side branch is involved [31]. Therefore, according to Medina lesion classification, the bifurcation lesion types (1, 1, 1), (0, 1, 1), and (1, 0, 1) are true bifurcation lesions. The Medina classification seems intuitive in the sense that the most obstructed disease bifurcation is labeled as (1, 1, 1). A secondary goal of this

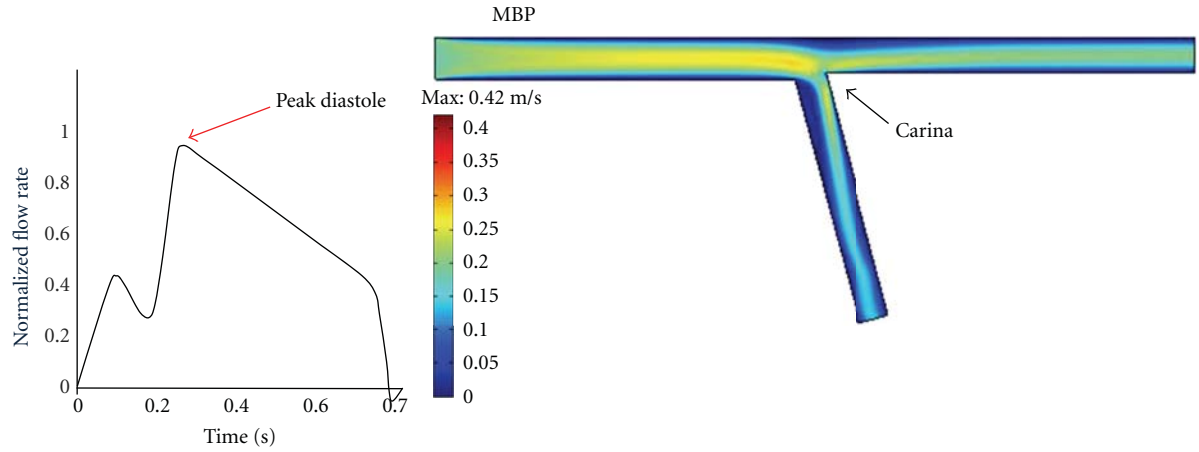

Figure 2: Velocity field in coronary artery bifurcation at peak diastole.

study is to assess, on the WSS basis, if the bifurcation type (1, 1, 1) do correspond to the most severe condition.

For the study of blood flow, we assumed that blood can be represented by an incompressible fluid which is governed by the conservation of mass and the conservation of momentum leading to the Navier-Stokes and the continuity equations:

$$\rho\left(\frac{\partial \vec{u}}{\partial t} + \vec{u}\cdot\nabla\vec{u}\right) = -\nabla p + \mu(\nabla^2\vec{u}),$$
$$\nabla\cdot\vec{u} = 0, \tag{1}$$

where, ρ denotes the density of the fluid ($\mathrm{kg\,m^{-3}}$), $\vec{u}$ the velocity vector ($\mathrm{m\,s^{-1}}$), p the pressure (Pa), and μ the dynamic viscosity of fluid (Pa.s).

Wall shear stress was determined as the product of viscosity (μ) and the shear rate ($\dot{\gamma}$). The shear rate, in two dimensions is defined according to:

$$\dot{\gamma} = \sqrt{\left(2\left(\frac{\partial \vec{u}}{\partial x}\right)^2 + \left(\frac{\partial \vec{u}}{\partial y} + \frac{\partial \vec{v}}{\partial x}\right)^2 + 2\left(\frac{\partial \vec{v}}{\partial y}\right)^2\right)}, \tag{2}$$

where $\vec{u}$ and $\vec{v}$ are the velocity components [32].

To solve the governing equations, a set of boundary conditions is required. In the present study, we assumed that the vascular bed maintains a constant flow in both healthy and stenosed artery.

The flows were considered unsteady, laminar, and fully developed throughout the study section; hence, the velocity distribution in the inlet was set to be parabolic as expressed by (3):

$$u = u_{\max}\left[1 - \left(\frac{R}{R_a}\right)^2\right], \tag{3}$$

where R is the radial position and R_a the inner radius of the artery.

Time-dependant velocity was taken from the literature for the left coronary artery during the cardiac cycle [33]. The waveform has a period $T = 0.7$ s, where $0 < t$ (sec) < 0.2 is systolic and $0.2 < t$ (sec) < 0.7 is diastolic phase. The maximum velocity magnitude at resting condition varies between 0.15 m/s and 0.25 m/s for a coronary artery of 4 mm in diameter. The arterial flow at peak diastole in MBP is 102.2 mL/min [34, 35]. For the outlet of the vessels, a traction-free boundary condition was imposed [36]. The Newtonian blood properties in this model are blood viscosity $\mu = 0.0035$ Pa.s, and blood density $\rho = 1060\,\mathrm{Kg/m^3}$, respectively [37].

3. Results and Discussions

Pulsatile hemodynamic analyses were carried out in healthy and stenotic bifurcations to study the influences of the constriction location on flow conditions and WSS distributions.

3.1. Flow Simulation Corresponding to Healthy Coronary Artery Bifurcation. A model of the healthy coronary artery bifurcation was developed and the corresponding velocity field and WSS distributions were investigated. The computed velocity field at peak diastole is presented in Figure 2.

Velocity profiles in the normal coronary artery bifurcation are skewed toward the carina, resulting in higher velocity along the inner walls and lower velocity along the outer walls.

For a Newtonian flow, WSS is the magnitude of the tangential shear forces acting on the wall by the fluid and is determined by the wall shear rate (gradient of velocity at the wall) multiplied by the viscosity of the fluid ($\tau = \mu\dot{\gamma}$). It is observed that, the gradient of velocity creates significant changes in the WSS on the inner and outer walls of MBD and SB. Distribution of WSS in the healthy artery at peak diastole is shown in Figure 3.

The distribution of WSS in Figure 3(a) shows the regions of high shear stress at the carina which is drastically greater than the WSS throughout the majority of the vessel walls.

The endothelial cells (lining the arterial walls) are exposed to shear stress variations due to periodic nature of blood flow. The physiological magnitude of the WSS ranges

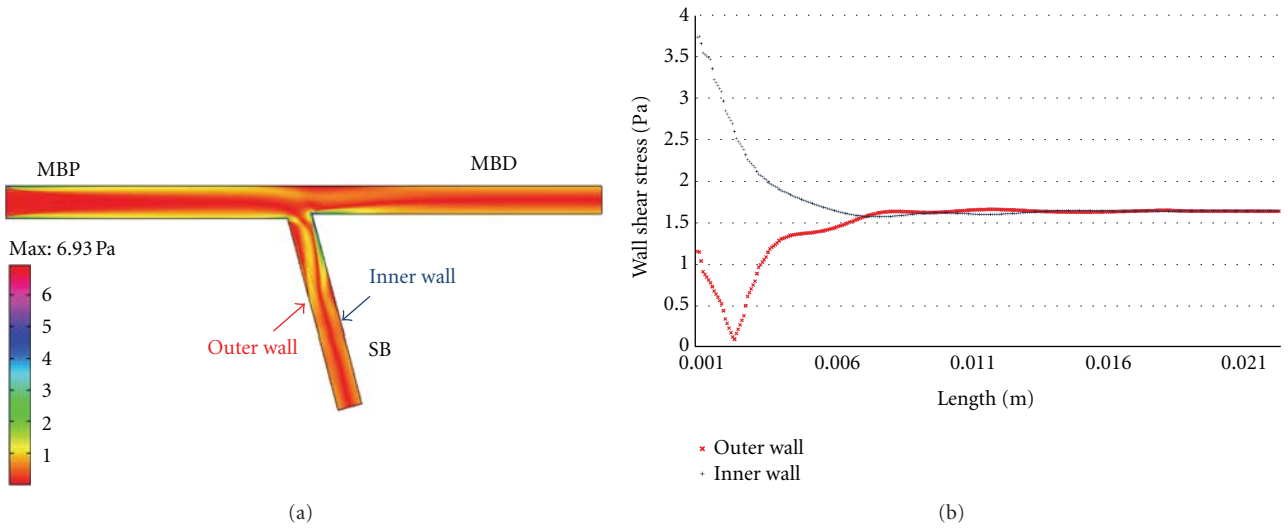

Figure 3: Distributions of WSS in the healthy coronary artery bifurcation (a) and WSS along the inner and outer walls of SB (b).

from 1 to 7 Pa in normal arteries [38]. Wall shear stress outside this range can potentially generate mechanisms that lead to vascular pathology. Lower values of WSS may contribute to the atherosclerotic process and therefore are considered "athero-prone," while WSS higher than this range may activate platelets and consequently "high-shear" induced thrombosis [38]. Prior *in vitro* and *in vivo* researches locate the atherosclerosis mostly within regions of disturbed blood flow, where WSS is below <0.5 Pa [39]. The WSS values along the inner and outer walls depicted in Figure 3 indicate that a small portion of the luminal surface is exposed to such low WSS at peak diastole in the non-diseased bifurcation model. The larger value of the WSS at peak diastole occurs on the SB inner wall downstream the carina. The results indicate that on the SB, low WSS values occur on the outer wall. The low WSS distribution on the outer walls is in accordance with the localization of atherosclerotic lesions in these areas. Indeed, there is strong evidence that low WSS values are possibly correlated to the lesion localization [39–41].

3.2. Flow Simulation of Bifurcation Lesions (1, 1, 1), (0, 1, 1), and (1, 0, 1). Having discussed the flow condition and WSS distribution in healthy bifurcation, we next proceed to inspect the flow condition and WSS distribution in three lesion types of the Medina lesion classification (Figure 1). In clinical medicine, the severity of stenoses is commonly defined as the percentage of occlusion using diameter measurements: % stenosis $= (d_1 - d_2)/d_1 * 100\%$, where d_1 is the artery diameter and d_2 is the constricted diameter. As the disease advances, the percentage of stenosis also increases. The geometry of stenoses used in this simulation is the same geometry as Ahmed and Giddens used in their experimental work [42]. Symmetric moderate (50%) and severe (75%) stenoses with Gaussian symmetric surface morphology are imposed at the MBP, MBD, and SB, respectively.

The computational model and mechanical properties are built based on the coronary artery bifurcation detailed in section one. The obstructions in MBP, MBD, and SB are far from the outlet so that the flow can return to a nearly fully developed state and the outlet boundary condition does not influence activities occurring upstream.

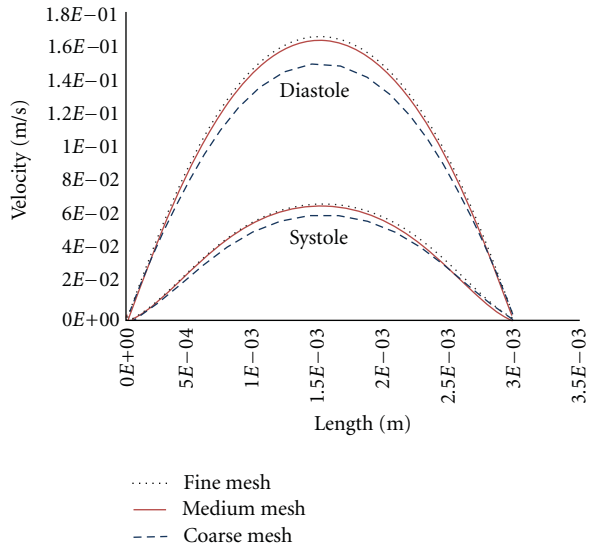

Figure 4: Velocity fields in peak systole and peak diastole in SB for three mesh densities.

For the flow modelling, mesh sensitivity analysis was carried out for bifurcation lesions (1, 1, 1), (0, 1, 1), and (1, 0, 1) for three different mesh densities and velocity fields, and WSS values were compared for different number of elements. Unsteady simulations were performed using a coarse, medium, and fine mesh of the geometry to estimate the mesh sensitivity for the arterial bifurcation geometry throughout the cardiac cycle. In bifurcation lesion (1, 1, 1) with 50% stenosis, we used a coarse mesh (8665 elements); a medium mesh (13,097 elements); a fine mesh (19,625 elements).

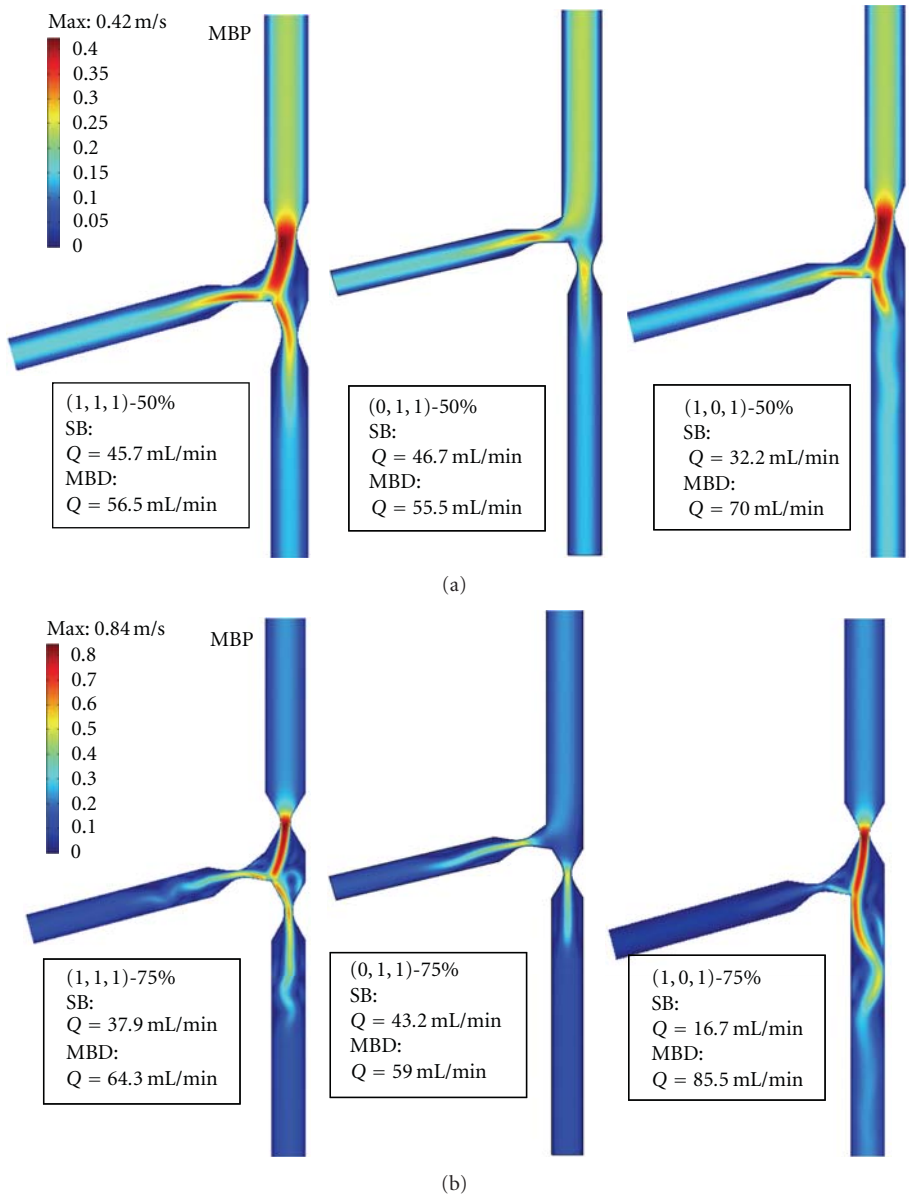

Figure 5: Maps of the velocity field magnitude and corresponding flow rates in 50% (a) and 75% (b) stenosed bifurcations.

Results were analyzed in term of the velocity profile and WSS along the MBD and SB. The velocity profiles and WSS for the coarse mesh density showed maximum 8% difference with the medium mesh. The results showed that the velocity field and WSS values have maximum 1% difference in the medium and fine mesh densities. Considering the negligible difference between medium and fine mesh densities and also the computing time, the medium mesh with mesh density of 13,097 elements was employed. For illustration, for bifurcation type (1, 1, 1), we present the velocity fields in peak systole and peak diastole in SB for three mesh densities in Figure 4.

Transient simulations were performed for stenosed coronary artery bifurcations and the corresponding velocity fields and shear stress distributions were investigated. In Figure 5, the three representative snapshots of the magnitude of the velocity field for 50% and 75% stenoses are shown at peak diastole ($t = 0.27$ s) for bifurcation lesion types (1, 1, 1), (0, 1, 1) and (1, 0, 1) of Medina lesion classification.

The simulation results presented in Figure 5 shows a dramatically different velocity profile of the blood flow in the downstream of stenotic bifurcations and demonstrated the influence of the bifurcation lesion types on the blood flow pattern, such as flow separation and recirculation zones. The maximum velocity in bifurcation lesions with 50% and 75% stenoses are about 0.42 m/s and 0.84 m/s, respectively which are related to the stenosed bifurcations with constriction in their MBP. Downstream the lesions, the flow decelerates and reverses near the walls due to the viscous effects. The bifurcation lesion types with greater stenoses (75%),

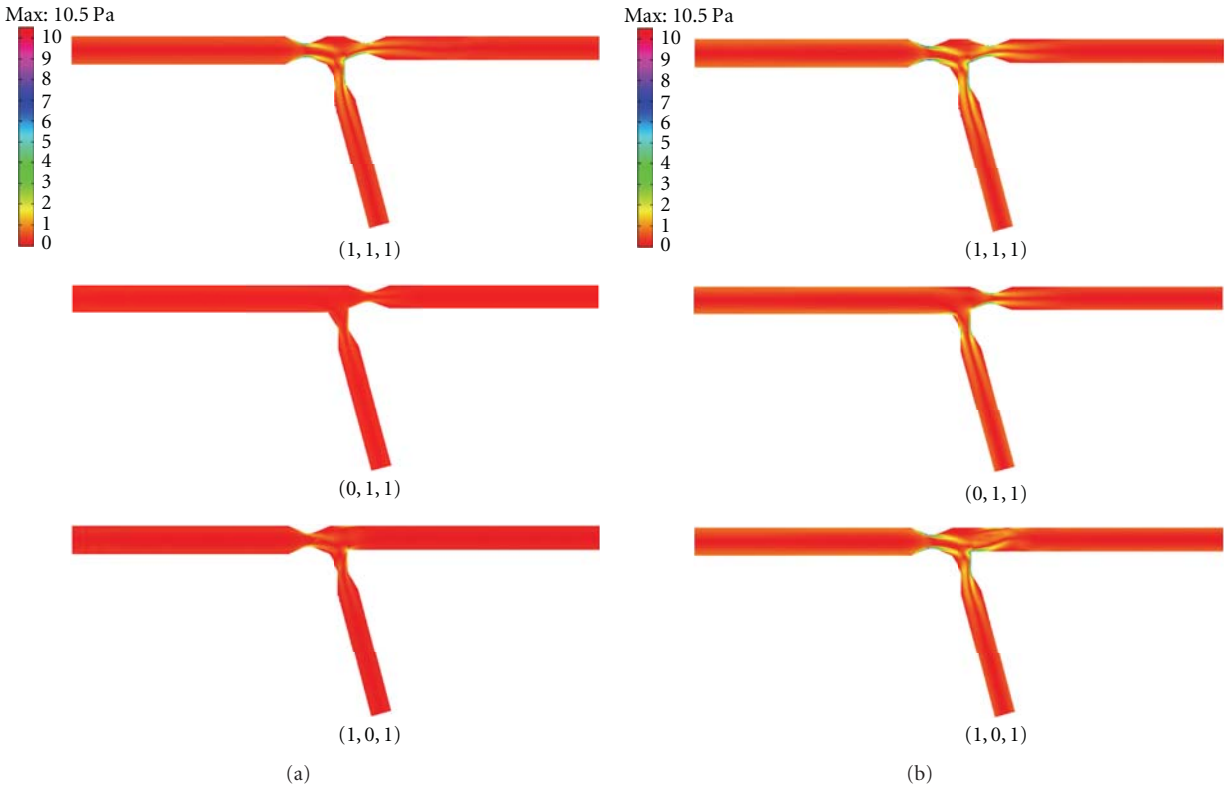

Figure 6: Wall shear stress at peak systole (a) and peak diastole (b) in true bifurcation lesions.

Table 1: The ratio of SB flow to MBP flow.

Diameter reduction	(1, 1, 1)	(0, 1, 1)	(1, 0, 1)
50%	Q_{SB}/Q_{MBP} = 0.44	Q_{SB}/Q_{MBP} = 0.45	Q_{SB}/Q_{MBP} = 0.31
75%	Q_{SB}/Q_{MBP} = 0.37	Q_{SB}/Q_{MBP} = 0.42	Q_{SB}/Q_{MBP} = 0.16

experience more flow separation, and bigger recirculation zones downstream the stenoses compare to bifurcation lesions with 50% stenoses. The results presented in Figure 5 also show that bifurcations with constriction in both MBD and SB (1, 0, 1) has the lowest magnitude of blood streaming into the SB. We calculated the ratio of the magnitude of the SB flow to the total MBP flow at peak diastole for all bifurcation lesions. The flow values were determined from converged simulation results and velocity profiles at 2.4 cm ($8D_{MBD}$) and 1.62 cm ($6D_{SB}$) distal to the lesions in MBD and SB. As a consequence of presence or absence of lesions in MBD and MBP, various hemodynamic conditions occur in SB with the same percentage of stenosis (Figure 5). The ratio of maximal blood flow achievable in a stenotic SB to the maximal blood flow in MBP in various bifurcation lesion types for intermediate and severe stenoses are summarize in Table 1.

As it is described in Table 1, in bifurcation lesion (1, 0, 1), the maximal diastolic SB flow in intermediate and severe stenoses is 31% and 16% of the total MBP flow. The results support that, the lower blood flow in the SB creates a crucial condition for this branch in bifurcation lesion (1, 0, 1) compared to bifurcation lesions (1, 1, 1), and (0, 1, 1) respectively.

3.3. Wall Shear Stress (WSS) of the Bifurcation Lesion Types. WSS is one of the most important factors in developing atherosclerosis, and arterial branches are found more prone in formation of arterial plaques [20–23]. Although atherosclerosis is a disease affecting the vascular system as a whole, it has uneven distribution in SB and MBD with considerable differences for different bifurcation lesion types. Therefore, the WSS distribution is studied along the inner and outer walls of SB and MBD for true bifurcations (1, 1, 1), (0, 1, 1), and (1, 0, 1) associated with the Medina lesion classification.

At peak diastolic point of a cardiac cycle, the WSS fields for true bifurcation lesions with 50% stenoses are presented in Figure 6.

The distribution pattern shows that, at the MBP and upstream the flow divider, WSS is uniform. The peak values of the WSS are at the center of stenosis and at the carina of bifurcation. The WSS value at the inner and outer walls peaks at the center of stenosis and reaches the minimum in the post-stenosis region and then recovers gradually in the downstream stenosis along the arterial wall until it levels off. As mentioned, low WSS regions which are linked with

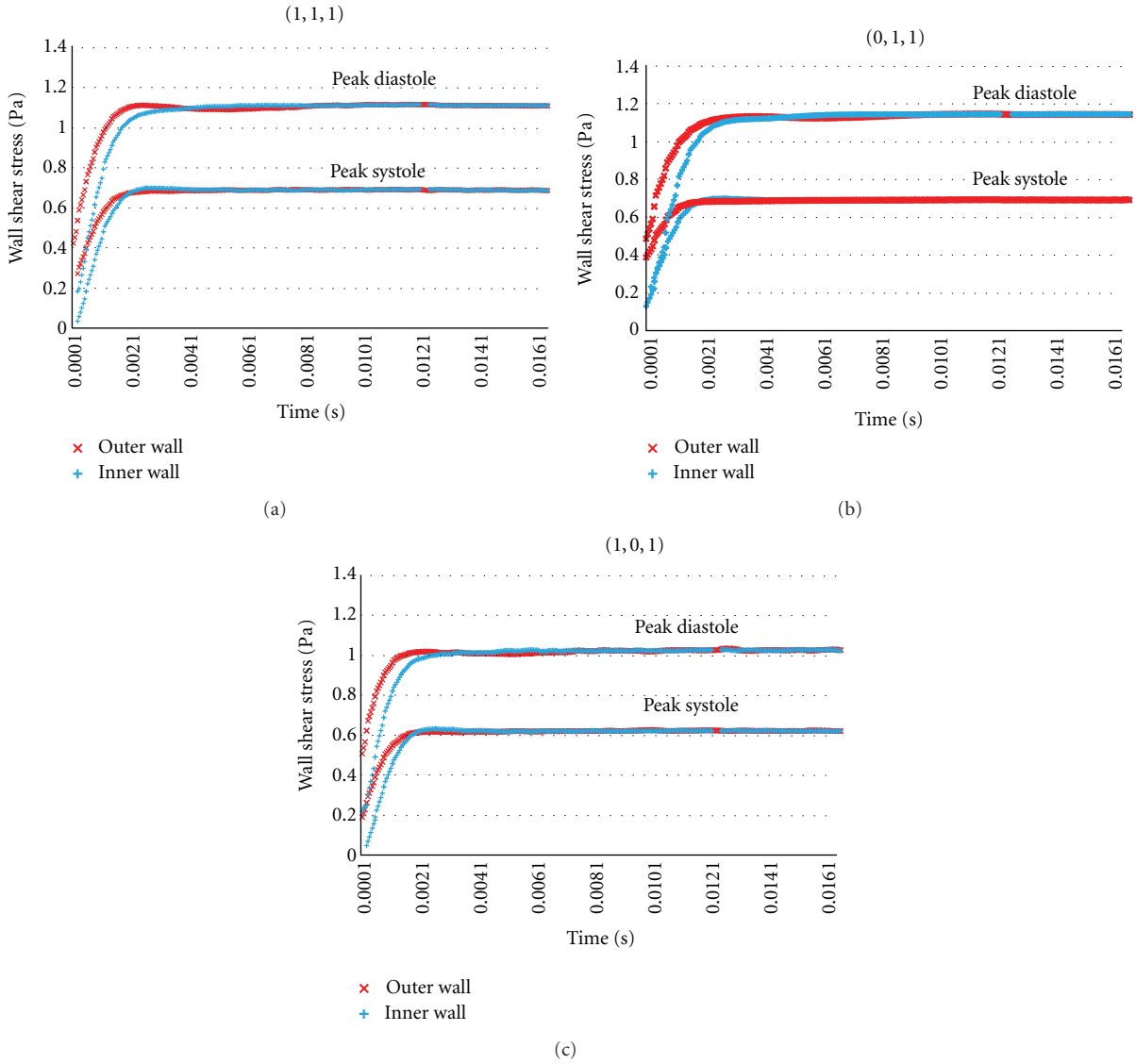

Figure 7: Wall shear stress on the outer and inner walls of SB and peak diastole.

atherosclerosis progression occur within the recirculation zone downstream the stenoses on the inner and outer walls.

Wall shear stress distribution on the inner and outer walls of SB downstream the stenosis is studied for bifurcation types (1, 1, 1), (0, 1, 1), and (1, 0, 1). The variation of WSS downstream the lesions on the outer and inner walls of SB at peak diastole are presented in Figure 7.

Comparing WSS values along the inner and outer walls between normal (Figure 3) and atherosclerotic bifurcations (Figure 7) revealed that the arteriosclerotic walls contain more regions exposed to low WSS values. In arteriosclerotic bifurcations, the magnitude of WSS on inner and outer walls of bifurcation type (1, 0, 1) both in post stenotic region and along the arterial wall is smaller than the corresponding magnitudes in bifurcation types (1, 1, 1) and (0, 1, 1).

Low WSS regions which are associated with atherosclerosis progression occur within the recirculation zone downstream the stenoses. In bifurcation lesions with stenosis in their SB, low WSS regions were observed in the poststenosis regions is the SB. We now examine the time-dependant behavior of the WSS in the poststenosis region on the outer wall of SB. For this purpose, three consecutive points (A, B, and C) are considered downstream the stenosis on the outer wall. Point A is located 0.1 mm downstream the stenosis. The A-B and B-C distances are 1.5 mm. The temporal variation of WSS downstream the lesions, at three consecutive points on the outer wall of SB for true bifurcation are presented in Figure 8.

The change of WSS throughout the cardiac cycle is highly correlated to flow velocities. The WSS characterizes the forces that longitudinally act on the vessel wall. At peak systole and peak diastole, when the blood flow parallel to the wall is fast, these forces are higher. At each individual point on the SB wall, the maximum value of WSS in all bifurcation types is related to the peak systolic and peak diastolic of a cardiac cycle. The maximum value of WSS for bifurcation lesion

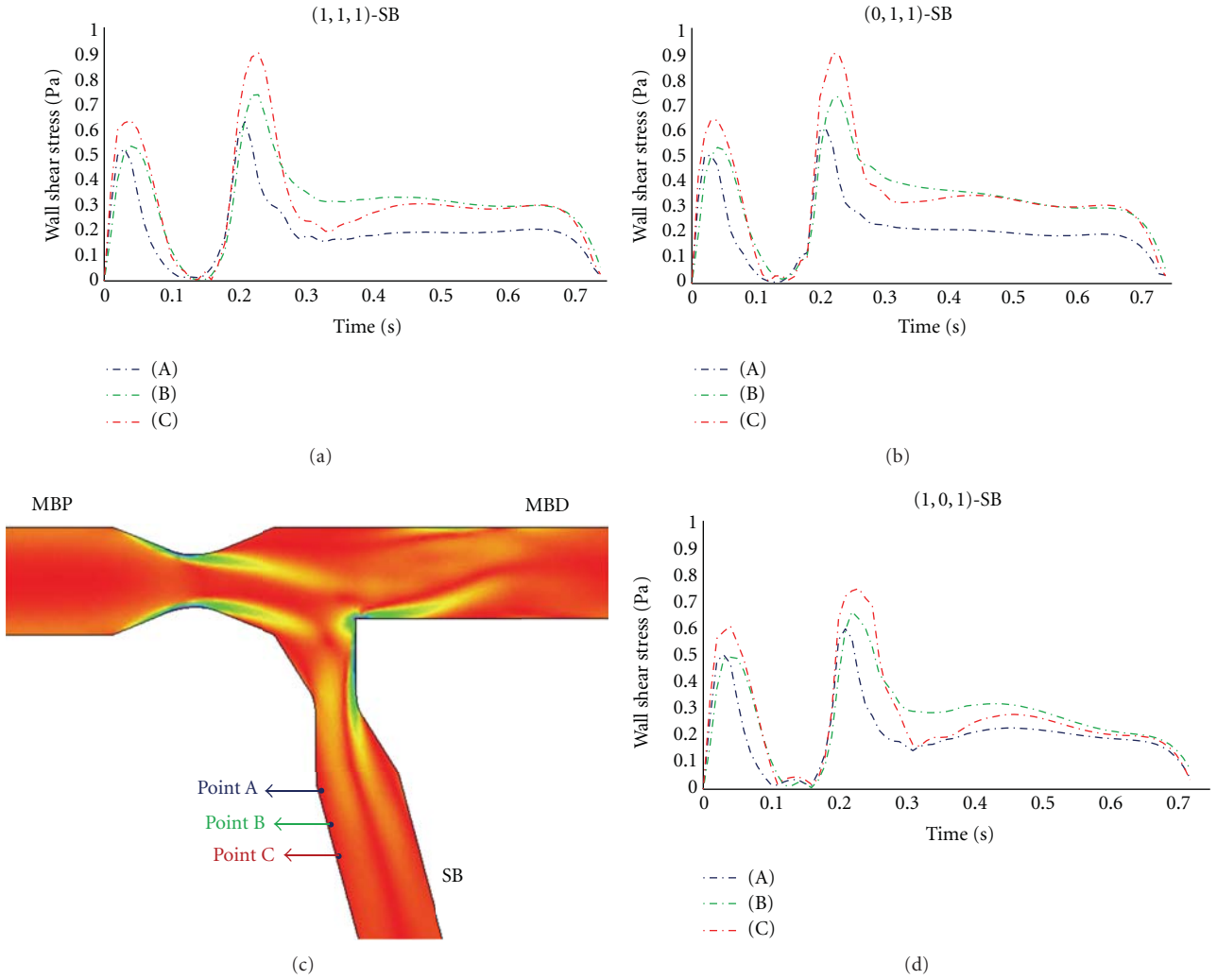

Figure 8: Temporal WSS at three points on the outer walls of SB for true bifurcation lesions.

types (1, 1, 1) and (0, 1, 1) at peak systolic and diastolic points are 0.65 Pa and 0.9 Pa. The corresponding WSS for lesion type (1, 0, 1) is 0.58 Pa and 0.75 Pa revealing that the minimum magnitude of WSS is related to the lesion type (1, 0, 1). The low values of WSS are mostly in the deceleration phase which possess two third of a cardiac cycle duration.

To assess how WSS pattern changes in MBD along the entire wall in all time steps of a cardiac cycle, the mean WSS values along the inner and outer walls downstream the lesions are computed for 68 nodes in bifurcation lesion types (1, 1, 1) and (0, 1, 1) and for 78 nodes in bifurcation lesion type (1, 0, 1). The mean WSS values are determined at each time step and mean WSS values along the inner and outer walls of MBD during a cardiac cycle are presented in Figure 9.

The distribution pattern of WSS on the MBD reveals that, most parts of the luminal surface are exposed to WSS within the physiological range. Comparisons of the WSS distributions in bifurcation lesion types (1, 1, 1), (0, 1, 1), and (1, 0, 1) shows that during the diastolic period, arterial regions downstream bifurcation lesion types (1, 1, 1), (0, 1, 1) exposes to lower magnitudes of WSS.

As another important hemodynamic parameter, WSS is studied in true bifurcation lesions. Predictions of WSS distribution downstream the stenosis is useful in the understanding of the effects of disturbed flow on endothelial cells and blood elements near the wall and can be used to support medical decision.

The results of the present study should be interpreted within the constraints of certain limitations. First, the geometries used in this work are a series of idealized two dimensional axisymmetric stenoses in idealized arterial bifurcation. In our problem, stenoses configurations and percentages are fixed while in reality they may vary and occur in different places along the vessel. Another geometric limitation of the present study is the fact that we do not take the composition of the compliance of the vessels; all the vessels are considered as rigid wall boundaries. The simulations do not take into consideration the non-Newtonian property of the blood. Indeed, while blood behaves generally like a Newtonian fluid

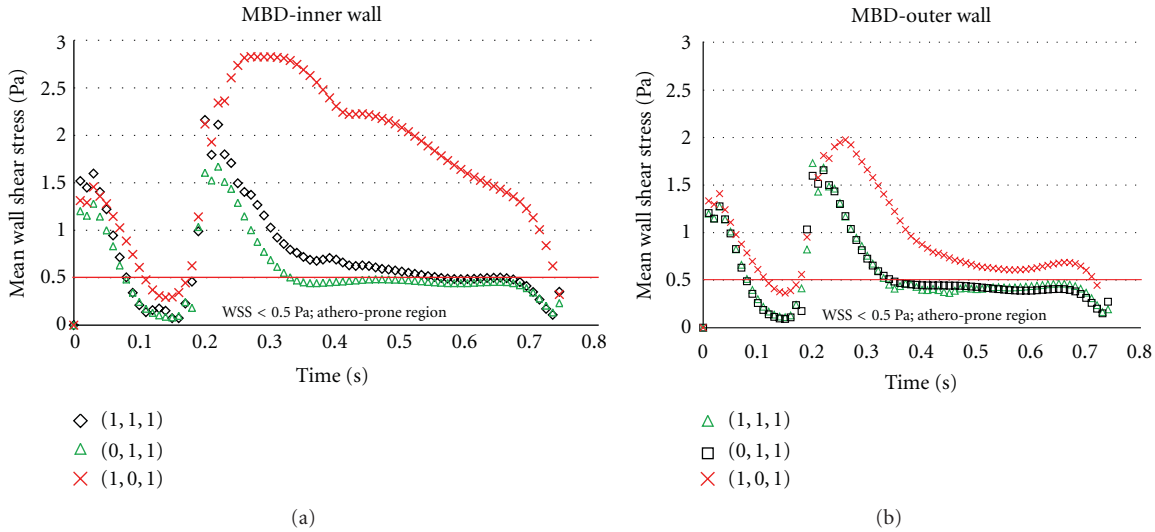

Figure 9: Mean WSS value along the inner and outer walls of MBD during a cardiac cycle.

at high shear rates, the non-Newtonian properties may affect the blood flow patterns and shear stress results at low shear rate regions. In addition, our geometric model is based on a representation of a straight blood vessel, while they may be curved in reality. The vessel curvature can have significant effect on the skewness of the velocity profile and the general behavior of the flow.

4. Conclusion

Most experimental and numerical studies of pulsatile flow through stenotic arteries have been performed assuming a simple vessel and there are no studies of hemodynamic changes associated with various bifurcation lesion types to date especially in the context of the Medina lesion classification. The present study is motivated by the need to understand the flow condition and WSS distributions in various bifurcation lesion types in a coronary artery bifurcation. We have investigated the flow ratio and time-dependence patterns of WSS resulting from the numerical simulation of pulsating hemodynamic flows in healthy and stenosed coronary artery bifurcations. Various stenoses configurations were considered according to Medina lesion classification and a detailed numerical result for time-dependent WSS distributions that may be involved in lesion initiation and progression is highlighted. The main results of this study are that different bifurcation type determines different flow ratio and WSS distributions in SB. In detail, the ratio of SB flow to MBP flow was less in both 50% and 75% for (1, 0, 1) bifurcation lesion type compared to (0, 1, 1) and (1, 1, 1). Examinations of the WSS distribution in true bifurcation lesions showed that on the SB, in terms of athero-prone regions, the lesion type (1, 1, 1) is not likely the worst case because the results support that lesion type (1, 0, 1) resulted in lower values of WSS on both inner and outer walls especially in the deceleration phase of the cardiac cycle. The results indicated that in the bifurcation lesion types, the flow condition and WSS distribution in SB are influenced by the lesion morphologies which cannot be fully assessed by quantitative coronary angiographic parameters.

References

[1] I. H. Tanboga, M. Ekinci, T. Isik, M. Kurt, A. Kaya, and S. Sevimli, "Reproducibility of syntax score: from core lab to real world," *Journal of Interventional Cardiology*, vol. 24, no. 4, pp. 302–306, 2011.

[2] F. Zhang, L. Dong, and J. Ge, "Simple versus complex stenting strategy for coronary artery bifurcation lesions in the drug-eluting stent era: a meta-analysis of randomised trials," *Heart*, vol. 95, no. 20, pp. 1676–1681, 2009.

[3] M. Pan, J. Suárez De Lezo, A. Medina et al., "Simple and complex stent strategies for bifurcated coronary arterial stenosis involving the side branch origin," *American Journal of Cardiology*, vol. 83, no. 9, pp. 1320–1325, 1999.

[4] E. Jorgensen and S. Helqvist, "Stent treatment of coronary artery bifurcation lesions," *European Heart Journal*, vol. 28, no. 4, pp. 383–385, 2007.

[5] I. Iakovou, L. Ge, and A. Colombo, "Contemporary stent treatment of coronary bifurcations," *Journal of the American College of Cardiology*, vol. 46, no. 8, pp. 1446–1455, 2005.

[6] J. Popma, M. Leon, and E. J. Topol, *Atlas of Interventional Cardiology*, Saunders, Philadelphia, Pa, USA, 1994.

[7] A. M. Spokojny and T. M. Sanborn, "The bifurcation lesion," in *Strategic Approaches in Coronary Intervention*, S. G. Ellis and D. R. Holmes, Eds., p. 288, Williams and Wilkins, Baltimore, Md, USA, 1996.

[8] T. Lefèvre, Y. Louvard, M. C. Morice et al., "Stenting of bifurcation lesions: classification, treatments, and results," *Catheterization and Cardiovascular Interventions*, vol. 49, pp. 274–283, 2000.

[9] R. D. Safian, "Bifurcation lesions," in *Manual of Interventional Cardiology*, R. D. Safian and M. Freed, Eds., pp. 221–236, Physicians' Press, Royal Oak, Mich, USA, 2001.

[10] G. Sianos, M. A. Morel, and A. P. Kappetein, "The SYNTAX score: an angiographic tool grading the complexity of

coronary artery disease," *Eurointervention*, vol. 1, no. 2, pp. 219–227, 2005.

[11] M. R. Movahed and C. T. Stinis, "A new proposed simplified classification of coronary artery bifurcation lesions and bifurcation interventional techniques," *Journal of Invasive Cardiology*, vol. 18, no. 5, pp. 199–204, 2006.

[12] A. Medina, J. Suarez de Lezo, and M. A. Pan, "A new classification of coronary bifurcation lesions," *Revista Espanola de Cardiologia*, vol. 59, no. 2, p. 183, 2006.

[13] T. Asakura and T. Karino, "Flow patterns and spatial distributions of atherosclerotic lesions in human coronary arteries," *Circulation Research*, vol. 66, no. 4, pp. 1045–1066, 1990.

[14] B. I. Tropea, S. Glagov, and C. K. Zarins, *Hemodynamics and Atherosclerosis*, Futura, Armonk, NY, USA, 1997.

[15] C. G. Caro, J. M. Fitz-Gerald, and R. C. Schroter, "Arterial wall shear and distribution of early atheroma in man," *Nature*, vol. 223, pp. 1159–1161, 1969.

[16] A. M. Malek, S. L. Alper, and S. Izumo, "Hemodynamic shear stress and its role in atherosclerosis," *Journal of the American Medical Association*, vol. 282, no. 21, pp. 2035–2042, 1999.

[17] P. H. Stone, A. U. Coskun, Y. Yeghiazarians et al., "Prediction of sites of coronary atherosclerosis progression: in vivo profiling of endothelial shear stress, lumen, and outer vessel wall characteristics to predict vascular behavior," *Current Opinion in Cardiology*, vol. 18, no. 6, pp. 458–470, 2003.

[18] M. A. J. Gimbrone, J. N. Topper, T. Nagel, K. R. Anderson, and G. Garcia-Cardena, "Endothelial dysfunction, hemodynamic forces, and atherogenesis," *Annals of the New York Academy of Sciences*, vol. 902, pp. 230–239, 2000.

[19] K. S. Cunningham and A. I. Gotlieb, "The role of shear stress in the pathogenesis of atherosclerosis," *Laboratory Investigation*, vol. 85, no. 1, pp. 9–23, 2005.

[20] K. C. Koskinas, C. L. Feldman, Y. S. Chatzizisis et al., "Natural history of experimental coronary atherosclerosis and vascular remodeling in relation to endothelial shear stress: a serial, in vivo intravascular ultrasound study," *Circulation*, vol. 121, no. 19, pp. 2092–2101, 2010.

[21] C. Cheng, D. Tempel, R. van Haperen et al., "Atherosclerotic lesion size and vulnerability are determined by patterns of fluid shear stress," *Circulation*, vol. 113, no. 23, pp. 2744–2753, 2006.

[22] D. N. Ku, D. P. Giddens, C. K. Zarins, and S. Glagov, "Pulsatile flow and atherosclerosis in the human carotid bifurcation. Positive correlation between plaque location and low and oscillating shear stress," *Arteriosclerosis*, vol. 5, no. 3, pp. 293–302, 1985.

[23] S. Fabregues, K. Baijens, R. Rieu, and P. Bergeron, "Hemodynamics of endovascular prostheses," *Journal of Biomechanics*, vol. 31, no. 1, pp. 45–54, 1997.

[24] C. von Birgelen, S. G. Airiian, G. S. Mintz et al., "Variations of remodeling in response to left main atherosclerosis assessed with intravascular ultrasound in vivo," *American Journal of Cardiology*, vol. 80, no. 11, pp. 1408–1413, 1997.

[25] J. B. Hermiller, C. E. Buller, A. N. Tenaglia et al., "Unrecognized left main coronary artery disease in patients undergoing interventional procedures," *American Journal of Cardiology*, vol. 71, no. 2, pp. 173–176, 1993.

[26] T. C. Gerber, R. Erbel, G. Gorge, J. Ge, H. J. Rupprecht, and J. Meyer, "Extent of atherosclerosis and remodeling of the left main coronary artery determined by intravascular ultrasound," *American Journal of Cardiology*, vol. 73, no. 9, pp. 666–671, 1994.

[27] Z. Kaimkhani, M. Ali, and A. M. A. Faruqui, "Coronary artery diameter in a cohort of adult Pakistani population," *Journal of the Pakistan Medical Association*, vol. 54, no. 5, pp. 258–261, 2004.

[28] C. Godino, R. Al-Lamee, C. La Rosa et al., "Coronary left main and non-left main bifurcation angles: how are the angles modified by different bifurcation stenting techniques?" *Journal of Interventional Cardiology*, vol. 23, no. 4, pp. 382–393, 2010.

[29] D. G. Rizik, K. J. Klassen, and J. B. Hermiller, "Bifurcation CAD: current techniques and future directions: morphology of the bifurcation," *Journal of Invasive Cardiology*, vol. 20, no. 2, pp. 82–90, 2008.

[30] S. H. Na, B. K. Koo, J. C. Kim et al., "Evaluation of local flow conditions in jailed side branch lesions using computational fluid dynamics," *Korean Circulation Journal*, vol. 41, no. 2, pp. 91–96, 2011.

[31] Y. Louvard, A. Medina, and G. Stankovic, "Classification of coronary artery bifurcation lesions and treatments," *Eurointervention*, vol. 6, supplement J, pp. 31–35, 2010.

[32] J. F. Ladisa, J. I. Guler, L. E. Olson et al., "Three-dimensional computational fluid dynamics modeling of alterations in coronary wall shear stress produced by stent implantation," *Annals of Biomedical Engineering*, vol. 31, no. 8, pp. 972–980, 2003.

[33] I. Faik, R. Mongrain, R. L. Leask, J. Rodes-Cabau, E. Larose, and O. F. Bertrand, "Time-dependent 3D simulations of the hemodynamics in a stented coronary artery," *Biomedical Materials*, vol. 2, pp. S28–S37, 2007.

[34] Z. D. Zhang, M. Svendsen, J. S. Choy et al., "New method to measure coronary velocity and coronary flow reserve," *American Journal of Physiology*, vol. 301, no. 1, pp. H21–H28, 2011.

[35] W. G. Hundley, R. A. Lange, G. D. Clarke et al., "Assessment of coronary arterial flow and flow reserve in humans with magnetic resonance imaging," *Circulation*, vol. 93, no. 8, pp. 1502–1508, 1996.

[36] J. S. Stroud, S. A. Berger, and D. Saloner, "Numerical analysis of flow through a severely stenotic carotid artery bifurcation," *Journal of Biomechanical Engineering*, vol. 124, no. 1, pp. 9–20, 2002.

[37] N. Benard, R. Perrault, and D. Coisne, "Computational approach to estimating the effects of blood properties on changes in intra-stent flow," *Annals of Biomedical Engineering*, vol. 34, no. 8, pp. 1259–1271, 2006.

[38] Y. S. Chatzizisis, M. Jonas, A. U. Coskun et al., "Prediction of the localization of high-risk coronary atherosclerotic plaques on the basis of low endothelial shear stress-an intravascular ultrasound and histopathology natural history study," *Circulation*, vol. 117, no. 8, pp. 993–1002, 2008.

[39] B. Fox, K. James, B. Morgan, and A. Seed, "Distribution of fatty and fibrous plaques in young human coronary arteries," *Atherosclerosis*, vol. 41, no. 2-3, pp. 337–347, 1982.

[40] C. Velican and D. Velican, "Incidence, topography and light-microscopic feature of coronary atherosclerotic plaques in adults 26–35 years old," *Atherosclerosis*, vol. 35, no. 1, pp. 111–122, 1980.

[41] G. Nakazawa, S. K. Yazdani, A. V. Finn, M. Vorpahl, F. D. Kolodgie, and R. Virmani, "Pathological findings at bifurcation lesions: the impact of flow distribution on atherosclerosis and arterial healing after stent implantation," *Journal of the American College of Cardiology*, vol. 55, no. 16, pp. 1679–1687, 2010.

[42] S. A. Ahmed and D. P. Giddens, "Velocity measurements in steady flow through axisymmetric stenoses at moderate Reynolds numbers," *Journal of Biomechanics*, vol. 16, no. 7, pp. 505–516, 1983.

Hindawi Publishing Corporation
Modelling and Simulation in Engineering
Volume 2012, Article ID 651434, 12 pages
doi:10.1155/2012/651434

Review Article

A CFD Simulation on How the Different Sizes of Silica Gel Will Affect the Adsorption Performance of Silica Gel

John White

School of Engineering, University of Birmingham, Birmingham B15 2TT, UK

Correspondence should be addressed to John White, jxw998@bham.ac.uk

Received 6 December 2011; Revised 12 January 2012; Accepted 17 January 2012

Academic Editor: Guan Heng Yeoh

The application of computational fluid dynamics (CFD) in the area of porous media and adsorption cooling system is becoming more practical due to the significant improvement in computer power. The results from previous studies have shown that CFD can be useful tool for predicting the water vapour flow pattern, temperature, heat transfer, flow velocity, and adsorption rate. This paper investigates the effect of silica gel granular size on the water adsorption rate using computational fluid dynamics.

1. Introduction

The adsorption properties of silica gel have been studied for many years as silica gel is used in many industries including adsorption cooling systems. Past research have shown experimentally that the adsorpitivity of silica gel granules depend on their size. The purpose of this work was to study the effect of granule size on the adsorption properties of silica gel by using CFD and comparing the simulation results to those obtained experimentally.

To design an efficient adsorber bed, flow, and temperature, adsorption information is essential. Studies of fluid dynamics and heat transfer in adsorber beds date back to the early twentieth century [1] (Andersson, 1961.) The early investigation of flow in porous media packed beds provided mainly such bulk information as pressure drop correlations [2]. Predict pressure loss for flow in adsorber beds [3, 4]. Computational fluid dynamics (CFD) provides an innovative approach to model and analysing the local flow and the effect of silica gel size on adsorption performance of a packed bed. CFD simulation of porous media local flow and heat transfer based on CFD technique has increasingly been reported in recent years in fields of packed bed flow and heat transfer modelling [5, 6]. CFD simulation was based on fundamental principles of diffusion and adsorption/desorption of porous materials. In this study, an integrated CFD model was developed to model and simulate the adsorption dynamics of water vapour in three different sizes of silica gel in a fixed bed adsorption column. The developed integrated model was used to determine the adsorption capacity of the three silica gel as a function of time, based on different operating conditions.

The simulated results were compared with pass research papers experimental data and found to give a good agreement. The effect of various influencing parameters such as velocity and silica gel porosity were studied to investigate their influences on the adsorption capacity.

1.1. Methods

1.1.1. 3D Geometry of Silica Gel Packing. Geometric models of the silica gel adsorber bed systems are generated for a tube of 25 mm length of 100 mm diameter.

The size of silica gel that are use in this CFD simulation is

Silica gel granular size 1 mm
Silica gel granular size 2 mm
Silica gel granular size 3 mm.

Adsorbent particle size affects how the water vapour flows through the adsorber bed. Smaller particles (higher mesh values) larger particles (lower mesh values).

First we selected the silica gel to particle sizes the silica gel were selected in the ranges of 40–60 mesh, 60–100 mesh, and 100–200 mesh.

2. Modelling Strategies for Silica Gel Adsorber Beds

In this study, an integrated CFD model was developed to simulate the adsorption dynamics of water vapour of silica gel granules in a fixed bed adsorption column using the solidworks flow simulation module. The model consists of two modes of operation, the water vapour adsorption and the desorption mode. In each mode, the water vapour flow profile surrounding the granules was determined by solving the Navier-Stokes equations and the resulting velocity profile was regarded time invariant and stored for later use. Also, the time-dependent mass transfer both outside and inside the porous silica gel due to its adsorpitivity was simulated through a user-defined function developed to solve the Brunauer, Emmett and Teller (BET) equation [1] for both adsorption and desorption processes. The developed model was used to determine the adsorption capacity of three different sizes of silica gel granules namely; 1 mm, 2 mm, and 3 mm as a function of time at different operating temperatures. The simulation results were compared with past experimental data and found to give a good agreement.

2.1. Modelling of Vapour Flow in Silica Gel Particle. The porous media capabilities of flow simulation are used to simulate a porous media silica gel which allows you to model the volume that the silica gel occupies as a distributed resistance instead of discretely modelling all of the individual passages within the silica gel, which would be impractical or even impossible. We consider the influence of the porous medium permeability type (isotropic and unidirectional media of the same resistance to flow) on the water vapour mass flow rate distribution over the silica gel. We will observe the latter through the behaviour of the water vapour flow trajectories distributed uniformly over the model's inlet and passing through the porous silica gel. Additionally, by cooling the flow trajectories by the flow velocity the vapour residence time in the porous media can be estimated, which is also important from the silica gel adsorption of water vapour effectiveness viewpoint. As a first introduction to CFD a simple model was created the model represented one silica granule in a tube as shown in (Figure 1) the flow inlet and flow outlet.

The silica gel granule in the tube was designed with the dimensions of 1 mm, 2 mm and 3 mm this was then used in the validation model. With this model it was tried to fit CFD data to generally accepted experimental data. This one granule was then clone to 40 granule 60 and 120 these clone granule was then simulated in a tube bed (see Figure 2).

This limitation of granules was necessary to keep the model reasonable in size with a mesh density comparable to the validation model. A series of runs was conducted at a number of flow velocities, see Table 3. In all these runs, the centrally located granules had a defined temperature of 20°C. The tube wall temperature was set at 20.5°C to create a 0.5°C temperature difference between the granule and the fluid at infinite distance. The water vapour that flowed through the tube was defined at 20°C at the entrance. The temperature of the through the granules was simulated and recorded.

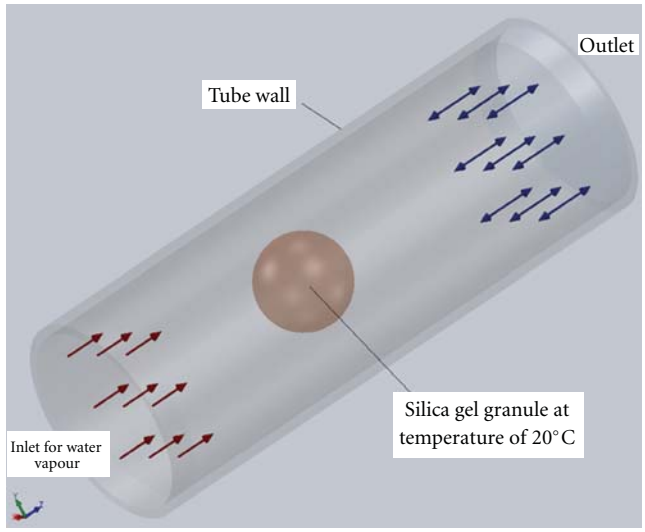

Figure 1: One silica gel in a tube geometry used for validation of CFD against theoretical models.

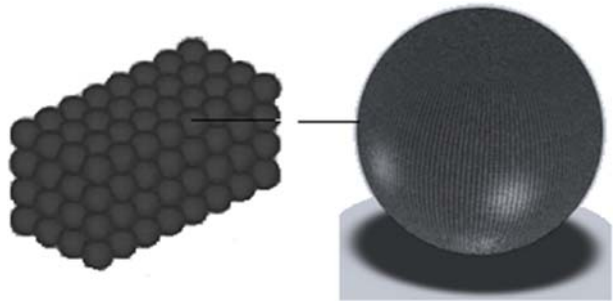

Figure 2: This one granule was then clone to 36 granule 65 and 114 granules.

A constant diffusion coefficient D_e was assumed according to the reference of [7] Sakoda et al. (1984). The spherical silica gel particle with initial conditions of water content $m_r = 0$ and a temperature T_{in} is instantaneously exposed to vapour flow. The diffusion equation in the silica gel particle is

$$\frac{\partial m_r}{\partial t} = \frac{1}{r^2}\,\frac{\partial}{\partial r}\left(D_e r^2 \frac{\partial m_r}{\partial_r}\right). \tag{1}$$

The initial condition and boundary conditions for (1) are

$$\begin{aligned} m_r(r; t = 0) &= 0, \\ \left.\frac{\partial m_r}{\partial r}\right|_{r=0} &= 0, \\ m_r\left(r = \frac{d_p}{2}, t\right) &= m_s(T, x, P). \end{aligned} \tag{2}$$

The m_r is local water content of a silica gel particle in the radial direction and the m_e is the equilibrium water content on the particle surface. The water content averaged in a silica gel particle is given by

$$m = \frac{24}{d_p^3}\int_0^{dp/2}\left(1 - e_p\right) r^2 m_r dr, \tag{3}$$

where the porosity in a silica gel particle was fixed at $e_p = 0.38$ for 1 mm silica gel, 0.38 for 2 mm silica gel and 0.34 for the 3 mm silica gel.

3. CFD Governing Equations

The transport phenomena can be divided into adsorption and water vapour flow in the adsorber bed, silica gel granules surfaces Navier-Stokes equations for flow are used to solve the water vapour flow phase [1, 3, 7–11]:

$$\frac{\partial \vec{u}}{dt} = -\frac{1}{\rho}\nabla p + \eta \Delta \vec{u}, \qquad \nabla \cdot \vec{u} = 0. \tag{4}$$

The p represents pressure, η dynamic viscosity and ρ density of the fluid the velocity flow can be simulated in first. This simulated data is then stored and used for solving the convection-diffusion equation [1]:

$$\frac{\partial c}{\partial t} = -\vec{u} \cdot \nabla c + D \cdot \Delta c. \tag{5}$$

The c represents the water vapour molecule adsorbed into the silica gel, and D the diffusion flow coefficient in the silica gel. In contrast to diffusion, an effective diffusivity D_e must be applied [1, 3, 9–11]:

$$\frac{\partial c_p}{\partial t} = D_e \cdot \Delta c_p - \frac{1-\varepsilon_e}{\varepsilon_e}\frac{\partial q}{\partial t}, \qquad D_e = \frac{\varepsilon_i D}{\theta}. \tag{6}$$

The c_p represents the water vapour molecule adsorbed within the silica gel particle. The mass transfer resistance between the silica gel surface is also modelled [1]:

$$\vec{n} \cdot (-D\nabla c + c\vec{u}) = k_f\left(c - c_p\right), \qquad -\vec{n} \cdot \left(-D_e\, \nabla c_p + c_p \vec{u}\right) = k_f\left(c_p - c\right). \tag{7}$$

The $\vec{n}$ represents the normal vector of the outer silica surface. The driving force of transport over the particle boundary is relative to the adsorption difference, and k_f is the corresponding mass transfer coefficient. The adsorber beds in the CFD simulation are simulated with far less silica gel granules than in a real adsorber bed. In order to simulate similar systems, the effective diffusivity D_e is increased. The adsorption of the water vapour molecules at the silica surfaces is described by a classical Langmuir-type kinetic [1, 3, 7–10]:

$$\frac{\partial q}{\partial t} = k_a \cdot c \cdot (q_{\max} - q) - k_d \cdot q. \tag{8}$$

The k_a and k_d represent adsorption and desorption rates, $q_{\max}$ maximum capacity, and q the current occupation of binding sites at the surface.

3.1. Desorption of Vapour in Porous Materials. When considering desorption in a porous material one must considers vapour transport the Lattice Boltzmann equation can be expressed as

$$\frac{\partial s}{\partial t} = r\left(k_p c^p - s^q\right). \tag{9}$$

This can be done with Lattice Boltzmann multi physics extension by applying a local rule describing the change of the adsorption rate $\partial s/\partial t$ on the water vapour concentration C and the adsorbed mass S deposited per unit volume of the porous media matrix.

With parameters $k_p > 0$ and exponents p, q fulfilling $p/q \leq 1$. At equilibrium, that is, for $\partial s/\partial t = 0$, this model reduces to a Freundlich isotherm:

$$s = kc^n, \tag{10}$$

with $k = {k_p}^{1/q}$ and $n = p/q$.

4. CFD Modelling Method

In all types of CFD modelling there are some factors that determine the difficulty of modelling granules packed adsorption beds. In a silica gel packed bed the amount of packing and the narrow region between them makes its modelling more complicated. One way of solving this problem is to model a single granule of silica gel in CAD software.

This single granule can then be clone into thousands of granule then pack into a 3D adsorption bed (see Figure 3). The clone pack silica gel can then be inserted as a parasolid CAD file then one could applied a porous media material using a CFD software called flow simulation. Then, this porous media could be solved by using a finite control-volume method.

4.1. Smaller Arrangements of Silica Gel Granules. The amount of silica gel granules in a real adsorber bed cannot be reproduced in a three-dimensional model using CFD tools. However, to simplify the numerical calculations you can simulate smaller arrangements of silica gel granules. In this study, there are three silica gel sizes in the adsorber beds these beds contain 36, 65, and 114 particles, respectively (see Figure 4).

Different porosities were obtained by changing the particle sizes and arrangements. Constant thermo physical properties at 20°C were assumed for the water vapour. Periodic boundary conditions were imposed on the boundaries of the computational domain. The inflow into the domain was set as a velocity inlet with the outflow set as the pressure outlet boundary condition. The dimensions and porosities of the porous media used in the simulation were based on the experimental research are listed in Table 1. The constant contact areas between the particles were calculated based on the desired porosity.

4.2. Computational Mesh Domain. In this work, the mesh creation was done using flow simulation, a general-purpose

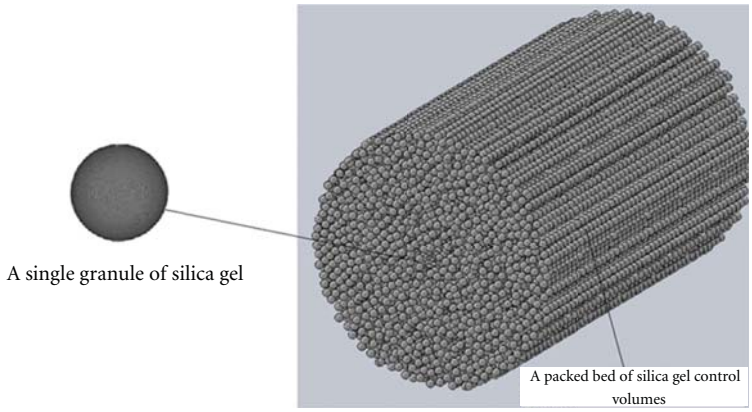

Figure 3: Thousands of granule pack the silica gel into a 3D adsorption bed.

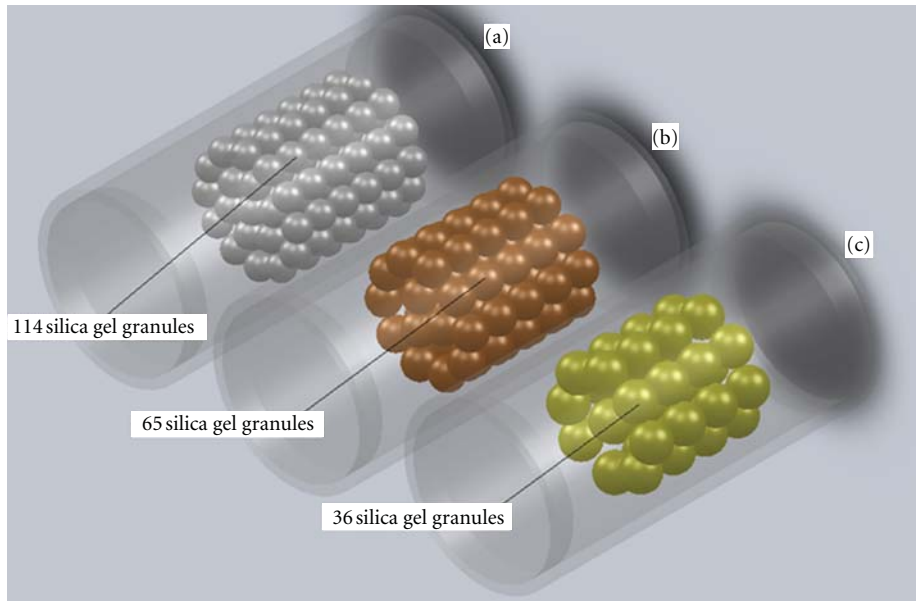

Figure 4: The three adsorption bed tube containing the numerically created example packing with (a) 36 granules, (b) 65 granules, (c) 114 granules.

Table 1: Geometry and mesh parameters.

Test section	Porous media sizes (mm)	Porosity ε	Total number of elements
No. 1	1 mm	0.38	1065623
No. 2	2 mm	0.38	1122425
No. 3	3 mm	0.34	1097191

program providing a variety of automatic meshing strategies. All the simulation, in this exercise were conducted first with automatic meshing and then secondly modified manually to help determine the influence of mesh density on the outcome of the simulation.

4.3. A Porous Sample with Nonuniform Porosity. The mesh domain was split into 1065623 cells containing 1122425 faces and 1097191 nodes.

The grid was then partitioned along the principal axis into 3 segments to allow the domain to reduce simulation time on computer see Figure 5.

4.4. 3D Silica Gel Granules Packing Arrangements. When simulating the adsorption of water vapour on porous silica gel the volume of silica gel packing and pore spacing will depend upon the size of silica gel. But in some sense the relationship between size and pore spacing can be more complex because of the influence of packing arrangements.

For example, the packing of spherical porous media of 1 mm uniform size in Figure 6(a) when a simulation was completed on this type of packing arrangement, the porosity was 0.45. But when the simulation was simulated in Figure 6(b) the porosity was 0.26 and when a simulation was completed in the Figure 6(c), it was 0.38, this arrangement was a more realistic packing arrangement, this was a random arrangement. In a real-world scenario, adsorption bed would

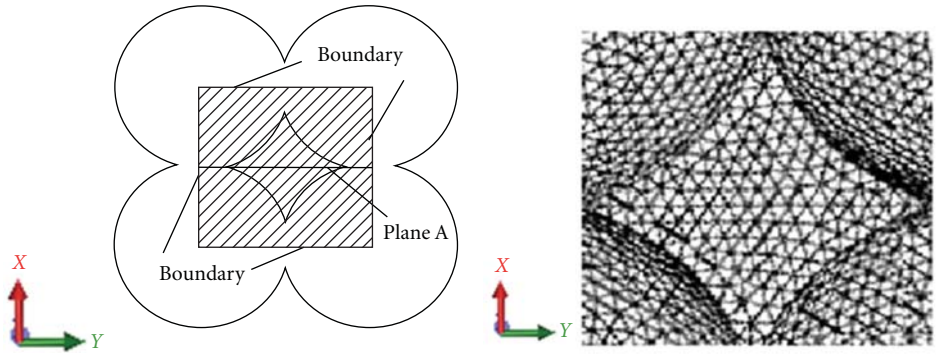

Figure 5: Schematic diagram of the computational domain.

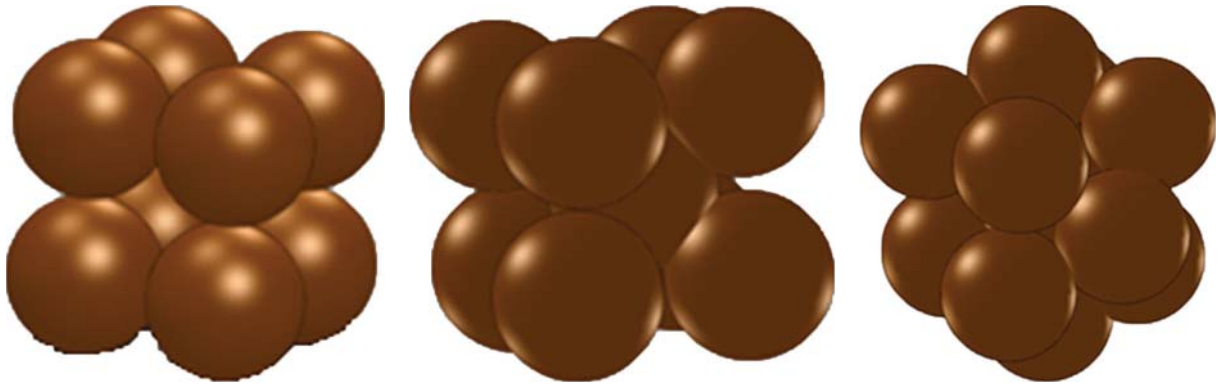

Figure 6: Arrangements of the silica gel particles for CFD simulation.

have randomly packing of silica gel and not uniform arrangement. So, it was determined that this was the packing arrangement to be used in all CFD simulation.

4.5. CFD Mesh Generation. For all types of geometries the creation of the mesh has different obstacles. In the meshing of silica-gel-packed bed geometry, the major issue is resolving the areas where two solid surfaces touch the contact points.

Because of this fact, the silica gel radii were reduced by about 2% in order to avoid mesh failures in the area of the silica gel contact points (see Figure 7).

4.6. Porous Media Simulations. A porous material had to be defined for the adsorbent used in the simulation. Materials were found in different sources, one of the source was in ([8] Akisawa, Saha (2001), [3] Akira , Alam (2005)). Type A and Type RD were created with a density of 730 kg/m^3, for type A and a density of 800 kg/m^3, for type RD, a heat capacity of 0.921 J/kgK, and a thermal conductivity of 0.174 W/mK (see Table 2).

By studying the table above, you can see that Type A silica gel and Type RD have similar physical properties which give them similar adsorption/desorption characteristics at different regeneration temperatures [8].

Table 2: Thermophysical properties of silica gel.

	Type A	Type 3A	Type RD
Specific surface area (m^2/g)	650	606	650
Porous volume (mL/g)	0.36	0.45	0.35
Average pore diameter (A)	22	30	21
Apparent density (kg/m^3)	730	770	800
pH value	5.0	3.9	4.0
Water content (wt.%)	<2.0	0.87	—
Specific heal capacity (kJ/kg K)	0.921	0.921	0.921
Thermal conductivity (W/m K)	0.174	0.174	0.198
Mesh sire	10–40	60–200	10–20

4.7. Porosity of Silica Gel Used in CFD Simulation. Porosity is the effective porosity of the porous medium, defined as the volume fraction of the interconnected pores with respect to the total porous medium volume; here, the porosity is equal to 0.36. The porosity will govern the water vapour flow velocity in the porous medium channels, which, in turn, governs porous medium efficiency. The porosity of the granules is defined as the ratio of the volume of the total pore space filled by the fluid to the total volume of the porous medium, all within the domain of interest. Since mesh cells in

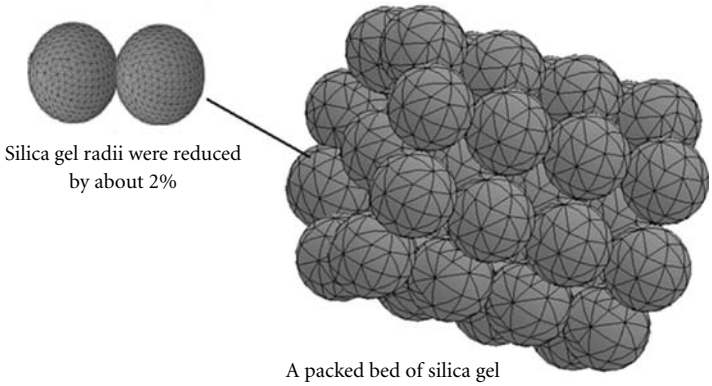

Figure 7: 3D dimensional display and detail of the control volumes in the fluid region near particle-to particle contact points.

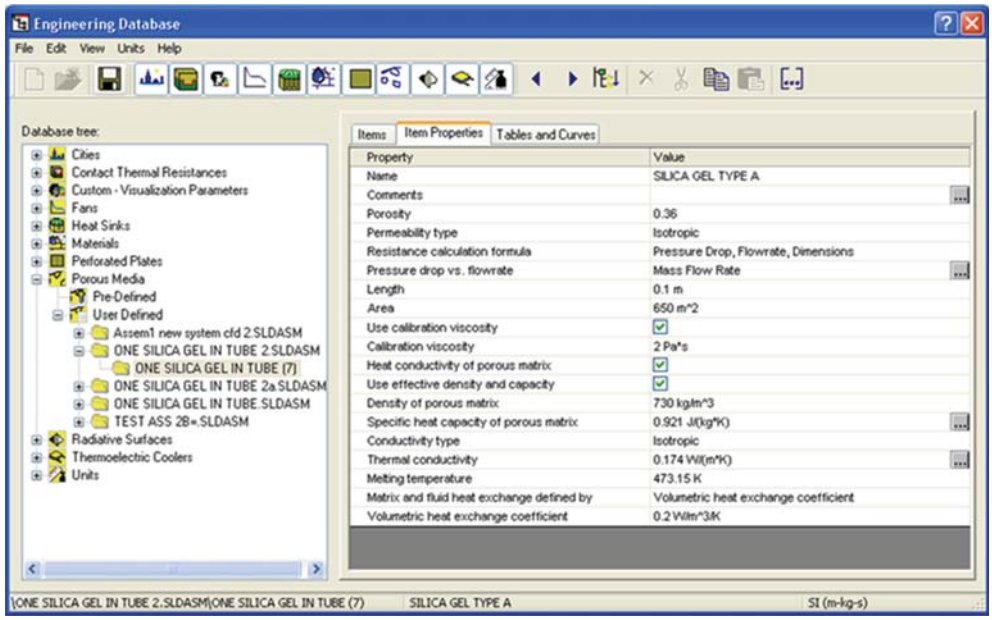

Figure 8: To define a porous medium in this simulation you need to specify the porous medium's properties (porosity, permeability type, etc.) in the *engineering database* and then apply the porous medium to a silica gel in the assembly see Figure 8.

the domain have been tagged as solid or fluid, the volume of total pore space can easily be obtained numerically by finding the sum of volumes of the cells tagged as fluid. Similarly, the volume of the solid matrix is the sum of volumes of the cells tagged as solid. Finally, the total medium volume is simply the sum of the volumes of all cells, see also Figure 9.Then the porosity is defined by the following equation:

$$\frac{\Delta P}{L} = -\alpha U_s^2 - \beta U_s. \tag{11}$$

For some materials which have nonconstant porosity (Benenati and Brosilow), there are various techniques available to generate numerical porous media with the same nonuniform characteristics.

4.8. Pressure Drop and Mass Transfer. The pressure drop and water vapour flow rate caused by the different size of silica gel perpendicular to the flow direction together with the mass transfer coefficient are very important in determining optimal packing design.

Table 3: Simulated pressure drop of different spacer arrangement.

Inlet velocity (m/s)	Pressure drop size 1 mm (kPa/cm)	Pressure drop size 2 mm (kPa/cm)	Pressure drop size 3 mm (kPa/cm)
0.5	0.27	0.32	0.35
1.0	0.92	1.05	1.13
2.0	2.19	2.60	3.02

Table 2 shows the pressure drop for different simulated silica gel size and arrangement.

It can be seen that the pressure drop in the different size of silica gel arrangements in the adsorption tube increased

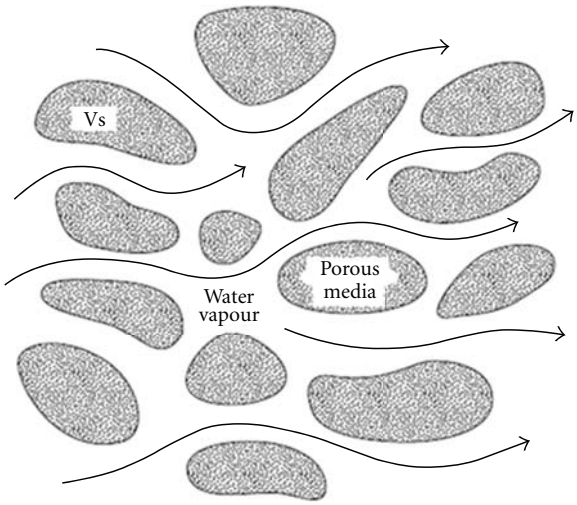

Figure 9: A typical domain of a porous medium two phase problem.

significantly with inlet velocity. The silica gel size 1 mm has the lowest pressure drop values are observed. This may be partly due to the fact that the diameter of these silica gel arrangement are smaller than the two silica gel 2 mm and 3 mm arrangement in the adsorption tubes. The pressure drop for silica gel size 2 mm is slightly higher than 3 mm silica gel this is also because of the different size effect on flow of vapour.

4.9. Boundary Conditions Used in Simulation. The boundary conditions determine the flow and thermal variables on the boundaries of the physical model. There are a number of boundary conditions:

(i) flow inlet and exit boundaries: pressure inlet, velocity inlet, pressure outlet;

(ii) wall, repeating, and limit boundaries: wall, symmetry;

(iii) internal fluid, solid;

(iv) internal face boundaries: porous, wall, interior.

In our model we use a velocity inlet at the flow inlet of the adsorption bed, this boundary condition defines a flow velocity at the inlet of the bed. The flow exit boundary is defined as a pressure outlet; the outlet pressure is defined as atmospheric pressure. The bed and packing interiors are defined as boundaries. The wall boundaries separate the fluid zone, vapour, in between the silica gel particles from the wall zones [4, 5, 12–14].

With the determination of the boundary conditions, the physical model has been defined and a numerical solution can be provided. It was then necessary to determine how the solution will be established. This was done by setting the iteration parameters. With all boundary conditions defined, a number of additional parameters and solving schemes were selected.

An initial condition was assigned to the model and was used to help speed the convergence of the computation. The computation is an iterative process that solves the governing equations for flow and energy in each simulated cell. Depending on the complexity of the model and the computer resources available, CFD simulation can take anywhere from minutes to days [10]. The results of the simulation can be viewed and manipulated with post-processing software once the simulation has converted to a solution.

4.10. Postprocessing the Simulation Data. When the simulation has converged, the last dataset is stored as a final solution. This dataset has a record of the status of all elements in the model, temperature, densities, pressures, flow aspects, and so forth. To be able to interpret the data, it needs to be ordered and reduced to comprehensible sizes [15]. This displaying of the data is called postprocessing and makes it possible to compare the different simulations with each other and with external data. There was as many ways of displaying the data as there were data points so it was important to select the data representation that was required for the desired data comparison. Some of the standard options available are contour plots and velocity vector plots. Contour plots will give a plot in the defined data point collection, this can be a plane or a volume, of contours of another variable. For example, a plane can be defined as a constant x coordinate plane (y-z plane), we can then make a contour plot showing temperature contours in this plane. In the same plane, a velocity contour plot can be made showing absolute velocities of the fluid in the defined plane. Other variables that can be used for contour plots are magnitude of velocity components, turbulence components, pressure, and so forth. Velocity vector plots can be made to get an insight into the flow patterns in the overall geometry or detailed at specific locations [3, 9–11].

4.11. Fluid Flow Fundamentals. For iteration, CFD solvers use generalized fluid flow and energy balances based on the Navier-Stokes equations. The balances are generalized so the user can influence which elements are added in the balance and which are not. The number of balances to be solved is also user defined; it can be advantageous to not solve all balances initially. The generalized balances that are used by the flow simulation commercial CFD package are the Navier-Stokes equations for conservation of mass and momentum, when it is set to calculate laminar flow without heat transfer. Additional equations are solved for heat transfer, species mixing or reaction, or κ and ε for turbulent cases [16].

5. Results and Discussion

The present CFD simulation attempts to clarify the adsorption characteristics of the adsorption bed packed with spherical silica gel type A under the boundary condition of parameters such as a width of packed bed, the inlet water vapour velocity, and granule size of silica gel.

5.1. Granules Packing Gap between Wall. To be able to solve for turbulent flow in a CFD simulation, it was necessary to introduce a small gap between the wall and the silica gel

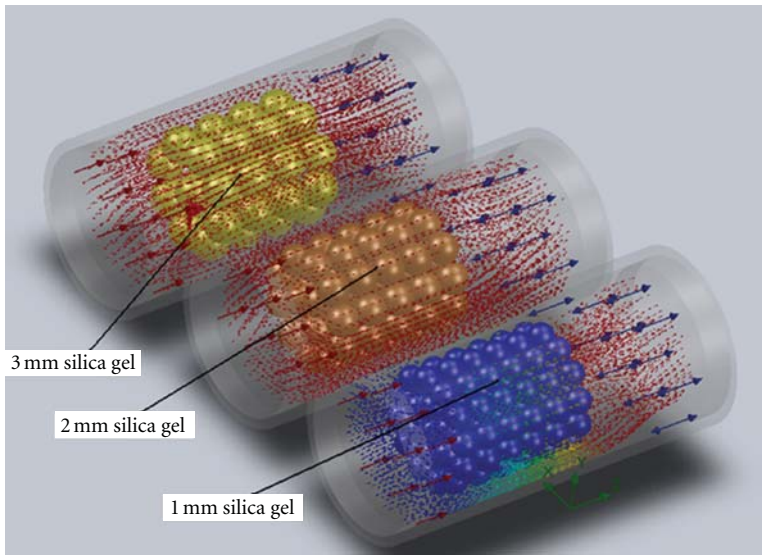

Figure 10: Flow profile in an adsorber test beds.

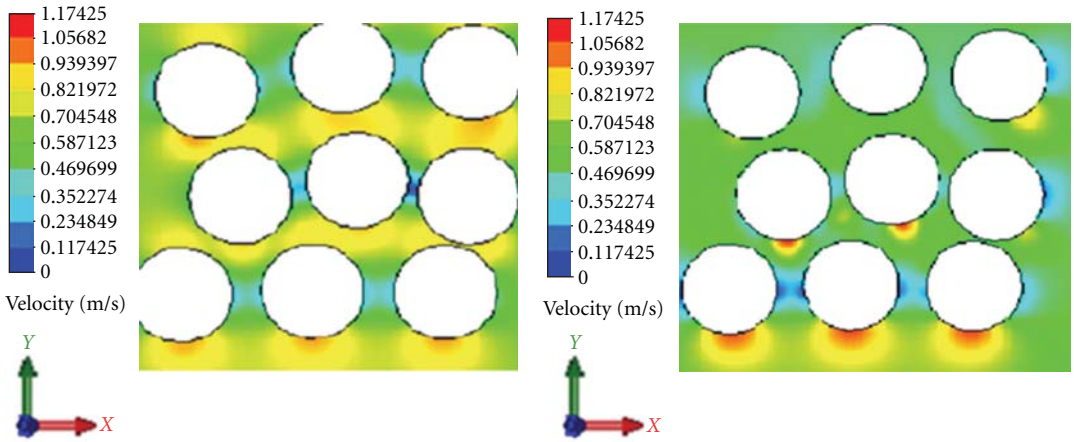

Figure 11: Velocity vectors profile in an axial cut model velocity profile expressed in m/s.

granules. It was shown from comparisons of flow profiles at several gap sizes that the small gaps used in the final model did not affect the stagnant flow area around the contact points.

6. CFD Validation against Theoretical Models

The CFD simulation model has been used to simulate the water vapour adsorption and desorption onto silica gel porous media, heat transfer, and velocity. The results simulated using the CFD model were compared with the experimental data. Based on the simulation results, the data demonstrated a good agreement with the experimental data with maximum error (Figure 10). Based on the good agreement of the model results, several important operating parameters were varied to study the influence of these parameters on water vapour adsorption performance.

6.1. Velocity Profiles. In all CFD simulation, it was notice that the water vapour flow in the middle of the porous media granules and the wall channel as expected. It was also noticed that velocity increased by the inlet and velocity in some constrained areas of the adsorption bed. Stagnation points and secondary flows were also noticed near the contact points (Figure 11).

It can be noticed that all simulations show a good correlation with Ergun's equation, turbulence, and velocity model. The packing of the silica gel granules is clearly visible; also note the practical difference between the interior of the bed and the near-wall region where the packing of the spheres is constrained by the presence of the wall. This lowers the porosity in these regions and a significant fraction of the flow is being channelled through this region.

In (Figure 12) it can be notice that the velocity vectors of water vapour flows in the middle of the silica gel granules

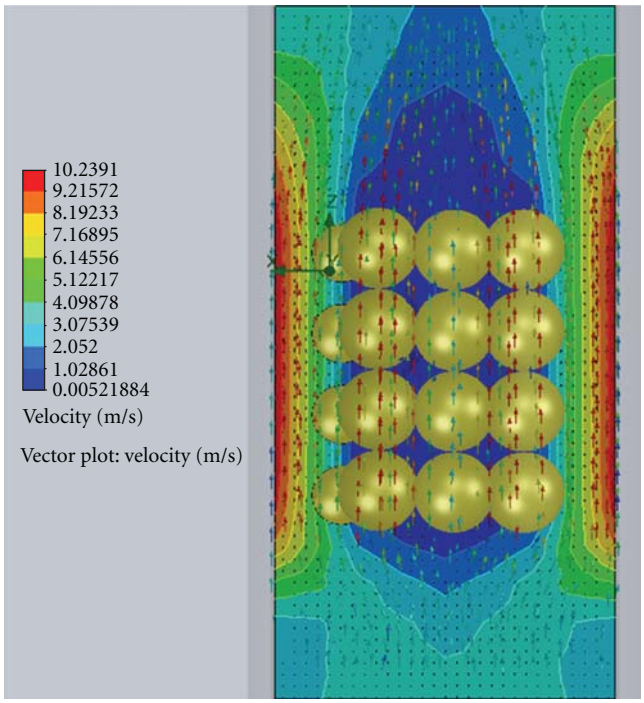

FIGURE 12: Velocity vectors plot of the water vapour velocity field in a packed bed the inlet.

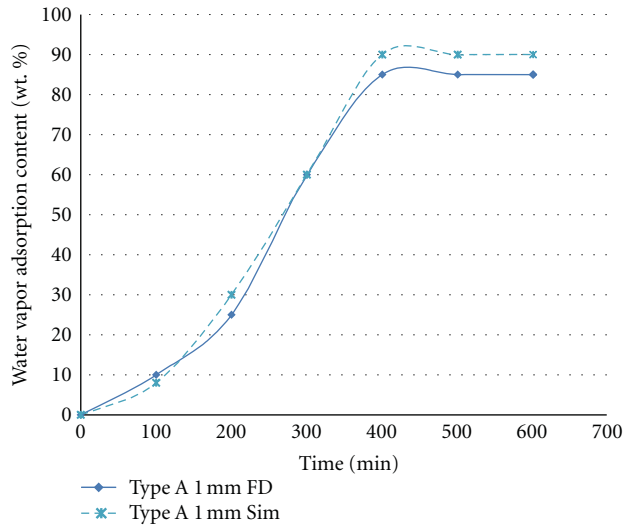

FIGURE 13: Influence of the silica gel size and number on the breakthrough curve.

packing and by the walls of the tube adsorption bed. It can also be seen that the velocity vectors increasing by the inlet of the adsorption bed tube.

One advantage of computational simulation of the flow is the sheer volume of data available for analysis; in particular, here, flow velocities at every point in the bed, which are available for statistical analysis.

6.2. Effect of Flow Velocity. Flow velocity has a directly proportional effect over heat transfer when forced convection takes place. An increase on flow velocity leads to an increase on kinetic energy. This fact generates a better heat transfer coefficient.

The velocity variation within the porous medium depends on the structure of the porous media, as manifested via the pressure drop. The pressure drops occurring across the porous medium are attributed to several factors, including form drag, viscous drag from bounding wall, and inertia force. The obtained results confirm that the pressure drop is a linear function of flow velocity [1–3, 9–17].

6.3. The Performance of the Silica Gel. The performance of the silica gel systems is commonly illustrated and evaluated on the basis of adsorption of the water vapour molecules in the adsorber bed over time. These simulations reveal the impact of silica gel granule adsorption rates:

$$\overline{C} = \frac{1}{A} \cdot \int_A c dA. \tag{12}$$

Figure 13 shows the resulting CFD simulations with the three example of silica gel. The breakthrough curves become steeper for models that contain smaller silica gel, which is crucial for good adsorption performance of the adsorber bed [1, 5, 7, 11, 15–17].

6.4. Water Vapour Flow Profile. The water vapour molecules adsorption accumulation on the silica gel is shown in (Figure 13). In this study, an integrated CFD model was developed to simulate the adsorption dynamics of water vapour of silica gel granules in a fixed bed adsorption column using the Solidworks flow simulation module, the model consists of two modes of operation: the water vapour adsorption and the desorption mode. In each mode, the water vapour flow profile surrounding the granules was determined by solving the Navier-Stokes equations and the resulting velocity profile was regarded time invariant and stored for later use. Also, the time-dependent mass transfer both outside and inside the porous silica gel due to its adsorpitivity was simulated through a user defined function developed to solve the Brunauer, Emmett, and Teller (BET) equation [1] for both adsorption and desorption processes. The developed model was used to determine the adsorption capacity of two different sizes of silica gel granules, namely, 3.5 mm and 5 mm as a function of time at different operating temperatures.

In Figure 14, the water molecules stick to the surface of the silica gel the same as the Brunauer, Emmett and Teller model of multilayer adsorption method [12, 13], in the CFD simulation, the water vapour molecules is a randomly distributed on to the porous silica gel material surface.

6.5. Water Vapour Adsorption Profile. The CFD simulation determine the distribution of water vapour molecules in the flow vapour phase and the adsorption of adsorbed vapour molecules on the silica gel surfaces. (Figure 15) shows some views of typical adsorption of water vapour molecules (a),

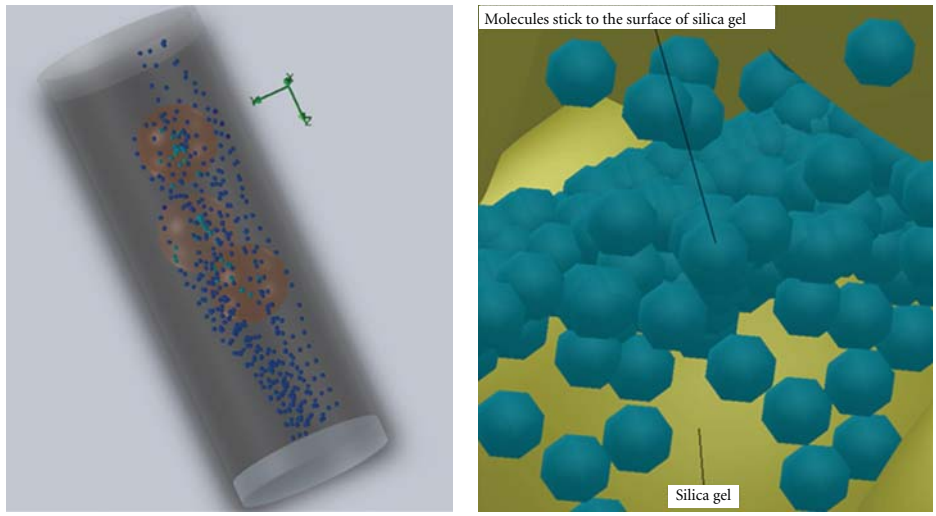

(a) (b)

Figure 14: The adsorption starting to take place with the formation of multilayer of adsorbate on adsorbent.

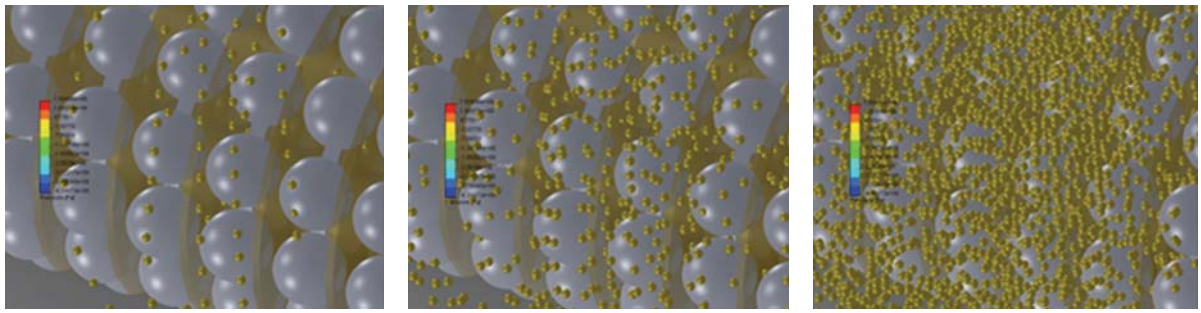

(a) $t = 129$ sec (b) $t = 350$ sec (c) $t = 700$ sec

Figure 15: Concentration profiles for c and q at different times in a column filled with 100 silica gel beads.

(b) and (c) at different times of the adsorption of the beds $t = 129$ sec, $t = 350$ sec, and $t = 700$ sec [1, 7, 8].

6.6. CFD Simulation of Desorption of Water Vapour from Silica Gel. When attempting to simulate the desorption of water vapour from silica gel, it was necessary to create a user defined function (*UDF*); the major challenge in the use of CFD simulation of the desorption of water vapour from silica gel is the complex interconnected void space silica gel has. In traditional 2D mathematical approaches, the engineers use to largely ignoring this fact. In CFD simulation, this is not ignored, it is model into the 3D model of the porous media, see Figure 16. In order to simulate desorption, we had to create a function called desorption that would take several inputs (material, fluid, pressure, flow rate, and whatever factors affect the silica gel calculations).

The desorption of water vapour for silica gel was simulated on a 3D test with one silica then was tested on a 3 silica gel then ultimately on a 40 silica gel simulation.

6.7. The Heat Transfer Performance. The CFD simulation showed that the heat transfer performance of the silica gel adsorption bed is one of the important factors to affect the adsorption efficiency of the bed. The surface temperature of the silica gel was measured in the simulation to get a batter understand of the heat transfer performance of the silica gel. The water temperatures of 70°C, 80°C, and 90°C were used to heat the silica gel different surface temperatures to help one to understand the heat transfer performance of the adsorber bed with silica gel. Figure 17 shows that the silica gel surface temperature increased steadily in the bigger silica gel sizes as compared to the smaller sizes and its surface temperature was lower than that of the smaller sizes of silica gel. As was expected, the heat transfer performance in the smaller sizes was better than that of the bigger silica gel sizes.

7. Pros and Cons

CFD provides a cost-effective means to analyse, demonstrate, and improve the performance of industrial designs; to trouble-shoot manufacturing and process problems. It is a very powerful tool for the simulation of fluid flows. CFD is a knowledge-based activity. It still relies heavily on the knowledge of the user. It is particularly important to

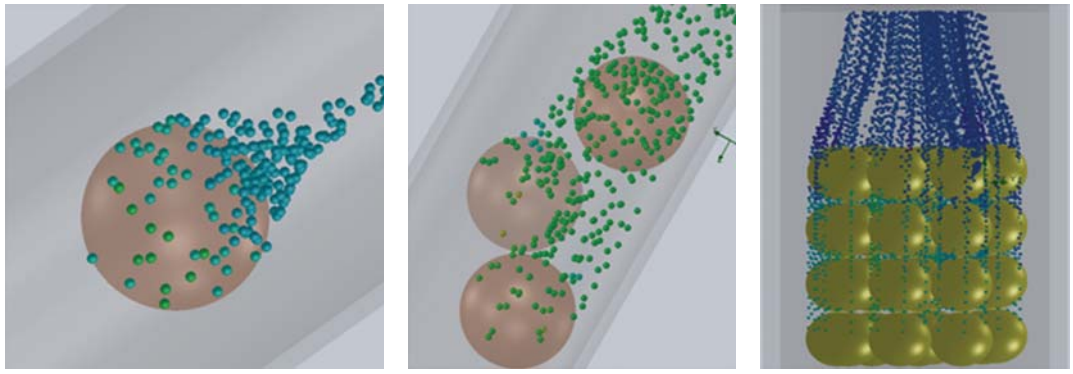

(a) (b) (c)

Figure 16: Desorption of water vapour in porous materials.

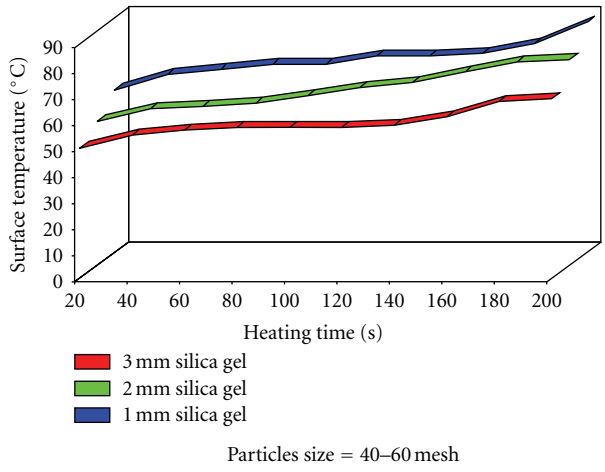

Figure 17: The variation of the surface temperature of silica gel size with the heating time.

understand its bounds of applicability and the consequences of limitations in physical and numerical submodels.

8. Conclusions

A CFD model was developed for simulating the adsorption of water vapour on silica gel granules and used to study the effect of granule sizes indicating that reducing the granule size increases the adsorption. It can be concluded that CFD is a promising tool in evaluating heat transfer behaviour in an adsorption bed. Further CFD studies, with a larger silica gel and porous medias, are required in the future simulation to show whether they will produce this.

Notations

a: Surface area of silica gel
C_0: Inlet concentration (kg m^{-3})
C: Bed concentration (kg m^{-3})
C_2: Inertia resistance coefficient (m)
D: Molecular diffusivity (m^2 sec^{-1})
D_p: Particles diameter (m)
K: Mass transfer coefficient (sec^{-1})
P: Partial pressure (Pa)
q: Adsorbent capacity (mmol g^{-1})
q_s: Maximum capacity (mmol g^{-1})
t: Time (sec)
u: Water vapour velocity (x-direction) (m sec^{-1})
v: Water vapour velocity (y-direction) (m sec^{-1})
w: Water vapour velocity (z-direction) (m sec^{-1}).

Greek Symbols

ε: Bed fraction (Porosity)
ρ_s: Particles density (kg m^{-3})
ρ: Fluid density (kg m^{-3})
α: Viscous resistant coefficient (m^{-1})
μ: Fluid viscosity (Ns m^{-2})

Abbreviation

CFD: Computational fluid dynamics
LDF: Linear driving force
UDS: User's defined scalars
UDF: User's defined functions.

References

[1] F. Augier, C. Laroche, and E. Brehon, "Application of computational fluid dynamics to fixed bed adsorption calculations: effect of hydrodynamics at laboratory and industrial scale," *Separation and Purification Technology*, vol. 63, no. 2, pp. 466–474, 2008.

[2] K. S. Chang, M. T. Chen, and T. W. Chung, "Effects of the thickness and particle size of silica gel on the heat and mass transfer performance of a silica gel-coated bed for air-conditioning adsorption systems," *Applied Thermal Engineering*, vol. 25, no. 14-15, pp. 2330–2340, 2005.

[3] A. Akahira and K. C. A. Alam, "Experimental investigation of mass recovery adsorption refrigeration cycle," *International Journal of Refrigeration*, vol. 28, no. 4, pp. 565–572, 2005.

[4] M. Rahimi and M. Mohseni, "CFD modeling of the effect of absorbent size on absorption performance of a packed bed

column CFD," *Korean Journal of Chemical Engineering*, vol. 25, no. 3, pp. 395–401, 2007.

[5] G. E. Mueller, "Radial void fraction distributions in randomly packed fixed beds of uniformly sized spheres in cylindrical containers," *Powder Technology*, vol. 72, no. 3, pp. 269–275, 1992.

[6] S. Murakami, S. Kato, K. Ito, and Q. Zhu, "Modeling and CFD prediction for diffusion and adsorption within room with various adsorption isotherms," *Indoor Air*, vol. 13, no. 6, pp. 20–27, 2003.

[7] A. Sakoda and M. Suzuki, "Fundamental study on solar powered adsorption cooling system," *Journal of Chemical Engineering of Japan*, vol. 17, no. 1, pp. 52–57, 1984.

[8] A. Akisawa, B. B. Saha, K. C. Ng et al., "Experimental investigation of the silica gel-water adsorption isotherm characteristics," *Applied Thermal Engineering*, vol. 21, no. 16, pp. 1631–1642, 2001.

[9] A. V. Anikeenko, N. N. Medvedev, M. K. Kovalev, and M. S. Melgunov, "Simulation of gas diffusion in porous layers of varying structure," *Journal of Structural Chemistry*, vol. 50, no. 3, pp. 403–410, 2009.

[10] D. C. Wang, J. Y. Wu, Z. Z. Xia, H. Zhai, R. Z. Wang, and W. D. Doub, "Study of a novel silica gel–water adsorption chiller. Part II. Experimental study," *International Journal of Refrigeration*, vol. 28, no. 7, pp. 1084–1091, 2005.

[11] J. G. I. Hellström and T. S. Lundström, "Flow through porous media at moderate reynolds number," in *Proceedings of the 4th International Scientific Colloquium Modelling for Material Processing*, Riga, Latvia, June 2006.

[12] K. S. W. Sing, "Adsorption methods for the characterization of porousmaterials," *Advances in Colloid and Interface Science*, vol. 76-77, pp. 3–11, 1998.

[13] L. D. Gelb and K. E. Gubbins, "Characterization of porous glasses: simulation models, adsorption isotherms, and the brunauer-emmett-teller analysis method," *Langmuir*, vol. 14, no. 8, pp. 2097–2111, 1998.

[14] M. F. Liou, *A numerical study of transport phenomena in porous media*, Ph.D. thesis, Department of Mechanical and Aerospace Engineering, Case Western Reserve University, 2005.

[15] H. Inaba, J. K. Seo, and A. Horibe, "Numerical study on adsorption enhancement of rectangular adsorption bed," *Heat and Mass Transfer*, vol. 41, no. 2, pp. 133–146, 2004.

[16] C. Horváth and H.-J. Lin, "Band spreading in liquid chromatography: general plate height equation and a method for the evaluation of the individual plate height contributions," *Journal of Chromatography A*, vol. 149, pp. 43–70, 1978.

[17] J. Goworek and W. Stefaniak, "Investigation on the porosity of silicagel by therm aldesorption of liquids," *Materials Chemistry and Physics*, vol. 32, no. 3, pp. 244–248, 1992.

Hindawi Publishing Corporation
Modelling and Simulation in Engineering
Volume 2012, Article ID 327929, 12 pages
doi:10.1155/2012/327929

Research Article

A Study of the Location of the Entrance of a Fishway in a Regulated River with CFD and ADCP

Anders G. Andersson,[1] Dan-Erik Lindberg,[2] Elianne M. Lindmark,[1] Kjell Leonardsson,[2] Patrik Andreasson,[1] Hans Lundqvist,[2] and T. Staffan Lundström[1]

[1] *Division of Fluid Mechanics, Luleå University of Technology, 971 87 Luleå, Sweden*
[2] *Department of Wildlife, Fish and Environmental Studies, Swedish University of Agricultural Sciences, 901 83 Umeå, Sweden*

Correspondence should be addressed to Anders G. Andersson, aneane@ltu.se

Received 9 December 2011; Accepted 29 February 2012

Academic Editor: Guan Heng Yeoh

Simulation-driven design with computational fluid dynamics has been used to evaluate the flow downstream of a hydropower plant with regards to upstream migrating fish. Field measurements with an Acoustic Doppler Current Profiler were performed, and the measurements were used to validate the simulations. The measurements indicate a more unstable flow than the simulations, and the tailrace jet from the turbines is stronger in the simulations. A fishway entrance was included in the simulations, and the subsequent attraction water was evaluated for two positions and two angles of the entrance at different turbine discharges. Results show that both positions are viable and that a position where the flow from the fishway does not have to compete with the flow from the power plant will generate superior attraction water. Simulations were also performed for further downstream where the flow from the turbines meets the old river bed which is the current fish passage for upstream migrating fish. A modification of the old river bed was made in the model as one scenario to generate better attraction water. This considerably increases the attraction water although it cannot compete with the flow from the tailrace tunnel.

1. Introduction

Computational fluid dynamics (CFD) is used to simulate the flow within a tailrace channel of a hydropower plant with the purpose to scrutinize alternative positions of an entrance to a fishway. The simulations are carried out on full scale implying a length of the virtual model of 320 m, a typical width of 75 m, a typical depth of 10 m, and a maximum inlet flow rate of 1000 m^3/s. A numerical challenge with the large scale is to fulfill conditions of a sufficiently resolved flow structure at locations with high gradients (e.g., at boundaries) and a good mesh overall with a decent usage of computational resources (Marjavaara and Lundström [1]). Another challenge is the validation of the simulations which is here done by measurement with an Acoustic Doppler Current Profiler (ADCP).

Studies of tagged Atlantic salmon and sea trout in the unregulated river Vindelälven in northern Sweden during 1995–2005 have shown that only a third of the upstream migrating fish find their way to their natural spawning grounds (Lundqvist et al. [2]). The main reason for this is the Stornorrfors power plant located downstream the confluence between the rivers Vindelälven and Umeälven, the latter being a regulated river. A major issue at the power plant is that the fish are attracted into the tailrace channel from the turbines rather than migrating up through the old river bed that offers a fishway around the turbines (Rivinoja et al. [3]). The flow rate from the turbines is typically 20 times larger than the flow rate from the old river bed and its entrance into the confluence is very wide. Hence, fluid flow conditions for the old river bed to attract fish are limited. The fact that migrating fish are attracted to the tailrace of the turbines instead of the weaker current from the fishway is a common problem (Arnekleiv and Kraabøl [4], Webb [5]). The difficulties of upstream migrating fish coming across in regulated rivers in northern Sweden have been documented by, for example, Rivinoja [6], Lindmark [7], and Lindmark and Gustavsson [8].

There are two major measures that are being considered for improving the upstream migration of fish at the Stornorrfors power plant. One is to construct a new fishway in the form of a fish ladder from the tailrace channel since a majority of the fish reside there for a long period of time during the migration season. The other alternative is to create better attraction water from the old river bed into the confluence area. The alternatives are here modeled with CFD, and the attraction water created using given configurations is examined. The interest in numerical simulations of flows in rivers is increasing, and, due to the rapid development of user-friendly efficient codes and computer power in recent years, more advanced models than before can be applied in areas such as fish migration, habitat modeling, sedimentation transport, erosion, and dam safety. Olsen and Stokseth [9] created a model of the Sokna River in Norway where they applied a k-ε turbulence model and a porosity-based model for large roughness elements in the river bed showing good resemblance with observed data. The SSIIM model suggested by Olsen has been validated against LDA measurements in a meandering channel on a lab scale (Wilson et al. [10]) where the model showed the ability to capture secondary currents. CFD has also been applied to the River Cole, Birmingham, UK (Clifford et al. [11]), and the River Thame, Birmingham, UK (Booker [12]), where the potential for use in habitat modelling was discussed. A numerical model of a 4 km stretch of the Columbia River downstream of the Wanapum Dam has been performed and calibrated against measured data highlighting the importance of bed roughness for accurate flow predictions (Sinha et al. [13]). Dargahi [14] used the commercial code Fluent to model fluid flow and sediment transport in the River Klarälven, Sweden, and validated the results with ADCP measurements. The design of a submerged flow guiding device to increase the survivability of downstream migrating fish has been performed in the commercial code CFX-10 (Lundström et al. [15]). Simulations of flow in an ice-covered channel with the k-ω turbulence model with different roughness values for river bed and ice-cover resulted in a 16% increase in mean flow depth of the channel (Yoon et al. [16]). The effects of submerged weirs in natural channels to improve the navigation conditions for barges have been investigated numerically (Jia et al. [17, 18]).

Rakowski et al. [19] used field-measured data with ADCP to validate their CFD simulations of a 2.7 km reach starting downstream of the Bonneville powerhouse and spillway with total river flows between 3275 m^3/s and 11328 m^3/s. The velocities were measured and averaged over a 10 minutes period to get adequate representation of the mean velocity. When comparing the CFD simulations (steady state, k-ε turbulence model) to ADCP data, the modeled velocity was slightly lower than the measured, but within the standard deviation of the field velocity. Viscardi et al. [20] also used ADCP measurements to validate CFD simulations in a 3 km stretch of the Paraná de las Palmas River with flow rates ranging from 2200 to 5000 m^3/s (steady state, k-ε turbulence model, rigid lid, bed roughness Manning $n = 0.025$). In their case, the velocities were averaged over 2 seconds in each vertical sample in order to minimize the effect of the tidal change and the velocities correspond reasonable accurate. To summarize, two-equation turbulence models are in most cases used to simulate the flow in rivers and no one is considering how attraction water from a fishway competes with the flow in the river.

2. Geometry

The actual geometry in the present study consists of four parts, the tunnel from the turbines, the tailrace channel, the old river bed, and the confluence area, see Figure 1 where the tailrace channel and the old river bed are defined. The confluence area is located where the water from the old river bed and the tailrace channel meet, while the tunnel from the turbines is located upstream the tailrace channel. CFD calculations are performed on all parts except the old river bed, while velocity measurements are only reported for a couple of transects within the tailrace channel.

3. Experimental

To measure topology and water velocity downstream Stornorrfors power plant, an ADCP was used. The ADCP has four transducers directed into the water. The transducers send out sound waves that reflect on small particles traveling with the water, and the transducers detect the Doppler frequency of the reflected sound waves. These frequencies are proportional to the velocity of the water (the particles). ADCP is a relatively fast way of measuring velocities in field and to calculate river discharge. The ADCP used in this case is a RiverBoat RioGrande, and the data processing was performed with the software Winriver II, both from RD Instruments.

The bathymetry in the area was measured using two setups. The ADCP was dragged besides a motorboat with a pole and rope, which enabled measurements close to the shoreline. By combining the bottom-tracking feature of the ADCP with GPS data, a point cloud consisting of ADCP provided depths at specific satellite coordinates was obtained. The ADCP however fails to find the bottom of the deepest area in the tailrace channel; hence, a SIMRAD EY60, GPT 200 kHz, split beam echo sounder with the transducer mounted vertically on the boat was used near the tailrace tunnel outlet. There is a small shallow part of the tailrace that is located above and behind the tunnel outlet. The GPS reception was very low this far into the spillway due to the surrounding terrain which caused large uncertainties in the acquired coordinates. The length of this region is approximately 50 m, and observations suggest that it consists of a slow circulating flow and the assumption was made that this part of the spillway does not have any significant effect on the flow in the remaining channel. It was thus omitted from the numerical model, and the entrance to this innermost part was excluded from the geometry. The points of measurements are shown in Figure 1(a).

For the velocity measurements, a steel wire was stretched across the tailrace channel and the ADCP was tethered to it. A manual winch enabled the ADCP to travel across the channel and capture the velocities in the entire cross-section. The transect T1 in Figure 1(a) was measured on several

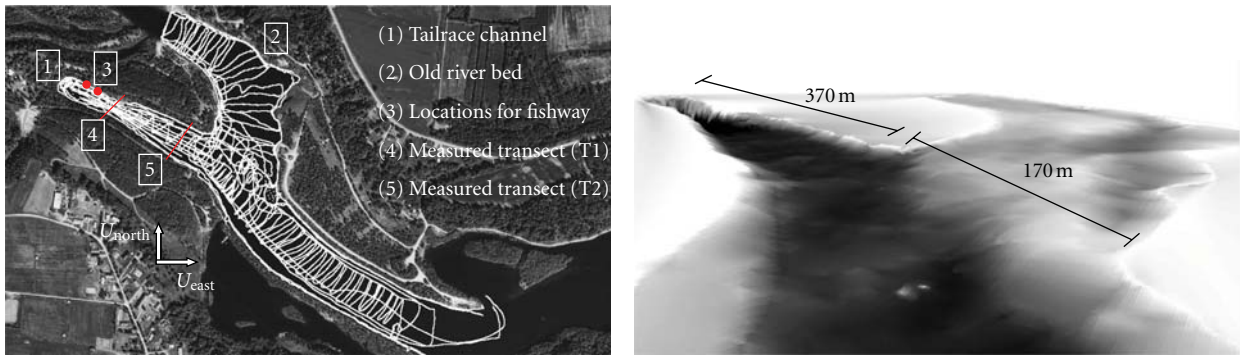

(a) (b)

Figure 1: (a) Aerial photograph of tailrace channel and confluence area downstream Stornorrfors power plant. White lines (points) represent data points used in geometry creation. Please notice the cardinal direction. (b) Visualization of the confluence area, tailrace channel, and old river bed looking upstream. Darker grey represents a larger channel depth.

occasions at different turbine discharges and a minimum of four times at each flow. Three vertical profiles in the T1 transect and three in the T2 transect were measured during a minimum of 600 s. The profiles were collected when the flow rate through the power plant was ~500 m^3/s (according to the discharge calculation in WinRiver and data from the hydropower company). Profiles were measured with a time difference of 0.95 s between ensembles. During measurements, the distance to the shore was measured with a laser distance meter. The total width of the T1 section was measured to 40 m, and the profiles were located at 16, 23, and 32 m from the south shore. Transect T2 had a measured width of 85 m, and the verticals were located 30, 44, and 59 m from the north shore.

The accuracy of the ADCP depends on many factors, such as side-lobe interference, ringing, and ADCP-flow interaction that exclude the ADCP from doing any measurements near the water surface or close to the bottom of the river (Simpson and Oltmann [21]). Nystrom et al. [22] compared ADCP accuracy with an Acoustic Doppler Velocimeter (ADV) in a lab flume within which the turbulence intensity of the flow was 0.1. The ADCP measurements were carried out during 15 min, and the error was less than 3% in the areas away from the boundaries not being affected by ringing, side lobe interference, and flow disturbance.

4. Numerical Setup

The point cloud collected with ADCP and SIMRAD seen in Figure 1 was converted to a bottom surface in the software Imageware 13. The surface was imported to Ansys Icem Cfd 11 where a solid model was created. The formed geometry was divided in two parts, the tailrace channel and the confluence area between the channel and the old river bed. The simulation volumes were discretized as tetrahedral elements in the CFD model. Local refinements of the grid were carried out in areas of simulated attraction water to increase the resolution in the most interesting parts of the flow. All simulations were carried out with the commercial software CFX11 from Ansys Inc. A mesh sensitivity study of the tailrace channel was performed with different numerical grids, ranging from 239 k to 7389 k nodes. The velocity in the east direction was evaluated at T1 and T2 for the different grids and the conclusion was that the coarsest mesh did not capture the flow field with sufficient accuracy. A mesh with 526 k nodes however produced a very similar flow field to that of the 7389 k mesh with significantly lower computational cost. Hence, the final grids for the tailrace channel consisted of ~500 k nodes and the confluence area of ~600 k nodes.

In reality, the water from the power plant goes through an approximately 4 km long tunnel before entering the tailrace channel. To create a realistic inlet boundary condition for the simulations, this tunnel was modeled separately and the velocity profile at the end of the tunnel was used at the inlet of the tailrace channel simulations. The tunnel was given a sufficient length to give a fully developed velocity profile, and the tunnel walls were given a wall roughness of a typical excavated rock.

The high-resolution advection scheme was used for solving the equations of fluid motion and turbulence closure. The high-resolution scheme uses a close to second-order solution in areas with low variable gradients, and, in areas where the gradients change sharply, it will be close to a first-order solution (ANSYS [23]). The incompressible Reynolds-Averaged Navier Stokes equation and the continuity equation are expressed as

$$\frac{\partial U_i}{\partial t} + U_j \frac{\partial U_i}{\partial x_j} = -\frac{1}{\rho}\frac{\partial P}{\partial x_i} + \nu \nabla^2 U_i - \frac{\partial}{\partial x_j}\left(\overline{u_j u_i}\right), \qquad \frac{\partial U_i}{\partial x_i} = 0, \tag{1}$$

where U is the mean part of the velocity component, P is the pressure, ν is the viscosity of the fluid, ρ is the fluid density, and $\overline{u_j u_i}$ are the Reynolds stresses. All simulations were run with the k-ε turbulence model with scalable wall functions.

In the k-ε turbulence model, Reynolds stresses are linearly related to the strain:

$$-\overline{u_j u_i} = 2\nu_T S_{ij} - \frac{2}{3}k\delta_{ij}, \tag{2}$$

where k is the turbulent kinetic energy, ν_T is the eddy viscosity, and S_{ij} is the mean strain tensor defined as

$$S_{ij} = \frac{1}{2}\left(\frac{\partial U_j}{\partial x_i} - \frac{\partial U_i}{\partial x_j}\right). \tag{3}$$

The eddy viscosity is modeled as

$$\nu_T = C_\mu \frac{k^2}{\varepsilon}, \tag{4}$$

where $C\mu$ is a model constant and ε is the turbulent dissipation rate. For more information, see Launder and Spalding [24]. The RMS residual target for all simulations was set to 10^{-6}. This convergence target could not be achieved with a steady-state solver due to initial fluctuations of the flow. Simulations were instead run on a transient solver until it approached a steady solution and the final values from the simulation were used. A physical time step of 0.5–2 s was selected depending on grid size, and the solution was considered steady when the velocity in 18 monitored points throughout the domain had been virtually constant for at least 1000 time steps.

The water surface was modeled as a rigid lid with zero friction. This approximation is viable when the surface level variation is smaller than 10% of the total channel depth (Rodriguez et al. [25]). The outlets are given a pressure type boundary condition. The bottom surface of the numerical model was defined as a rough wall. A scalable wall function that uses an extension of the method suggested in [24] was selected for near wall modeling. The dimensionless velocity u^+ in the logarithmic layer close to the rough wall is typically written as

$$u^+ = \frac{U_t}{u_\tau} = \frac{1}{\kappa}\ln y^+ + B - \Delta B, \tag{5}$$

where

$$y^+ = \frac{u_\tau \Delta y}{\nu}, \quad u_\tau = \sqrt{\frac{\tau_\omega}{\rho}}, \tag{6}$$

and where u_τ is the friction velocity, U_t is the velocity tangent to the wall at a distance Δy from the wall, y^+ is the nondimensional wall unit, τ_ω is the wall shear stress, κ is the von Karman constant, B is a constant, and ΔB is the so-called roughness characterization function. Since the roughness of the channel is not well documented, a global representation of roughness was selected. The wall roughness can be described as an equivalent sand-grain roughness, k_s (ANSYS [23]). With this formulation, the roughness characterization function can be described as (White [26])

$$\Delta B = \frac{1}{\kappa}\ln(1 + 0.3k_s^+), \tag{7}$$

where the dimensionless roughness height k_s^+ is defined as

$$k_s^+ = \frac{u_\tau k_s}{\nu}. \tag{8}$$

To obtain a realistic value for the equivalent sand-grain roughness of the channel, an empirical Gauckler-Manning coefficient n that describes the channel is selected (Arcement and Schneider [27]). The advantage of using the Manning's n instead of other coefficients is that n is nearly constant regardless of flow depth, Reynolds number ($\mathrm{Re} = 4UR_h/\nu$), or k_s/R_h for fully developed turbulent flow over a rough surface (Yen [28]). The selected n is used to calculate a Darcy friction factor f given by

$$f = \frac{8gn^2}{R_h^{1/3}}. \tag{9}$$

The friction factor obtained is then used to find k_s from the Colebrook-White formula (Colebrook [29])

$$\frac{1}{\sqrt{f}} = -2\log_{10}\left(\frac{k_s}{3.71 \cdot 4R_h} + \frac{2.51}{\mathrm{Re}\sqrt{f}}\right), \tag{10}$$

and the derived k_s is finally used for input into the simulations. In the present case, the second term in (10) can be neglected due to the high Reynolds number of the flow.

The wall function approach is common in river simulations since the scales of roughness are very costly to model physically in problems of such large scales. The limitations of this method are discussed by Patel [30]. Since the roughness is only an approximation and is difficult to measure in reality, a parameter study was here performed in the numerical model with a flow rate of 350 m^3/s from the turbines.

With no surface roughness, the jet leaving the tunnel barely leaves the bottom of the channel which does not seem likely with regards to the characteristics of free surface channel flow, see Figure 2. With a k_s value of 0.3 m (Manning $n \approx 0.033$) which can be considered typical for a rock excavated channel such as the tailrace channel, the flow characteristics change considerably. The jet emerging from the tunnel now moves towards the free surface of the channel. Increasing k_s to 0.5 m (Manning $n \approx 0.037$) did not affect the solution in any major way, and all following simulations on the tailrace channel, were run with $k_s = 0.3$ m.

Two ways of improving the upstream fish migration around the power plant were studied: a new fishway in the tailrace channel and higher attraction to the old river bed. In the tailrace channel, two positions and two angles of a new fishway entrance were evaluated. The positions were selected from previous observations of fish during the migration season. The dimensions of the entrance were $2 \times 2.7\ \mathrm{m}^2$, and the flow rate used was $10\ \mathrm{m}^3/\mathrm{s}$. The two inlet angles of the fishway entrance were perpendicular and 45° to the main flow.

The modification of the confluence area to improve the attraction to the old river bed was realized by adding a wall at a distance from the river bank directing nearly all the flow in the old river bed to a narrow open channel between the wall and the shoreline. In such opening the water may

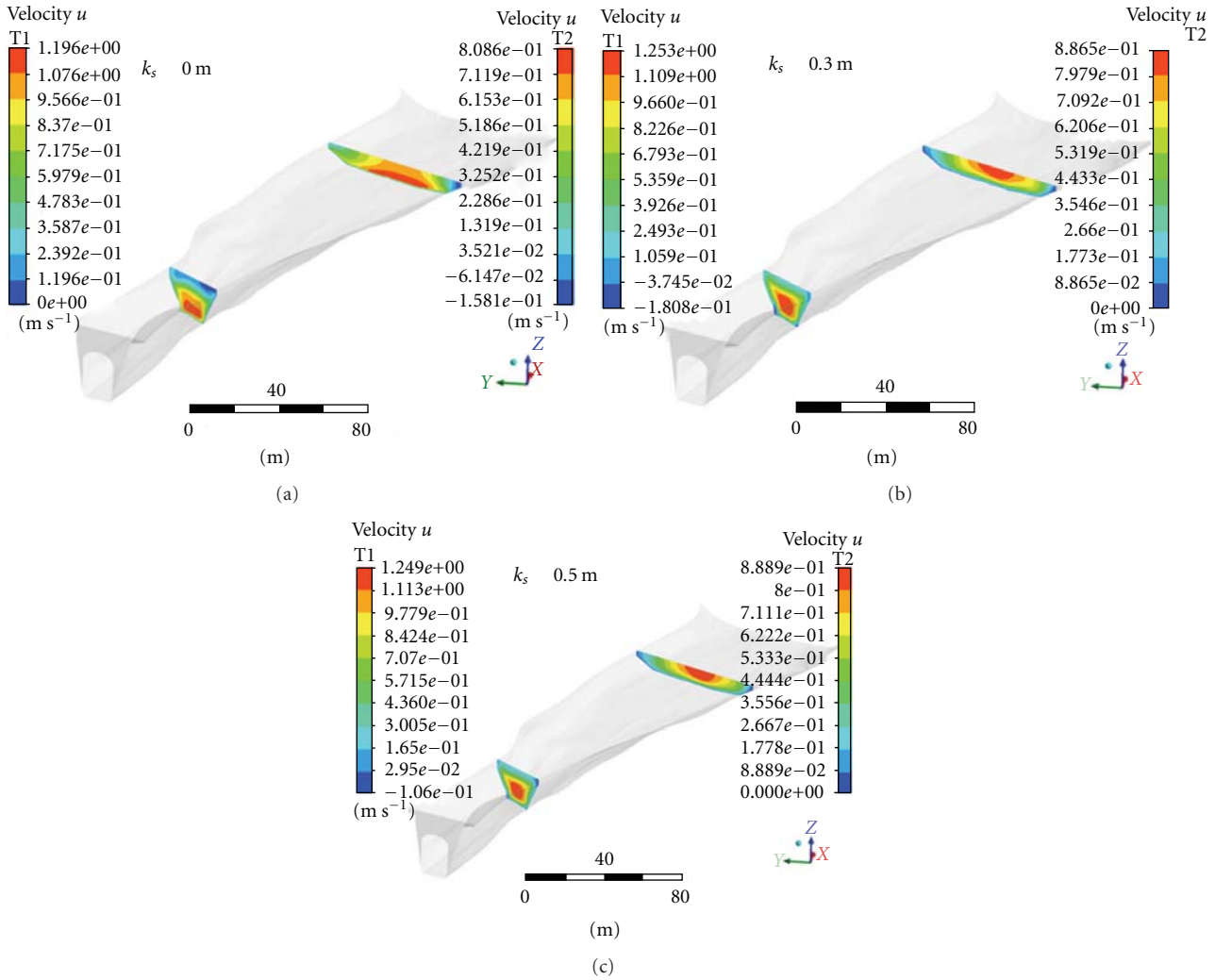

FIGURE 2: Parameter study of the wall roughness in the tailrace channel showing the development of the velocity profile at two different cross-sections for three different roughness values. The characteristics of the flow change completely when the equivalent sand-grain roughness increases from 0.0 to 0.3 m increasing it further to 0.5 m giving no noticeable additional effect.

be accelerated with a ramp, for instance, as suggested in Lindmark and Gustavsson [8] and Green et al. [31]. The flow in the old river bed was set to 20 m^3/s and that from the tailrace tunnel to 500, 750, and 1000 m^3/s, representing a low flow, a normal flow, and a flow close to the maximum flow, respectively.

5. Results and Discussion

The characteristics of the flow will be described followed by a comparison to experimental data, and finally the results from simulation of attraction water will be presented.

5.1. Characterization of the Flow in the Simulations. The flow exiting the tunnel takes the form of a jet that gradually develops into an open channel flow profile. Approximately after 2/3 of the channel length, the jet maximum velocity is at the surface of the water as can be seen in Figure 3.

The jet however influences the surface orientation flow much earlier in the channel as revealed by plots of vorticity and turbulence intensity in a plane at 1 m depth, see Figures 4(a) and 5(a). High-vorticity areas are found at the bottom of the channel near the edges of the channel and at one large area of recirculation after the expansion, near the north shore, but there is also a noticeable rotation of the flow close to the surface near the inlet of the tailrace channel, see Figures 4(a) and 4(b). This is also reflected by relatively high turbulence intensity in this area, see Figures 5(a) and 5(b).

5.2. Comparison to Experiments. The results from ADCP measurements in the tailrace channel yield an unstable behavior of the flow, see Figure 6 showing a $12 \times 12\,m^2$ section in the middle of the T1 transect at five different times where the raw data from the ADCP has been averaged to $1 \times 1\,m^2$ cells. The measurements were taken in succession, and the velocities have been normalized with transect average

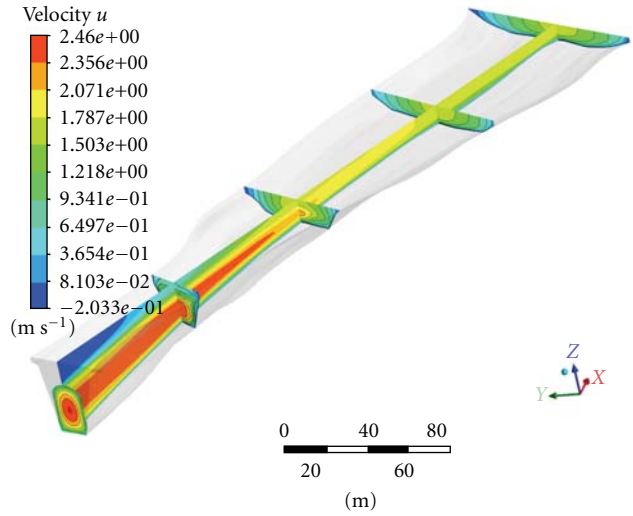

Figure 3: Development of the turbine jet as seen in a section along the channel, cross-sections T1, T2, one intermediate cross-section, inlet, and outlet.

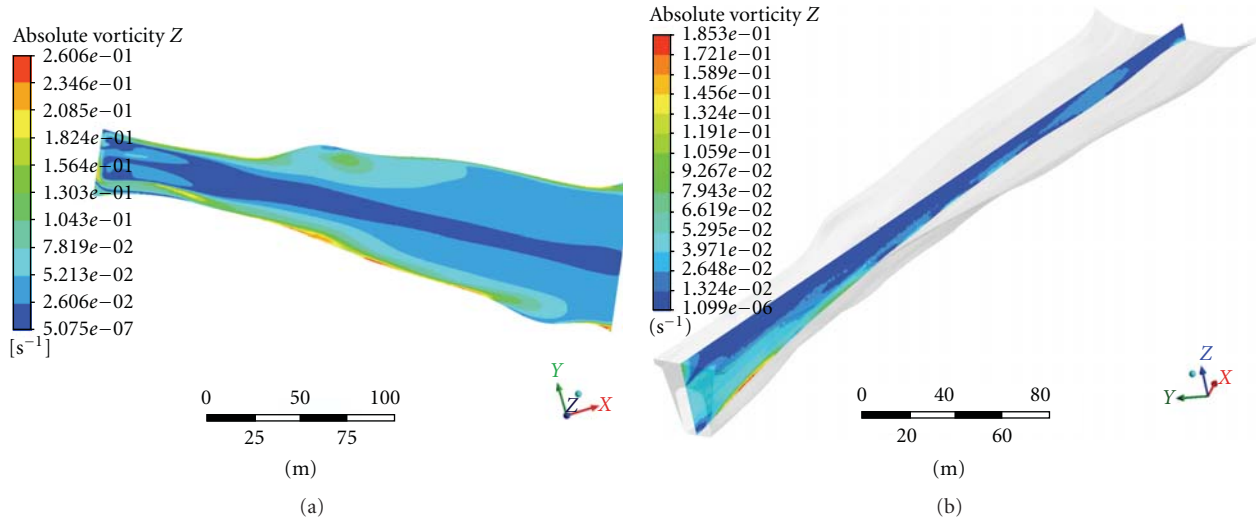

Figure 4: (a) Magnitude of the vertical vorticity in a plane at 1 m depth. (b) Magnitude of the vertical vorticity in a section along the channel.

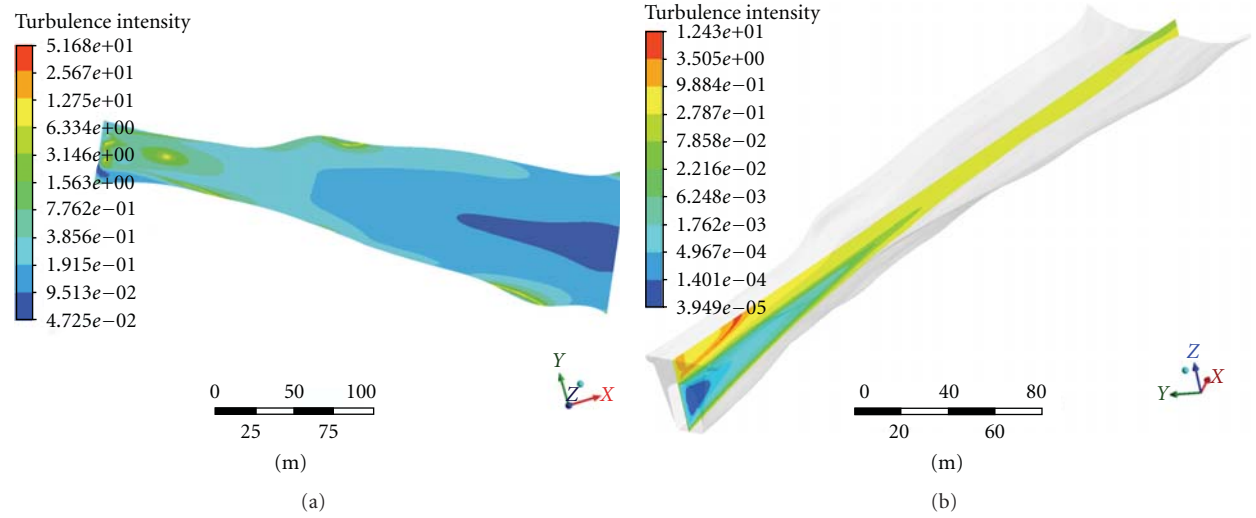

Figure 5: (a) Turbulence intensity (logarithmic scale) in a plane at 1 m depth. (b) Turbulence intensity (logarithmic scale) in a section along the channel.

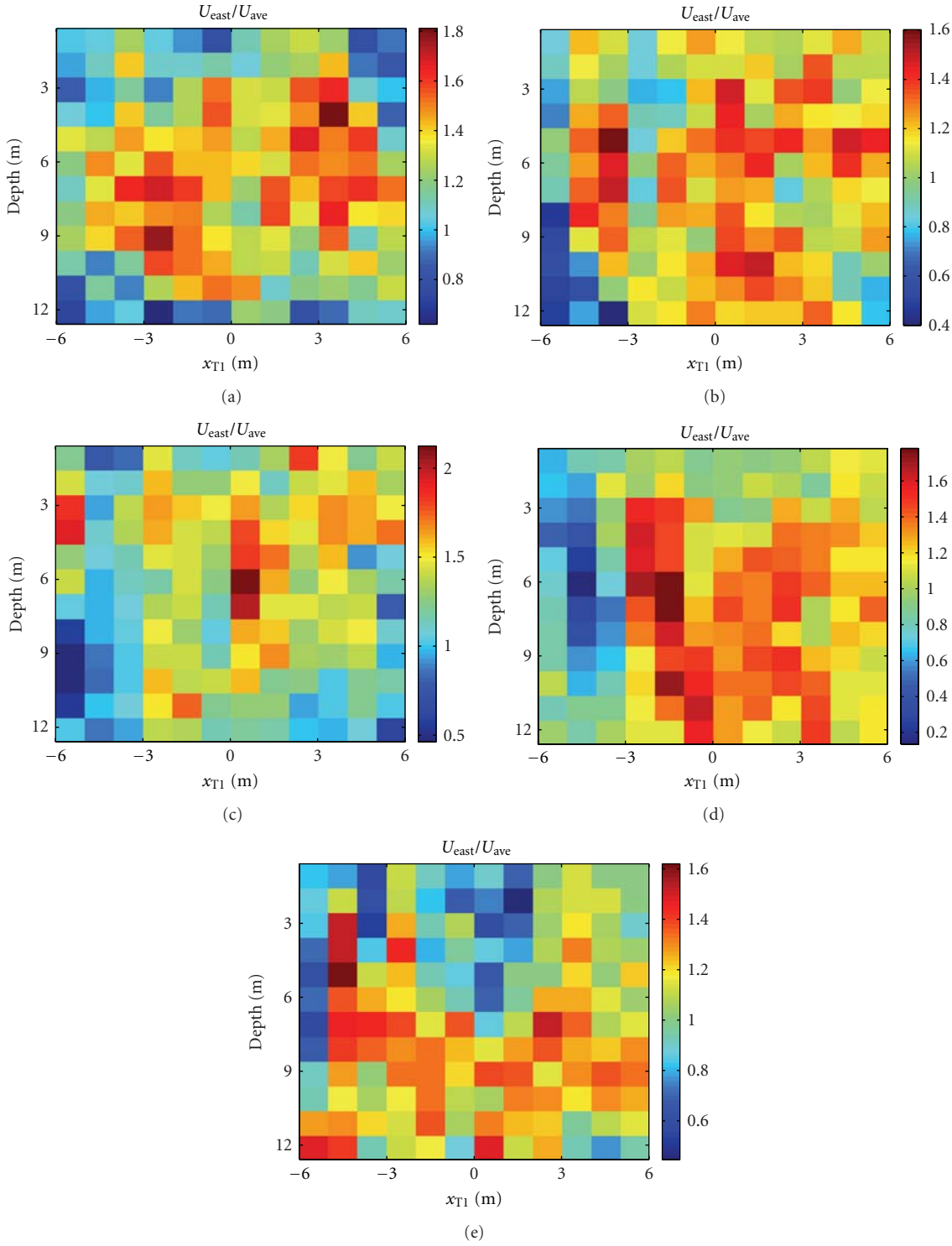

FIGURE 6: Five individual measurements for a section of $12 \times 12\ m^2$ from transect T1. Red indicates high velocity and blue low velocity. The area with high velocity changes position as a function of time.

velocity to account for minor differences in total flow from the tunnel. The jet stemming from the tunnel is apparent in all transects but not as well defined as in the simulations, compare Figures 3 and 6. To examine the time dependence of the flow, the ADCP was kept in the same position and the velocity was measured during a longer period of time. Three vertical profiles at 15, 22, 31 m from the south shore were measured. The standard deviation from the mean distance was 0.01-0.02 m. The results from the measurements show a highly fluctuating flow. Initial frequency analysis does not

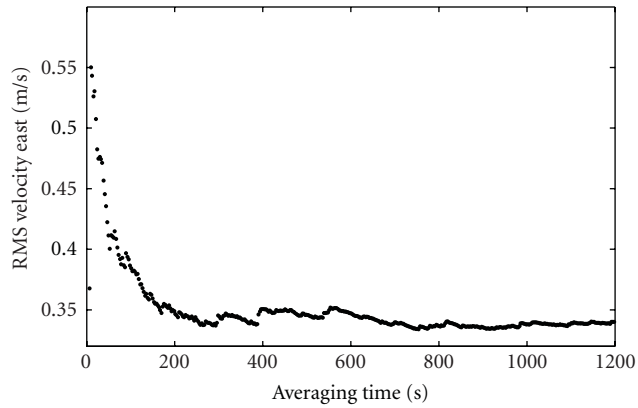

Figure 7: RMS of the east velocity component as a function of the averaging time. The velocities are from the profile 22 m from the south shore at 5 m depth in transect T1.

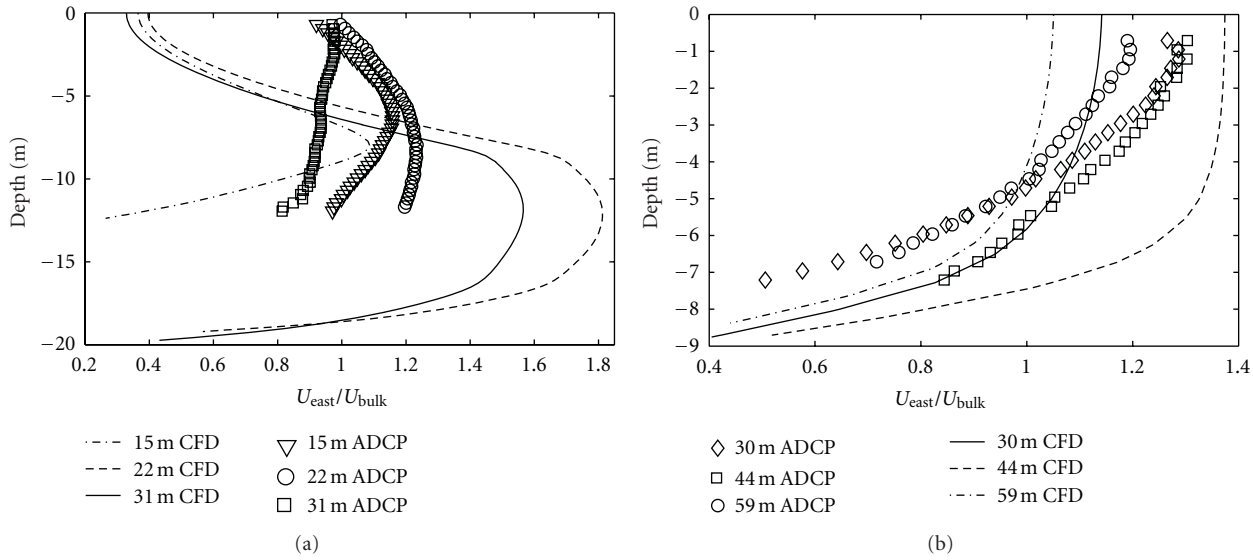

Figure 8: (a) Comparison between vertical velocity profiles in experiments and simulation in verticals at 15 m, 22 m, and 31 m from the south shore, respectively, for transect T1. U_{east} is the velocity in the east direction. (b) Comparison between simulations and measurements in verticals at 30 m, 44 m, and 59 m from the north shore, respectively, for transect T2. U_{east} is the velocity in the east direction.

indicate any periodicity; however, it cannot be excluded that fluctuations are influenced by large-scale structures of the flow, originating from upstream instabilities. How the RMS velocity (east) stabilizes with time is shown for the profile at 22 m in Figure 7. From the results, it is concluded that, to measure representative mean velocities, each profile must be measured during at least 600 s. The measurements over a *complete* transect presented in Figure 6 took about 120 s which means that these measurements by no means represent the mean velocity in that transect which explains the different velocity patterns.

To validate the simulations, time-averaged velocities of fixed-point measurements at both T1 and T2 are derived. The agreement between simulation and experiment at T1 is rather poor, see Figure 8(a) where normalized velocity profiles are compared. The velocity is normalized with the bulk velocity $U_{bulk} = Q/A_{T1}$, where Q is the flow rate and A_{T1} is the area of the T1 transect being 516 m^2 as derived from the virtual model. The jet that exits the tunnel appears closer to the water surface in the measurements than in the simulations, and it is much more diffuse in the measurements. This is most apparent for the measurements at 31 m at T1 where measurements indicate a plug flow while the simulations yield a sinus-shaped profile. Hence, there is a discrepancy at the surface and at the bottom and the jet penetrates the surface much earlier in reality as compared to the simulations. For T2, the agreement between simulations and experiments is better especially close to the free surface, see Figure 8(b). The maximum velocity of the flow in the middle of the channel is lower in the experiments than in reality, while it is actually higher towards the shores indicating a more diffusive flow also in this transect. One reason for the differences, especially apparent in T1, might be the inlet boundary condition in the simulations, which is described

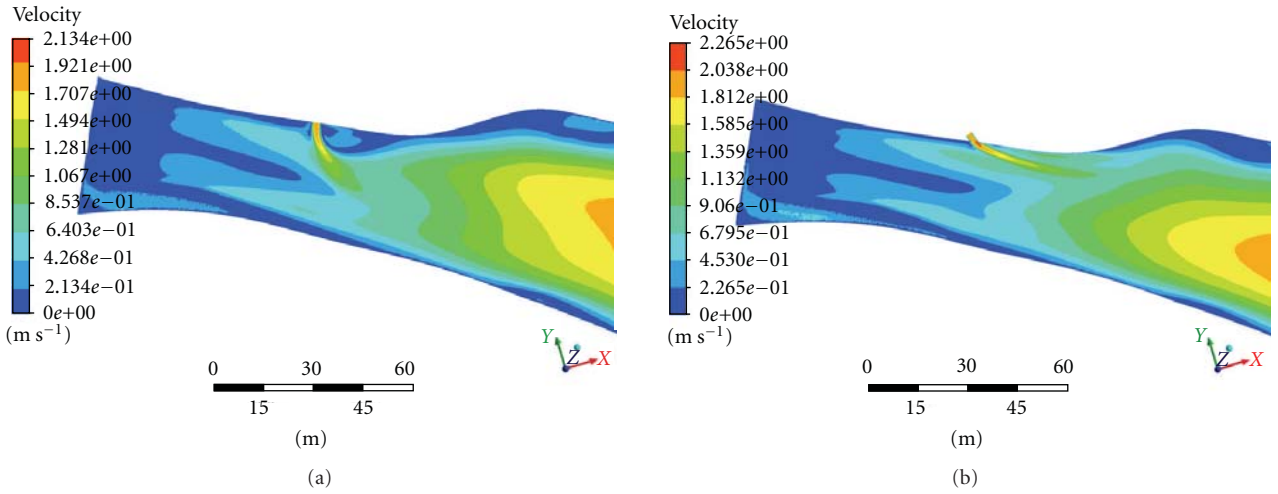

Figure 9: Fishway inlet at position 1 with 0° and 45° angle. The flow rate through the power plant is 750 m^3/s, and the velocities are shown at 1 m depth.

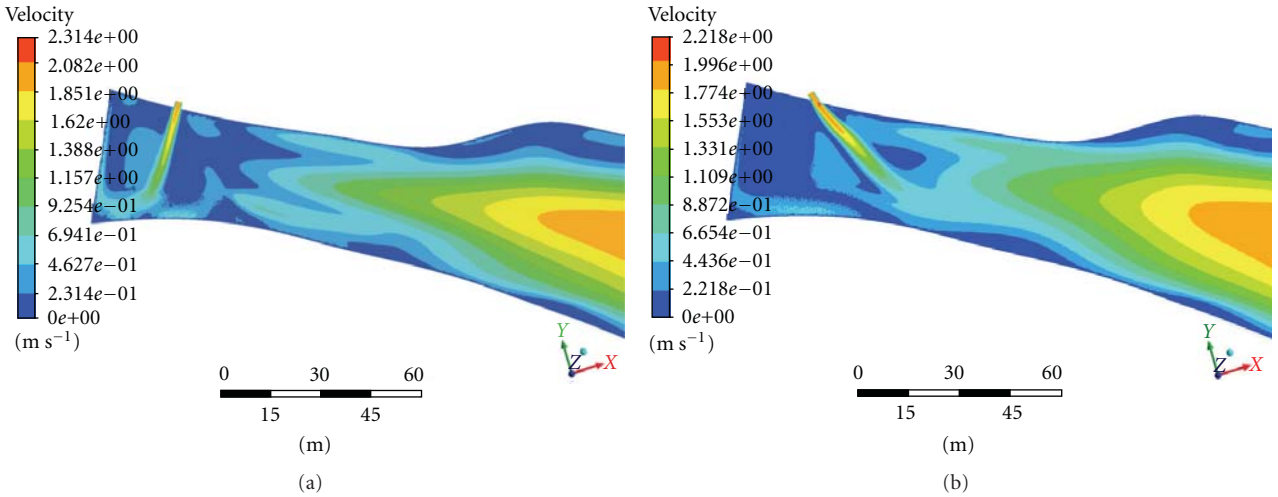

Figure 10: Fishway inlet at position 2 with 0° and 45° angle. The flow rate through the power plant is 750 m^3/s, and the velocities are shown at 1 m depth.

as a stationary velocity profile where in reality effects of the turbines, larger discrete wall roughness elements or sudden changes in discharge may come into play. Other contributing factors may be difference between model geometry and real geometry as to surface roughness, for instance, and oversimplified modeling of turbulence or that the rigid lid assumption creates unphysical behavior when the jet from the tailrace tunnel approaches the water surface of the tailrace. It is also likely that the flow field is smeared out by the method to measure the velocity field. The discrepancy between simulations and measurements is a subject for future research as to turbulence intensity, for instance. When later on discussing the results from the simulations with the fishway entrances, it should be remembered that the jet is more diffuse and surface orientated in reality as compared to the simulations.

5.3. Simulation of Attraction Water. For position 1 in the tail race channel, the perpendicular entrance gives a noticeable jet that stretches to the center of the tail race channel while the angled inlet gives a jet that aligns with the flow from the tailrace tunnel and reaches further downstream, see Figure 9. Even better attraction water is created at the second position as shown in Figure 10. Since the small jet from the fishway does not collide with the large jet from the tailrace tunnel, the generated attraction water stretches further out in the channel, see Figure 11. Noticeable attraction water was created even at the highest flow (1000 m/s) from the turbines, see Figure 12. The relatively high-vorticity levels and turbulence intensities are thus too weak to influence the attraction water to any larger extent. Hence, position 2 is, as to generation of attraction water, a better choice than position 1. This conclusion is strengthening by the fact that, in

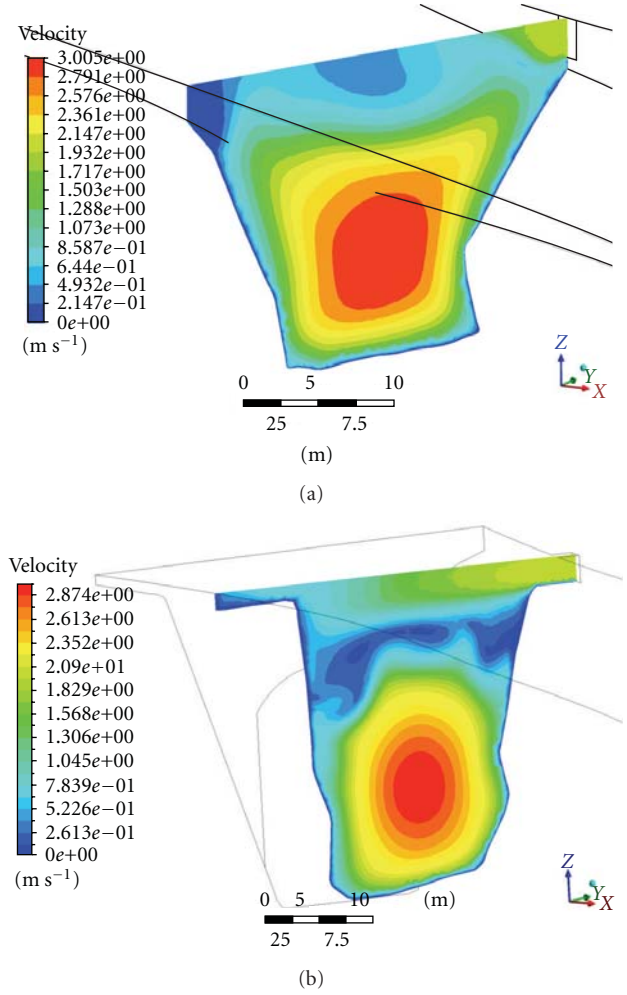

Figure 11: Fishway outlet (upper right corner) at positions 1 and 2 with 0° angle. The flow rate through the power plant is 750 m^3/s.

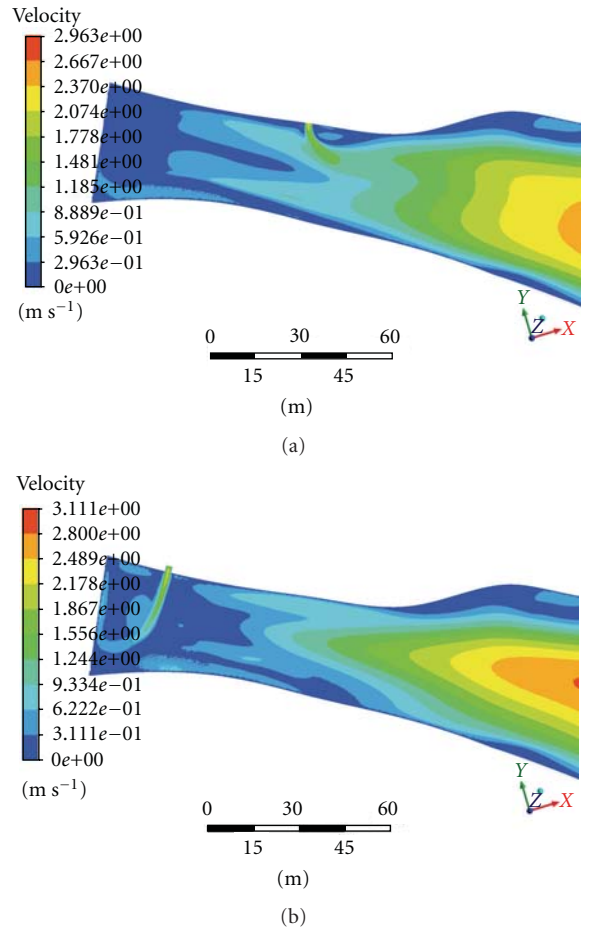

Figure 12: Fishway outlet at positions 1 and 2 with 0° angle. The flow rate through the power plant is 1000 m^3/s.

reality, the jet from the turbines is more surface orientated which probably will make the attraction water created at position 1 less prominent than obtained in the simulations and from the turbines stressing the fact that the fishway should be placed as long into the tail race channel as possible for optimum generation of attraction water.

When scrutinizing possible improvement of the attraction water from the old river bed, the simulations yield a rather different result. The attraction water cannot compete with the flow from the tail race channel except in an area quite close to the shore, see Figure 13 where the simulated attraction water competes with two flow rates from the turbines (500 and 750 m^3/s). As compared with the current situation, this modification of the confluence would still provide considerable improved attraction water along the north side (the right-hand side in the simulated results in Figure 13 and see Figure 1 for cardinal directions). This should improve the probability that fish migrating upstream on the north side of the river or fish exiting the tailrace tunnel on the north side find the fish passage in the old river bed.

6. Conclusion

The measurements show that the flow is considerably more unstable in reality as compared to the simulations. The flow fields in the simulations are therefore less diffuse as to time-averaged quantities, and the tailrace jet from the tunnel outlet is stronger but less surface orientated in the simulations as compared to reality. Keeping this in mind, a number of additional conclusions can be made from the work here presented. A fishway in the tailrace channel can generate noticeable attraction water for all relevant flows from the turbines. Of the cases studied, the simulations show that position two gives considerably stronger attraction water as compared to position one. It is likely that this difference is enlarged by the diffusivity of the tailrace jet existing in reality. By a concentration of the flow from the old river bed, noticeable attraction water can be created at the confluence area. In this case, the attraction water only stretches a short distance into the tailrace flow since this flow is completely surface orientated in the confluence area. However, if the fish migrate along the north shore, they will sense the attraction water.

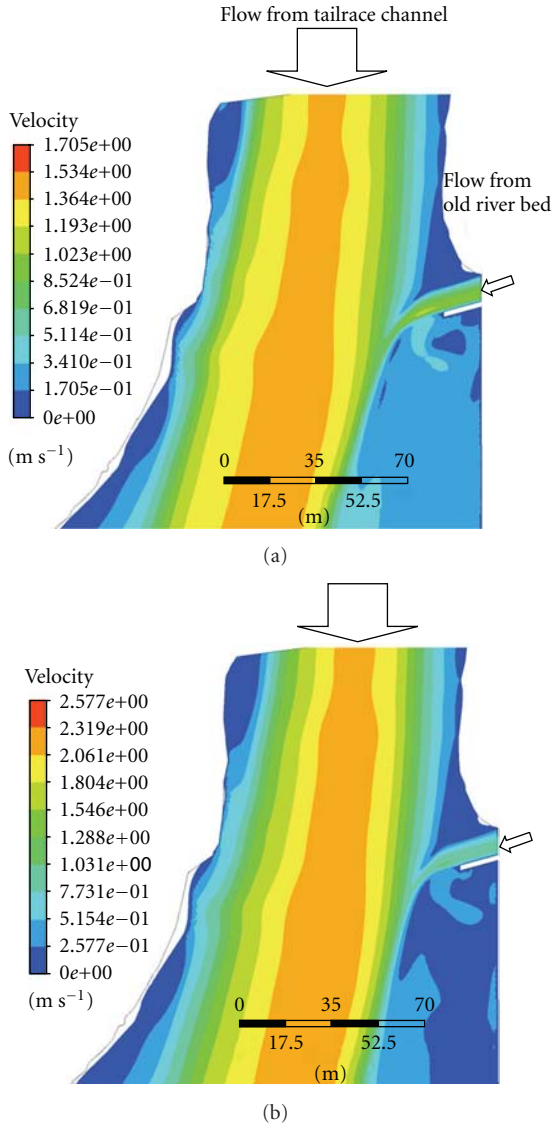

FIGURE 13: Confluence area with flow rate from the turbines of 500 m^3/s and 750 m^3/s and flow rate in the old river bed is 20 m^3/s. A wall is inserted 10 m from the north shore.

Acknowledgments

This work was financed by Vattenfall AB and Umeå Kommun. The authors also acknowledge Vindeln Utveckling that always kept their administration in phase with the real EU time and the National Board of Fisheries for their suggestions on the design of this study.

References

[1] D. Marjavaara and S. Lundström, "Response surface-based shape optimization of a Francis draft tube," *International Journal of Numerical Methods for Heat and Fluid Flow*, vol. 17, no. 1, pp. 34–45, 2007.

[2] H. Lundqvist, P. Rivinoja, K. Leonardsson, and S. McKinnell, "Upstream passage problems for wild Atlantic salmon (*Salmo salar* L.) in a regulated river and its effect on the population," *Hydrobiologia*, vol. 602, no. 1, pp. 111–127, 2008.

[3] P. Rivinoja, S. Mckinnell, and H. Lundqvist, "Hindrances to upstream migration of atlantic salmon (*Salmo salar*) in A Northern Swedish River caused by a hydroelectric power-station," *River Research and Applications*, vol. 17, no. 2, pp. 101–115, 2001.

[4] J. V. Arnekleiv and M. Kraabøl, "Migratory behaviour of adult fast-growing brown trout (*Salmo trutta*, L.) in relation to water flow in a regulated Norwegian river," *Regulated Rivers: Research and Management*, vol. 12, no. 1, pp. 39–49, 1996.

[5] J. Webb, "The behaviour of adult Atlantic salmon ascending the rivers Tay and Tummel to Pitlochry dam," Scottish Fisheries Research Report 48, 1990.

[6] P. Rivinoja, *Migration problems of Atlantic Salmon (Salmo salar L.) in Flow Regulated Rivers*, Ph.D. thesis, Swedish University of Agricultural Sciences, Department of Aquaculture, Umeå, Sweden, 2005.

[7] E. M. Lindmark, *Flow design for migrating fish*, Ph.D. thesis, Luleå University of Technology, Division of Fluid Mechanics, Luleå, Sweden, 2008.

[8] E. Lindmark and H. Gustavsson, "Field study of an attraction channel as entrance to fishways," *River Research and Applications*, vol. 24, no. 5, pp. 564–570, 2008.

[9] N. R. B. Olsen and S. Stokseth, "Three-dimensional numerical modelling of water flow in a river with large bed roughness," *Journal of Hydraulic Research*, vol. 33, pp. 571–581, 1995.

[10] C. A. M. E. Wilson, J. B. Boxall, I. Guymer, and N. R. B. Olsen, "Validation of a three-dimensional numerical code in the simulation of pseudo-natural meandering flows," *Journal of Hydraulic Engineering*, vol. 129, no. 10, pp. 758–768, 2003.

[11] N. J. Clifford, N. G. Wright, G. Harvey, A. M. Gurnell, O. P. Harmar, and P. J. Soar, "Numerical modeling of river flow for ecohydraulic applications: Some experiences with velocity characterization in field and simulated data," *Journal of Hydraulic Engineering*, vol. 136, no. 12, pp. 1033–1041, 2010.

[12] D. J. Booker, "Hydraulic modelling of fish habitat in urban rivers during high flows," *Hydrological Processes*, vol. 17, no. 3, pp. 577–599, 2003.

[13] S. K. Sinha, F. Sotiropoulos, and A. J. Odgaard, "Three-dimensional numerical model for flow through natural rivers," *Journal of Hydraulic Engineering*, vol. 124, no. 1, pp. 13–23, 1998.

[14] B. Dargahi, "Three-dimensional flow modelling and sediment, transport in the River Klarälven," *Earth Surface Processes and Landforms*, vol. 29, no. 7, pp. 821–852, 2004.

[15] T. S. Lundström, J. G. I. Hellström, and E. M. Lindmark, "Flow design of guiding device for downstream fish migration," *River Research and Applications*, vol. 26, no. 2, pp. 166–182, 2010.

[16] J. Y. Yoon, V. C. Patel, and R. Ettema, "Numerical model of flow in ice-covered channel," *Journal of Hydraulic Engineering*, vol. 122, no. 1, pp. 19–26, 1996.

[17] Y. Jia, S. H. Scott, Y. Xu, S. Huang, and S. S. Y. Wang, "Three-dimensional numerical simulation and analysis of flows around a submerged weir in a channel bendway," *Journal of Hydraulic Engineering*, vol. 131, no. 8, pp. 682–693, 2005.

[18] Y. Jia, S. Scott, Y. Xu, and S. S. Y. Wang, "Numerical study of flow affected by bendway weirs in victoria bendway, the mississippi river," *Journal of Hydraulic Engineering*, vol. 135, no. 11, pp. 902–916, 2009.

[19] C. L. Rakowski, L. L. Ebner, and M. C. Richmond, "Fast-track design efforts using CFD: Bonneville second powerhouse," in *World Water and Environmental Resources Congress: Critical Transitions in Water and Environmental Resources Management*, pp. 1790–1798, July 2004.

[20] J. M. Viscardi, A. Pujol, V. Weitbrecht, G. H. Jirka, and N. R. B. Olsen, "Numerical simulations on the Paraná de las Plamas River," in *Proceedings of the 3rd International Conference on Fluvial Hydraulics, River Flow*, Lisbon, Portugal, 2006.

[21] M. R. Simpson and R. N. Oltmann, "Discharge-measurement system using an acoustic Doppler current profiler with applications to large rivers and estuaries," *US Geological Survey Water-Supply Paper*, vol. 2395, 1993.

[22] E. A. Nystrom, C. R. Rehmann, and K. A. Oberg, "Evaluation of mean velocity and turbulence measurements with ADCPs," *Journal of Hydraulic Engineering*, vol. 133, no. 12, pp. 1310–1318, 2007.

[23] ANSYS, *Ansys CFX User manual Ver. 11*, Ansys, Inc, 2007.

[24] B. E. Launder and D. B. Spalding, "The numerical computation of turbulent flows," *Computer Methods in Applied Mechanics and Engineering*, vol. 3, no. 2, pp. 269–289, 1974.

[25] J. F. Rodriguez, F. A. Bombardelli, M. H. García, K. M. Frothingham, B. L. Rhoads, and J. D. Abad, "High-resolution numerical simulation of flow through a highly sinuous river reach," *Water Resources Management*, vol. 18, no. 3, pp. 177–199, 2004.

[26] F. M. White, *Viscous Fluid Flow*, McGraw Hill, New York, NY, USA, 1991.

[27] G. J. Arcement and V. R. Schneider, "Guide for selecting Manning's roughness coefficients for natural channels and flood plains," *US Geological Survey Water-Supply Paper*, vol. 2339, 1989.

[28] B. C. Yen, "Open channel flow resistance," *Journal of Hydraulic Engineering*, vol. 128, no. 1, pp. 20–39, 2002.

[29] C. F. Colebrook, "Turbulent flow in pipes with particular reference to the transition region between the smooth- and rough-pipe laws," *Journal of the Institution of Civil Engineers*, vol. 11, pp. 133–156, 1939.

[30] V. C. Patel, "Perspective: flow at high reynolds number and over rough surfaces—Achilles Heel of CFD," *Journal of Fluids Engineering*, vol. 120, no. 3, pp. 434–444, 1998.

[31] T. M. Green, E. M. Lindmark, T. S. Lundström, and L. H. Gustavsson, "Flow characterization of an attraction channel as entrance to fishways," *River Research and Applications*, vol. 27, pp. 1290–1297, 2011.

Hindawi Publishing Corporation
Modelling and Simulation in Engineering
Volume 2012, Article ID 458368, 7 pages
doi:10.1155/2012/458368

Research Article

Simulating the Effects of Structural Parameters on the Hydraulic Performances of Venturi Tube

Yanqi Sun and Wenquan Niu

College of Water Resources and Architectural Engineering, Northwest A & F University, Yangling, Shaanxi 712100, China

Correspondence should be addressed to Wenquan Niu, nwq@vip.sina.com

Received 19 December 2011; Accepted 17 January 2012

Academic Editor: Guan Heng Yeoh

The effects of Venturi structural parameters on its hydraulic performance were studied, which provided theoretical basis for the design of Venturi injector. With an inlet diameter of 50 mm, based on the method of computational fluid dynamics (CFD), the effects of the structural parameters (such as throat taper, throat contraction ratio, and throat length) on their hydraulic performance (such as outlet faceted average velocity, minimum pressure, and critical pressure) were studied under different inlet pressures and pressure differences between inlet and outlet. A power function relationship existed between the mean velocity in outlet section and pressure difference, with an approximate flow stance index of 0.53. Minimum pressure occurred in the throat inlet wall and there was a linear relationship between the minimum pressure and the pressure difference at the inlet and outlet. The throat contraction ratio was the main factor on the effect of Venturi injector performance, which was positively correlated with outlet velocity, negatively to critical pressure, the minimal in-tube pressure, coefficient of local head loss, and fertilizer absorption ratio. For designing Venturi injector, contraction ratio should be reasonably selected according to the coefficient of local head loss and fertilizer absorption ratio.

1. Introduction

Drip irrigation is a controlled local irrigation. While irrigating, fertilizer mixed in water is delivered to the crop root zone, which not only saves fertilizer and a lot of labors, but also improves fertilizer use efficiency and reduces production costs. Fertilization device is one of the main devices in the drip irrigation system. At present, commonly applied devices for fertilization include pressure difference fertilizer applicator, fertilizer pumper, and Venturi injector [1–3].

Due to its simple structure, convenient operation, the Venturi injector has a wide application in the production agriculture. Therefore, the effects of structural parameters of the injector on its hydraulic performance were studied, which is important to improve and enhance its work performance [4]. Two-part Venturi tube was studied by Hou [5], Sha and Hou [6], Sheng [7], and Sun and Wu [8], and structural parameters of the Venturi tube were determined. Li et al. [9] and Jin et al. [10] investigated the relationship among throat pressure, front and back pressure difference, and designing parameters of paralleled Venturi tube, who also suggested the optimal selection of parameters of front and behind inclinations of paralleled Venturi tube. Chen et al. [11] and Wang et al. [12] employed CFD to determine the relationships between the structural parameters of the Venturi applicator and its fertilization performance and suggested that when the inlet pressure and the slot position keep constant, the suction of the Venturi injector would increase with the decrease of throat diameter and the length of contraction section, and the increase of slot diameter. However, few studies have reported aiming at the effects of Venturi structural parameters on its fertilization performance, and there is little theoretical information available on the design of Venture injectors with better fertilization performance and lower head loss.

The objective of this study was to determine the effects of structural parameters of Venturi tube on its hydraulic performance based on the method of CFD. Results of this study may provide theoretical basis for the design of better Venturi injector and may suggest a broader alternative for further researches on the effect of Venture structural parameters on the hydraulic performance.

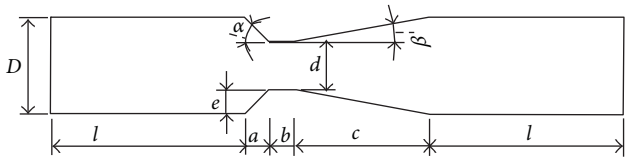

Figure 1: Structural diagram of Venturi injector.

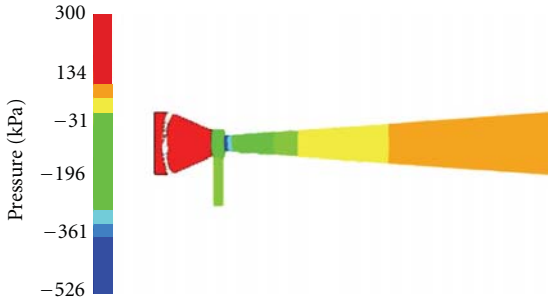

Figure 2: Pressure profile patterns of Venturi injector.

Table 1: Structural Parameters of Venturi injector.

D/(mm)	λ_1	λ_2	α/(rad)	β/(°)
50	0.25, 0.30 0.40, 0.50	1.0, 1.5, 2.0	1.57, 2.09, 2.62	10

2. Methods and Materials

2.1. Physical Model and Parameters. In the structural diagram of Venturi injector, D is inlet and outlet diameter (mm), l is inlet and outlet length (mm), a is contraction length (mm), b is throat length (mm), c is expansion length (mm), d is throat diameter(mm), e is radius difference between inlet and throat (mm), α is contraction ratio (rad), and β is expansion angle (°) (Figure 1).

For the structural parameters of Venturi injector (Table 1), the throat contraction ratio (λ_1) is the ratio between the throat diameter and inlet diameter, namely, $\lambda_1 = d/D$; throat length-diameter ratio (λ_2) is ratio between the throat length and the throat diameter, namely, $\lambda_2 = b/d$. Based on a factorial experiment design of the structural parameters in Table 1, a total of 36 treatments were obtained. The simulations were conducted at different inlet pressures and pressure differences between inlet and outlet. The inlet pressures were 100, 150, 200, 250, and 300 kPa, respectively, and the outlet pressures are shown in Table 2.

2.2. Mathematical Model. Water flow in the Venturi injector could be regarded as incompressible, steady flow, which is consistent with mass and momentum conservation law. Therefore, the basic equations include the continuity equation (1) and the Navier-Stokes equation(2)

$$\frac{\partial u}{\partial x} + \frac{\partial v}{\partial y} + \frac{\partial w}{\partial z} = 0, \tag{1}$$

Table 2: Outlet pressures under the different inlet pressures of Venturi injector.

Inlet pressure/kpa	Outlet pressure/kpa
100	90, 80, 70, 50, 40
150	130, 110, 90, 70, 50
200	160, 140, 120, 100, 80
250	200, 170, 130, 100, 70
300	240, 200, 150, 120, 100

where u, v, ω (m/s) means the flow rate component in x, y, z direction, respectively

$$\begin{aligned}
\frac{\partial(\rho u)}{\partial t} + \nabla(\rho u U) &= -\frac{\partial p}{\partial x} + \mu\nabla^2 u + F_x,\\
\frac{\partial(\rho v)}{\partial t} + \nabla(\rho v U) &= -\frac{\partial p}{\partial y} + \mu\nabla^2 v + F_y,\\
\frac{\partial(\rho \omega)}{\partial t} + \nabla(\rho \omega U) &= -\frac{\partial p}{\partial z} + \mu\nabla^2 \omega + F_z,
\end{aligned} \tag{2}$$

where t (s) is time, U (m/s) is velocity vector, ρ (kg/m^3) is the water density, p (Pa) is pressure of fluid tiny body, μ (Pa·s) is dynamic viscidity coefficient of water, F_x, F_y, F_z means component of mass force on unit volume at x, y, z, respectively. When the mass force is only the gravity and Z axis is vertical, then comes $F_x = 0$, $F_y = 0$, and $F_z = -\rho g$.

According to microscale theory and experimental study, transition Reynolds number in small scale is less than that of the macroscale. When the flow channel was bended and variable, except at the part near the wall, other flows were the turbulent. Therefore, the standard k-ε turbulence model was used for numerical simulation. In the k-ε turbulence model, turbulent kinetic energy was k, dissipation ratio was ε.

2.3. Meshing. CFD software FLUENT6.2 was used for simulation analysis. In this software, differential equations could be simplified into algebraic equations via the finite volume method, one-order upwind difference scheme for its calculation. SIMPLE algorithm was employed for the calculation of noncoupling of pressure rate of the discrete equations. Convergence criteria were the second iteration residuals of the adjacent dependent variables. The two-dimensional model was established using AutoCAD, with GAMBIT2.2.30 to mesh, each section set fully structured hexahedral grid of 1 mm diameter, generated about 30000 grids.

3. Results and Discussions

3.1. Pressure Difference and the Mean Velocity at Outlet Cross-Section. According to the numerical simulation, the distributions in the flow and pressure fields of Venturi injector were obtained, and the outlet velocity and minimal in-tube pressure could be calculated. The relationship between pressure difference and the discharge velocity at outlet could be expressed as follows:

$$v = k \cdot h^x, \tag{3}$$

Table 3: Regression coefficients of pressure differences and velocity of Venturi injector.

Simulation	k	x
M1	0.40	0.53
M2	0.39	0.53
M3	0.40	0.53
M4	0.36	0.53
M5	0.36	0.53
M6	0.36	0.53
M7	0.35	0.53
M8	0.34	0.53
M9	0.34	0.53
M10	0.48	0.53
M11	0.48	0.53
M12	0.47	0.53
M13	0.44	0.53
M14	0.45	0.53
M15	0.44	0.53
M16	0.42	0.53
M17	0.42	0.53
M18	0.42	0.53
M19	0.67	0.53
M20	0.65	0.53
M21	0.66	0.53
M22	0.60	0.53
M23	0.60	0.53
M24	0.60	0.53
M25	0.57	0.53
M26	0.56	0.53
M27	0.56	0.53
M28	0.84	0.53
M29	0.84	0.53
M30	0.84	0.53
M31	0.77	0.53
M32	0.76	0.53
M33	0.76	0.53
M34	0.73	0.53
M35	0.73	0.53
M36	0.72	0.53

where v (m/s) is the velocity at cross-section, k is the velocity coefficient, h (kPa) is pressure difference of inlet and outlet, and x is flow stance index.

Regression analyses were conducted for the 36 simulation results according to (3) and the regression coefficients are presented in Table 3.

As shown in Table 3, for different combinations of structural parameters, Venturi tube flow index, x, was about 0.53 and fairly constant. This is consistent with the criteria of flow discrimination pattern in microirrigation emitter suggesting that the flow is turbulent flow. In addition, the structural parameters had little effect on flow stance index x while they had greater effect on velocity coefficient k.

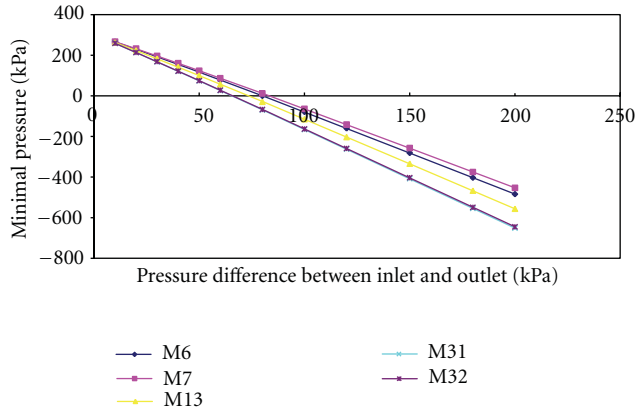

Figure 3: Lines of pressure differences and minimum pressure of Venturi injector.

3.2. Pressure Difference and the Minimal In-Tube Pressure. The simulations showed that the minimal in-tube pressure always occurred at the junction of contraction section and the throat of Venturi injector (Figure 2).

At a given inlet pressure, the minimal in-tube pressure would decrease with the increase of pressure difference between the inlet and outlet. For instance, when the inlet pressure was 100 kPa and pressure difference between the inlet and outlet was increased from 10 to 60 kPa, the minimal in-tube pressure of treatment M1 would decrease from 62 to −146 kPa. When the pressure difference between the inlet and outlet was determined, the minimal in-tube pressure would increase with the increase of the inlet pressure, and the quantitative relationship was presented as follows:

$$H_1 - H_2 = h_1 - h_2, \tag{4}$$

where H_1, H_2 (kPa) are different inlet pressures, h_1, h_2 are the minimal in-tube pressures corresponding to H_1 and H_2, respectively. Taking the treatment M1 as an example, when the pressure difference is 60 kPa, and the inlet pressure increases in sequence from 100 kPa, 150 kPa, 200 kPa to 300 kPa, the minimal in-tube pressure would be −146 kPa, −96 kPa, −46 kPa, and 54 kPa in sequence, with the same increase amplitude as inlet pressure.

Through a conversion of minimal in-tube pressure according to (4), the minimal in-tube pressures at different pressure differences with an inlet pressure of 300 kPa were obtained (Figure 3), and regression analysis was conducted according to the following equation (5). The regression coefficients are showed in Table 4

$$h_{\min} = m \cdot h + h', \tag{5}$$

where $h_{\min}$ (kPa) is the minimal in-tube pressure, m is the coefficient of pressure difference, h' (kPa) is the ideal pressure, and h (kPa) is the pressure difference between inlet and outlet.

The correlation lines of all pressure differences and the minimal pressures intersected at one point (Figure 3). When the inlet pressure was 300 kPa and the pressure difference

Table 4: Regression coefficient of minimum pressure and pressure differences of Venturi injector.

Simulation	m	h_{min}
M1	−4.33	311
M2	−4.30	313
M3	−4.31	311
M4	−3.97	312
M5	−3.95	312
M6	−3.96	312
M7	−3.80	312
M8	−3.74	311
M9	−3.78	312
M10	−4.38	312
M11	−4.47	312
M12	−4.40	312
M13	−4.32	313
M14	−4.31	313
M15	−4.32	315
M16	−3.98	312
M17	−3.98	313
M18	−3.99	313
M19	−4.99	312
M20	−4.94	313
M21	−4.88	312
M22	−4.75	314
M23	−4.79	315
M24	−4.76	315
M25	−4.33	313
M26	−4.35	314
M27	−4.35	314
M28	−5.06	309
M29	−5.12	310
M30	−5.08	310
M31	−4.80	312
M32	−4.77	312
M33	−4.81	313
M34	−4.44	312
M35	−4.45	312
M36	−4.44	312

between inlet and outlet was 0, the minimum in-tube pressure is 312.6 kPa. When the liquid in the tube was the ideal liquid (the ideal liquid has neither the wall friction, nor the viscous force), and the pressure difference between the inlet and outlet was 0, the fluid maintained a uniform linear motion, movement only occurred with the conversion of kinetic energy and potential energy, meanwhile there was no energy exchange with the environment. In this ideal state, the maximal pressure within the tube would be the 312.6 kPa. According to (4) and (5), the following expression can be obtained:

$$h_1' - h_2' = H_1 - H_2, \tag{6}$$

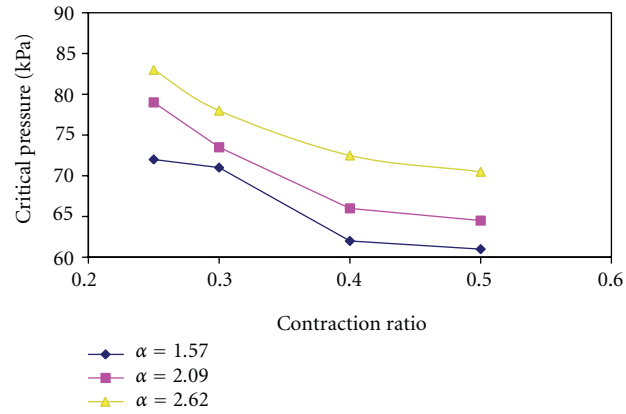

Figure 4: Effects of throat contraction ratio on critical pressure of Venturi injector.

where h_1', h_2' (kPa) are the ideal pressures corresponding to the inlet pressure of H_1, H_2, respectively.

Therefore, the minimum in-tube pressure could be calculated with the following expression:

$$h_{min} = m \cdot h + h_{min}' + H, \tag{7}$$

where h_{min}' (kPa) is the ideal pressure under the inlet pressure of 0 kPa, and H (kPa) is the inlet pressure.

3.3. The Effect of Structural Parameters on Critical Pressure Difference. Structural parameters have great effects on mini-pressure and Venturi injector flow (average velocity at the cross-section of the outlet). Through statistical analysis, the main structural parameters influencing the flow mainly include the throat contraction ratio, throat taper, throat diameter, contraction length, contraction ratio, the expansion part, and the throat length. The effects of the throat contraction ratio, throat taper, and throat diameter on the hydraulic performance were more significant.

When the inlet pressure was determinate and the minimum in-tube pressure was 0, the pressure difference between inlet and outlet h_{cr} could be obtained according to (7). When the pressure difference was greater than h_{cr}, the minimum in-tube pressure was negative; otherwise, the minimum in-tube pressure was positive. In this study, h_{cr} was defined as critical pressure difference between inlet and outlet and can be calculated as follows:

$$h_{cr} = -\frac{H + h_{min}'}{m}, \tag{8}$$

where h_{cr} (kPa) is critical pressure difference between the inlet and outlet.

When inlet pressure was 300 kPa, thus h_{cr} were calculated with (8). The effects of throat contraction ratio on h_{cr} were analyzed, and the fitting curves are shown in Figure 4.

As shown in Figure 4, when the throat contraction ratio was determined, critical pressure would increase with the increase of contraction taper (not cleaner). So Venturi injector should be designed to obtain optimal negative pressure, when the throat contraction ratio is determinate; throat

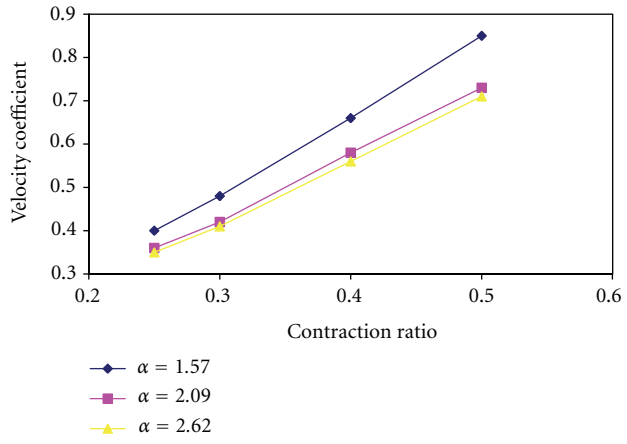

Figure 5: Effects of throat contraction ratio on velocity coefficient of Venturi injector.

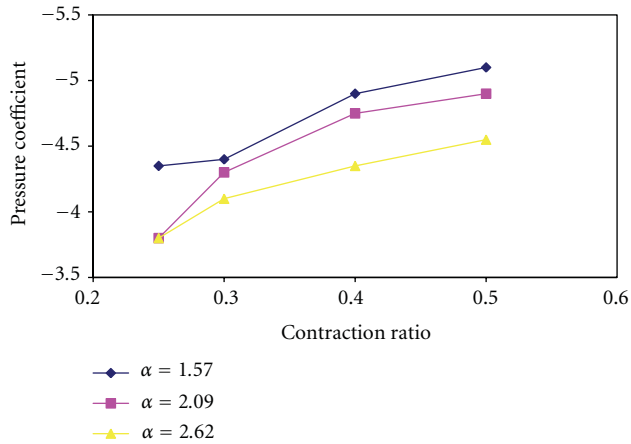

Figure 6: Effects of throat contraction ratio on pressure coefficient of Venturi injector.

taper should be appropriately shortened to get less head loss at optimal negative pressure and optimal fertilization effect. When contraction ratio was determinate, a negative correlation between h_{cr} and contraction ratio was demonstrated. That is to say, when the inlet pressure is given and other structural parameters remain constant, negative pressure is more easily to be obtained at the throat inlet. With the increase of throat contraction ratio, h_{cr} decrease would slow down. It is suggested that designing Venturi injector, contraction ratio would be reasonably selected, not to be too small.

3.4. Effect of Structural Parameters on the Outlet Velocity. When the inlet pressure was determined, the flow velocity was mainly determined by the throat contraction ratio and the contraction taper, but throat contraction ratio was more influential. As showed in Table 3, the regression value of the flow index at different treatments was constantly about 0.53. That is to say, the effect of structural parameters on the flow rate is its effect on the flow velocity coefficient k. The effects of throat contraction ratio and contraction taper on the flow velocity coefficient k were comprehensively analyzed, and the correlation curve of flow velocity between the throat contraction ration and contraction taper were mapped (Figure 5).

The velocity coefficient k tended to decline over the increase of throat taper, but the change would slow down gradually (Figure 5). The velocity coefficient k showed a tendency to increase with the increase of throat contraction ratio, and the tendency would speed up gradually. Therefore, the local head loss of Venturi injector would increase with the increase of throat taper or throat contraction ratio, while the mean velocity at outlet cross-section would decrease. Based on regression analysis, the equation of velocity coefficient with the diameter in 50 mm was as follows:

$$k = 0.1131 + 1.6469\lambda_1 - 0.0767\alpha, \qquad R^2 = 0.9944. \tag{9}$$

3.5. Effects of Venturi Structural Parameters on the Minimum Pressure in the Tube. The effect of Venturi structural parameters on minimum pressure is the effect on the pressure difference coefficient m. Through statistical analysis, the effects of throat contraction ratio and contraction taper on minimum pressure were more significant than effects of other structural parameters. According to the results in Table 4, the effects of throat contraction ratio α and contraction taper on the pressure difference coefficient m were analyzed, and the correlation curve of m with throat contraction ratio and contraction taper was established (Figure 6).

As shown in Figure 6, m and its contraction taper showed a positive correlation, which indicated that contraction taper greatly affects the pressure distribution. In order to obtain optimal negative pressure, throat taper should be appropriately increased. Negative correlation demonstrated between m and throat contraction ratio, m decreased with the increase of throat contraction ratio, and the decrease would slow down. That is to say, when the inlet and outlet diameters remained unchanged, and other structural parameters are kept constant, the absolute minimum pressure would increase with the increase of tube diameter at throat. When the throat contraction ratio is ≤0.5, if the throat diameter is too small, the flow velocity at the throat would be too large, and thus easily causes vaporization, which is not conducive to produce good negative pressure. Therefore, the throat diameter should be appropriately increased to produce effective intake negative pressure. m could also be expressed in the following equation:

$$m = -4.4030 - 3.1284\lambda_1 + 0.5290\alpha, \qquad R^2 = 0.963. \tag{10}$$

3.6. Effects of Structural Parameters on Head Loss and Fertilizer Absorption Ratio. Due to the small length of venturi injector, the frictional head loss can be ignored in calculation, and the calculation formula of local head loss is as follows:

$$h_j = \zeta \frac{v^2}{2g}, \tag{11}$$

where h_j (m) is local head loss, which stands for the pressure difference between inlet and outlet in this study, ζ (%) is the coefficient of local head loss, v (m/s) is the average flow speed of outlet section, and g (9.8m^2/s) is acceleration of gravity.

Local head loss ζ was calculated through (11). The results showed that the local head loss of Venturi injector was very great. The value of ζ tested here is between 2.25 and 13.27. When contraction ratio λ_1 is between 0.25 and 0.50, the value of ζ would drop quickly with the increase of λ_1, while other structure parameters had little influence on ζ, so it can be expressed approximately like that $\zeta = 0.5\lambda_1^{-2.16}$. In addition, it is also found that coefficient of local head loss (ζ) fell with the increase of the pressure difference, which may be caused by the change of flow pattern. Using Reynolds number to analyze the flow pattern in tube through the following formula:

$$R_e = \frac{vd}{\nu}, \tag{12}$$

where R_e (%) is Reynolds number, ν stands for kinematic viscosity coefficient of water (m^2/s), when the temperature is 20°C, $\nu = 1.01 \times 10^{-6}$ m^2/s.

The calculation results of (12) show the Reynolds number is between 14356 ~ 335643, so it is turbulence due to the criterion of hydraulics. Besides, the Reynolds number, the mutual movement inside water flow, the energy conversion caused by mutual movement increase with the pressure difference, while the proportion of energy conversion caused by function between fluid and structure would decrease, which well-explained why the local head loss would decrease with the increase of pressure difference.

It is generally agreed that effective Venturi injector should have small coefficient of local head loss but greater fertilizer absorption ratio (η). The driving flow rate and the minimum pressure in tube of main tube were established in this study. Therefore, the amount of fertilizer absorption can be predicted in accordance with the tube hydraulics. Suppose there was a standard atmospheric pressure on liquid fertilizer surface, and the distance under the Venturi tube was 0.5 m, the diameter of fertilizer absorption tube was 8 mm, without considering local head loss, the amount of fertilizer absorption can be predicted according to the following equation:

$$q = A\sqrt{2gh_0}, \tag{13}$$

where q (m^3/s) is the amount of fertilizer absorption, h_0 is the head difference of fertilizer absorption tube between outlet and inlet, which means distance difference between liquid fertilizer surface with Venturi tube.

The results showed that fertilizer could be stably absorbed when the contraction ratio λ_1 was bigger than (0.4 or 0.5), the pressure difference between outlet and inlet was 80 kpa, and η was 0.5. However, when the contraction ratio λ_1 was less than 0.3, it may absorb fertilizer stably only when the pressure difference between outlet and inlet is 100 kpa. And when the pressure difference between outlet and inlet remained constant, η showed a tendency to decrease with the increase of contraction ratio λ_1.

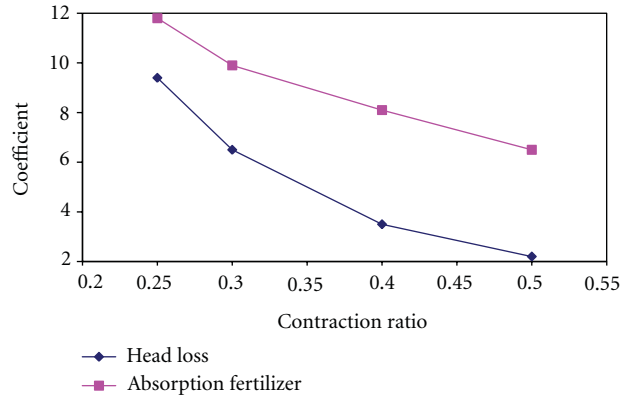

Figure 7: Effects of contraction ratio on head loss and absorption fertilizer of Venturi injector.

Figure 7 shows the correlation among the contraction ratio, local head loss, and fertilizer absorption ratio, when the pressure difference between outlet and inlet is 150 kPa, the pressure of inlet is 300 kPa. It can be found that the coefficient of local head loss and η would decline with increase of contraction ratio. Therefore, the throat diameter cannot be too big or too small when designing the Venturi injector; and it should be chosen in accordance with coefficient of local head loss and the diameter of throat part. The throat length has little influence on the critical pressure, the minimum pressure in tube, and the flow speed, which is in consistence with the findings in the literature.

4. Conclusions

(1) It is demonstrated that a strong relationship between the mean velocity at outlet section and the pressure difference, and the flow stance index was approximately 0.53; velocity coefficient was mostly influenced by throat taper and throat contraction ratio.

(2) The minimum pressure occurred in the throat inlet wall, and the location of minimum pressure was rarely influenced by the opening position and pore size of Venturi injector. There existed perfect linear relation between the minimum pressure and the pressure difference between at inlet and outlet. When the inlet pressure is determined, the curves of the pressure difference and the minimum pressure would come cross a fixed point. The coordinates of the point were not influenced by the pressure difference at the inlet and outlet.

(3) The structural parameters which influence the hydraulic performances of Venturi injector include throat taper, throat contraction ratio, throat length, and expansion section taper. More significant influence of throat contraction ratio was found among parameters affected by hydraulic performances. The results showed a positive correlation between the throat contraction ratio and the mean velocity at outlet section, and a negative correlation between throat contraction ratio and minimum pressure in tube.

(4) The results showed a negative relationship between coefficient of local head loss, absorption fertilizer ratio, and throat contraction ratio. So it is strongly recommended that when designing Venturi injector, contraction ratio should be reasonably selected according to the coefficient of local head loss and absorption fertilizer ratio.

Acknowledgments

This work is jointly supported by China 863 Plan (2011AA-100507).

References

[1] S. Z. Kang, X. T. Hu, H. J. Cai, and S. Y. Feng, "New ideas and development tendency of theory for water saving in modern agriculture and ecology," *Journal of Hydraulic Engineering*, vol. 35, no. 12, pp. 1–7, 2004.

[2] W. Q. Niu, P. T.Wu, and X. K. Fan, "Low-pressure drip irrigation system," *Water Saving Irrigation*, vol. 2, pp. 29–30, 2005.

[3] W. Niu, P. Wu, and X. Fan, "Method for calculating integrated flux deviation rate of micro-irrigation system," *Nongye Gongcheng Xuebao/Transactions of the Chinese Society of Agricultural Engineering*, vol. 20, no. 6, pp. 85–88, 2004.

[4] F. S. Li and S. N. Lu, "Study on the fertigation and it s application," *Plant Nutrition and Fertilizer Science*, vol. 6, no. 2, pp. 233–240, 2000.

[5] S. J. Hou, "Design on two par s pattern venturi tube," *Drainage and Irrigation Machinery*, vol. 13, no. 4, pp. 44–46, 1995.

[6] Y. Sha and S. J. Hou, "Experimental research on applying fertilizer apparat us of parallel Venturi tubes," *Drainage and Irrigation Machinery*, vol. 13, no. 2, pp. 37–39, 1995.

[7] X. M. Sheng, "Introduction of 100Ps-1 Venturi fertilizer applicator," *Water Saving Irrigation*, vol. 11, pp. 14–15, 2000.

[8] X. Y. Sun and S. Y. Wu, "Introduction of fertilizer applicator by pressure difference," *Water Saving Irrigation*, vol. 5, pp. 36–37, 2003.

[9] B. J. Li, H. P. Mao, and K. Li, "A study on the parallel connection Venturi tube and its parameter selection," *Drainage and Irrigation Machinery*, vol. 19, no. 1, pp. 42–45, 2001.

[10] Y. K. Jin, C. H. Xia, and B. L. Fang, "Research and development of Venturi fertilizer applicator series," *China Rural Water and Hydropower*, vol. 5, pp. 14–16, 2006.

[11] Z. B. Chen, H. J. Dou, S. W. Chen et al., "Numeral research on flow field of Venturi tube," *China Building Material Equipment*, vol. 4, pp. 61–63, 2005.

[12] M. Wang, X. Huang, and G. Li, "Numerical simulation of characteristics of Venturi Injector," *Transactions of the Chinese Society of Agricultural Engineering*, vol. 22, no. 7, pp. 27–31, 2006.

Hindawi Publishing Corporation
Modelling and Simulation in Engineering
Volume 2012, Article ID 632387, 16 pages
doi:10.1155/2012/632387

Research Article

Landing Gear Aerodynamic Noise Prediction Using Building-Cube Method

Daisuke Sasaki, Deguchi Akihito, Hiroshi Onda, and Kazuhiro Nakahashi

Department of Aerospace Engineering, Tohoku University, Aoba 6-6-01, Sendai 980-8579, Japan

Correspondence should be addressed to Daisuke Sasaki, sasaki@ad.mech.tohoku.ac.jp

Received 9 December 2011; Accepted 19 January 2012

Academic Editor: Guan Heng Yeoh

Landing gear noise prediction method is developed using Building-Cube Method (BCM). The BCM is a multiblock-structured Cartesian mesh flow solver, which aims to enable practical large-scale computation. The computational domain is composed of assemblage of various sizes of building blocks where small blocks are used to capture flow features in detail. Because of Cartesian-based mesh, easy and fast mesh generation for complicated geometries is achieved. The airframe noise is predicted through the coupling of incompressible Navier-Stokes flow solver and the aeroacoustic analogy-based Curle's equation. In this paper, Curle's equation in noncompact form is introduced to predict the acoustic sound from an object in flow. This approach is applied to JAXA Landing gear Evaluation Geometry model to investigate the influence of the detail components to flows and aerodynamic noises. The position of torque link and the wheel cap geometry are changed to discuss the influence. The present method showed good agreement with the preceding experimental result and proved that difference of the complicated components to far field noise was estimated. The result also shows that the torque link position highly affects the flow acceleration at the axle region between two wheels, which causes the change in SPL at observation point.

1. Introduction

Great progress has been made in Computational Fluid Dynamics (CFD) in the past several decades, and nowadays it plays an important role in the design and analysis for aircraft development. The emerging problem for the commercial aircraft development is how to reduce the airframe noise from high lift device and landing gear. CFD has been widely used to predict the flow around the high lift device to reduce the aerodynamic noise, whereas the application of CFD to the landing gear is still limited [1–6]. The landing gear is constructed with many bluff components, and thus the noise source is not singular but many and thus complicated. To predict the noise from the real landing gear geometry precisely, all the components need to be modeled in the computation to treat all the interaction effect. Japan Aerospace Exploration Agency (JAXA) has developed a research landing gear model with detailed components based on the current two-wheel landing gear to understand the noise generation mechanism by experiments and numerical analysis. The model, Landing gear Evaluation Geometry model (LEG), includes all the components even with pins, tubes, and cavity as shown in Figure 1 [4–6]. To analyze the flow and acoustic field of the landing gear, the computational capability to these complicated geometries and the high parallelization performance are required.

To satisfy all these demands, Building-Cube Method (BCM) has been proposed, which is a block-structured Cartesian mesh solver [7–13]. In BCM, three-dimensional flow fields are divided into various sizes of cuboids called "Cube," and the cubes are subdivided into equally spaced Cartesian meshes called "Cell." As the mesh resolution is determined according to the local cube size, fine meshes near the body and coarse meshes far from the body can be accomplished. Because of the uniform computational load at each cube, it is expected to achieve the high parallel performance even with the massive number of processors. Since BCM is a Cartesian-based mesh, a complicated geometry such as a landing gear with tiny components can be easily and instantly meshed [7, 13].

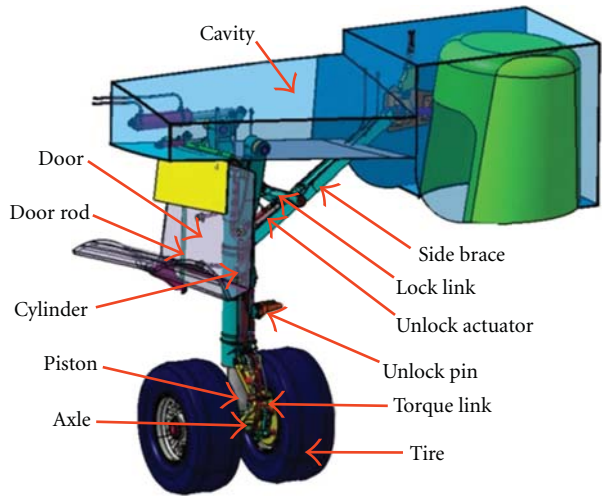

Figure 1: JAXA's two-wheel main landing gear model (LEG model) [4–6].

Compressible Navier-Stokes equation represents the propagation of sound wave, thus we can calculate aerodynamic sound directly in theory. However, because this propagation is a very tiny pressure fluctuation, it requires an enormous amount of mesh to calculate, and thus it is not a practical method. Therefore, we adopt aerodynamic/acoustic splitting method in this study. The pressure on a body surface is computed by an incompressible Navier-Stokes flow solver of BCM, and then the far-field sound level is estimated by means of Curle's equation [14]. In our previous result, the far-field noise from a landing gear was estimated but the large difference of SPL was observed [7]. In this paper, noncompact form of Curle's equation is adopted for far-field noise prediction to be able to handle acoustically noncompact objects. The method is validated using a circular cylinder case to estimate the far-field sound level. The present approach is then applied to JAXA's landing gear model, LEG geometry. The geometry is composed of many detail components: Main cylinder (strut), Center piston, Axle, Brake caliper, Brake disk, Wheel cap with cooling holes, and so forth. One of the objectives of this research is to evaluate the usefulness of non-compact form of Curle's equation against the landing gear noise by comparing with experimental data. Another is to investigate the influence of a torque link position and wheel cap shape to local flow features and also far-field aerodynamic noise. Through the computational analysis, the usefulness of the present method toward airframe noise estimation is discussed.

2. Numerical Method

2.1. Splitting Method. There are two major approaches for the aeroacoustic analysis: the direct method and the splitting method. In this paper, we adopt the latter, as it is popular particularly for low Mach number flows. The flowfield is analyzed by an unsteady flow simulation and the sound propagation is calculated by an acoustic analogy. Three-dimensional incompressible flow solver is used as a flow solver and Curle's equation is adopted as aeroacoustic analogy. Firstly, the pressure fluctuation on the body surface is calculated by the BCM flow solver. Based on the time-dependent surface pressure, far-field Sound Pressure Level (SPL) is obtained via the Curle's equation.

2.2. Flow Analysis. BCM is based on a multiblock structure of equally spaced Cartesian meshes to achieve the simplicity in the mesh generation, in the spatially higher-order solution algorithm, and in the postprocessing. These features of simplicity of the Cartesian mesh apply to all stages of a flow computation and eases memory requirement per node. These factors will become more important for large-scale computations on expected near-future high performance computers. The computational mesh consists of many cuboids which include equally spaced Cartesian mesh as shown in Figure 2. It shows cube and cell distribution around NACA0012 airfoil. These cuboids in Figure 2(a) are called as "cube," and Cartesian mesh in each cube are called as "cell" in Figure 2(b). Since the number of mesh points is completely the same in all the cubes regardless the cube size, high parallel efficiency is accomplished as the computation is parallelized based on cube. The mesh resolution is controlled by each cube size, thus the geometrical size of cube becomes large as the increase of distance from a wall boundary. In the present approach, the body surface is approximated as staircase representation for the simplicity. To improve the local mesh resolution, selected cubes can be subdivided.

Governing equations of the present solver are incompressible Navier-Stokes equations as follows:

$$\frac{\partial \mathbf{u}}{\partial t} + (\mathbf{u}\cdot\nabla)\mathbf{u} = -\nabla p + \frac{1}{\mathrm{Re}}\nabla^2\mathbf{u}, \qquad \operatorname{div}\mathbf{u} = 0. \tag{1}$$

The staggered arrangement is employed with finite difference scheme in terms of the spatial accuracy. In this study, the convective term is discretized by Kawamura-Kuwahara scheme based on a third-order upwind scheme [15]. The pressure term is solved by Red-Black SOR method, and the diffusion term is discretized by a second-order central difference scheme. The time integration uses Fractional-Step method, and the temporal velocity field is solved by second-order Adams-Bashforth explicit method [12]. Simple linear interpolation is employed for the data interchange for the compromise between computational efficiency and accuracy. Higher-order interpolation maintains the computational accuracy and the mass conservation; however, it deteriorates the computational efficiency and increases memory usage. Thus, the smallest cubes are allocated around the body and also the wake region in the present computation to minimize the influence of linear interpolation between different size cubes.

2.3. Acoustic Analysis. The general theory about the aeroacoustic generation was developed by Lighthill in 1952 [16]. Lighthill transformed the Navier-Stokes and continuity equations to form an exact, inhomogeneous wave equation,

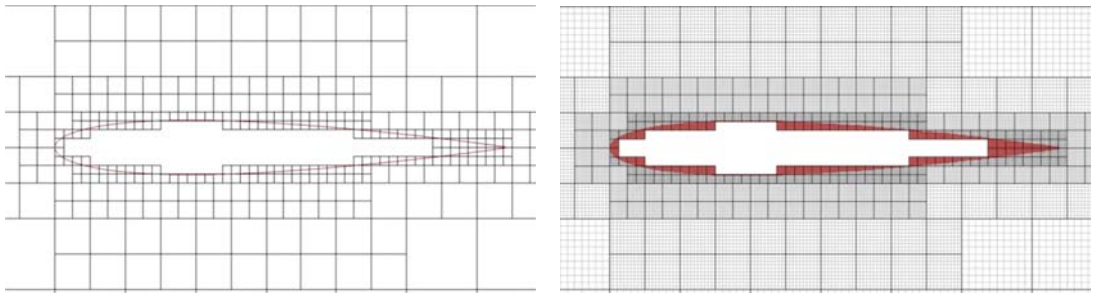

(a) Cube allocation (b) Cell distribution

Figure 2: Cube and cell distribution around an airfoil with BCM.

where the source terms were considered only within turbulent flow region. The Lighthill equation, which represents the sound propagation in the static fluid, is described as follows:

$$\frac{\partial^2 \rho'}{\partial t^2} - c_0^2 \nabla^2 \rho' = \frac{\partial^2 T_{ij}}{\partial x_i \partial x_j}. \tag{2}$$

The equation means that the aeroacoustic noise is generated by quadrupole source in the static fluid. The Lighthill equation does not consider the existence of an object in the flow. Curle revealed that sound source was generated by quadrupole source at the turbulent flow and dipole source at the surface of an object, and led to the following equation:

$$\rho' = \frac{1}{4\pi c_0^2} \frac{\partial^2}{\partial x_i \partial x_j} \int_V \frac{\left[T_{ij}\right]}{r} dV - \frac{1}{4\pi c_0^2} \frac{\partial}{\partial x_i} \int_S \frac{[P_i]}{r} dS. \tag{3}$$

Curle's equation was obtained by the transformation of the Lighthill equation to form an exact integral equation. However, the equation is not easy to solve since it requires the computation of volume integration and space derivative. Curle's equation can be simplified with the assumption of low speed flow. The first term of (3) can be ignored because the magnitude of the term is square of the Mach number. The space derivative is then converted into temporal differentiation, and the equation is represented as follows:

$$P_a = \frac{1}{4\pi c_0} \frac{x_i}{r^2} \frac{\partial}{\partial t} \int P_i\left(y, t - \frac{r}{c_0}\right) dS. \tag{4}$$

This compact form of Curle's equation means that the sound pressure at the observation point from the object is computed via the surface pressure fluctuation. This equation is valid when the acoustically compact condition is satisfied. The compact condition is that the sound wavelength is much longer compared to the characteristic length of an object, and also the sound observation point is far away enough from the object compared to the sound wavelength. In this study, the following noncompact form of Curle's equation is introduced to treat the acoustic field where the acoustically compact is not satisfied

$$P_a = \frac{1}{4\pi} \int \frac{x_i - y_i}{r^2} \left(\frac{1}{c_0}\left[\frac{\partial P_i}{\partial t}\right] + \frac{[P_i]}{r}\right) dS. \tag{5}$$

The sound source position is not singular in the equation unlike (4). The equation is named non-compact Curle's equation in this study, whereas (5) is named compact Curle's equation for the distinction. To measure the SPL at the observation point, the pressure fluctuation calculated by the Curle's equation is transformed into the fluctuation in the frequency domain by FFT (Fast Fourier Transform). Then, it is substituted into the following equation:

$$\mathrm{SPL} = 10 \log_{10}\left(\frac{{P_e}^2}{{P_0}^2}\right). \tag{6}$$

Here, P_e is the effective value of the sound pressure fluctuation calculated by the FFT, and P_0 is the reference sound pressure in air, whose value is 2.0×10^{-5} [Pa].

3. Circular Cylinder

3.1. Computational Condition. A circular cylinder is used for the validation of aeroacoustic noise prediction using the present aerodynamic/acoustic splitting method of BCM and Curle's method. The BCM meshes based on the cylinder diameter D (0.04 m) is generated in the computational domain shown in Figure 3. The computational domain size is $50D \times 50D$, and the cylinder height is $12.5D$ (0.5 m). The minimum mesh spacing is $1.0 \times 10^{-2} D$, and the total number of cells amounts to 100 million. Cube allocation from the side view is shown in Figure 3(b), where finer cube is used behind the cylinder to distribute high-resolution mesh in the wake region. Reynolds number is 2.0×10^4 based on the cylinder diameter, uniform flow velocity is 7.5 m/s, and the observation point is $25D$ (1.0 m) aside from the cylinder. Sommerfeld boundary condition is used at the downstream boundary condition to prevent the unphysical reflection of pressure wave at the boundary. In the FFT calculation, the sampling frequency is 1,280 Hz (6.3 in nondimensional frequency), the frequency resolution is 2.5 Hz (0.133 in non-dimensional frequency). FFT length is 512, FFT average is 10 times, and the overlap is 50%. The parameters used in the computation are summarized in Table 1.

3.2. Result. The computational result of SPL is compared with experimental data [17] as shown in Figure 4. Both the results of compact Curle's equation (2) and non-compact

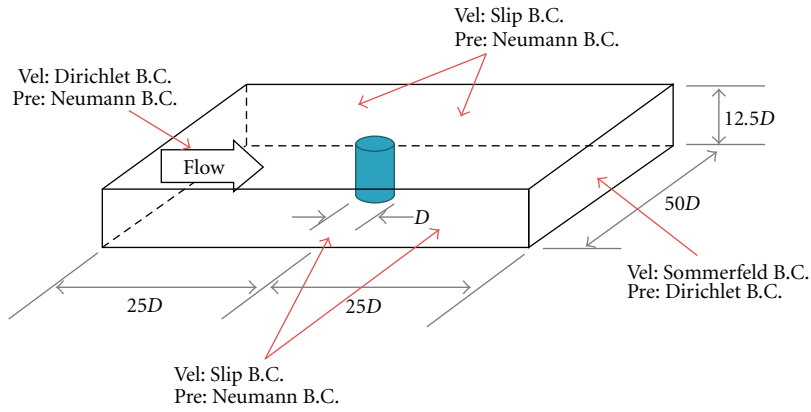

(a) Computational domain

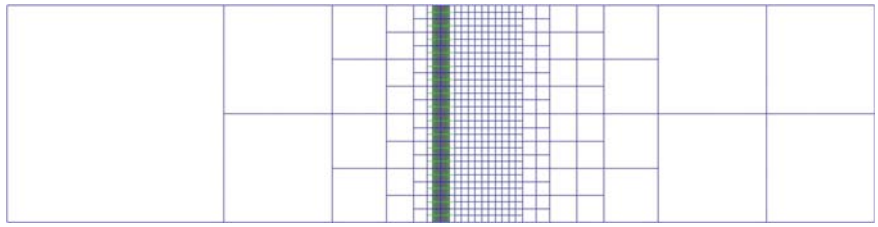

(b) Cube allocation (viewed from the side)

Figure 3: Computational domain with boundary conditions and Cube allocation.

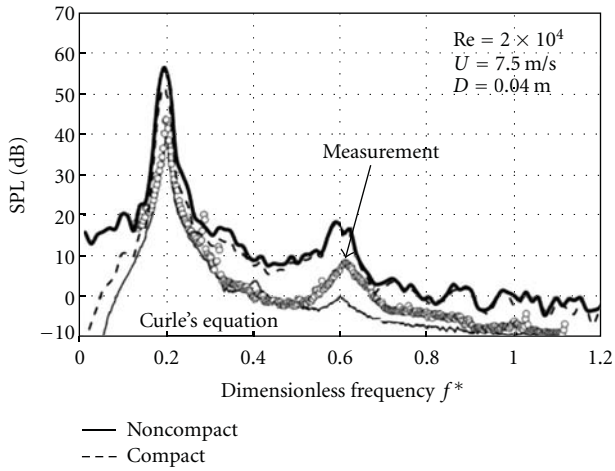

Figure 4: SPL spectrum of computational end experimental results.

Table 1: Computational condition of a circular cylinder.

Reynolds number, Re	2.0×10^4
Characteristic length, D	0.04 [m] (cylinder diameter)
Freestream velocity	7.5 [m/s]
Computational domain	$50D \times 50D \times 12.5D$
Minimum mesh spacing	$1.00 \times 10^{-2}D$
Total number of cells	about 100 million
Sampling frequency	6.3 [−] (1280 Hz)
Frequency resolution	0.133 [−] (2.5 Hz)
Length of FFT	512
Averaging	10 times
Overlap	50%

Curle's equation (3) are plotted for comparison. The bold line is calculated by the non-compact Curle's equation, the dot-line is calculated by compact Curle's equation, the circle is the experimental result, and the slim line is calculated by the authors of [17] using compact Curle's equation. The spectrum of the non-compact Curle's equation is generally matched with those of compact Curle's equation and experiment. However, the SPL of first peak is much higher compared to the experiment. This is because non-compact Curle's equation considers the near-field pressure fluctuation (pseudo acoustic wave). Meanwhile, the effect of pseudo acoustic wave is removed for the experimental result. The raw SPL at the first peak of experiment is 51.7 dB, and then the difference with non-compact result becomes 4 dB (55.0 dB by non-compact SPL at the first peak). The usefulness of the present splitting method is validated, though the difference between compact and non-compact Curle's equation is small for the case of cylinder.

4. LEG Model

4.1. Computational Condition. The simplified LEG model is used for the simulation to understand the influence of axle region to flows and far field noise. As shown in Figure 5, the simplified LEG geometry is composed of a main cylinder (strut), a center piston, a torque link, axle and brake components, and two wheels. The simplified LEG model

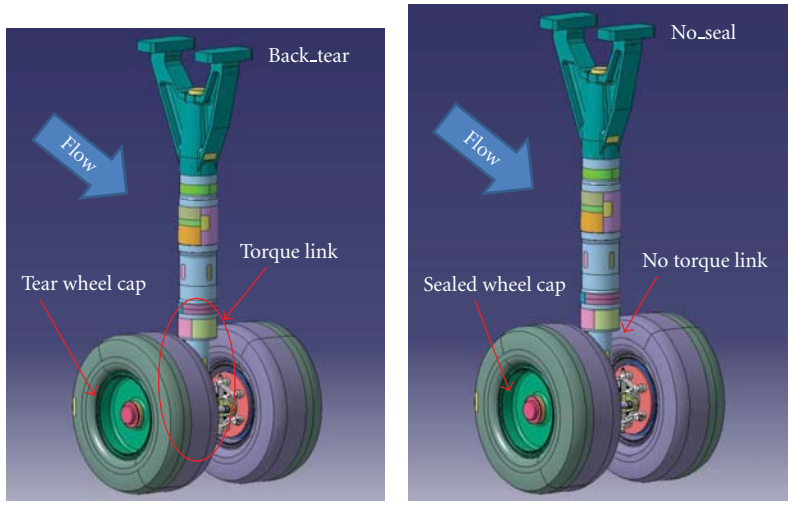

(a) BACK_TEAR configuration (b) NO_SEAL configuration

Figure 5: Simplified LEG geometries for computation.

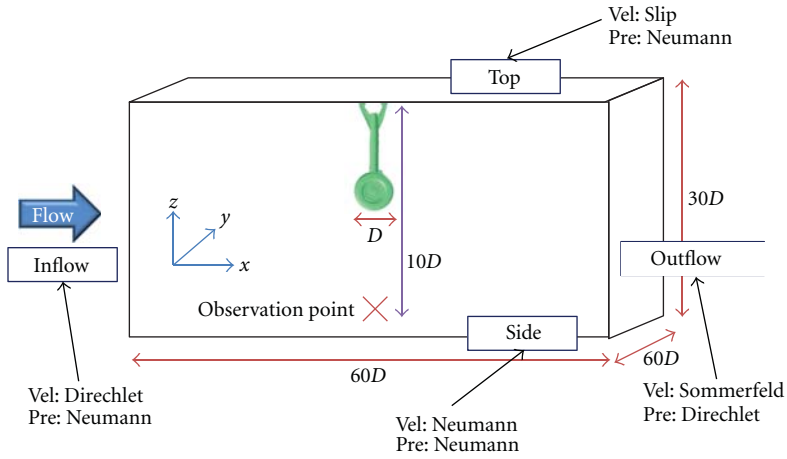

(a) Computational domain with boundary conditions

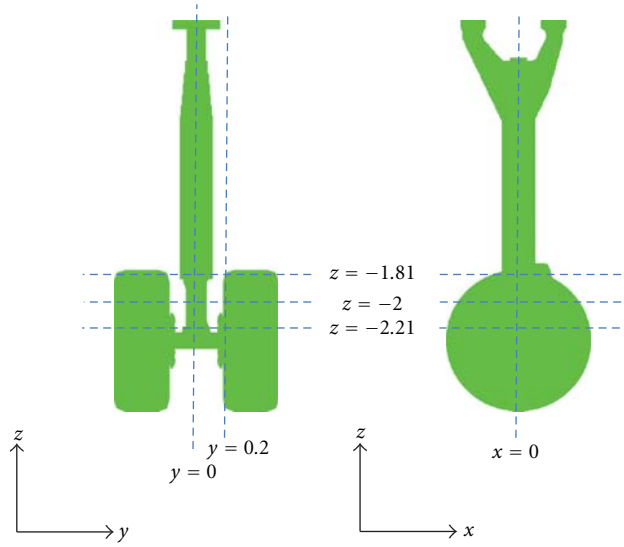

(b) Model with cross sections

Figure 6: Computational domain and model cross sections.

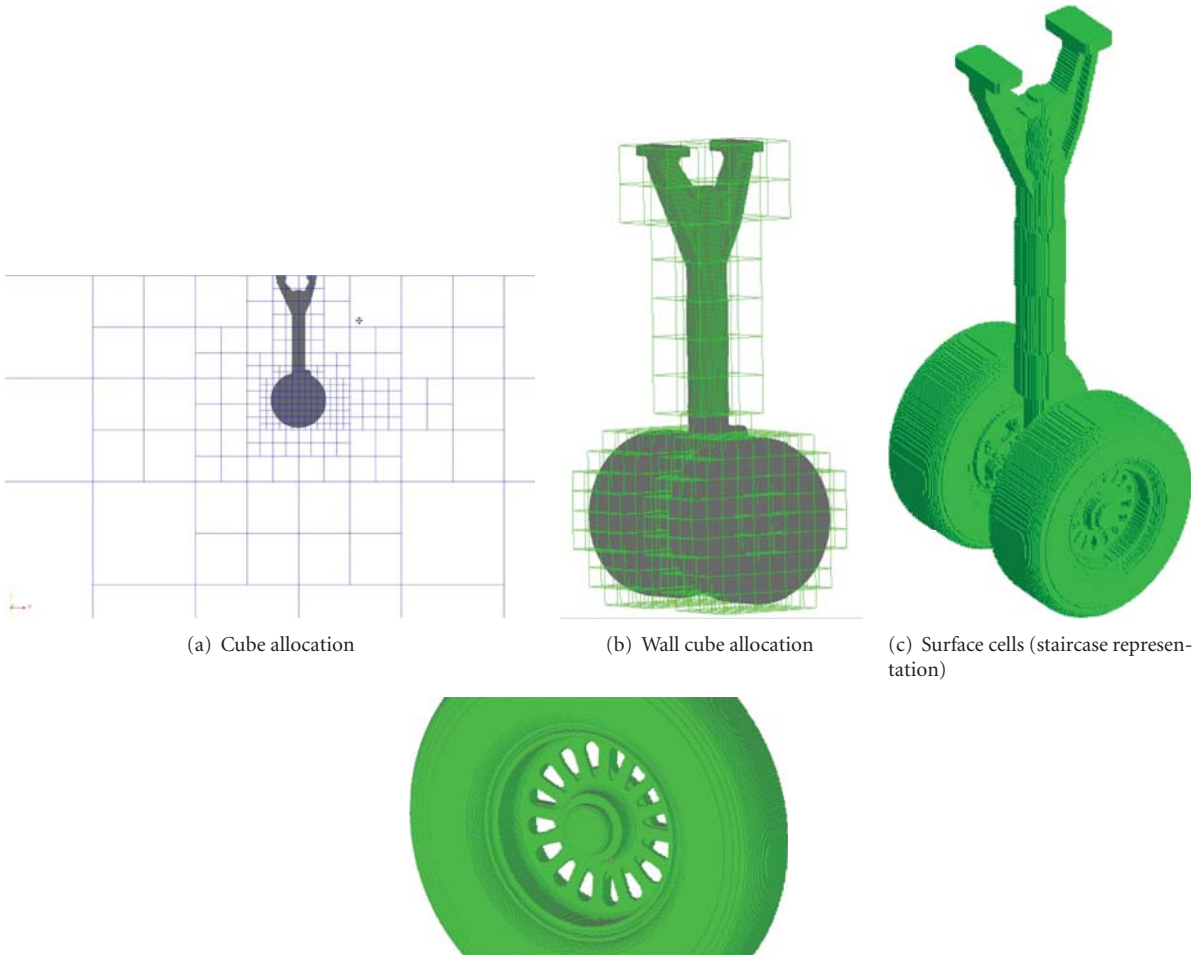

(a) Cube allocation

(b) Wall cube allocation

(c) Surface cells (staircase representation)

(d) Cells at wheel

Figure 7: Computational mesh for LEG geometry.

does not have other major components such as a door, a side-brace, and cavity shown in Figure 1. The torque link position is variable, so that the torque link can be attached in front of the strut, behind the strut (Figure 5(a)), or even removed (Figure 5(b)) to evaluate the influence of torque link to the flowfield and aerodynamic noise. In addition, there are two types of wheel cap prepared: the sealed cap (Figure 5(b)) and the tear-shaped cooling holes on the cap (Figure 5(a)). The cooling holes are penetrating the wheel cap, thus the tiny flow paths exist in the wheel. Computations are conducted for the six configurations by changing the position of the torque link and by changing the wheel cap geometry as summarized in Table 2. Each name in the table means [*Torque link position*]_[*Wheel cap type*]. BACK_TEAR geometry is that the torque link is attached backward the strut (BACK) and the wheel cap is tear-shaped cooling holes type (TEAR) as shown in Figure 5(a).

The BCM meshes based on the wheel diameter D (0.4 m) are generated for the six LEG geometries. The computational domain size is $60D \times 60D \times 30D$, and the LEG geometry is attached to slip wall as shown in Figure 6(a). Figure 6(b) shows the model with several cross-sections where the computed flowfields are compared. Cube allocation from the side view is shown in Figure 7(a). Subdivided cubes are allocated at the wake region to improve the mesh resolution. Wall cubes around the wheel region are also refined as shown in Figure 7(b). The whole surface cells with staircase representation is shown in Figure 7(c). Cooling holes at the wheel are sufficiently represented with the minimum mesh spacing of $3.66 \times 10^{-3}\, D$ (based on the wheel diameter) as shown in Figure 7(d). The total number of cells amounts about 90 million, and the flow computations are conducted on the vector-parallel supercomputer of NEC SX-9 16 CPUs.

Table 2: Six LEG configurations.

Name	Torque link position	Wheel cap type
BACK_SEAL	BACK	SEALED
BACK_TEAR	BACK	TEAR (Cooling Hole)
FRONT_SEAL	FRONT	SEALED
FRONT_TEAR	FRONT	TEAR (Cooling Hole)
NO_SEAL	NO (REMOVED)	SEAL
NO_TEAR	NO (REMOVED)	TEAR (Cooling Hole)

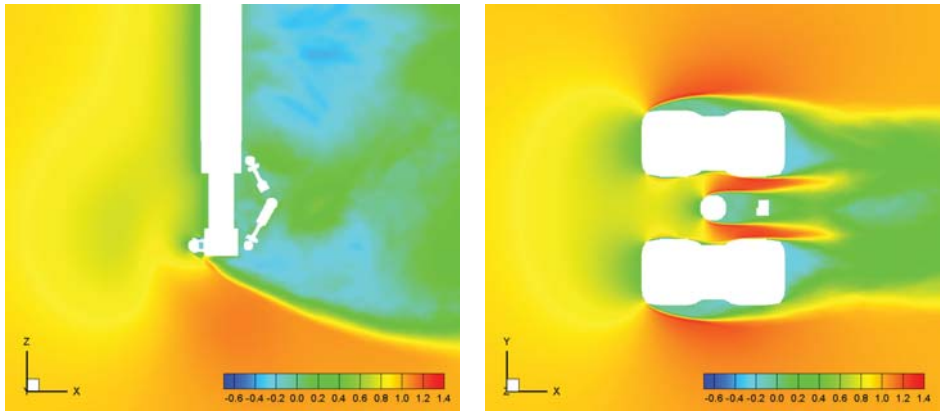

(a) Cross section at $y = 0.0$ (b) Cross section at $z = -2.00$

Figure 8: Computed mean velocity component in the freestream direction.

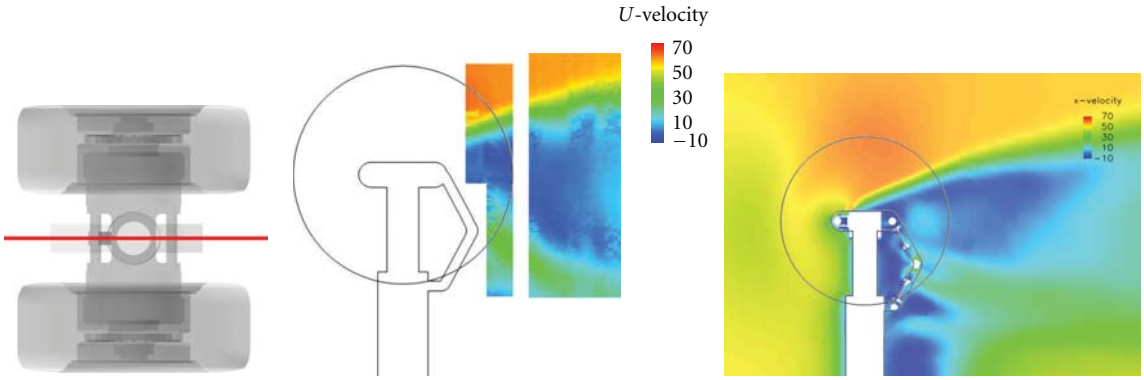

(a) PIV measurement (left) and computation (right) at cross section y

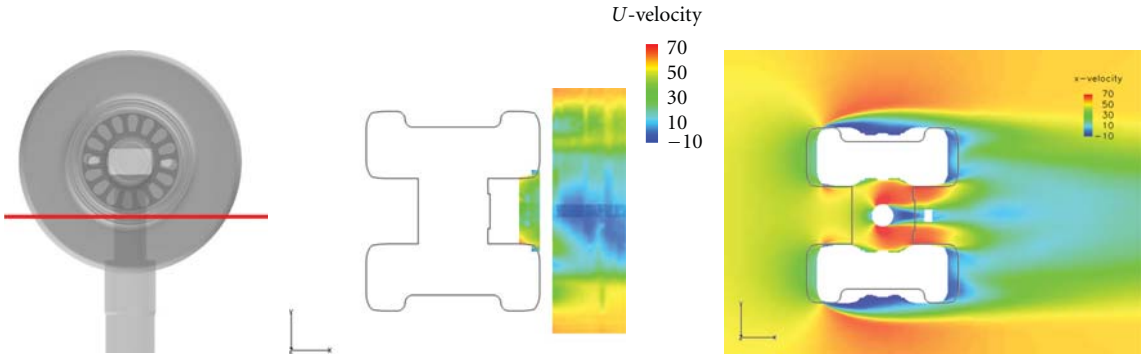

(b) PIV measurement (left) and computation (right) at cross section z

Figure 9: Mean velocity component in the freestream direction by Murayama et al. [6].

Reynolds number is 1.49 million based on the wheel diameter D, uniform flow velocity is 54.4 m/s, and the observation point is 14.71D below the model. In the FFT calculation, the sampling frequency is 10 kHz (75 in non-dimensional frequency), the frequency resolution is 20 Hz (0.147 in non-dimensional frequency). The other setting is same as the cylinder case: FFT length 512, FFT average 10 times, and the overlap 50%. Table 3 summarizes the computational condition.

4.2. LEG with Backward Torque Link Configuration. The LEG configuration with backward torque link and wheel cap of cooling holes (BACK_TEAR) is used for comparison. The mean velocity component in the freestream direction at the two sections ($y = 0.0$ and $z = -2.00$) is shown in Figure 8. Figure 8(a) shows the flowfield at the center of the landing gear, and the separation from the axle is observed. The geometry is upside down, but the result is in reasonable agreement with Murayama's PIV measurement data and

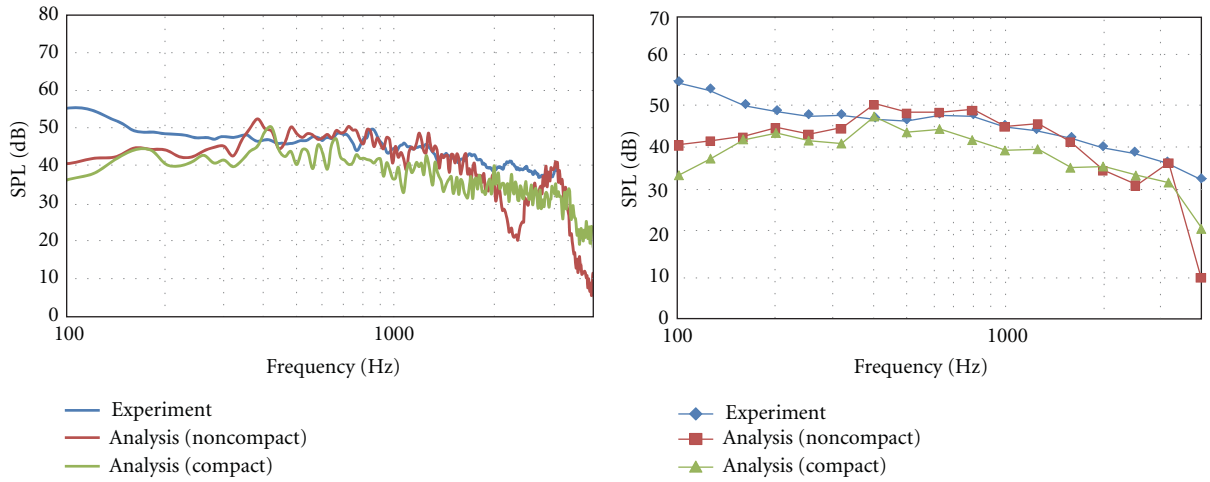

(a) Narrow band (b) 1/3-octave band (experimental scale)

Figure 10: Comparison of SPL spectrum by experiment and computations.

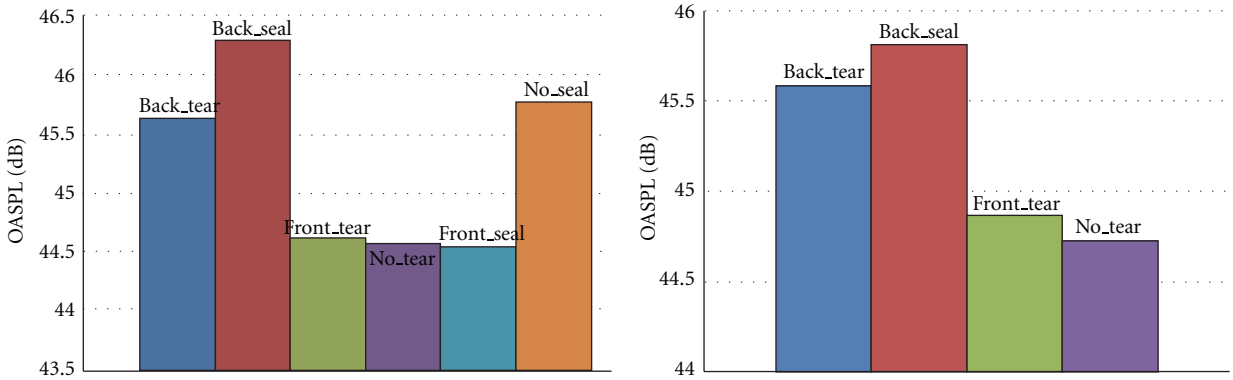

(a) Computational result (b) Experimental result

Figure 11: Comparison of OASPL of different LEG configurations.

Table 3: Computational condition of LEG model.

Reynolds number, Re	1.49×10^6
Characteristic length, D	0.4 [m] (wheel diameter)
Freestream velocity	54.4 [m/s]
Computational domain	$60D \times 60D \times 30D$
Minimum mesh spacing	$3.66 \times 10^{-3}D$
Total number of cells	About 90 million
Sampling frequency	75 [−] (10 [kHz])
Frequency resolution	0.147 [−] (20 [Hz])
Length of FFT	512
Averaging	10 times
Overlap	50%

computational result [6] in Figure 9(a). Figure 8(b) shows the velocity field near the axle region. The flow acceleration due to the existence of the center cylinder and the torque link is observed. The flowfield are similar to the PIV data and computation; however the acceleration region is larger compared to the referenced computation.

The SPL spectrum in narrow band and also the converted spectrum to 1/3 octave band (experimental scale) are plotted in Figure 10. The figures include numerical results based on compact and non-compact forms of Curle's equations, and also experimental result. The SPL based on compact Curle's equation shows a 10 dB difference compared to experiments as compared to the previous result in [7]. By applying non-compact Curle's equation, the SPL values between 200 and 3,000 [Hz] frequency range are much improved, and the values are closely agreed with experimental data. The sharp decrease of SPL is shown in the present computation at the higher frequency range. The problem needs to be solved for more accurate prediction in the entire frequency domain but this can be caused due to the lack of mesh resolution. Since the background noise is not considered in the computations, the SPL of the lower frequency range is smaller compared to the experiment.

4.3. OASPL for Six LEG Configurations. To compare the noise level of the six LEG configurations, the Overall SPL (OASPL)

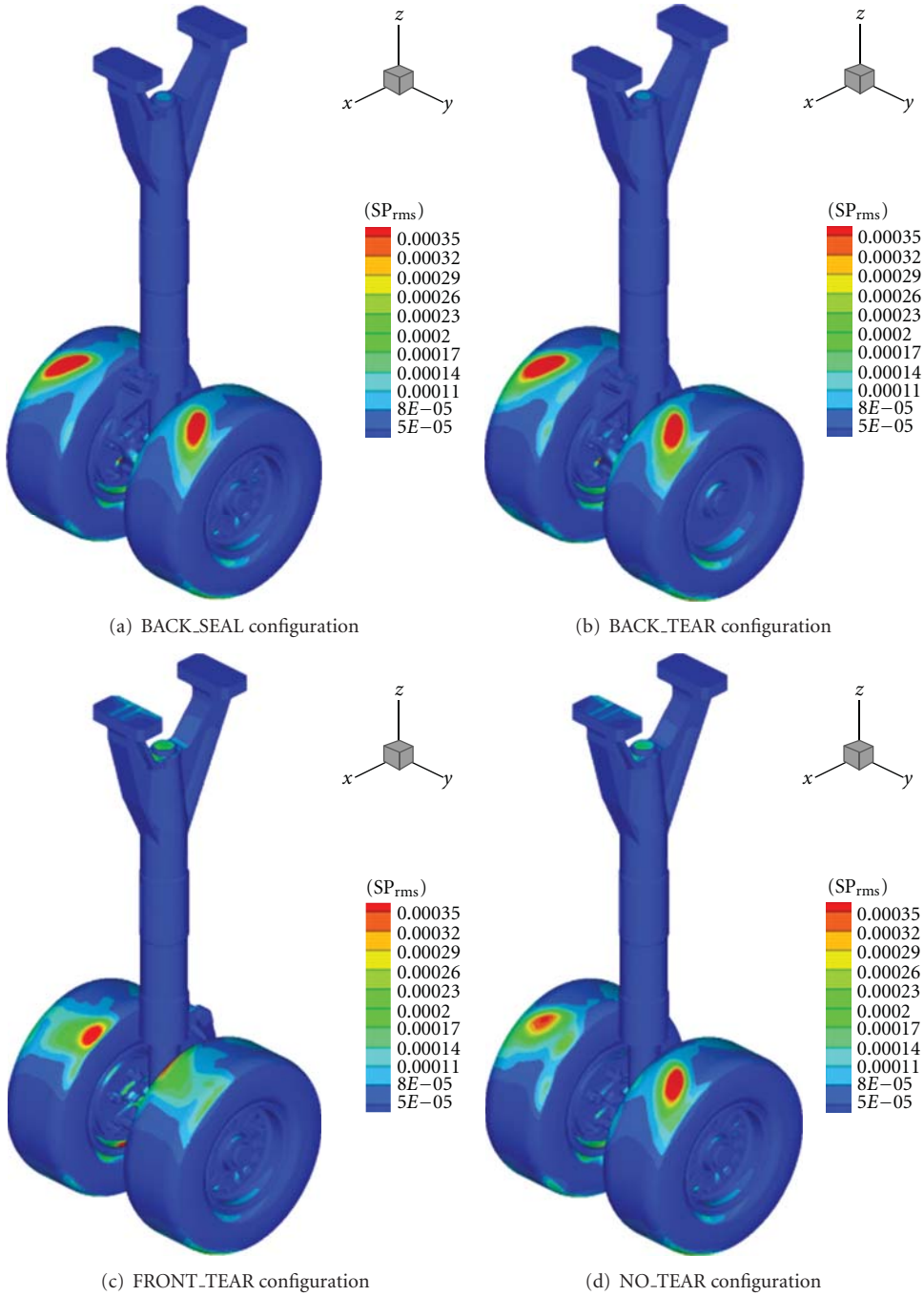

(a) BACK_SEAL configuration

(b) BACK_TEAR configuration

(c) FRONT_TEAR configuration

(d) NO_TEAR configuration

Figure 12: Comparison of surface sound pressure fluctuation of different LEG configurations (viewed from behind the landing gear).

is computed in this section. The OASPL is computed by integrating the power of spectrums as follows:

$$\mathrm{OASPL} = 10\log_{10}\left(\frac{\sum_{f_1}^{f_2} p^2}{{P_0}^2}\frac{\Delta f}{f_2 - f_1}\right). \tag{7}$$

In this study, the integral range of frequency is from 220 to 3,500 [Hz] because the range shows reasonable agreement with the experiment in the previous section.

The computational and experimental OASPL values of the LEG configurations are shown in Figure 11. Four out of six configurations were examined by the experiment, while all the six configurations were evaluated by the present computations. In the experimental result, the torque link position highly affects the OASPL. When the location is behind the piston, higher OASPL values are observed. The noisiest configuration is BACK_SEAL in the experiment. The computational result shows that the tendency of OASPL is in qualitative agreement with the experiment; the BACK_SEAL

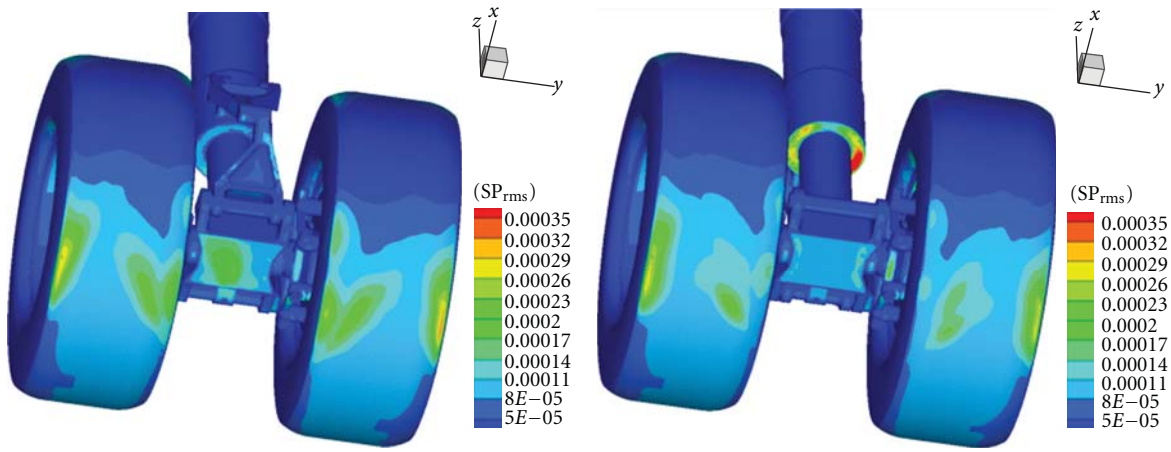

(a) BACK_TEAR configuration (b) FRONT_TEAR configuration

Figure 13: Comparison of surface sound pressure fluctuation below the wheel.

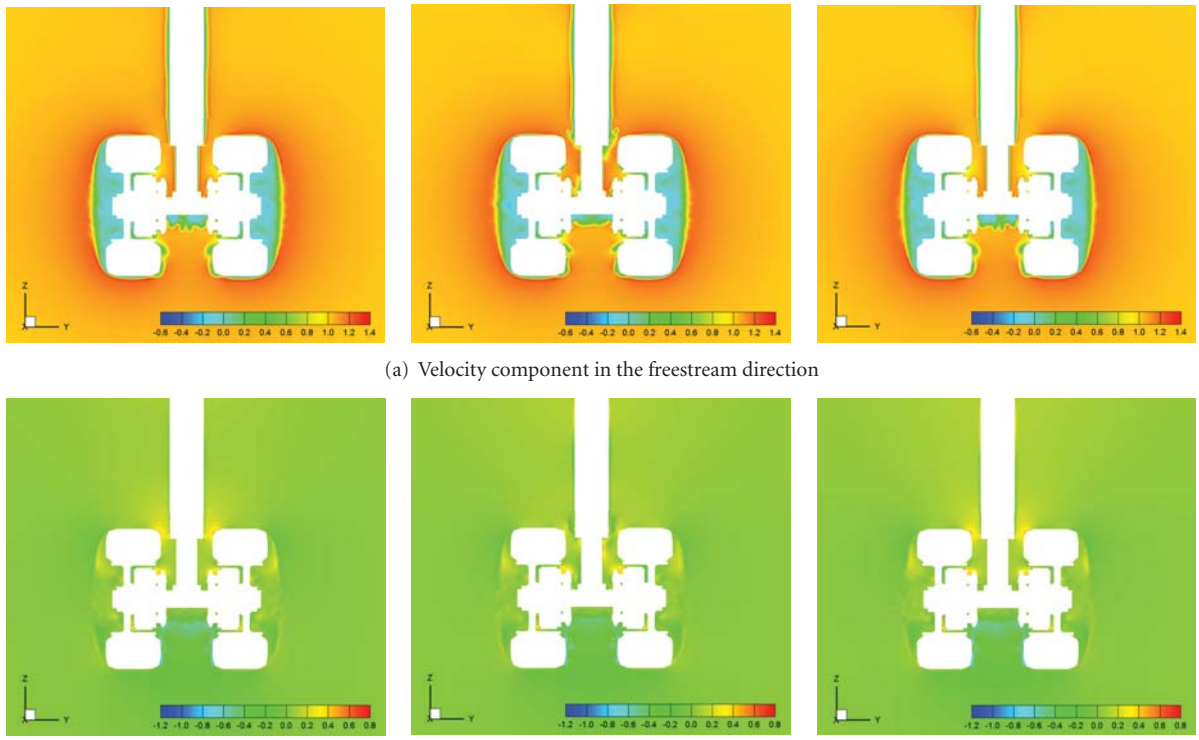

(a) Velocity component in the freestream direction

(b) Velocity component in the vertical direction

Figure 14: Computed mean velocity component at cross section $x = 0.0$ (left: BACK_TEAR, center: FRONT_TEAR, right: NO_TEAR).

is noisiest, and the second is BACK_TEAR of the four. From the computational results, OASPL values tend to be high when the torque link position is behind the piston or removed from the geometry together with the sealed wheel cap. On the other hand, when the torque link is attached in front of the piston against the flow, the values are almost the same regardless the wheel cap type: sealed or tear holes. This indicates that the torque link position highly affects the far-field aerodynamic noise from landing gear as its existence drastically changes the flow characteristics.

Sound pressure fluctuation on the surface (SP_{rms}) is calculated by non-compact form of Curle's equation. Since the Curle's equation converts surface pressure fluctuations to the noise at the observation point, the surface with larger SP_{rms} has larger contribution to the noise. The surface sound pressure fluctuations of the four configurations (BACK_SEAL, BACK_TEAR, FRONT_TEAR, NO_TEAR) are plotted in Figure 12. It is observed that one part of the upper wheel (toward the root of landing gear) shows the higher values. The appearance of BACK_SEAL, BACK_TEAR,

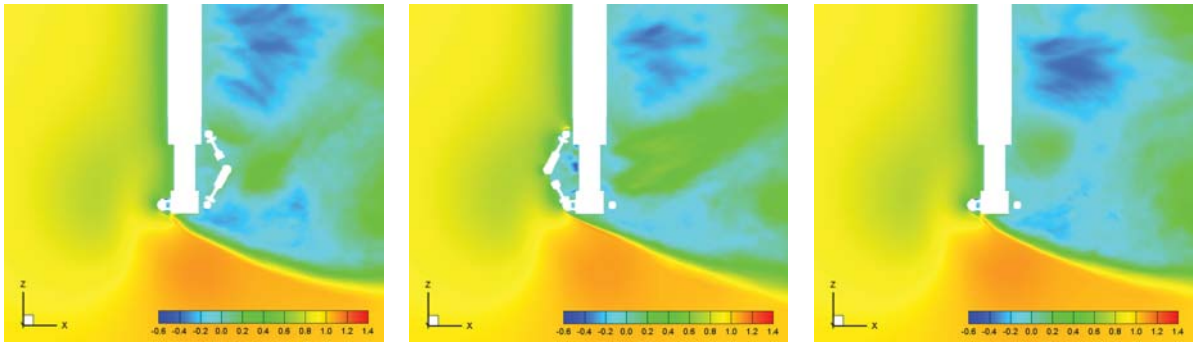

(a) Velocity component in the freestream direction

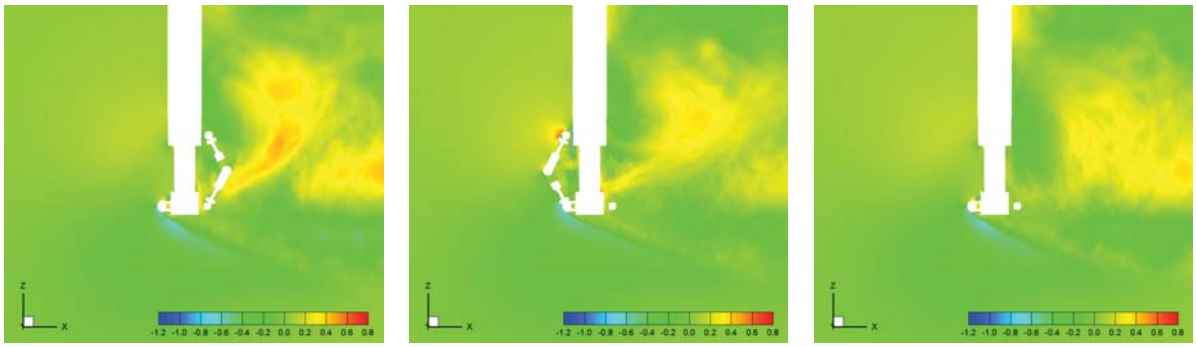

(b) Velocity component in the vertical direction

Figure 15: Computed mean velocity component at cross section $y = 0.0$ (left: BACK_TEAR, center: FRONT_TEAR, right: NO_TEAR).

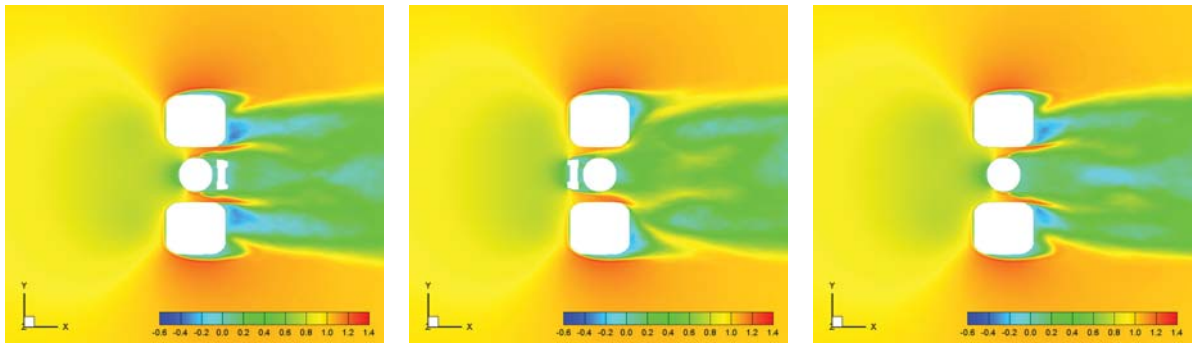

(a) Velocity component in the freestream direction

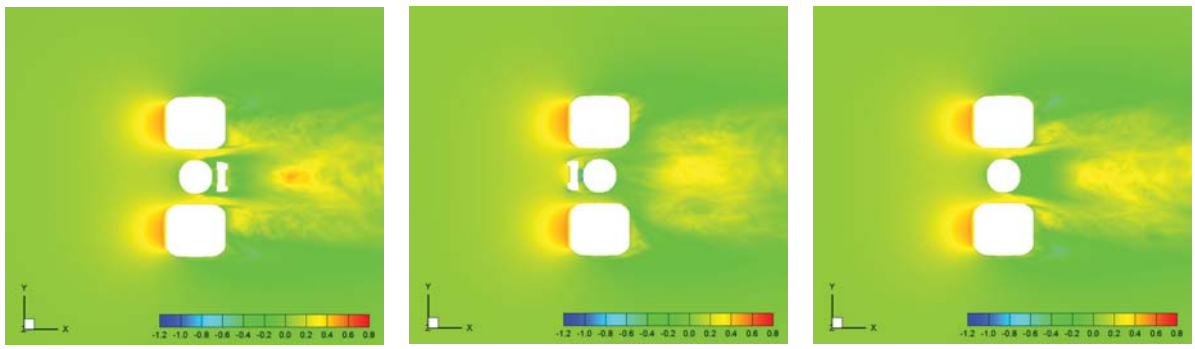

(b) Velocity component in the vertical direction

Figure 16: Computed mean velocity component at cross section $z = -1.81$ (left: BACK_TEAR, center: FRONT_TEAR, right: NO_TEAR).

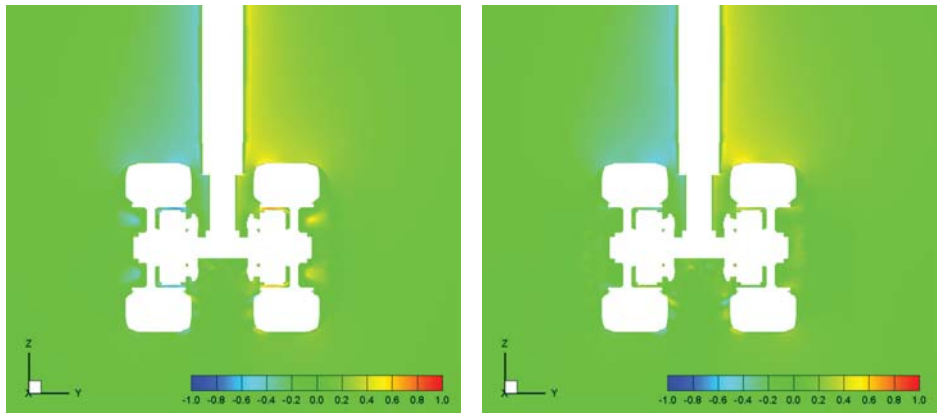

Figure 17: Computed mean velocity component in the horizontal direction at cross section $x = 0.0$ (left: BACK_TEAR, right: BACK_SEAL).

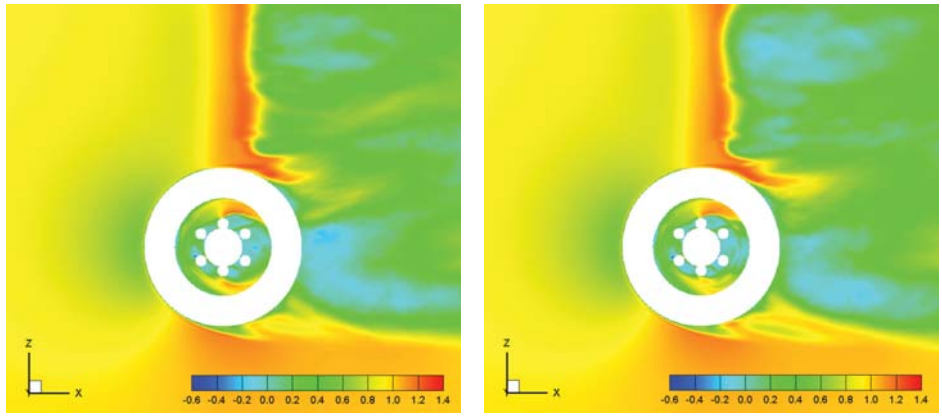

(a) Velocity component in the freestream direction

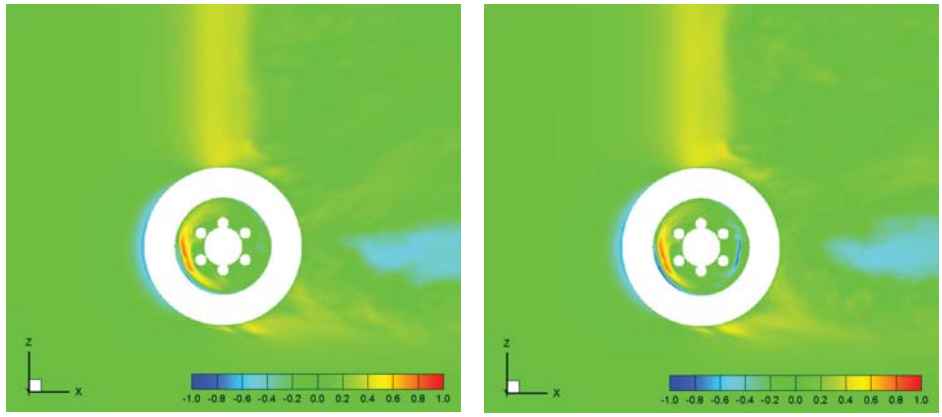

(b) Velocity component in the vertical direction

Figure 18: Computed mean velocity component in the horizontal direction at cross section $y = 0.2$ (left: BACK_TEAR, right: BACK_SEAL).

and NO_TEAR are almost identical, whereas the values of NO_TEAR are slightly lower. Large difference is observed for FRONT_TEAR geometry as the higher value's region is shifted and the values get weaker. The difference is caused by the torque link position to be attached at the front.

4.4. Influence of Torque Link Position. As discussed in the previous section, forward torque link position affects the flow-field and reduces the noise compared to the backward torque link position. Surface sound pressure fluctuations at the axle for BACK_TEAR and FRONT_TEAR are shown in Figure 13. The difference is observed below the axle (toward observation point) and also the junction between the main cylinder and the piston. In addition to these areas, difference of upper wheel region as shown in Figure 12 causes the OASPL difference of the two geometries.

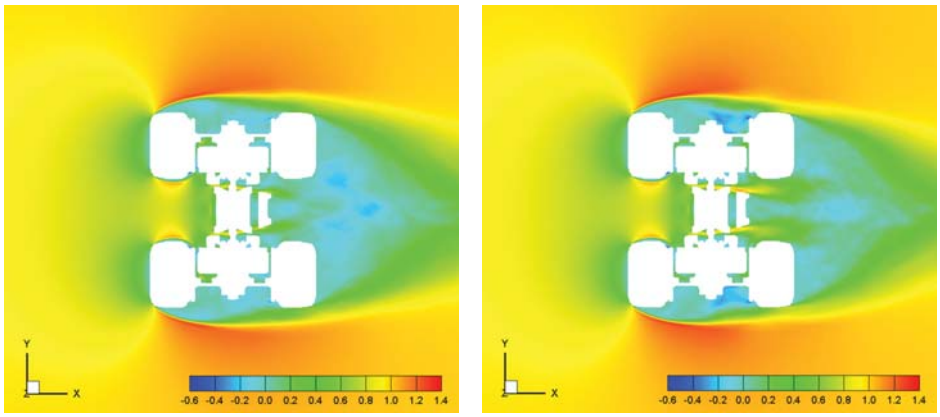

(a) Velocity component in the freestream direction

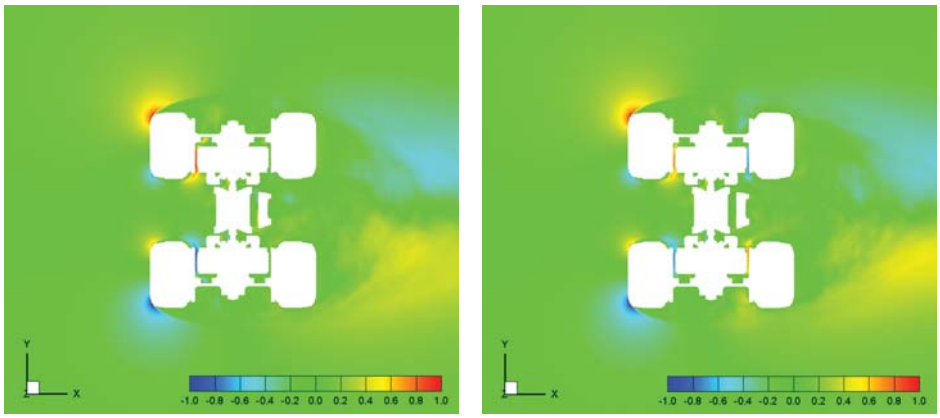

(b) Velocity component in the horizontal direction

Figure 19: Computed mean velocity component at cross section $z = -2.21$ (left: BACK_TEAR, right: BACK_SEAL).

Three LEG configurations with forward/backward and without torque link are used to investigate the effect of torque link position: BACK_TEAR, FRONT_TEAR, NO_TEAR. Figures 14–16 show the mean velocity component of the three configurations at different cross-sections. Time-averaged velocity component at $x = 0.0$ section shows the large velocity difference at the main cylinder and the piston for BACK_TEAR and FRONT_TEAR as shown in Figure 14. The flow at the wheel corner (edge) is accelerated toward the landing gear root in BACK_TEAR, while the acceleration is weaker in FRONT_TEAR. This causes the difference of sound pressure fluctuations in Figure 12, and also the OASPL in Figure 11. Figure 15 shows the difference of the three geometries at $y = 0.0$ due to the existence of the torque link. The change is appeared in front of the strut (separation) and behind the strut (wake region). In BACK_TEAR configuration, the backward torque link causes the flow circulation and the flow turning toward the root of landing gear in the wake. Figure 16 shows that the velocity between the wheel and the piston is accelerated in BACK_TEAR and NO_TEAR configurations. On the other hand, the acceleration in FRONT_TEAR is weaker because the existence of forward-attached torque link prevents the flow toward the freestream direction and also vertical direction (along with the cylinder).

When the torque link is attached forward (against the flow), the flow through the two wheels at axle region is not much accelerated. When the torque link is attached behind the cylinder or the torque link is removed, the flow between the two wheels is greatly accelerated, and this causes the large surface pressure fluctuations and also the noise increase at the observation point.

4.5. Influence of Wheel Cap Geometry. The influence of wheel cap geometry is discussed in this section. The LEG geometry with the sealed wheel (BACK_SEAL) and the LEG geometry with the tear-shaped cooling holes (BACK_TEAR) are used for comparison. Figure 17 shows the mean velocity component in horizontal direction at $x = 0.0$. In BACK_TEAR configuration, the flow is induced from inside the wheel to outside the wheel through cooling holes, whereas no flow goes through the sealed wheel cap in BACK_SEAL configuration. Figures 18 and 19 show the mean velocity components of the two geometries at different cross sections. The difference of the flowfield is relatively small. It is observed that the flow at the front part of axle region goes into the wheel disk space for both configurations as shown in Figures 18(b) and 19(b). The difference is shown at the rear part of axle. The flow from the inside of wheel is induced to the outside of the wheel through the cooling holes in

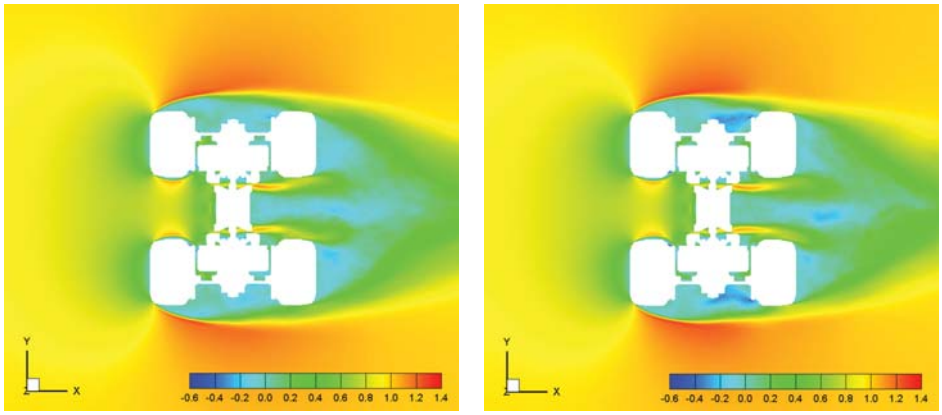

(a) Velocity component in the freestream direction

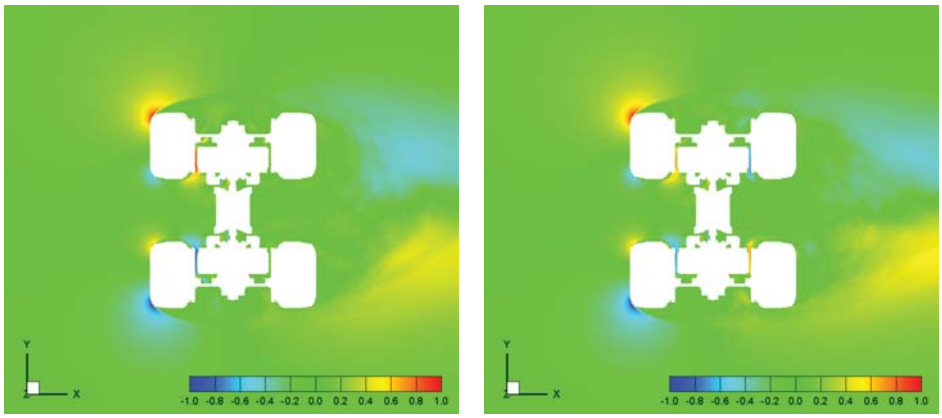

(b) Velocity component in the horizontal direction

Figure 20: Computed mean velocity component at cross section $z = -2.21$ (left: NO_TEAR, right: NO_SEAL).

BACK_TEAR as already described, and thus the flow does not go back to the rear axle area. On the other hand, in BACK_SEAL, the flow similarly goes inside the wheel disk region at front, but the flow goes through the disk space and finally goes back to the rear axle area as shown in Figures 18(b) and 19(b). Because of the sealed cap, the flow only goes through the internal part of the wheel and this causes the slight acceleration of flow in the freestream direction as shown in Figures 18(a) and 19(a). This can be the reason that the BACK_SEAL shows the larger OASPL value compared to BACK_TEAR.

In the geometry without torque link, the OASPL of sealed wheel cap (NO_SEAL) is higher compared to the cap with cooling holes (NO_TEAR). Figure 20 shows the comparison of NO_TEAR and NO_SEAL at $z = -2.21$ section. The internal flow inside the wheel (brake disk region) is similar to the geometry with backward torque link, where the induced flow from inside the wheel to the outside through the holes is observed for NO_TEAR configuration but the flow is returned to the rear axle region for NO_BACK as shown in Figure 20(b). The velocity in the freestream direction is almost identical, though the circulated flow at outside of the wheel is observed at NO_SEAL as no induced flow through the sealed cap exists. In this case, the acceleration of the flow at the axle region is similar to both the geometry, but the level of OASPL is different for the wheel cap type.

The wheel cap affects the local flows of internal wheel part such as brake disk due to the induced flows through the cooling holes; however, the contribution to the noise is quite complex. The far-field noise is determined with the interaction of the induced flow with other components.

5. Conclusion

In this study, aerodynamic/acoustic splitting method based on Cartesian-mesh incompressible flow solver and non-compact form of Curle's equation was proposed to evaluate the far-field noise from a landing gear. The present method was first validated on a circular cylinder case, where the computation with non-compact form of Curle's equation is qualitatively in agreement with the experiment. The approach was then applied to JAXA landing gear model to evaluate the influence of torque link position and wheel cap type. The velocity component in the freestream direction of the configuration with backward torque link and cooling holes cap was reasonably in agreement with experiment and another computation. Due to the introduction of Curle's equation in non-compact form, the computed SPL levels were well matched with the experiment, whereas a large

discrepancy was observed in the past. OASPL values were also compared with the experiment, and the tendency of the OASPL for different geometry was qualitatively captured. The velocity component of the different LEG configuration was compared, and the results showed that the torque link position had a large influence on the flow characteristics at the axle region between the two wheels and in the wake region. The torque link when in forward position prevented the acceleration of flow between the wheels, which reduced the far field noise. When the wheel cap had cooling holes, the flow induced from the inside of the wheel to the outside through the cooling holes was observed. On the other hand, when the wheel cap was sealed, the flow inside the wheel went through the internal component of brake disk space, and finally goes back to the rear part of axle region. The contribution of the wheel cap itself to the far field noise was difficult to assess as there was also interaction of the induced flow with other components. The present approach was proved to be effective in evaluating the effects of tiny detailed components attached to landing gear for the purpose of far-field aerodynamic noise prediction. Because the flows and aerodynamic noises of a landing gear are quite affected by the detail components and their interactions, a detailed model is required in future simulations and evaluations of low noise components and devices.

Nomenclature

BCM: Building-Cube Method
$c_{0:}$ Speed of sound
D: Characteristic length
i, j: Index coordinates
L_{ij}: Lighthill's stress tensor
LEG: JAXA Landing gear Evaluation Geometry model
OASPL: Overall sound pressure level
P: Static pressure on body surface
P_0: Reference sound pressure in air
P_a: Sound pressure fluctuation
P_e: Effective sound pressure
r: Distance to observation point
Re: Reynolds number
S: Surface
SPL: Sound pressure level
SP_{rms}: Sound pressure fluctuation
t: time
$\mathbf{u}$: Velocity vector
x: Coordinates of sound observation point
y: Coordinates of sound source point
V: Volume
ρ: Density.

Acknowledgments

The authors sincerely thank Dr. M. Murayama, Dr. T. Imamura, and Dr. K. Yamamoto at Japan Aerospace Exploration Agency because they provided us the LEG model and experimental data. Computations in this paper were conducted by NEC SX-9 at Cyber Science Center, Tohoku University. This work was supported by JSPS KAKENHI 21226018.

References

[1] A. Keating, P. Dethioux, R. Satti et al., "Computational aeroacoustics validation and analysis of a nose landing gear," in *Proceedings of the 15th AIAA/CEAS Aeroacoustics Conference*, May 2009.

[2] D. P. Lockard, M. M. Choudhari, M. R. Khorrami et al., "Aeroacoustic simulations of tandem cylinders with subcritical spacing," in *Proceedings of the 14th AIAA/CEAS Aeroacoustics Conference*, May 2008.

[3] P. R. Spalart, M. L. Shur, M. K. Strelets, and A. K. Travin, "Reprint of: towards noise prediction for rudimentary landing gear," in *Proceedings of the IUTAM Symposium on Computational Aero-Acoustics for Aircraft Noise Prediction*, vol. 1, pp. 283–292, 2010.

[4] T. Imamura, T. Hirai, K. Amemiya, Y. Yokokawa, S. Enomoto, and K. Yamamoto, "Aerodynamic and aeroacoustic simulations of a two-wheel landing gear," in *Proceedings of the IUTAM Symposium on Computational Aero-Acoustics for Aircraft Noise Prediction*, pp. 293–302, March 2010.

[5] Y. Yokokawa, T. Imamura, H. Ura, H. Kobayashi, H. Uchida, and K. Yamamoto, "Experimental study on noise generation of a two-wheel main landing gear," in *Proceedings of the 16th AIAA/CEAS Aeroacoustics Conference*, June 2010.

[6] Y. Murayama, K. Yokokawa, H. Hiroyuki et al., "Computational and experimental study on noise generation from tire-axle regions of a two-wheel main landing gear experimental study on noise generation of a two-wheel Main landing gear," in *Proceedings of the 17th AIAA/CEAS Aeroacoustics Conference*, 2011.

[7] H. Onda, R. Sakai, D. Sasaki, and K. Nakahashi, "Unsteady flow aerodynamic noise analysis around JAXA landing gear model by building-cube method," in *Proceedings of the 49th AIAA Aerospace Sciences Meeting*, 2011.

[8] K. Nakahashi and L. S. Kim, "Building-cube method for large-scale, high resolution flow computations," in *Proceedings of the 42nd AIAA Aerospace Sciences Meeting and Exhibit*, pp. 676–684, January 2004.

[9] K. Nakahashi, "High-density mesh flow computations with pre-/post-data compressions," 2005.

[10] K. Nakahashi, A. Kitoh, Y. Sakurai, and M. Meinke, "Three-dimensional flow computations around an airfoil by building-cube method," in *Proceedings of the 44th AIAA Aerospace Sciences Meeting*, pp. 13361–13370, January 2006.

[11] S. Takahashi, T. Ishida, K. Nakahashi et al., "Study of high resolution incompressible flow simulation based on cartesian mesh," in *Proceedings of the 47th AIAA Aerospace Sciences Meeting Including the New Horizons Forum and Aerospace Exposition*, January 2009.

[12] S. Takahashi, *Study of large scale simulation for unsteady flows*, Ph.D. dissertation, Department of Aerospace Engineering, Tohoku University, Tokyo, Japan, 2009.

[13] T. Ishida, S. Takahashi, and K. Nakahashi, "Efficient and robust cartesian mesh generation for building-cube method," *Journal of Computational Science and Technology*, vol. 2, no. 4, pp. 435–446, 2008.

[14] N. Curle, "The influence of solid boundaries upon aerodynamics sound," *Proceedings of Royal Society of London, Series A*, vol. 231, pp. 505–514, 1955.

[15] T. Kawamura and K. Kuwahara, "Computation of high reynolds number flow around a circular cylinder with surface roughness," in *Proceedings of AIAA 22nd Aerospace Sciences Meeting*, 1984.

[16] M. J. Lighthill, "On sound generated aerodynamically," *Proceedings of Royal Society of London, Series A*, vol. 211, pp. 564–587, 1952.

[17] C. Kato, Y. Takano, A. Iida, H. Fujita, and M. Ikegawa, "Numerical prediction of aerodynamic sound by Large Eddy simulation (1st Report, Aerodynamic sound radiated from two-dimensional circular cylinder)," *Japan Society of Mechanical Engineers, Series B*, vol. 60, no. 569, pp. 126–132, 1994 (Japanese).

Hindawi Publishing Corporation
Modelling and Simulation in Engineering
Volume 2012, Article ID 973601, 17 pages
doi:10.1155/2012/973601

Research Article

Detailed CFD Modelling of Open Refrigerated Display Cabinets

Pedro Dinis Gaspar,[1] L. C. Carrilho Gonçalves,[1] and R. A. Pitarma[2]

[1] *Electromechanical Engineering Department, University of Beira Interior, Rua Fonte do Lameiro-Edifício 1 das Engenharias, 6201-001 Covilhã, Portugal*
[2] *Mechanical Engineering Department, Polytechnic Institute of Guarda, High School of Technology and Management, Avenida Dr. Francisco Sá Carneiro No. 50, 6300-559 Guarda, Portugal*

Correspondence should be addressed to Pedro Dinis Gaspar, dinis@ubi.pt

Received 8 January 2012; Accepted 3 February 2012

Academic Editor: Guan Heng Yeoh

A comprehensive and detailed computational fluid dynamics (CFDs) modelling of air flow and heat transfer in an open refrigerated display cabinet (ORDC) is performed in this study. The physical-mathematical model considers the flow through the internal ducts, across fans and evaporator, and includes the thermal response of food products. The air humidity effect and thermal radiation heat transfer between surfaces are taken into account. Experimental tests were performed to characterize the phenomena near physical extremities and to validate the numerical predictions of air temperature, relative humidity, and velocity. Numerical and experimental results comparison reveals the predictive capabilities of the computational model for the optimized conception and development of this type of equipments. Numerical predictions are used to propose geometrical and functional parametric studies that improve thermal performance of the ORDC and consequently food safety.

1. Introduction

Nowadays, the energy spent during the commercialization of food products stored at refrigerated temperatures is about 50% of the total consumption of energy of a typical supermarket [1]. The growing of energy consumption in the commercial sector is due to the increasing demand of large quantities of perishable food products in urban areas and to an effective rigorous regulation of the sector as well as quality and food safety requirements of consumers. In past decades, the investments and costs associated with food refrigeration increased with the installation of refrigeration equipment to maintain perishable products in perfect conditions for consumption [2]. This trend continues as the worldwide demand for commercial refrigeration equipment that is projected to rise 5.2% annually through 2014. Beverage equipment demand will post the fastest gains among products. Reach-in and walk-in coolers and freezers are expected to post solid gains due to their widespread use in all of the major markets. Display cabinets will benefit from a growing middle class, which will spur gains in the food and beverage retail segment [3]. A large part of the refrigeration equipments installed in supermarkets, and retail stores are vertical open refrigerated display cabinets (ORDCs). This merchandising solution contributes to the largest part of electrical energy consumption related with refrigeration on these sites [4]. This type of appliance is equipped with a recirculating air curtain that establishes an aerothermodynamics barrier between the conservation space and the environment, without physical restrictions for the consumer. Thus, the product to be acquired can be seen and handled without inconvenience.

The air curtain reduces the infiltration of exterior air at higher dry bulb temperature and specific humidity. The effectiveness of this aerothermodynamics barrier changes with thermal and mass-diffusive effects that affect thermal entrainment. These effects, among others, depend on flow instabilities and boundary effects. These conditions lead to

a decrease in conservation quality of food products and greater energy consumption and costs. In what concerns this topic, it must be highlighted that the ambient air infiltration load is around 67% to 77% of ORDC cooling load as exposed by Gaspar et al. [5]. The thermal entrainment of hot ambient air in empirical recirculating air curtains is due to inbalance of air distribution between discharge air grille (DAG) and perforated backpanel (PBP), and consequently to air curtain temperature, velocity, and thickness values as described by D'Agaro et al. [6] and Gray et al. [7]. Also, refrigerated air leakage from the bottom part of the frontal opening (*cold leg effect*) increases the energy loss to surroundings. Those facts, with the remaining heat gain components [1], lead to an increase of thermal load and consequently higher energy consumption. ASHRAE [8] points out that thermal load reduction is the first step for a better energy efficiency of refrigeration equipments that may be accomplished by air curtain optimization, reducing the thermal entrainment with ambient air, as well as the temperature of air returned to the evaporator. Therefore, most of research in this field, both experimental and numerical, to evaluate the thermal performance of ORDC focus on air curtain. Due to similarity, the research on nonrecirculating air curtains is helpful. It is mainly related with heat and mass transfer studies, considering the impinging jet of several angles, different initial velocities, temperatures and thicknesses, and generation/suppression of turbulence inside air stream [9–14]. Although, due to specific characteristics of air curtains installed in ORDC, researchers carried out two- (2D) and three- (3D) dimensional computational fluid dynamics (CFD) parametric studies. Cortella et al. [15] and Navaz et al. [16] evaluated the influence of DAG velocity in thermal performance, quantifying the air infiltration through the frontal opening. Axell and Fahlén [17] developed a CFD-parametric study to evaluate the influence of air curtain height/width ratio and inlet velocity on the thermal performance. Navaz et al. [18] evaluated the optimum operating condition based on entrained air amount, taking into account the jet width and velocity and inlet turbulence intensity. Foster et al. [19] developed 3D CFD models to analyse the effect of changing size and position of the evaporator coil, width and angle of DAG, and inserting baffle plates into the upper duct. D'Agaro et al. [6] carried out 2D and 3D CFD-parametric studies to evaluate the influence of: longitudinal ambient air movement; display cabinet length, and air curtain temperature on the extremity effects and how it reflects on ORDC performance. Chen [20] developed CFD-parametric studies to evaluate the thermal barrier performance of air curtains, adjusting the length/width ratio and its discharge angle, the height/depth ratio of the cavity, and the dimension and position of shelves. Ge and Tassou [21] developed correlations for heat transfer across air curtain with reasonable agreement with experimental data in steady-state conditions. Ge et al. [22] developed an ORDC model integrating CFD and cooling coil models. The airside inputs of the cooling coil model are the outputs of the CFD model, and, inversely, the airside outputs from the cooling coil model are used to update the boundary conditions of the CFD model. The use of the validated integration model of the ORDC allows several analyses such as the optimal designs of the geometrical structures of ORDC, curtains and coils, and further of alternative control strategies and operating states. However, this type of simulation is computationally expensive.

Other research works were just experimental, such as the study developed by Chen and Yuan [23] to evaluate the influence of ambient air temperature and relative humidity, indoor airflow, DAG velocity, PBP airflow, and night-covers application, on the performance of an ORDC. Gray et al. [7] also conducted an experimental study to evaluate the effect of perforation pattern of PBP on the airflow distribution. Among the experimental techniques used by researchers are thermocouple thermometry, hot-wire/film anemometry, laser Doppler anemometry, digital particle image velocimetry, hygrometry, tracer gases, and infrared thermography. Other method that can be used to evaluate the thermal performance of an ORDC, based on the thermal barrier provided by the air curtain, consists in the thermal entrainment factor (TEF) calculation [6, 18, 23, 24]. This formulation was adopted by Gaspar et al. [5] to evaluate air curtain TEF for different environmental conditions (air temperature, relative humidity and velocity, magnitude, and direction) and how it influences the thermal performance of the ORDC.

The experimental techniques described above are reliable and provide results with a high degree of confidence, but its use is labour intensive and time consuming, involving high costs, being the results dependent on ORDC geometry, DAG parameters, and ambient air conditions. By other hand, the development of a complex simulation model requires large computational resources, being the computational results untrustworthy, until reliability and accuracy are checked by comparison with experimental data. Although the significant progress of CFD codes in geometry creation, data transfer from CAD/CAE packages, improvement of meshing tools, numerical robustness, and well-validated physical models for specific classes of physical phenomena, made them desirable in the design phase as an expedite analysis method. However, none of CFD research works cited above has modelled the several devices that make part of the refrigeration system. Hence, this study provides a detailed CFD model that combines the characteristics of aforementioned works. It considers a 2D CFD simulation of an ORDC taking into account the air flow through internal ducts, across fans, evaporator and grilles, and the thermal response of food products. The objective is to provide a complete CFD design tool for this type of equipment, allowing fast and efficient development of parametric studies devoted to predict how operational and geometrical modifications can improve the ORDC performance. This paper presents some results derived from experimental testing to define boundary conditions and to validate numerical predictions, the physical-mathematical and numerical model formulations, the CFD-modelling parameters and methodology for complete simulation of the air flow and heat transfer of an ORDC. The nonisothermal turbulent flow and temperature field characteristics are predicted, and several parametric studies to improve the ORDC performance are designed.

2. Experimental Testing

2.1. Experimental Apparatus. Figure 1(a) shows the midplane cross-section of the open refrigerated display cabinet (ORDC) experimentally tested and numerically modelled on heat and mass transfers. The air is drawn by fans located in front of the evaporator. The air passing through the evaporator is cooled below the conservation temperature of the perishable products exposed in equipment's shelves. This air is convected to the rear duct, where part of it is discharged inside the conservation space at low velocity through the perforated backpanel (PBP). The other part of this air mass flow rate will supply the air curtain, which develops vertically between discharge (DAG) and return (RAG) air grilles.

The authors have already performed extensive experimentation on this ORDC model [5]. It is a self-contained system, in which the condensing unit and controls are built into the cabinet structure (beneath the cabinet, taking up the entire lower part). Its dimensions are $1900 \times 796 \times 1911$ mm ($L \times W \times H$). It has four shelves and a well tray, being its frontal opening height, H_c, 1209 mm (see Figure 1(a)). The evaporator is housed under the well tray and integrated with refrigerant feed and return lines. Temperature regulation and defrosting are digitally conducted by an electronic thermostat, being the cooling system fan-assisted (four forward fans that blow air through the coil).

The experimental test was performed in a climate chamber Aralab Fitoclima 650000 EDTU. The test probes described in Table 1 and placed inside the cabinet as shown in Figure 1(b) (conservation space measuring locations (CSMLs)) and Figure 1(c) (air curtain measuring locations (ACMLs)) were connected to a data acquisition system Intab PC-Logger 3100. A probe-positioning system is used to evaluate the 3D effects of thermal entrainment on air curtain and properties variations along length and height of the conservation space [25]. The probe-positioning system was settled on each shelf of the equipment to measure air temperature, relative humidity, and velocity for three positions across the air curtain width and eight vertical cross-sections along the equipment's length. The positioning system moved the test probes in 240 mm increments for the 1800 mm length of shelves, taking 1 min to move between positions to reduce flow perturbation. Also, the properties values were acquired 1 min after reaching each position to ensure flow stabilization. The experimental results obtained with this point measuring technique along the air curtain and conservation space coordinates show a similar behaviour to the experimental results obtained by Gray et al. [7], Chen and Yuan [23], and Evans et al. [26]. It was found that the average variation of air temperature was 0.4 K, and of air-relative humidity was 4.5% which are not particularly significant. Based in these results, the probes were distributed in the midplane of the equipment's length. In order to consolidate and extend the measurements data, a thermoanemometer AM 4003 was used to measure air temperature and velocity near DAG and RAG, at the refrigeration unit (compressor + condenser) and at several heights of PBP. Pressure loss was measured using a micromanometer Air Instruments Resources MP3KDS near inlets and outlets (DAG, RAG, and PBP). The temperature of internal surfaces was obtained with K-type thermocouple contact probe using a digital thermometer FLUKE 51 (location n.°9). Additionally, several sets of experimental tests were performed to evaluate the influence of surrounding air in air temperature, velocity, and humidity inside the conservation space [5].

2.2. Testing Procedure and Results. The experimental testing follows the procedure defined by EN-ISO Standard 23953 [27] for test room climate class n.°3, which considers air temperature ($T_{amb} = 298$ K; air relative humidity, $\phi_{amb} = 60\%$; air velocity magnitude, $v_{amb} = 0.2\ m\ s^{-1}$, with direction parallel to the frontal opening plane of the ORDC, that is, $\theta_{amb} = 0°$) and for M-package temperature class M1 ($272.15\ K \leq T_{prod} \leq 278.15\ K$). The experimental test followed the procedure described in Gaspar et al. [5]. Table 2 contains the average values of the parameters measured during this period and their statistical parameters: maximum and minimum values, standard deviation (σ), standard error of mean (s), and variance (σ^2). Notice that overall values of air temperature and relative humidity inside conservation space (probes location n.°0 to n.°4) consider the average values along equipment's length and height.

3. Mathematical Formulation

The turbulent air flow and nonisothermal heat transfer process are modelled by a 2D (length midplane neglecting extremity effects) steady-state mathematical model. The basic equations governing transport phenomena in an ORDC are continuity, momentum, and energy [28]. For application on the computational domain, the airflow modelling is coupled to products modelling, where within the latter region the convection term is neglected.

The air is considered as an ideal gas. Considering that flow can be driven by buoyancy forces in specific zones of the domain, the Boussinesq approximation is applied. Thus, density has a constant value in all solved equations, except for the buoyancy term in the momentum equation where it is determined as function of temperature differences. So, reference density is set to $\rho_{ref} = 1.17\ kg\ m^{-3}$ for the operating conditions defined by test room climate class n.°3 [27].

The energy equation is developed as function of temperature in steady state with constant specific heat. Further simplifications are accomplished neglecting viscous dissipation due to flow characteristics.

The turbulence is modelled by the RNG k-ε model [29] since in previous works [30–33] its ability to model turbulence was assessed in comparison with other models (Spalart-Allmaras, k-Ω, standard k-ε). The comparison of numerical results shows the applicability of k-ε models type for simulation of a wide range of flows with minimum coefficients adjustment and also for its relatively simple formulation. The numerical predictions obtained with standard and RNG k-ε models were similar. The latter model was used due to its constants revaluation and additional term in dissipation rate equation, to improve the precision of flow simulation.

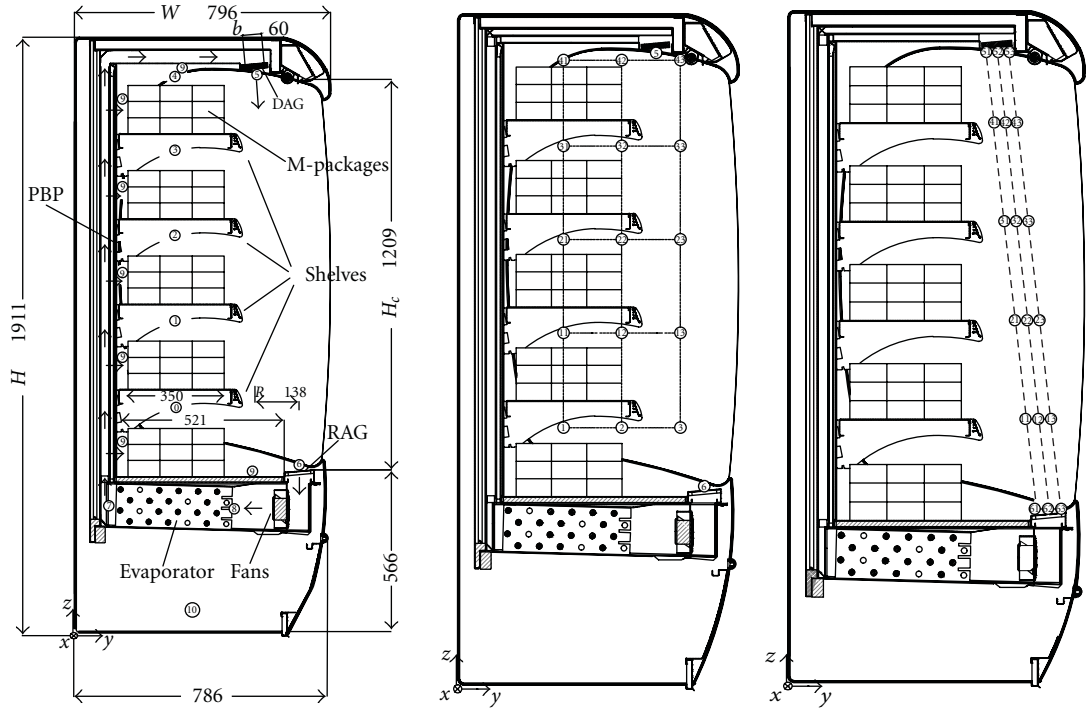

(a) Display cabinet configuration and dimensions

(b) Conservation space measuring locations (CSML)

(c) Air curtain measuring locations (ACML)

Figure 1: Configuration of open vertical refrigerated display cabinet and measuring probes locations.

Table 1: Description of test probes and its location (see Figure 1(a)).

Loc.	Type	Accuracy	Property	Ref.	Location
0–4	K-type thermocouple	±0.5 K	Temperature	T_{cons}	Conservation space
	Hygrometer (odd measuring locations)	±3%	Relative humidity	ϕ_{cons}	
5	K-type thermocouple	±0.5 K	Temperature	T_{DAG}	DAG
	Hot-wire anemometer	±0.1 m s^{-1} (±10%)	Velocity	v_{DAG}	
	Hygrometer	±3%	Relative humidity	ϕ_{DAG}	
6	K-type thermocouple	±0.5 K	Temperature	T_{RAG}	RAG
	Hot-wire anemometer	±0.1 m s^{-1} (±10%)	Velocity	v_{RAG}	
	Hygrometer	±3%	Relative humidity	ϕ_{RAG}	
7	K-type thermocouple	±0.5 K	Temperature	$T_{evap,out}$	Evaporator outlet*
8	K-type thermocouple (contact)	±0.5 K	Temp. (surface)	$T_{evap,in}$	Evaporator inlet*
9	K-type thermocouple (contact)	±0.5 K	Temp. (surface)	T_{surf}	Interior surfaces
10	Ammeter (Clamp-on)	±0.02 A (±2%)	Electric current	I	Power source

*The surface temperature of the air side-wall pipe is measured at the evaporator inlet while at the outlet is measured the air temperature.

The set of model equations is suitable for fully turbulent flow. To account for viscous effects and high gradients in proximity of walls, the turbulence model equations are used in conjunction with empirical wall functions. The complete description and implementation details of wall functions in turbulence models can be found in Rodi [34] and Launder and Spalding [35].

The influence of ambient air-relative humidity is considered by making use of a species transport model. The fluid is considered as a mixture of dry bulb air and water

Table 2: Experimental average results for climatic class n.°3-EN-ISO std. 23953.

Parameter	T_{cons}	ϕ_{cons}	T_{DAG}	ϕ_{DAG}	v_{DAG}	T_{RAG}	ϕ_{RAG}	v_{RAG}	$T_{evap_{out}}$	$T_{evap_{in}}$	I
Unit	K	%	K	%	m s^{-1}	K	%	m s^{-1}	K	K	A
Mean value	277.1	86.2	276.0	82.4	1.5	282.4	88.1	1.7	272.1	272.3	8.7
σ	0.5	1.9	1.1	4.8	3.0×10^{-2}	0.6	2.2	9.0×10^{-2}	1.1	2.4	2.9
σ^2	0.3	3.8	1.1	23.1	0.6×10^{-3}	0.4	4.9	7.2×10^{-3}	1.3	5.9	8.1
s	3.0×10^{-2}	7.0×10^{-2}	6.0×10^{-2}	4.0×10^{-2}	1.4×10^{-3}	4.0×10^{-2}	1.0×10^{-2}	4.8×10^{-3}	6.0×10^{-2}	1.0×10^{-2}	2.0×10^{-2}
Min. value	275.8	82.5	274.8	68.6	1.1	280.7	82.9	1.1	270.0	270.3	0.3
Max. value	278.2	98.4	287.3	99.5	1.6	284.6	92.7	1.9	276.4	289.0	8.9

vapour. The heat gain of ORDC by thermal radiation is one of most important cooling load components [5]. A surface-to-surface radiation model (based in surfaces view factors calculation) is used to take this heat gain component into account.

4. Numerical Model

The mathematical model is a set of coupled nonlinear partial differential equations, describing mass, momentum, and energy conservation which can be simultaneously and interactively solved. The equations set was solved using the pressure-based, nonstructured grid, finite volume method CFD code FLUENT.

4.1. Geometry and Computational Mesh. The 2D geometry closely follows a mid-cross-section of ORDC. An automatic orthogonal unstructured mesh generator (Gambit) was used to develop the computational grid. The mesh was refined in the internal ducts, near fans, evaporator, DAG, and RAG vicinities and across air curtain, where velocity and temperature gradients are expected to be higher. The grid size was refined to predict accurately heat transfer by conduction inside the conservation products. Grid dependence tests were carried out for models with different grid size, that is, increasing number of control volumes (cells): (a) 17 939 cells, (b) 72 350 cells, (c) 110 029 cells, and (d) 350 533 cells. From the comparison with experimental results, the computational mesh of model (c) provides numerical results independent of grid size both in solid and fluid regions. The computational domain, grid, and boundary conditions location are shown in Figure 2. Notice that connected but independent mesh zones were defined near DAG, RAG, fans, evaporator, and internal ducts in order to speed up the process of developing future parametric studies of geometrical and/or functional modifications and the analysis of their influence on the ORDC overall performance.

4.2. Discretization of the Partial Differential Equations. The computational procedure is based on a numerical iterative process using the *pressure-implicit with splitting of operators* (PISOs) algorithm [36] for pressure-velocity coupling. This algorithm was derived from *semi-implicit method for pressure-linked equations* (SIMPLEs) algorithm [37], but it has higher performance, and it is more efficient as described by Jang et al. [38].

The equations were discretized in the control volume form using MUSCL differencing scheme. The *monotone upstream-centered schemes for conservation laws* (MUSCLs) scheme proposed by Van Leer [39], derives from *central differencing scheme* (CDS) and *second-order upwind* (SOU) *differencing scheme*) as described by Patankar [37]. It is a differencing scheme with low numerical diffusion; that is, it shows higher spatial precision for all types of computational grids and for complex flows. In this study, the comparison with experimental results shows that numerical predictions computed with MUSCL scheme are more realistic and precise. The models run on a server Intel Xeon DualCore 2.33 GHz (4 MBytes internal cache) with 16 GBytes RAM.

4.3. Boundary Conditions. Boundary conditions (BCs) of common practice in numerical simulations, defined for climatic class n.°3 of EN-ISO Standard 23953 [27], are imposed in the computational domain.

4.3.1. Ambient Boundary Condition. The ambient boundary is simulated by an "opening" type BC, that is, a constant pressure boundary which allows both inflow and outflow. The pressure value is considered to be the total pressure based on the normal component of the velocity when flow enters the domain and static pressure when it leaves the domain. The ambient air temperature is supposed to be $T_{amb} = 298.15$ K, and the water vapour mass fraction for $\phi_{amb} = 60\%$ is $Y_{v,\,amb} = 11.80$ g$_v$ kg$_m^{-1}$. The radiative black body temperature is assumed to be $T_{bb} = 298.15$ K for the algebraic calculation of radiative view factors as described by Modest [40]. A black body emissivity value ($\varepsilon = 1$) is assumed in this BC.

Free stream values for turbulent kinetic energy and its dissipation rate are assumed on the free boundary at this fixed-pressure condition set in terms of turbulence intensity, $I_t = 10\%$, (the worst situation considers the effects of consumers passage in front of equipment, of air-conditioning system operation and the influence of pressure perturbations) and hydraulic diameter of equipment's frontal opening to ambient, $D_h = 1.2$ m, as being the characteristic turbulence length scale. The values of parameters specified at fixed pressure BC are shown in Table 3.

The influence of the distance at which this free boundary is defined is not consensual as it affects the predicted

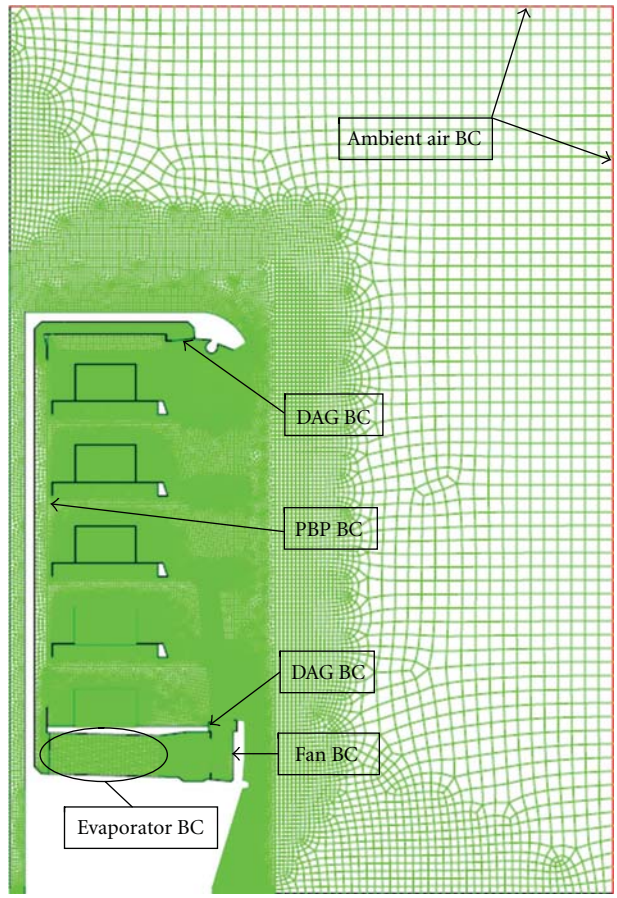

Figure 2: Computational model geometry and grid, and boundary conditions location.

solutions. The numerical studies of ORDC developed by Cortella et al. [15], and George and Buttsworth [41] consider this BC at 2/3 and 5/4, respectively, of the equipment width. Bhattacharjee and Loth [9] stated that this BC should be imposed far away from zone of interest in the computational domain, likewise at a distance of $40b$, being b the air curtain width. Gaspar et al. [42] tested different distances of this free BC to ascertain the effect on the numerical predictions of temperature and velocity within an ORDC. The following cases were tested: (1) $1/3W$; (2) $2/3W$; (3) W; and (4) $3/2W$, being W the width of the ORDC. Based on comparison between numerical predictions and experimental values, the precision of numerical results increases with the distance at which is defined the BC. Thus, the fixed pressure BC was defined at a distance equal to $3/2W$ from the frontal opening of the equipment since it allows modelling the flow with heat and mass transfers more precisely.

4.3.2. Wall Boundary Condition

(1) Shear Boundary Condition. Wall boundary conditions are used to bound fluid and solid regions. At the walls a nonslip BC (zero velocity) is considered.

Table 3: Values imposed at the fixed pressure boundary condition.

Parameter	Variable	Unit	Value
Relative pressure	p	Pa	0.00
Temperature	T_{amb}	K	298.15
Turbulence intensity	I_t	%	10.00
Hydraulic diameter	D_h	m	1.20
Black body temperature	T_{bb}	K	298.15
Emissivity	ε	—	1.00
Water vapour mass fraction	Y_v	$g_v\ kg_m^{-1}$	11.80

(2) Thermal Boundary Conditions

Heat Flux Boundary Conditions. An adiabatic BC is defined for walls not considered in heat transfer calculation. However, a heat flux BC is used to simulate heat generated by the illumination (85% for fluorescent lamp *OSRAM L58W/20*) and heat flux through conduction across material layers that compose the equipment walls. The heat flux across them is determined by Fourier Law using a global heat transfer coefficient determined by the conductive thermal resistances of each wall material. The experimental values of surface temperature on the internal and external sides of the

Table 4: Walls heat flux boundary condition.

Surfaces	Variable	Unit	Value
Illumination (*OSRAM L58W/20*)	$\dot{q}_{\text{ilum}}$	W m^{-2}	10.00
Interior surfaces of the equipment			
Top	$\dot{q}_{\text{duct, top}}$	W m^{-2}	6.08
Rear	$\dot{q}_{\text{duct, rear}}$	W m^{-2}	7.63
Bottom (well tray)	$\dot{q}_{\text{duct, bottom}}$	W m^{-2}	6.96

Table 5: Tylose (equivalent solid food products) thermal characteristics.

Parameters	Variable	Unit	Value
Density	ρ	kg m^{-3}	1.11×10^3
Specific heat ($T > T_{\text{cong}}$)	C_{p1}	$\text{kJ kg}^{-1}\,\text{K}^{-1}$	3.70
Thermal conductivity (279.15 K)	k	$\text{W m}^{-1}\,\text{K}^{-1}$	0.39

equipment are used. Table 4 shows the heat flux values fixed as BC.

Species Boundary Conditions. A zero-gradient condition for water vapour mass fraction is assumed at walls.

Radiation Boundary Conditions. It is necessary to specify the emissivities of different surfaces to use a surface-to-surface radiation model. Constant emissivities are fixed for the internal surfaces of the equipment $\varepsilon_{\text{sup}} = 0.9$ and for external ground, $\varepsilon_{\text{ground}} = 0.7$. It is considered the black body emissivity, $\varepsilon_{\text{bb}} = 1$, for the external enclosure surfaces.

4.3.3. Product Load (Solid Region). Following EN-ISO Standard 23953 [27] and ISO 15502 [43], the products simulators are made of tylose, in which thermal characteristics are similar to meat. Considering values given by ASHRAE [44], the equivalent solid thermal characteristics to simulate food products are shown in Table 5.

4.3.4. Air Pressure Drop through the PBP: Porous Medium. The detailed flow simulation across perforation of the back-panel requires a very high grid refinement and consequently a huge computational effort. Thus, PBP was modelled as a porous medium to simplify the numerical model. The thickness of PBP is 1.6 mm. The porous medium is composed by 520 grid cells (4 grid cells along thickness and 130 grid cells along height): $\Delta y = 0.4$ mm and $\Delta z = 20$ mm. The porous medium is modelled by the addition of a momentum source term corresponding to Forchheimer law to the standard fluid flow equations [45]. The source term is composed of two components: a viscous loss term (Darcy's law, the first term on the right-hand side of (1)), and an inertial loss term (the second term on the right-hand side of (1)) due to high flow velocities [45] and low thickness to hole diameter ratio [46]. We have

$$S_i = -\left(\frac{\mu}{k} v_i\right) - \left(C_2 \frac{1}{2} \rho |v_i| v_i\right). \tag{1}$$

Table 6: PBP parameters: porous medium.

Parameters	Variable/Expression	Unit	Value
Porosity	$\varepsilon = V_v / V_t$	—	2.60×10^{-2}
Permeability	$k = \varepsilon D_{\text{hole}}^2 / 12$	m^2	4.91×10^{-8}
Viscous resistance coefficient	k_x^{-1}	m^{-2}	2.56×10^7
Loss coefficient	K [49]	—	8.65
Inertial resistance coefficient	$C_2 = (K/\delta)(1/\varepsilon)^2$	m^{-1}	8.00×10^6

In (1), v is the average value of fluid velocity through the surface normal to flow, k is the medium permeability, and C_2 is the inertial resistance factor. The permeability of perforated surfaces is defined by Bear [45] and Tang et al. [47], in which the thickness of the porous medium, δ, has an analogical correspondence to the perforation diameter, D_{hole} as described in (2). We have

$$k = \frac{\varepsilon \delta^2}{12}, \tag{2}$$

where ε is the porosity (*void* fraction), that is, the volume fraction of fluid within the porous region (i.e., the open volume fraction of the medium) given by the ratio between the open volume and total volume of porous medium (see (3)). One finds that

$$\varepsilon = \frac{V_v}{V_t} = 1 - \frac{V_s}{V_t}. \tag{3}$$

The constant value parameter C_2 provides a correction for inertial losses in porous medium. This constant can be viewed as a loss coefficient per unit length along flow direction, thereby allowing the pressure drop to be specified as a function of dynamic head (see (4)). As this factor is specified for fully open porous cells, the loss coefficient, K, must be converted into dynamic head loss, considering the same flow rate per unit length of porous region [48, 49]. So we have

$$C_2 = \frac{K}{\delta}\left(\frac{v_p}{v_0}\right)^2 = \frac{K}{\delta}\left(\frac{1}{\varepsilon}\right)^2, \tag{4}$$

where v_0 and v_p are respectively the fluid velocities of the fully open porous medium and of flow passage through the porous medium. The loss coefficient is calculated as proposed by Idel'Cik [50]. The values imposed at PBP are shown in Table 6.

4.3.5. Air Pressure Drop through DAG and RAG: Porous Medium Model Simplification. The air pressure drop is experimentally measured at DAG and RAG. Equation (5) represents a one-dimensional simplification of the porous media model defined at the faces that simulate these grilles. The thin porous medium has a finite thickness, δ, over which the pressure change is defined as a combination of Darcy's Law and Forchheimer inertial loss term. We obtain that

$$\Delta p = -\left(\frac{\mu}{k} v + C_2 \frac{1}{2} \rho v^2\right) \delta. \tag{5}$$

The fixed parameters on these BC based in geometrical characteristics of grilles and experimental measures of air temperature and relative humidity are shown in Table 7.

4.3.6. Heat and Mass Transfer and Pressure Drop Modelling across the Evaporator. The ORDC contains a wavy fin and tube heat exchanger (evaporator). At the evaporator, it is specified a heat exchanger BC type in which are defined both pressure drop and heat transfer coefficient as functions of velocity in direction normal to the heat exchanger. The BC is specified at an infinitely thin face, and the pressure drop through the heat exchanger is assumed to be proportional to the dynamic head of the fluid. The friction factor, $f = 0.0078$, is calculated through the empirical correlation (6) proposed by Wang et al. [51]. We have

$$\begin{aligned} f &= 0.05273\ \mathrm{Re}_{Dc}^{f1}\left(\frac{P_d}{X_f}\right)^{f2}\left(\frac{F_p}{P_t}\right)^{f3} \\ &\quad\times\left[\ln\left(\frac{A_0}{A_t}\right)\right]^{-2.726}\left(\frac{D_h}{D_c}\right)^{0.1325} {N_{tl}}^{0.02305}, \\ f1 &= 0.1714 - 0.07372\left(\frac{F_p}{P_l}\right)^{0.25}\ln\left(\frac{A_0}{A_t}\right)\left(\frac{P_d}{X_f}\right)^{-0.2}, \\ f2 &= 0.426\left(\frac{F_p}{P_t}\right)^{0.3}\ln\left(\frac{A_0}{A_t}\right), \\ f3 &= \frac{-10.2192}{\ln(\mathrm{Re}_{Dc})}. \end{aligned} \tag{6}$$

The pressure drop, $\Delta p = 8.33\,\mathrm{Pa}$, is calculated by (7) proposed by Kays and London [52], being contraction, K_c, and expansion, K_e, loss coefficients given by McQuiston and Parker [53]. We have

$$\begin{aligned} \Delta p = \frac{G^2}{2\rho_{\mathrm{in}}}\Bigg[& f\frac{A_0}{A_c}\left(\frac{\rho_{\mathrm{in}}}{\rho_m}\right) + (K_c + 1 - \sigma^2) \\ & + 2\left(\frac{\rho_{\mathrm{in}}}{\rho_{\mathrm{out}}} - 1\right) - (1 - \sigma^2 - K_e)\frac{\rho_{\mathrm{in}}}{\rho_{\mathrm{out}}}\Bigg]. \end{aligned} \tag{7}$$

The heat transfer modelling through a heat exchanger BC type in the CFD code requires the specification of overall heat transfer coefficient, U, and refrigerant (R404A) temperature, $T_{\mathrm{refrig,in}}$, at the main entrance of evaporator. The variation of refrigerant temperature across evaporator (with phase change process) is reduced [54], so its value can be considered constant. It is assumed no superheating of refrigerant, and all heat transfer is on the two-phase zone at constant temperature. The value determined for the overall heat transfer coefficient, $U = 124.16\,\mathrm{W\,m^{-2}\,K^{-1}}$, is referred to the air temperature downstream of heat exchanger, $T_{a,\mathrm{out}}$. Based in the equation of energy conservation and considering the experimental values of air properties upstream and downstream the heat exchanger, the value of refrigerant temperature at heat exchanger entrance, $T_{\mathrm{refrig,in}} = 271.05\,\mathrm{K}$, is determined by a trial and error-iterative procedure. These parameter values are based in the heat balance of the evaporator, determined with the average experimental values.

The heat flux from heat exchanger to surrounding fluid, $\dot{q}_{\mathrm{evap}} = 124.31\,\mathrm{W\,m^{-2}}$, is determined by (8). Taking into account the total surface area of the evaporator, A_0, this value is consistent with the ORDC's cooling load determined by Gaspar et al. [5]. We have

$$\dot{q}_{\mathrm{evap}} = \frac{\dot{m}\,C_p}{A_0}\left(T_{a,\mathrm{in}} - T_{a,\mathrm{out}}\right) = U\left(T_{a,\mathrm{out}} - T_{\mathrm{refrig,in}}\right). \tag{8}$$

However, since the evaporator is modelled as an infinitely thin BC, it is necessary to obtain the equivalent heat flux based on surface areas ratio given by (9). We obtain that

$$\dot{q}_{\mathrm{eq}} = \frac{A_0}{A_{\mathrm{eq}}}\dot{q}_{\mathrm{evap}} = 9414\,\mathrm{W\,m^{-2}}. \tag{9}$$

The determined equivalent overall heat transfer coefficient, $U_{\mathrm{eq}} = 910.42\,\mathrm{W\,m^{-2}\,K^{-1}}$, is assumed to be similar to a convective heat transfer coefficient. This simplification was based on the evaluation of empirical correlations for Colburn factor and friction factor available for heat exchangers with corrugated fins.

The mass transfer modelling through a heat exchanger BC type consists in the specification of a Dirichlet BC for water vapour mass fraction, considering the air dehumidification process. By psychometric analysis, the water vapour mass fraction specified at evaporator exit is $Y_v = 3.3722\,\mathrm{g_v\,kg_m^{-1}}$.

4.3.7. Fan Boundary Condition Modelling the Pressure Rise across the Fan. A discontinuous pressure rise across fans (infinitely thin face) is specified as a function of air velocity. The empirical characteristic curve which governs the relationship between head (pressure rise) and flow rate (velocity) across a fan element (obtained at the manufacturer: EBM Papst series 4500) is converted into a 4th-order polynomial relationship (10) and specified as BC. We obtain that

$$\Delta p = -1.61v^4 - 2.67v^3 + 22.7v^2 - 51.1v + 79.2. \tag{10}$$

4.4. Solution Monitoring and Control Techniques. The linear relaxation method is used to reduce high variation of dependent variables during the iterative process of calculation. Linear relaxation values ranged from 0.3 for pressure to 0.8 for momentum. The convergence monitoring was done by the sum analysis of absolute residuals of mean field variables. The iterative procedure run until a prescribed convergence criterion for absolute residuals ($\lambda \leq 12 \times 10^{-4}$) is met.

5. Results and Discussion

The CFD modelling of air flow and thermal patterns inside the conservation space of a vertical ORDC has an operation temperature varying from 273.15 K to 278.15 K. This type of equipment design still requires studies due to the major influence of the frontal ambient opening on the heat and mass transfers.

The numerical simulations allow the evaluation of air temperature, relative humidity, and velocity distributions within the equipment in order to propose possible paths for technical evolution. Only most significant results concerning

Table 7: DAG and RAG porous medium parameters.

Grille	Parameters	Variable/expression	Unit	Value
RAG	Pressure loss	Δp (experimental value)	Pa	2.30
	Porosity	$\varepsilon = V_v/V_t$	—	0.51
	Permeability	$k = \varepsilon D_h^2/12$	m^2	4.24×10^{-6}
	Loss coefficient	$K = 2\Delta p/\rho v^2$	—	1.33
	Inertial resist. coef.	$C_2 = (K/\delta)(1/\varepsilon)^2$	m^{-1}	5.34×10^3
DAG	Pressure loss	Δp (experimental value)	Pa	0.30
	Porosity	$\varepsilon = V_v/V_t$	—	0.72
	Permeability	$k = \varepsilon D_h^2/32 = \varepsilon \cdot (4 \cdot (3\sqrt{3}\, D_{\text{comb}}^2/8)/6r)^2/32$	m^2	2.76×10^{-7}
	Loss coefficient	[50]	—	2.67
	Inertial resist. coef.	$C_2 = (K/\delta)(1/\varepsilon)^2$	m^{-1}	2.15×10^2

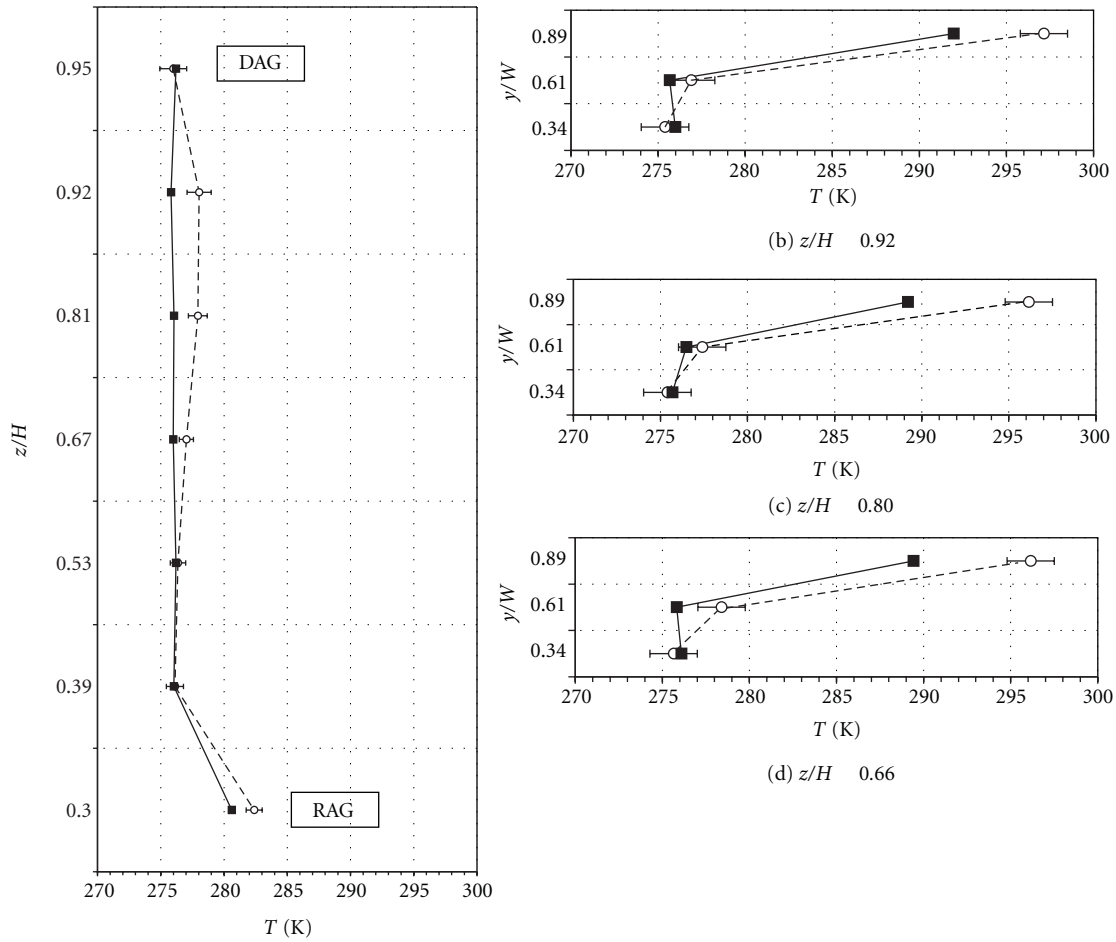

(a) y/W 0.38 (exception for $(y/W)_{\text{DAG}}$ 0.72 and $(y/W)_{\text{RAG}}$ 0.88)

(b) z/H 0.92

(c) z/H 0.80

(d) z/H 0.66

Figure 3: Comparative profiles of air temperature, T (y/W, z/H) (K) (see CSML in Figure 1(b)). (Legend: numerical: ■; experimental: ○).

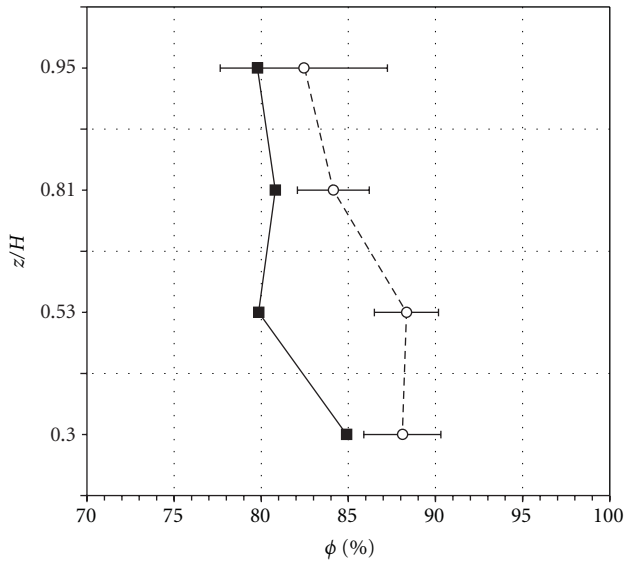

Figure 4: Comparative profiles of air-relative humidity, ϕ (y/W = 0.38, z/H) [%] (see CSML in Figure 1(b)). (Legend: numerical: ■; experimental: ◯).

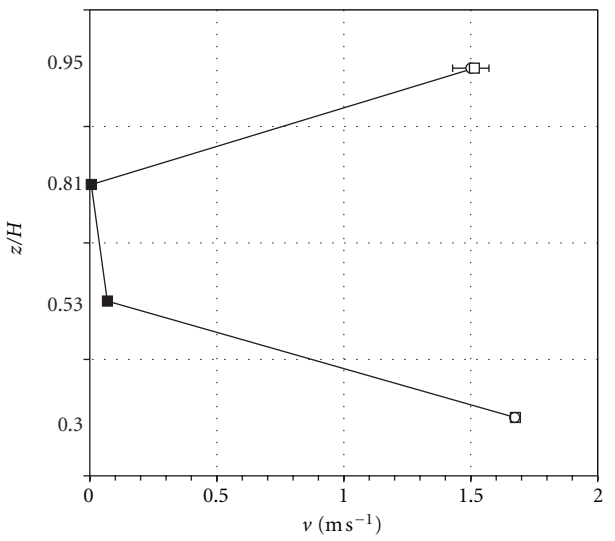

Figure 5: Comparative profiles of the air velocity, v (y/W = 0.38, z/H) ($\mathrm{m\,s^{-1}}$) (see CSML in Figure 1(b)). (Legend: numerical: ■; experimental: ◯).

flow properties and thermal behaviour are discussed here. The numerical predictions solution required approximately 4 h 30 m performing 10 000 iteration sweeps.

5.1. Comparison with Experimental Data. The validation of numerical predictions of the 2D ORDC model is accomplished by its comparison with experimental measurements data.

Figures 3, 4, and 5 show the comparative profiles, for different planes, of the experimental average values of air temperature, relative humidity, and velocity. The predicted steady-state air flow and heat transfer inside the ORDC both present a reasonable quantitative agreement. The experimental average points are represented by ◯, and numerical predictions points are represented by ■. For the validation points set (90 validation points), the minimum absolute deviations from experimental measures for air temperature, relative humidity, and velocity were respectively: e_T ($y/W = 0.34$, $z/H = 0.39$) = 0.08 K (conservation zone at 3rd shelf height), e_ϕ ($y/W = 0.52$, $z/H = 0.88$) = 0.26% (conservation at 4th shelf height), and e_v ($y/W = 0.52$, $z/H = 0.88$) = 0.002 $\mathrm{m\,s^{-1}}$ (near RAG). The highest quantitative discrepancies are found outside the air curtain limits on the external ambient side ($y/W \approx 1$), thus without relevant significance for the study.

Figure 6 shows the comparison of numerical predictions of product core average temperatures with experimental data obtained by Gill et al. [55] (ten retail stores were tested), Foster et al. [19] (difference between minimum and maximum package temperature is around 8 K), Evans et al. [26] (single average temperature value for all M-packages through its standard deviation), Gray et al. [7] (ORDC with inclined shelves), and Lu et al. [56] (evaporator in the back of the cabinet and possessing two air curtains). The predictions of core products temperature are compared with results from other studies because a uniform initial value for all products core temperature was not ensured. The products core temperatures are in the range of the results obtained by the abovementioned studies.

Considering the range of air temperature, relative humidity and velocity variations measured during experimental testing, the deviation between experimental data and numerical predictions is acceptable for this type of engineering application. The nonoverlapping between experimental and numerical results is due to experimental errors (measurements precision, physical phenomena perturbation, etc.), physical-mathematical model assumptions (2D, steady state, turbulence model, PBP and evaporator formulations, open boundary BC definition, etc.), numerical model (the purpose of the MUSCL scheme is to reduce the higher-order terms to first-order eliminating instabilities. However, its use for incompressible flows can damp the physical solution in some extend, providing nonphysical predictions especially in the vicinity of mixing layers and where instabilities occur), i.e., in the air curtain (a phenomenon also observed by D'Agaro et al. [6] and Hammond et al. [57]). Nevertheless, the combined analysis of experimental data and numerical predictions shows that the computational model follows the physical phenomena occurring in the real equipment.

5.2. Numerical Results Analysis and Discussion. The numerical predictions of air flow and heat transfer for the ORDC model subjected to climatic class n.°3 of EN-ISO Standard 23953 [27] are analysed in this section. This analysis will allow the development of numerical parametric studies to improve the global performance of this type of equipments.

5.2.1. Velocity Field Predictions. The numerical predictions of air velocity field are shown in Figure 7. It can be observed the main characteristics of air flow, low air velocity between

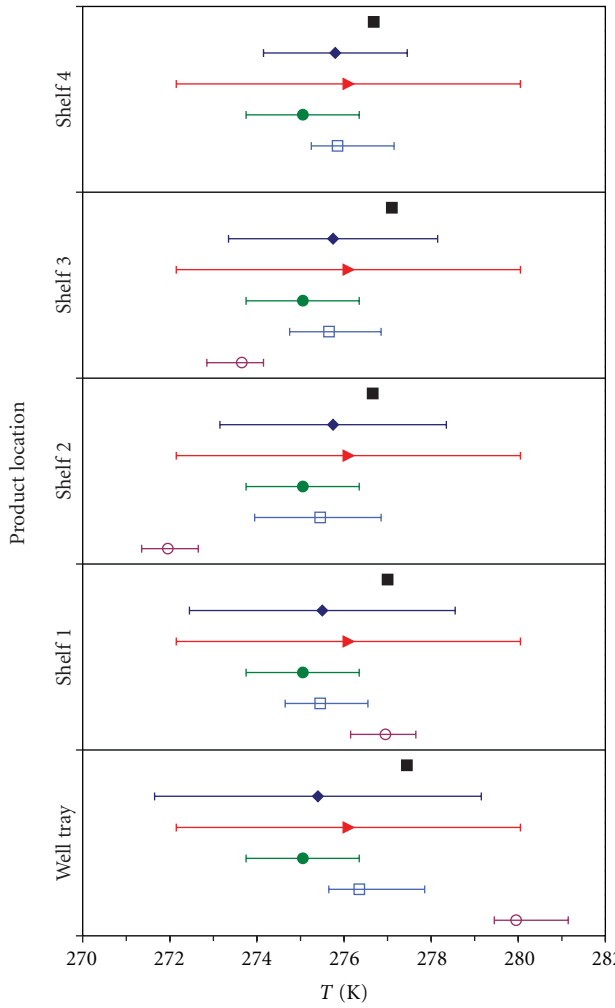

Figure 6: Comparative profiles of internal product temperature, T ($y/W = 0.33$, z/H) (K).

shelves in contrast with high velocities in ducts and at DAG exit. The thermal mixture between refrigerated air curtain and ambient is detected by the increase of air curtain thickness as it moves toward RAG.

A substantial spillage of refrigerated air to ambient can be observed in RAG vicinity due to increased mass flow rate as consequence of entrainment from air curtain. It is also related with the air curtain momentum weakening, being the air velocities quite smaller when compared to those near DAG. These effects convert into energy losses.

Flow details are analysed locally. Figure 8 shows the velocity vectors predictions near DAG and RAG. Several eddies that promote thermal mixture are predicted in DAG vicinity as shown in Figure 8(a). A parametric study where fan velocity and DAG angle influence on thermal performance are studied can provide valuable information to an improved design of the ORDC.

Some recirculations around food products are predicted, as well as the "plug flow" from PBP carrying heat towards air curtain. Other parametric study that can provide an insight about this condition is related to the PBP holes diameter and their distribution, homogeneous or not, in the panel.

The velocity vectors field near RAG is shown in Figure 8(b). Spillage to exterior ambient and eddies formation are predicted at this location. These conditions can be further analysed in a parametric study where different values of fan velocity and RAG angle are tested. Higher air velocities inside rear duct, smaller ones through PBP, and the lowest air velocities inside the conservation space are predicted. Also, vortices are predicted on duct curves, which consequently decrease the air velocity at DAG. Thus, a parametric study can be developed to analyse the inclusion of air guides or deflectors inside ducts to improve air flow by reducing friction. A recirculation region is predicted due to interaction between low velocity air in the conservation zone and high velocity of air curtain. This recirculation reduces air curtain momentum, decreasing its performance as aerothermodynamics barrier to ambient air.

5.2.2. Temperature Field Predictions. The homogeneity degree of temperature distribution in the refrigerated display space is shown in Figure 9. A temperature gradient rising along ORDC's width and height is predicted, suggesting

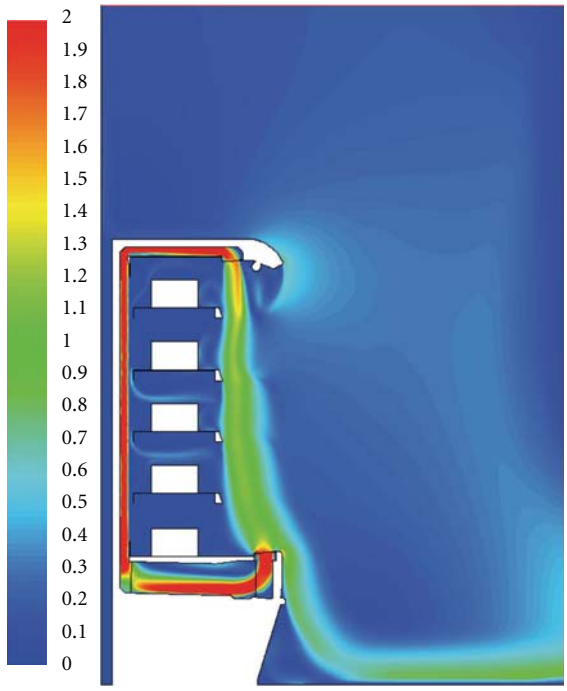

Figure 7: Velocity field numerical predictions for recirculated air curtain, v (m s^{-1}).

that thermal entrainment occurs. The radiation heat transfer affects mostly the surfaces "viewed" from the external environment. The maximum value of air temperature is predicted in the well tray. The internal temperature of products is not constant, as products located at shelves front are more exposed to thermal entrainment through air curtain and by thermal radiation. These results are in concordance with numerical predictions obtained by Cortella [58] and with experimental results obtained by Gill et al. [55], Foster et al. [19], and Evans et al. [26].

5.2.3. Relative Humidity Field Predictions. The numerical results of air relative humidity are coherent with psychometric analysis, that is, the air-relative humidity decreases with air temperature increase. At the interface region between air curtain and ambient, the relative humidity increases due to thermal interaction promoted by eddies development.

5.2.4. Mass Flow and Heat Transfer Rates across the Air Curtain Predictions. A region that virtually encloses air curtain boundaries is considered as shown in Figure 10. These boundaries enclose five control volumes (VC). The numerical results of mass flow (11) and heat transfer (12) rates per unit length are determined for each one. One has

$$\dot{m} = \rho v A \ (\mathrm{kg\,s^{-1}}), \tag{11}$$

$$\dot{Q} = \dot{m} C_p \Delta T \ (\mathrm{W}). \tag{12}$$

Figures 11 and 12 show the values and directions of mass flow and heat transfer rates across air curtain per unit length. These results indicate that air curtain gains thermal energy from ambient and conservation region. The latter gains are related to thermal radiation, illumination, and heat conduction through equipment walls.

The mass flow and heat transfer rates predictions show that recirculated air curtain gains energy from external and internal borders, $\Delta\dot{Q} = 411\,\mathrm{W\,m^{-1}}$. It gains energy from ambient at higher heights (East faces of VC n.°1, 2, 3, and 4) and losses energy near RAG (East face of VC n.°5) at the external border. Simultaneously, it loses energy to the conservation space (West faces of VC n.°1, 2, and 3) and gains it at lower heights (West faces of VC n.°4 and 5). These predictions show that the air curtain is a dynamic system, gaining and losing energy, depending on air velocity, turbulence, air mass ratio between discharge grille and perforated backpanel, among other factors. An air curtain that provides full protection is an unfeasible condition in ORDC. However, the analysis of CFD predictions, such as those provided by the CFD model described along this paper, can help to improve the aerothermodynamics blockage efficacy.

6. Conclusions

A CFD model of an ORDC, including ducts, grilles, perforated backpanel, evaporator, and fans, has been developed to simulate air fluid flow and heat transfer. The aim of the CFD model is to cover the simulation of both air curtain and air flow inside the ducts, which is not common way of using CFD in this type of application. The main objective consists in the development of a detailed CFD model which allows an expedite simulation of design improvements aimed to increase the thermal performance and to reduce the energy consumption of ORDC.

The characterization of air flow and heat transfer allows identifying parameters that can be adjusted and hence reducing the impact of thermal entrainment and improving global performance of ORDC. The main thermal load in this type of equipments is the infiltration of ambient air. The determination of parameters that influence the overall air curtain efficacy, likewise mass flow and heat transfer rates across it, can provide valuable information to performance improvement. The progressive downward thermal entrainment into the air curtain is very dependent on the development of eddies which trigger the mixing. The momentum reduction decreases air curtain stability. This condition promotes a nonuniform air temperature distribution inside the ORDC and influences temperature differences inside the products. Also, the predicted spillage of cold air to surroundings near RAG and the temperature value at this location affect the energy performance of the equipment.

The agreement between numerical predictions and experimental results is quite good and adequate to these type of engineering problems although the authors recognize that this model can be improved to perform transient regime simulations, and the possibility of considering three-dimensional effects will provide additional achievements. Nevertheless, this CFD model is suitable to investigate the

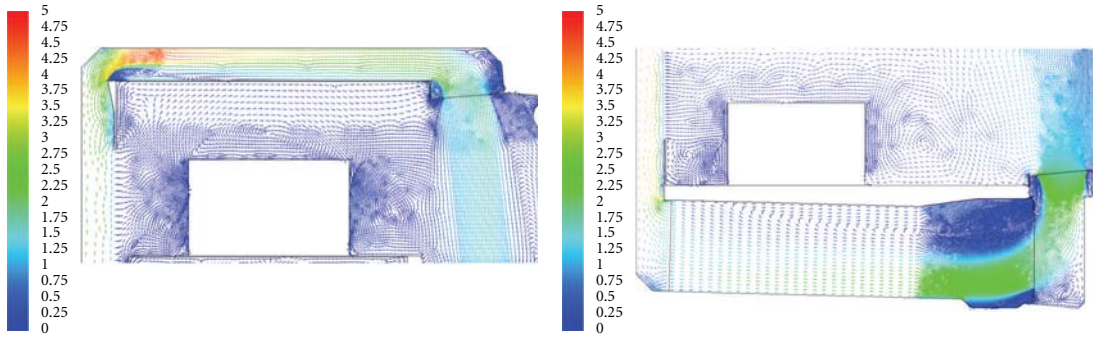

(a) DAG region, v (m s^{-1}) (b) RAG region, v (m s^{-1})

Figure 8: Velocity vectors field numerical predictions.

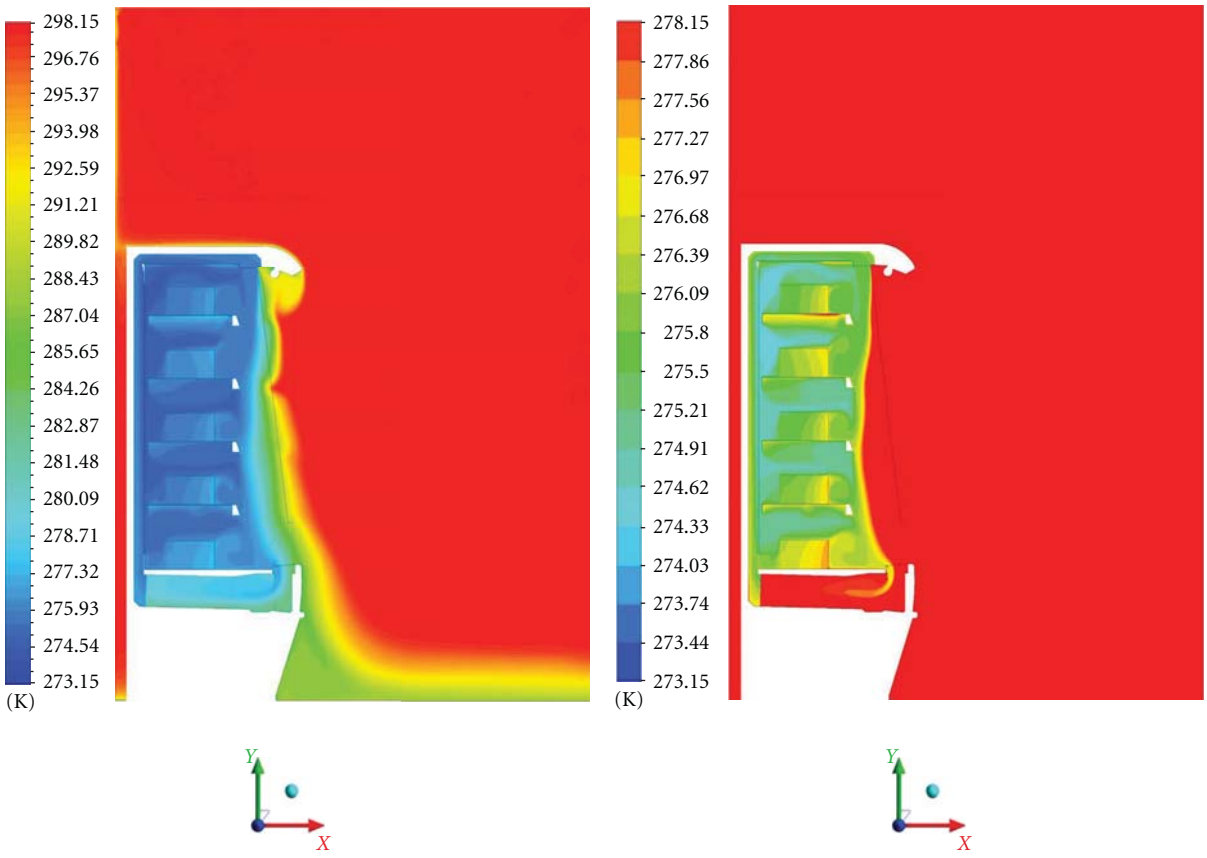

(a) computational domain (b) products conservation zone (reduced scale)

Figure 9: Temperature field numerical predictions, T (K).

effect of a number of modifications that affect the equipment's overall performance, that is, aiming the reduction of thermal entrainment rate and maintaining stable air curtain momentum until it reaches RAG.

Based on the numerical predictions analysis, several parametric studies can be developed to evaluate the influence of some parameters in thermal entrainment and temperature distribution homogeneity inside products conservation region, as these factors are directly related with food safety and energy consumption. As determined by the numerical predictions analysis, these parameters involve fans velocity; hole diameters and their distribution on the backpanel perforation; DAG and RAG angles; guides and deflectors inside ducts, among others. In the future, parametric studies of the abovementioned parameters based on this detailed CFD model will be developed with the aim to analyse design modifications that improve the overall performance of the open display cabinet.

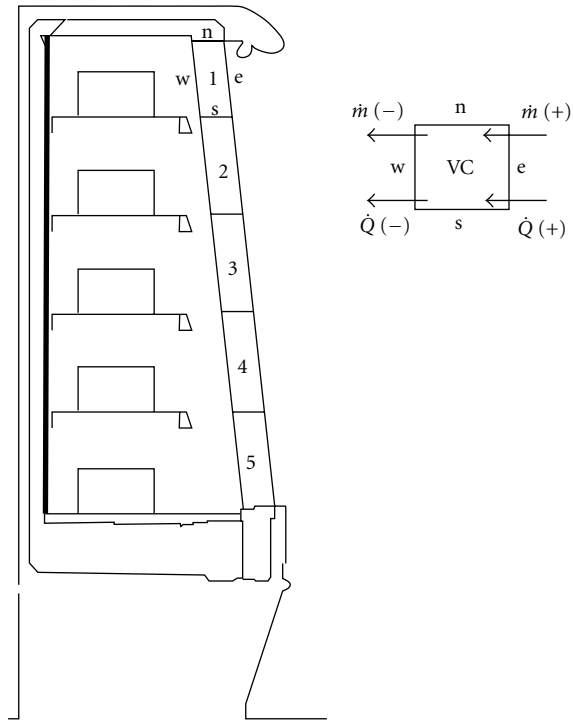

Figure 10: Subdivision of air curtain region by control volumes and sign convention of variables.

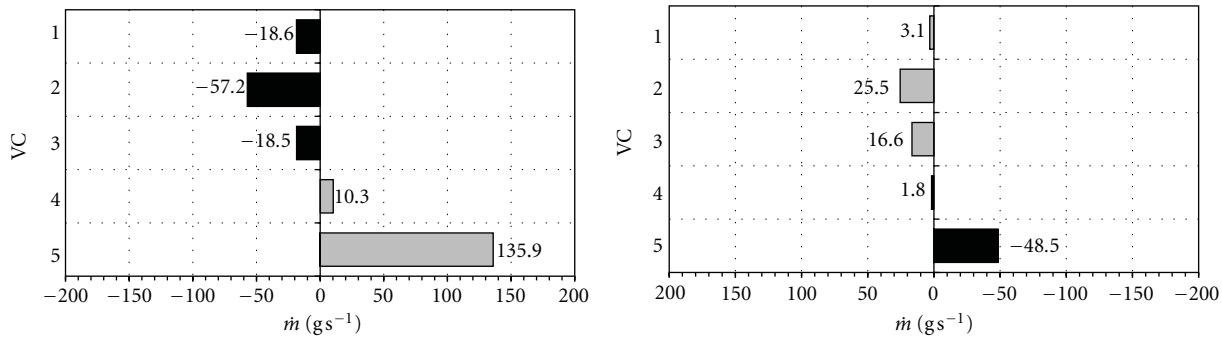

(a) West faces (w)

(b) East faces (e)

Figure 11: Mass flow rate predictions across East (exterior border) and West (interior border) of air curtain control volumes, per unit length.

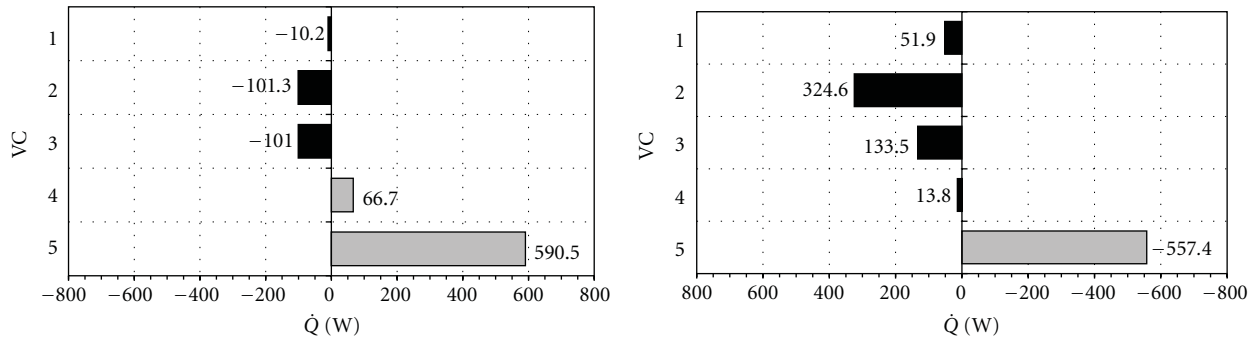

(a) West faces (w)

(b) East faces (e)

Figure 12: Heat transfer predictions across East (exterior border) and West (interior border) of air curtain control volumes, per unit length.

Nomenclature

A: Area, (m^2)
A_0: Total surface area, (m^2)
A_t: External tube surface area, (m^2)
b: Air curtain width, (m)
C_2: Inertial resistance coefficient, (m^{-1})
C_p: Specific heat, ($J\,kg^{-1}\,K^{-1}$)
D_c: Fin collar outside diameter, (m)
D_h: Hydraulic diameter, (m)
E: Energy, (J)
F: Force, (N)
f: Friction coefficient
F_p: Fin pitch, (m)
F_s: Fin spacing, (m)
g: Gravitational acceleration, ($m\,s^{-2}$)
G: Mass flux of the air based on minimum flow area, ($kg\,s^{-1}\,m^{-1}$)
H: Height, (m)
I_t: Turbulence intensity, (%)
K: Loss coefficient
k: Turbulent kinetic energy, ($m^2\,s^{-2}$); permeability, (m^2); thermal conductivity ($W\,m^{-1}\,K^{-1}$)
k^{-1}: Viscous resistance coefficient, (m^{-2})
L: Length, (m)
$\dot{m}$: Mass flow rate, ($kg\,s^{-1}$)
N_{tt}: Number of longitudinal tube row
p: Pressure, (Pa)
P_d: Waffle height, (m)
P_l: Longitudinal tube pitch, (m)
P_t: Transverse tube pitch, (m)
$\dot{q}$: Heat flux, ($W\,m^{-2}$)
$\dot{Q}$: Heat transfer rate, (W)
r: Radius, (m)
Re: Reynolds number
S: General source term
s: Standard error of mean
T: Temperature, (K)
U: Global heat transfer coefficient, ($W\,m^{-2}\,K^{-1}$)
v: Average velocity, ($m\,s^{-1}$)
W: Width, (m)
x, y, z: Spatial coordinates (along length, width, and height), (m)
X_f: Projected fin pattern length for one-half wavy length, (m)
Y_v: Water vapour mass fraction, ($kg_v\,kg_m^{-1}$).

Superscripts and Subscripts

0: Total surface
a: Air
amb: Ambient
bb: Black body
c: Air curtain; contraction; cross-sectional; fin collar
comb: Honey comb
cons: Conservation
e: Expansion
eq: Equivalent
evap: Evaporator
e, w, n, s: Control volume faces identification (East, West, North, and South)
f: Fin
h: Hydraulic
i: Component of cartesian directions according to x, y, and z
in: Input; upstream
m: Mixture
out: Output; downstream
ref: Reference
refrig: Refrigerant fluid
sup: Surface
t: Total; turbulent
v: Water vapour; void.

Greek Symbols

ρ: Density, ($kg\,m^{-3}$)
ε: Dissipation rate of turbulent kinetic energy, ($m^2\,s^{-3}$); emissivity; porosity
ϕ: Relative humidity, (%); general dependent variable
μ: Dynamic viscosity, ($kg\,m^{-1}\,s^{-1}$)
σ: Standard deviation; ratio of the minimum flow area to frontal area
σ^2: Variance
ω : Absolute humidity, ($kg_v\,kg_a^{-1}$)
δ : Thickness, (m)
λ : Convergence criterion.

Acronyms

ACML: Air curtain measuring location
BC: Boundary condition
CAD: Computer-aided design
CAE: Computer-aided engineering
CSML: Conservation space measuring location
DAG: Discharge air grille
ORDC: Open refrigerated display cabinet
PBP: Perforated backpanel
RAG: Return air grille
VC: Volume of Control
TEF: Thermal entrainment factor.

Acknowledgments

The authors wish to acknowledge the support of University of Beira Interior-Engineering Faculty-Electromechanical Engineering Department, Covilhã, Portugal (http://www.ubi.pt/) and of JORDÃO Cooling Systems, Guimarães, Portugal (http://www.jordao.com/). The authors do not have any conflict of interest is with the content of the manuscript.

References

[1] R. Faramarzi, "Efficient display case refrigeration," *ASHRAE Journal*, vol. 41, no. 11, pp. 46–54, 1999.

[2] F. Billard and J. L. Dupont, "Industry as a partner for sustainable development e Refrigeration. In: International Institute of Refrigeration (IIR)," Final Report Prepared for UNEP—United Nations Environment Programme, International Institute of Refrigeration (IIR), Paris, France, 2002.

[3] Freedonia, *World Commercial Refrigeration Equipment—Industry Study with Forecasts to 2014 & 2019*, The Freedonia Group Inc., Cleveland, Ohio, USA, 2011.

[4] D. Westphalen, R. Zogg, A. Varon, and M. Foran, "Energy savings potential for commercial refrigeration equipment," in *Final Report Prepared for Building Equipment Division Office of Building Technologies*, A. D. Little, Ed., U.S. Department of Energy (DOE), Cambridge, Mass, USA, 1996.

[5] P. D. Gaspar, L. C. C. Gonçalves, and R. A. Pitarma, "Experimental analysis of the thermal entrainment factor of air curtains in vertical open display cabinets for different ambient air conditions," *Applied Thermal Engineering*, 2010.

[6] P. D'Agaro, G. Cortella, and G. Croce, "Two- and three-dimensional CFD applied to vertical display cabinets simulation," *International Journal of Refrigeration*, vol. 29, no. 2, pp. 178–190, 2006.

[7] I. Gray, P. Luscombe, L. McLean, C. S. P. Sarathy, P. Sheahen, and K. Srinivasan, "Improvement of air distribution in refrigerated vertical open front remote supermarket display cases," *International Journal of Refrigeration*, vol. 31, no. 5, pp. 902–910, 2008.

[8] ASHRAE, *ASHRAE Handbook: Applications*, American Society of Heating, Refrigerating and Air-Conditioning Engineers Inc., Washington, DC, USA, 2006.

[9] P. Bhattacharjee and E. Loth, "Simulations of laminar and transitional cold wall jets," *International Journal of Heat and Fluid Flow*, vol. 25, no. 1, pp. 32–43, 2004.

[10] Y.-G. Chen and X. L. Yuan, "Simulation of a cavity insulated by a vertical single band cold air curtain," *Energy Conversion and Management*, vol. 46, no. 11-12, pp. 1745–1756, 2005.

[11] B. S. Field and E. Loth, "Entrainment of refrigerated air curtains down a wall," *Experimental Thermal and Fluid Science*, vol. 30, no. 3, pp. 175–184, 2006.

[12] A. M. Foster, M. J. Swain, R. Barrett, P. D'Agaro, and S. J. James, "Effectiveness and optimum jet velocity for a plane jet air curtain used to restrict cold room infiltration," *International Journal of Refrigeration*, vol. 29, no. 5, pp. 692–699, 2006.

[13] L. P. C. Neto, M. C. G. Silva, and J. J. Costa, "On the use of infrared thermography in studies with air curtain devices," *Energy and Buildings*, vol. 38, no. 10, pp. 1194–1199, 2006.

[14] J. J. Costa, L. A. Oliveira, and M. C. G. Silva, "Energy savings by aerodynamic sealing with a downward-blowing plane air curtain-A numerical approach," *Energy and Buildings*, vol. 38, no. 10, pp. 1182–1193, 2006.

[15] G. Cortella, M. Manzan, and G. Comini, "CFD simulation of refrigerated display cabinets," *International Journal of Refrigeration*, vol. 24, no. 3, pp. 250–260, 2001.

[16] H. K. Navaz, R. Faramarzi, M. Gharib, D. Dabiri, and D. Modarress, "The application of advanced methods in analyzing the performance of the air curtain in a refrigerated display case," *Journal of Fluids Engineering, Transactions of the ASME*, vol. 124, no. 3, pp. 756–764, 2002.

[17] M. Axell and P. Fahlén, "Design criteria for energy efficient vertical air curtains in display cabinets," in *Proceedings of the 21st IIR International Congress of Refrigeration*, International Institute of Refrigeration (IIR), Ed., International Institute of Refrigeration, Washington, DC, USA, 2003.

[18] H. K. Navaz, B. S. Henderson, R. Faramarzi, A. Pourmovahed, and F. Taugwalder, "Jet entrainment rate in air curtain of open refrigerated display cases," *International Journal of Refrigeration*, vol. 28, no. 2, pp. 267–275, 2005.

[19] A. M. Foster, M. Madge, and J. A. Evans, "The use of CFD to improve the performance of a chilled multi-deck retail display cabinet," *International Journal of Refrigeration*, vol. 28, no. 5, pp. 698–705, 2005.

[20] Y.-G. Chen, "Parametric evaluation of refrigerated air curtains for thermal insulation," *International Journal of Thermal Sciences*, vol. 48, no. 10, pp. 1988–1996, 2009.

[21] Y. T. Ge and S. A. Tassou, "Simulation of the performance of single jet air curtains for vertical refrigerated display cabinets," *Applied Thermal Engineering*, vol. 21, no. 2, pp. 201–219, 2001.

[22] Y. T. Ge, S. A. Tassou, and A. Hadawey, "Simulation of multi-deck medium temperature display cabinets with the integration of CFD and cooling coil models," *Applied Energy*, vol. 87, no. 10, pp. 3178–3188, 2010.

[23] Y.-G. Chen and X. L. Yuan, "Experimental study of the performance of single-band air curtains for a multi-deck refrigerated display cabinet," *Journal of Food Engineering*, vol. 69, no. 3, pp. 261–267, 2005.

[24] K.-Z. Yu, G. L. Ding, and T. J. Chen, "A correlation model of thermal entrainment factor for air curtain in a vertical open display cabinet," *Applied Thermal Engineering*, vol. 29, no. 14-15, pp. 2904–2913, 2009.

[25] P. D. Gaspar, L. C. C. Gonçalves, and R. A. Pitarma, "Experimental analysis of the thermal entrainment three dimensional effects in recirculated air curtains," in *Proceedings of the 10th International Conference on Air Distribution in Rooms (ROOMVENT '07)*, Helsinki, Finland, 2007.

[26] J. A. Evans, S. Scarcelli, and M. V. L. Swain, "Temperature and energy performance of refrigerated retail display and commercial catering cabinets under test conditions," *International Journal of Refrigeration*, vol. 30, no. 3, pp. 398–408, 2007.

[27] EN-ISO Standard, "Refrigerated display cabinets, parts 1 and 2," Tech. Rep. 23953, ISO-International Organization for Standardization, Geneva, Switzerland, 2005.

[28] J. H. Ferziger and M. Perić, *Computational Methods for Fluid Dynamics*, Springer-Verlag, Berlin, Germany, 3rd edition, 2002.

[29] V. Yakhot and S. A. Orszag, "Renormalization group analysis of turbulence. I. Basic theory," *Journal of Scientific Computing*, vol. 1, no. 1, pp. 3–51, 1986.

[30] P. D. Gaspar and R. A. Pitarma, "Desempenho de modelos de turbulência em regime convectivo misto-Aplicação a caso de estudo," in *Proceedings of Engenharia'03—Inovação e Desenvolvimento*, Universidade da Beira Interior, Covilhã, Portugal, 2003.

[31] P. D. Gaspar and R. A. Pitarma, "Simulação de equipamento industrial de refrigeração: estudo de caso," in *Proceedings of the 6th Congresso de Métodos Numéricos en Ingenieria/7th Congresso de Nacional de Mecânica Aplicada e Computacional*, Laboratório Nacional de Engenharia Civil, Lisboa, Portugal, 2004.

[32] P. D. Gaspar and R. A. Pitarma, "CFD Codes efficiency case study: ability to perform numerical simulations in the refrigerated compartment of a foodstuff transportation vehicle," in *Proceedings of the 9th International Conference on Air Distribution in Rooms (ROOMVENT '04)*, Coimbra, Portugal, 2004.

[33] P. D. Gaspar and R. A. Pitarma, "Evaluation of CFD codes by comparison of numerical predictions of an air-conditioned room case study," in *Advanced Computational Methods in Heat Transfer VIII*, B. Sundén, C. A. Brebbia, and A. Mendes, Eds., Computational Studies (5), WIT Press, Southampton, UK, 2004.

[34] W. Rodi, *Turbulence Models and Their Application in Hydraulics. A State of the Art Review*, International Association for Hydraulics Research, Madrid, Spain, 1980.

[35] B. E. Launder and D. B. Spalding, "The numerical computation of turbulent flows," *Computer Methods in Applied Mechanics and Engineering*, vol. 3, no. 2, pp. 269–289, 1974.

[36] R. I. Issa, "Solution of the implicitly discretised fluid flow equations by operator-splitting," *Journal of Computational Physics*, vol. 62, no. 1, pp. 40–65, 1986.

[37] S. V. Patankar, *Numerical Heat Transfer and Fluid Flow*, Hemisphere Publishing Corporation, Washington, DC, USA, 1980.

[38] D. S. Jang, R. Jetli, and S. Acharya, "Comparison of the PISO, SIMPLER, and SIMPLEC algorithms for the treatment of the pressure-velocity coupling in steady flow problems," *Numerical heat transfer*, vol. 10, no. 3, pp. 209–228, 1986.

[39] B. van Leer, "Towards the ultimate conservative difference scheme. V. A second-order sequel to Godunov's method," *Journal of Computational Physics*, vol. 32, no. 1, pp. 101–136, 1979.

[40] M. F. Modest, *Radiative Heat Transfer*, McGraw-Hill, New York, NY, USA, 1993.

[41] B. N. George and D. R. Buttsworth, "Investigation of an open refrigeration cabinet using computational simulations with supporting experiments," in *Proceedings of the 2000 ASME International Mechanical Engineering Congress and Exposition*, Orlando, Fla, USA, 2000.

[42] P. D. Gaspar, L. C. C. Gonçalves, and R. A. Pitarma, "Influência da localização da condição de fronteira de pressão fixa e constante na simulação de aberturas ao ar ambiente," in *Proceedings of the Congresso de Métodos Numéricos em Engenharia—(CMNE' 07)/Congresso Ibero Latino-Americano sobre Métodos Computacionais em Engenharia—(CILAMCE '07)*, Porto, Portugal, 2007.

[43] EN-ISO Standard, "Household refrigerating appliances-frozen food storage cabinets and food freezers-characteristics and test methods," Tech. Rep. 15502, ISO-International Organization for Standardization, Geneva, Switzerland, 2005.

[44] ASHRAE, *ASHRAE Handbook: Fundamentals*, American Society of Heating, Refrigerating and Air-Conditioning Engineers Inc., Washington, DC, USA, 1997.

[45] J. Bear, *Dynamics of Fluids in Porous Media*, Dover Publications Inc., Mineola, NY, USA, 1988.

[46] R. H. Perry and D. W. Green, *Perry's Chemical Engineers' Handbook*, McGraw-Hill, New York, NY, USA, 1997.

[47] L. Tang, K. A. Moores, C. Ramaswamy, and Y. Joshi, "Characterizing the thermal performance of a flow through electronics module (SEM-E format) using a porous media model," in *Proceedings of the IEEE 14th Annual Semiconductor Thermal Measurement and Management Symposium*, pp. 68–77, March 1998.

[48] T. S. Kwon, C. R. Choi, C. H. Song, and W. P. Baek, "A three-dimensional CFD calculation of boron mixing behaviors at the core inlet," in *Proceedings of the 10th International Topical Meeting on Nuclear Reactor Thermal Hydraulics (NURETH-10)*, Seoul, Korea, 2003.

[49] W. Tong, "Numerical analysis of flow field in generator end-winding region," *International Journal of Rotating Machinery*, vol. 2008, Article ID 692748, 2008.

[50] I. E. Idel'Cik, *Memento des Pertes de Charge-Coefficients dês Pertes de Charge Singulières et de Pertes de Charge par Frottement*, Direction dês Etudes et Recherces D'electricite de France, Eyrolles, Paris, France, 1969.

[51] C. C. Wang, Y. T. Lin, C. J. Lee, and Y. J. Chang, "Investigation of wavy fin-and-tube heat exchangers: a contribution to databank," *Experimental Heat Transfer*, vol. 12, no. 1, pp. 73–89, 1999.

[52] W. M. Kays and A. L. London, *Compact Heat Exchangers*, McGraw-Hill, New York, NY, USA, 3rd edition, 1984.

[53] F. C. McQuiston and J. D. Parker, *Heating, Ventilating, and Air Conditioning-Analysis and Design*, John Wiley & Sons, New York, NY, USA, 4th edition, 1994.

[54] R. Chandrasekharan, P. Verma, and C. W. Bullard, "Development of a design tool for display case evaporators," *International Journal of Refrigeration*, vol. 29, no. 5, pp. 823–832, 2006.

[55] C. O. Gill, T. Jones, A. Houde et al., "The temperatures and ages of packs of beef displayed in multi-shelf retail cabinets," *Food Control*, vol. 14, no. 3, pp. 145–151, 2002.

[56] Y. L. Lu, W. H. Zhang, P. Yuan, M. D. Xue, Z. G. Qu, and W. Q. Tao, "Experimental study of heat transfer intensification by using a novel combined shelf in food refrigerated display cabinets (Experimental study of a novel cabinets)," *Applied Thermal Engineering*, vol. 30, no. 2-3, pp. 85–91, 2010.

[57] E. Hammond, J. Quarini, and A. Foster, "Development of a stability model for a vertical single band recirculated air curtain sealing a refrigerated cavity," *International Journal of Refrigeration*, vol. 34, no. 6, pp. 1455–1461, 2011.

[58] G. Cortella, "CFD-aided retail cabinets design," *Computers and Electronics in Agriculture*, vol. 34, no. 1–3, pp. 43–66, 2002.

Hindawi Publishing Corporation
Modelling and Simulation in Engineering
Volume 2012, Article ID 631276, 15 pages
doi:10.1155/2012/631276

Research Article

The Role of Mesh Generation, Adaptation, and Refinement on the Computation of Flows Featuring Strong Shocks

Aldo Bonfiglioli,[1] Renato Paciorri,[2] and Andrea Di Mascio[3]

[1] *Dipartimento di Ingegneria e Fisica dell'Ambiente, Università della Basilicata, Viale Ateneo Lucano 10, 85100 Potenza, Italy*
[2] *Dipartimento di Ingegneria Meccanica e Aerospaziale, Università di Roma La Sapienza, Via Eudossiana 18, 00184 Rome, Italy*
[3] *Istituto per le Applicazioni del Calcolo M. Picone (IAC), Consiglio Nazionale delle Ricerche (CNR), Via dei Taurini 19, 00185 Roma, Italy*

Correspondence should be addressed to Aldo Bonfiglioli, aldo.bonfiglioli@unibas.it

Received 7 December 2011; Accepted 19 January 2012

Academic Editor: Guan Heng Yeoh

Within a continuum framework, flows featuring shock waves can be modelled by means of either shock capturing or shock fitting. Shock-capturing codes are algorithmically simple, but are plagued by a number of numerical troubles, particularly evident when shocks are strong and the grids unstructured. On the other hand, shock-fitting algorithms on structured grids allow to accurately compute solutions on coarse meshes, but tend to be algorithmically complex. We show how recent advances in computational mesh generation allow to relieve some of the difficulties encountered by shock capturing and contribute towards making shock fitting on unstructured meshes a versatile technique.

1. Introduction

A shock wave is a surface in a flow-field across which various thermodynamic and kinematic properties of the fluid appear, from a macroscopic viewpoint, to change discontinuously. In reality, shock fronts have a finite thickness, of the order of a few mean free paths, across which the physical properties change continuously. Since the shock thickness is much smaller than any macroscopic length scale, such as the radius of curvature of a curved shock, the assumption that the discontinuity thickness is negligible compared with any macroscopic dimension is a fundamental one in most engineering analyses of flows of practical interest.

From the mathematical modeling viewpoint, although it might be expected that a continuum approach based upon the Navier-Stokes equations fails to be valid at the microscopic length scale that characterises the width of a shock wave, Navier-Stokes solutions of the shock layer (in this context, by the term "shock layer" we refer to the microscopic region across which the fluid properties change from their upstream to their downstream values) agree reasonably well with experimental data, at least when the shocks are not too strong (in this paper, except where otherwise noted, when we mention the strength of a shock wave we refer to the magnitude of the jump in fluid properties that occurs through the shock; this might be defined in several ways, for example, by the ratio between the downstream and upstream pressures). Moreover, since changes across a shock wave occur only in the shock-normal direction, the problem is of one-dimensional nature so that closed-form or semianalytical solutions of the 1D Navier-Stokes equations can be obtained and provide the distribution of the various flow properties within the shock layer, see, for example, the book by Hayes [1] or the more recent one by Salas [2, Chapter 3.7].

In the vanishing viscosity limit, the shock width shrinks to zero, the fluid properties change discontinuously through the shock, which becomes a true discontinuity (in the mathematical sense), and the Rankine-Hugoniot jump relations (algebraic equations that connect the upstream and downstream flow properties with the shock speed) are obtained

from the 1D Navier-Stokes equations (see [3, page 136] and also the related discussion in [2, Chapter 3.7.4] for details).

Shifting from the theoretical to the numerical models actually used in the computation of flows with shocks, the dualism between viscous shocks, having a finite though microscopic thickness, and inviscid shocks, being a true discontinuity, shows up again in the two numerical approaches: shock capturing and shock fitting, that have been traditionally used in Computational Fluid Dynamics (CFD) to simulate shock waves.

Since shock thicknesses are of the order of a few mean free paths and the length of a mean free path is of the order of 10^{-7} m for air at standard conditions, it is easily seen that fully resolved Navier-Stokes simulations of a shock wave would require a large number of grid points within a microscopic region surrounding the shock front, in addition to those grid points that are needed to properly resolve the macroscopic features of the flow field. Although the tremendous advances in computer power "may bring computational fluid dynamics to a molecular scale, where shocks will cease to be discontinuities and have a real thickness, full of viscous and thermodynamical effects ..." [4], even nowadays, the inner structure of the shock waves is necessarily underresolved in a realistic Navier-Stokes simulation. This is precisely the situation that occurs when shock-capturing schemes, which represent the numerical model most commonly used nowadays, are used to solve flows with shocks. Shock-capturing discretizations, which date back to the work by von Neumann and Richtmyer [5], lay their foundations in the mathematical theory of weak solutions, which allows to compute all type of flows, including those with shocks, using the same discretization of the conservation law form of the governing equations at all grid cells. This has obvious consequences in terms of coding simplicity, since the same set of operations is repeated within all control volumes of the mesh, no matter how complicated the flow might be. Coding simplicity is the primary reason for the widespread use of shock-capturing schemes in the simulation of compressible flows. Coding simplicity comes not for free, however, and shock capturing solutions of flows featuring strong shock waves are sometimes characterised by large numerical errors and by the appearance of bizarre anomalies. The sources of the numerical errors are various. The most evident cause is the numerical thickness of the captured shock, which depends on the local mesh size and, for the reasons explained above, is always much larger than the physical shock thickness. Two other possible causes are the generation of spurious numerical oscillations [6–8] along the shock front and the reduction of the order of accuracy of the computed solution to a mere first order in the entire region downstream of a captured shock [6, 9–11]. Spurious oscillations arise when the faces of the control volumes of the mesh are not aligned with the shock front; loss of accuracy is probably due to the fact that the flow state of those gridpoints that fall inside a captured shock bear little resemblance with the physical shock structure and are rather to be seen as numerical artefacts. Among the various anomalies exhibited by shock-capturing discretizations, the most evident ones are the stagnation point anomalies [12–16] and the carbuncle phenomenon [17–19]. A large body of the literature has emerged over the last decades addressing possible cures to the aforementioned problems. Trying to give even a brief account of these attempts is well beyond the scope of the present paper, but it seems clear to the authors that none of these efforts has yet given birth to the "ultimate" shock-capturing scheme. Given up hope of finding such an ideal scheme, another chance to improve the quality of shock-capturing calculations consists in coupling the flow solver with a posteriori mesh generation/adaptation/refinement procedures. Indeed, the generation of a new mesh, tailored on the shock pattern and finer in the shock-normal direction, or the refinement/adaptation of an existing mesh not only allows to bring the captured shock thickness closer to (but still far from) its physical value, but also allows to improve the solution quality by aligning the faces of the control volumes with the shock front. Of course, improving the mesh quality alleviates the symptoms, but does not cure the disease. Nonetheless, it is true that good meshes help considerably in reducing the numerical errors induced by captured shock waves, thus significantly enhancing the quality of the computed solution in the entire region downstream of a shock. A discussion on the possible strategies to construct meshes that are better suited to capture shock waves is one of the goals of the present paper.

As already mentioned, however, a different approach for modeling shock waves within the continuum framework is possible: it is called shock fitting and, from a historical perspective, it is even older than shock capturing, since its first appearance is credited [2, Chapter 1], [20] to Emmons [21, 22]. Shock fitting consists in locating and tracking the motion of the discontinuities which are treated as boundaries between regions where a smooth solution to the governing PDEs exists. The Rankine-Hugoniot jump relations are used to calculate the space-time evolution of the discontinuity and the governing equations are discretized only within the smooth regions of the flow field. Shock-fitting methods have enjoyed a remarkable popularity at the dawn of CFD thanks to their ability to accurately compute flows featuring strong shocks on coarse grids using the modest computational resources available at that time. For a given mesh resolution, shock-fitting discretizations are characterized by smaller numerical errors than shock-capturing solutions because they are immune from all those sources of error, previously described, that arise along a captured shock front. Moreover, shock-fitting schemes do not suffer from the other numerical anomalies described previously.

Nonetheless, the exponential growth of computing power, along with the algorithmic difficulties that hindered the development of general-purpose codes based on the shock-fitting approach in the framework of structured meshes, decreed the gradual dismissal of the technique over the last decades. Simply stated, the slogan "one code for all flows" that has so much contributed to the popularity of shock-capturing discretizations does not carry over to shock fitting. Indeed, the two variations of the basic technique that have been so far proposed in the structured grid setting, that is, "boundary" shock fitting and "floating" shock fitting, are either algorithmically simple, but limited to topologically

simple configurations or more widely applicable, but algorithmically complex. Recently, a new shock-fitting technique for unstructured two- and three-dimensional meshes has been proposed and developed [23–27] by two of the authors of this article. This new technique reduces significantly the algorithmic difficulties encountered in the previous implementations of the shock-fitting technique within the structured-grid context. In this newly developed technique, the fitted shock fronts are moving boundaries that are free to float inside a computational domain discretized using triangles, in two space dimensions, or tetrahedra in three. This is achieved by locally regenerating the computational mesh in the neighbourhood of the fitted shocks while ensuring that the shock lines (or the shock surfaces in three dimensions) are always part of the mesh during their motion. The development of this new shock-fitting technique has been greatly furthered by the availability of public domain software libraries, developed over the last years, implementing a variety of tools for the generation of unstructured meshes.

This brief outline of the two types of numerical techniques used in the computation of flows featuring strong shocks highlights the role played by mesh generation/adaptation/refinement techniques in providing high-quality solutions. On the one hand, the use of these techniques improves the quality of shock-capturing solutions; on the other hand, the development of modern unstructured mesh generation tools is opening up new perspectives in the development of shock fitting techniques. To support this assertion, three different applications of mesh generation/adaptation/refinement techniques in the context of shock-capturing computations will be discussed and analysed in Section 2. Section 3 is devoted to shock-fitting: a brief review of the traditional "boundary" and "floating" techniques is given first, followed by the newly developed technique for unstructured meshes. Applications of the unstructured shock-fitting methodology both in two and three space dimensions is illustrated in Sections 3.1 and 3.2.

2. Shock Capturing

In this section we shall describe three different mesh adaptation and/or refinement techniques that can help improving the resolution of strong shock waves computed by means of shock-capturing discretizations. The results to be presented in the following paragraphs have been obtained using different codes, both in house and commercial; the discretization techniques used in the various codes will not be described here, but the reader will be referred to the relevant references for details.

2.1. Structured Mesh Adaptation. The first technique to be described consists in an in-house developed, mesh adaptation code, applied within a structured multiblock context. The selected test-case consists in the hypersonic flow past the ESA IXV capsule [28, 29], a lifting reentry body, see Figure 1(a), equipped with two variable deflection flaps (δ_L, δ_R) that allow an aerodynamically controlled reentry.

Table 1: IXV reentry vehicle: free-stream flow conditions and flap deflection angles.

M_∞	AoA (deg)	p_∞ (Pa)	T_∞ (K)	δ_L (deg)	δ_R (deg)
25	45	1.87	205.73	15	15

The free-stream flow conditions considered in the present case are those typical of a high speed and high altitude point along the reentry trajectory of the space capsule and they are summarised in Table 1. For the given flight conditions, the flow past the capsule is completely laminar and chemically reacting.

The numerical solutions have been computed by means of the commercial code CFD++, developed by Metacomp [30]. The Navier-Stokes equations are supplemented with the 5-species nonequilibrium model by Park [31] and a diffusion model based upon the Gupta-Yos model [32]. The boundary conditions at the solid walls employ the fully catalytic model and radiative equilibrium.

As mentioned previously, the most important source of numerical errors in the shock-capturing calculation of an hypersonic flow is the shock wave itself, which affects the solution quality of the entire flow-field downstream of the discontinuity. An effective mesh adaptation procedure must therefore be tailored for the shock.

Figure 1(b) shows the computational domain around half of the capsule. The computational domain has been split in ten blocks, whose topology has been chosen so as to allow an easy management of the cell clustering in the critical regions: the windward side, the bow shock, and the flaps.

Starting from this block-topology, a baseline mesh is generated using a commercial mesh generator. This mesh is characterised by cell clustering near the wall in order to capture the boundary layers, but no attempt has been made to refine the mesh within the shock regions. Figure 2(a) shows some details of the ten-block mesh; the pressure field computed on the this mesh is displayed in Figure 2(b). The baseline mesh has been modified by changing the spatial distribution of the mesh nodes belonging to the coordinate lines that are perpendicular to the body surface, on the basis of the pressure gradient distribution.

More specifically, the sequence of N mesh nodes (x_i^{baseline}) belonging to each coordinate line is replaced by a new sequence of N nodes (x_i^{adapted}), whose mesh spacing $\Delta s_i = \|x_{i+1} - x_i\|$ is computed as follows:

$$\Delta s_i^{\text{adapted}} = \frac{1}{w_i^{\text{adapted}}} \quad \forall i = 1,\ N-1, \tag{1}$$

where w_i^{adapted} is the weighting function that drives the cell clustering. Using (1), the mesh spacing will be finer in regions where the corresponding weighting function is large and vice versa. The weighting function w_i^{adapted} associated with the adapted mesh, defined as

$$\frac{1}{w_i^{\text{adapted}}} = \frac{c}{w_i^{\text{baseline}}} + \frac{(1-c)}{w_i^{p}} \tag{2}$$

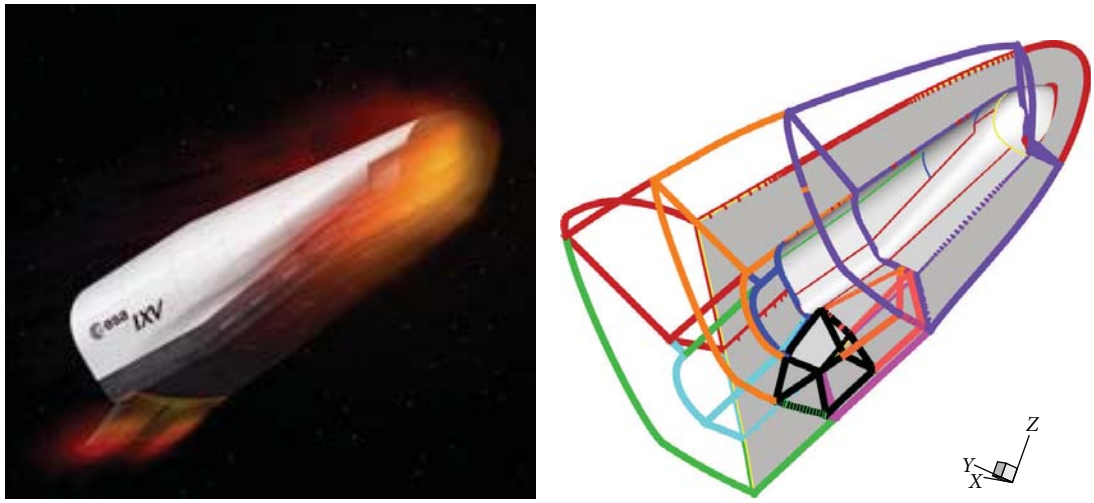

(a) Artist's impression of the IXV capsule (b) Computational domain

FIGURE 1: The ESA IXV vehicle.

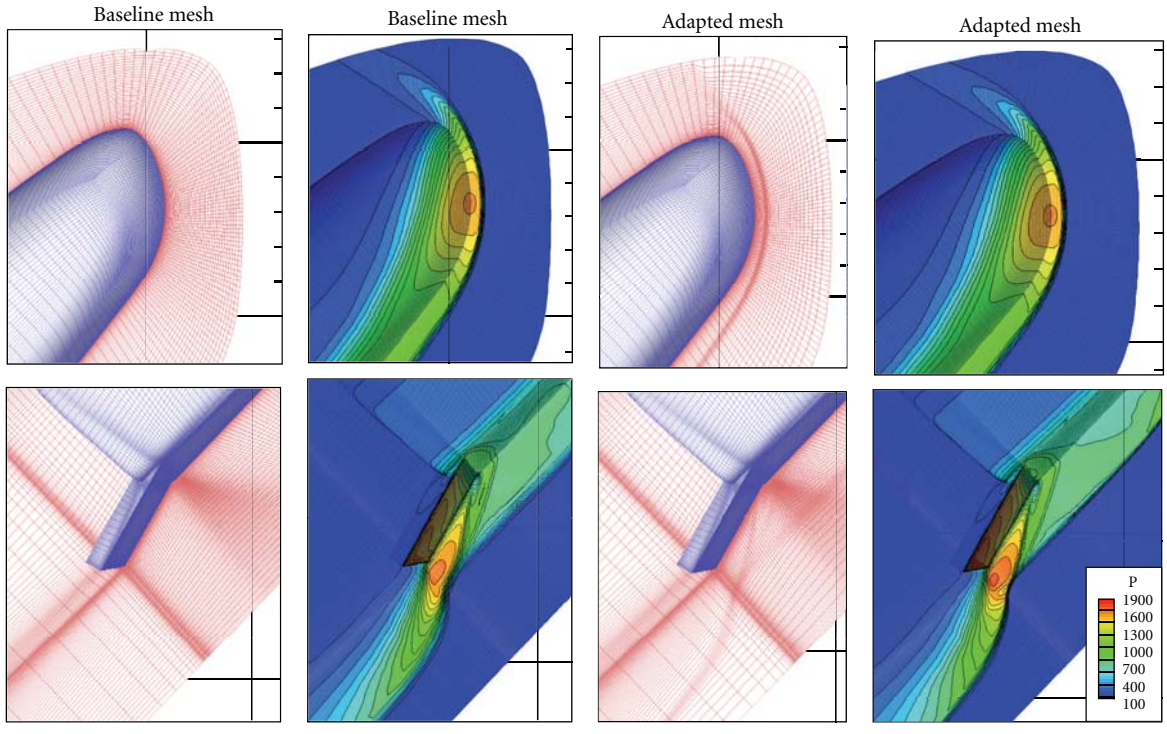

FIGURE 2: The ESA IXV vehicle: meshes and solutions.

is a weighted average of the corresponding weighting function, w_i^{baseline}, which is computed from the known mesh spacing of the baseline mesh:

$$w_i^{\text{baseline}} = \frac{1}{\Delta s_i^{\text{baseline}}} \quad \forall i = 1,\ N-1, \tag{3}$$

and a weighting function w_i^p based upon the pressure gradient distribution computed on the baseline mesh and normalised in such a way that:

$$\sum_{i=1}^{N-1} \frac{1}{w_i^p} = L, \tag{4}$$

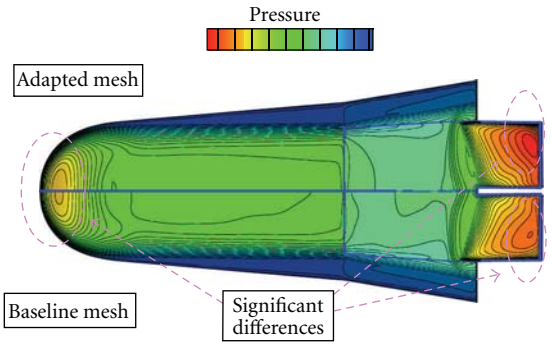

Figure 3: The ESA IXV vehicle: pressure distribution over the windward side of the vehicle.

where $L = \sum_{i=1}^{N-1} \Delta s_i^{\text{baseline}}$. The constant c in (2) is set equal to 0.5.

The comparison between Figures 2(a) and 2(c) shows how the baseline mesh has been modified using the aforementioned pressure-driven adaptation strategy. Note, in particular, that the procedure has been activated only in those blocks where strong shocks are present and it has the effect of clustering the grid points around the shock front and aligning the cell faces with the shock front. Moreover, the procedure does not significantly alter the cell distribution of the baseline mesh inside the boundary layer, because (2) combines the solution-dependent weighting function w_i^p with w_i^{baseline} that keeps track of the original distribution of mesh points within the near-wall region. As a result, only grid points located near the shocks, either on their upstream or downstream side, are moved towards the shock fronts.

The positive effects of the mesh adaptation procedure on the quality of the numerical solution can be observed by comparing Figures 2(b) and 2(d). In particular, the shock thickness computed on the adapted mesh is thinner than the one computed on the baseline mesh and the shock-shock interaction more clearly outlined. Moreover, the beneficial effects of the mesh adaptation procedure are not limited to the shock region but can also be observed on the surface of the capsule. Figure 3 compares the pressure distribution along the windward side of the vehicle obtained on the baseline mesh with that computed on the adapted mesh. The positive effects of mesh adaptation around the shocks are highlighted by the significant increase of the pressure levels that can be observed both in the nose region and on the surface of the flaps. Improving the prediction of the pressure distribution on the capsule's surface significantly enhances the reliability of the numerical estimate of the aerodynamic coefficients; this is particularly true for the moment coefficients that strongly depend upon the pressure distribution on the flaps.

A more comprehensive report of the results obtained by the application of this mesh adaptation technique to the computation of the flow field past the IXV vehicle can be found in [33].

2.2. Structured Mesh Refinement/Adaptation Using Overset Meshes. In this section we describe a more innovative mesh refinement/adaptation technique, suited for structured, multiblock, shock-capturing solvers, which is based upon the so-called "Chimera" or overset mesh approach.

Some early examples of application of the overset grid technology can be found in the pioneering papers by Volkov [34, 35], whereas some more recent applications are reported, for instance, in [36, 37]. This approach is extremely useful for the simulation of flows in domains with complex boundaries (as it happens to be the case in most engineering problems of practical interest), because it allows to mesh complex geometries with relative ease while retaining most of the computational advantages of algorithms based on block structured grids: simple data structure, easy application of iterative schemes based on geometrical multigrid, approximate factorisation techniques for implicit time integration, and so on. The flexibility and convenience of the Chimera approach lies in the process of grid generation, that can be carried out by producing individual pieces of grid around each portion of the frontier; the various blocks are then assembled in a global grid, letting them overlap. Of course, proper algorithms must be developed to compute grid connections at the block boundaries and possible "hole" cutting in the inner portion of each block.

Besides making grid generation more flexible, the overset grid capability can be exploited also for mesh refinement in regions where the solution is known to exhibit strong gradients, like wakes, strong expansions, and shocks. This capability will be illustrated with the following example, which consists in the calculation of the supersonic flow (free-stream Mach number equal to 3) past the space launcher VEGA, shown in Figure 4, during its ascent trajectory. The model equations are the Reynolds Averaged Navier-Stokes equations; the one-equation Spalart-Allmaras model [38] was used for turbulence closure. The CFD solver is an in-house code [39] that exploits the overset grid capability. The discretization is based on a finite volume scheme with second-order accurate ENO [40] approximation of the inviscid fluxes and centred approximation of the viscous terms.

The simulation was aimed at assessing the thermal flux on critical sections of the launcher surface (raceways, retro-rockets, junctions, etc.) and of the appendages (such as antennas, cameras, etc.); therefore, any single device protruding off the vehicle's surface has been carefully discretized, as shown in the detailed view of Figure 4(b). In addition to the geometrical description of the finest details of the launcher, overset meshes have also been exploited for local refinement in critical regions of the flow field.

A preliminary computation on a grid which is not refined in the interior of the domain provided the approximate location of the areas featuring strong gradients. Then, on the basis of this preliminary solution, new blocks were designed with a commercial CAD code and then discretized using a commercial grid generator. The overlapping blocks used for mesh refinement in various critical flow regions can be clearly seen in the left half of both frames of Figure 5. The right half of the two frames of Figure 5 shows the density contours computed on the adapted mesh. It can be seen that the overlapping grid technology can be an effective tool

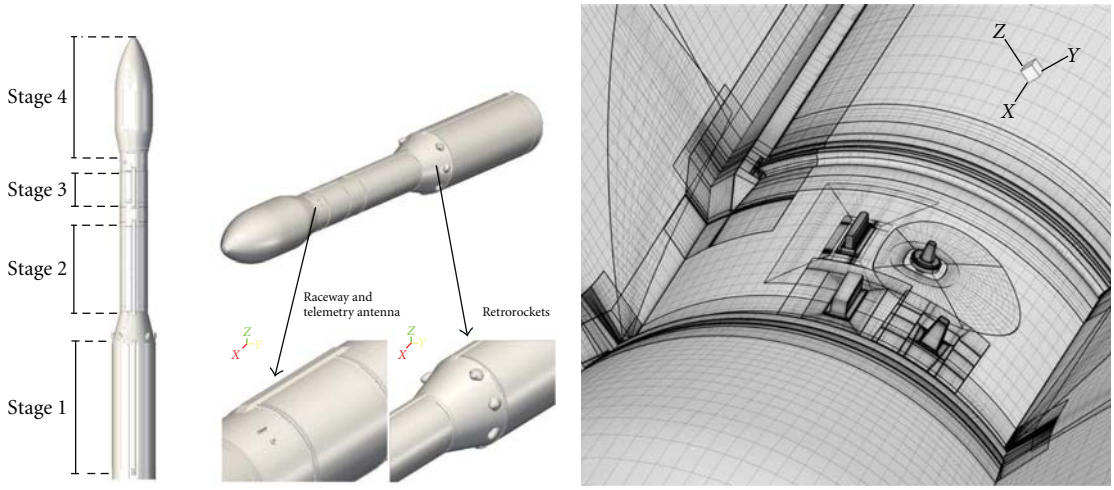

(a) Global view

(b) Detail of the surface grids around the antennas

FIGURE 4: Launcher Vega of the European Space Agency.

to improve the resolution of specific flow features, such as the bow shock shown in the right frame of Figure 5. The quality of the aforementioned mesh refinement technique might be further improved, particularly for shock waves, if coupled with a shock-detection algorithm capable of providing a reasonable approximation to the shape of the shock surface. The overlapping blocks might then be built with one set of coordinate lines perpendicular to the guessed shock surface. This kind of semiautomatic procedure for constructing approximate shock shapes has been used in conjunction with shock fitting and shall be described in Section 3.2.

2.3. Unstructured Grid: Anisotropic Mesh Adaptation. The third methodology to be described consists in the application of an Anisotropic Mesh Adaptation (AMA) technique to unstructured, triangular meshes. AMA is more suitable than the techniques discussed in the previous sections to simulate flows characterised by complex shock topologies. Indeed, unstructured grids clearly have the potential of making mesh adaptation much simpler than it is in the context of structured grids and allow to easily refine the computational mesh even when multiple shock interactions occur. In this section we report the authors' experience in using `angener` [41], a public domain anisotropic mesh generator. The AMA technique available in `angener` consists in building a mesh made of isotropic, almost equilateral triangles in a computational plane which are then transformed into the physical plane using a mapping governed by the Hessian of an appropriate scalar quantity, available from a previous calculation made on a different grid. In the calculations presented herein we have chosen the first component of the set of dependent variables: $\sqrt{p}$, which is adequate to resolve both shocks and contact discontinuities. Further details concerning the AMA technique implemented in the `angener` code can be found in [42]. The flow solver is `eulfs` [43, 44] an in-house, shock-capturing, vertex-centred code which uses second-order accurate, multidimensional upwind, Fluctuation Splitting schemes for the spatial discretization.

To assess the performances of the AMA technique, an Eulerian flow characterised by multiple interactions has been computed. The selected flow configuration is a type IV shock-shock interaction [45], as classified by Edney [46]. This type of interaction arises when a weak (with the term "weak" we here mean an oblique shock featuring a shock angle σ which is smaller than that corresponding to the maximum flow deflection for the given free-stream Mach number) oblique shock meets the bow shock produced by a supersonic stream impinging on a blunt nosed body. Figure 6 shows a sketch of the geometry and flow structure: in the present case the blunt body is a circular cylinder with radius R and the origin of the reference frame is located in the centre of the circle. The free-stream Mach number is $M_\infty = 10$ and the oblique shock, which forms an angle $\sigma = 10^\circ$ with respect to the undisturbed flow, crosses the x-axis at $x_P/R = 1.667$. A first triple point forms where the oblique shock impinges on the bow shock. A reflected shock and a contact discontinuity arise in this triple point and move downstream. The contact discontinuity separates the supersonic stream which has crossed the reflected oblique shock from the subsonic flow downstream of the bow shock. The reflected shock coming from the first triple point rejoins the bow shock in a second triple point where a new reflected shock and a contact discontinuity arise. The two contact discontinuities bound a supersonic jet which is directed towards the body surface, whereas the second reflected shock triggers a series of wave reflections inside the supersonic jet bounded by the two contact discontinuities. Figure 7 shows the density contours computed on an isotropic mesh which has been constructed using `delaundo` [47], a public domain frontal/Delaunay mesh generator [48]. Starting from the solution displayed in Figure 7(a), an adapted mesh has been constructed using `angener` and a solution has been computed on this new mesh using the `eulfs` code. The

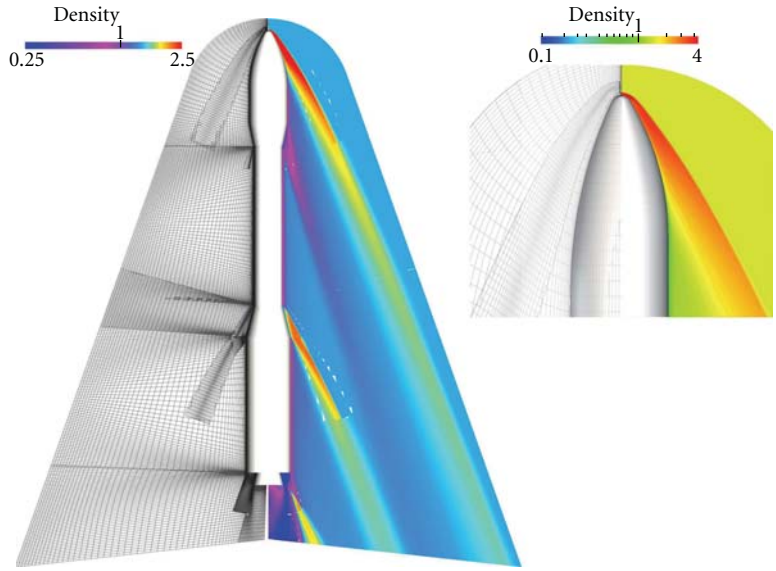

Figure 5: Launcher Vega: overlapping grid and density contours in the symmetry plane; global view and detail of the nose region.

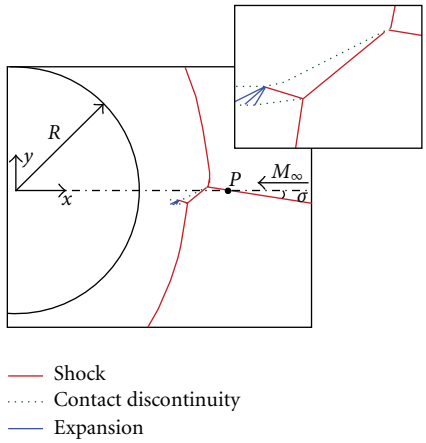

Figure 6: Type IV shock-shock interaction ($M_\infty = 10$): test case definition and flow sketch.

AMA/solution process has been repeated three times and the third mesh and the corresponding solution are displayed in Figure 7(b). The anisotropically adapted mesh features roughly twice as many nodes and triangles than the original mesh; notice that mesh refinement in the most "active" areas of the flow field is partially balanced by mesh coarsening in areas of smooth flow variations. It is clear that AMA allows to improve considerably the resolution of the interaction region; this allows not only to recognise the various flow features, which are indistinguishable in the solution computed on the uniform grid due to the large numerical thickness of the captured discontinuities in that region, but also to reduce the disturbances (even if these are not completely removed) that are generated along the bow shock: compare the density isolines computed within the shock layer (here and in the remainder of this paper, by the term "shock layer" we refer to the flow region bounded between the bow shock and the solid body), which are shown in the leftmost frames of Figures 7(a) and 7(b).

3. Shock Fitting

Nowadays, shock-fitting techniques are neither widely used nor even known to most CFD practitioners, so that it might be worth giving an historical background about the traditional shock-fitting techniques used in the structured grid setting and briefly explaining its new developments within the unstructured grid context.

The first shock-fitting calculation is credited to Emmons [21, 22], but the undisputed guru of this technique is certainly Moretti who, along with his students, has greatly contributed to the popularity of the technique. The recent book by Salas [2] describes the theoretical foundations of shock-fitting along with its practical implementation. Shock fitting, which until recently has only been used in the structured-grid setting, has historically evolved following two different algorithmic approaches: *boundary* shock fitting and *floating* shock fitting. In the boundary shock-fitting approach, the shock is made to coincide with one of the boundaries of the single- or multiblock mesh which is used to discretize the flow field. For example, Figure 8 describes the steady calculation of a bow shock about the fore-body a blunt nosed object: the fitted bow shock is the leftmost boundary of the computational mesh. Starting from the initial configuration shown in Figure 8(a), the grid is deformed, see Figure 8(b), due to the motion of the fitted shock front, until it settles to its final position, shown in Figure 8(c), which corresponds to vanishing shock speed. Figure 8(d) shows the computed flow field. Boundary shock fitting is an algorithmically simple technique, since the treatment of the algebraic relations that hold across the shock (the Rankine-Hugoniot relations) is confined to the boundary points and therefore no modification is required to the computational

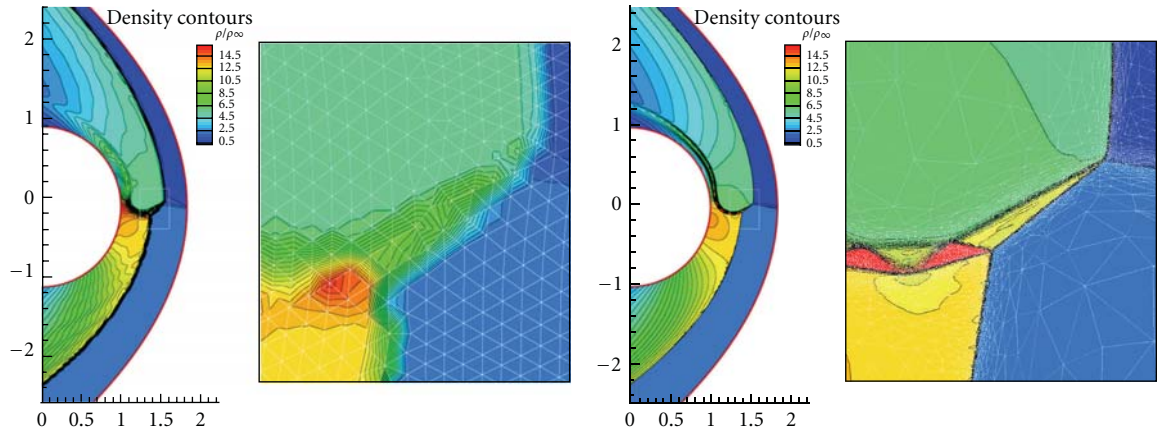

(a) Unadapted mesh: 10855 grid points, 21127 triangles

(b) Anisotropically adapted mesh: 21259 grid points, 42148 triangles

Figure 7: Type IV shock-shock interaction, $M_\infty = 10$: density isolines.

kernel of the code which is used to discretize the governing PDEs within the smooth regions of the flow field. This feature greatly simplifies the coding, but clearly makes the treatment of embedded and/or interacting shocks a "hard bone to chew" [49].

A step forward towards a technique capable of handling more complex flow configurations, as well as unsteady flows, was undertaken by Moretti with the development of the so-called floating shock fitting, see, for example, [50, 51]. In the floating version of the shock-fitting technique, the discontinuities are a collection of shock points, shown by open circles in Figure 9(a), which are allowed to move (float) freely over a fixed background structured grid. The shock front is described by its intersections with grid lines, which gives rise to x and y shock points, as sketched in Figure 9(b). The main features of the methodology are the same as those of the boundary fitting technique, except for the need of a special treatment for grid nodes neighbouring shocks. This is because approximating derivatives by differences between nodes located on opposite sides of a shock must be avoided and therefore, ad hoc finite difference formulae (see, e.g., [52, 53]) have to be used in this case. Moreover, since the x and y shock points are constrained to be located along the grid lines, see Figure 9(b), the technique is able to adequately describe isolated shocks, but it does not allow the precise treatment of the shock-shock interaction point, since the latter may be located in between grid-lines, as also sketched in Figure 9(b). The presence of an interaction point needs then to be modelled by appropriately modifying the calculation of the neighbouring shock points, see, for example, [54]. Floating shock-fitting codes have been used with success in the past to compute steady and unsteady two-dimensional flows involving shock reflections and shock interactions, see, for example, [50, 52, 55]. Very recently, the floating shock-fitting (denoted as front-tracking) technique has been reproposed by Rawat and Zhong [53] in the framework of high-order, structured-grid schemes. Nonetheless, floating shock fitting is an algorithmically complex technique, primarily because of the need to interface the inherently unstructured collection of points used to represent the shock fronts with the underlying structured mesh, which is described using the classical IJK data structure. A thorough account of these difficulties can be found in [53]. Taking advantage of the availability of public domain software libraries [56–60] that accomplish unstructured, volumetric, and surface mesh generation, a novel unstructured shock-fitting technique that combines features of both the boundary and floating shock-fitting techniques has been recently developed by two of the authors [23–27]. In this novel unstructured shock-fitting approach the shock front is discretized as a double-sided, triangulated surface (a polygonal curve in 2D) which is treated as a zero-thickness, internal boundary by the shock-capturing `eulfs` [43, 44] solver (whose main features have already been described in Section 2.3) which is used to discretize the governing PDEs within the computational domain. The two sides of the triangulated shock surface correspond to the upstream and downstream sides of the discontinuity. A set of dependent variables is assigned to each of the grid points which belong to both sides of the discontinuity. The local shock speed and nodal values on the high pressure side of the shock are computed by enforcing the Rankine-Hugoniot relations across the discontinuity. The shock is allowed to move over and independently of a background tetrahedral (triangular in 2D) grid which is locally adapted at each time step to ensure that the nodes and the triangles (edges in 2D) that make up the shock front are part of a constrained Delaunay tetrahedralization (triangulation in 2D). The coupling of the shock-fitting technique with a shock-capturing solver also enables a hybrid mode of operation in which some of the shocks are fitted, whereas all others are captured. The reader is referred to [23–27] for a detailed description of the two-, respectively three-dimensional, version of this novel unstructured shock-fitting approach; here we report some examples demonstrating how the advances in unstructured mesh generation enabled us to bring shock fitting back to life.

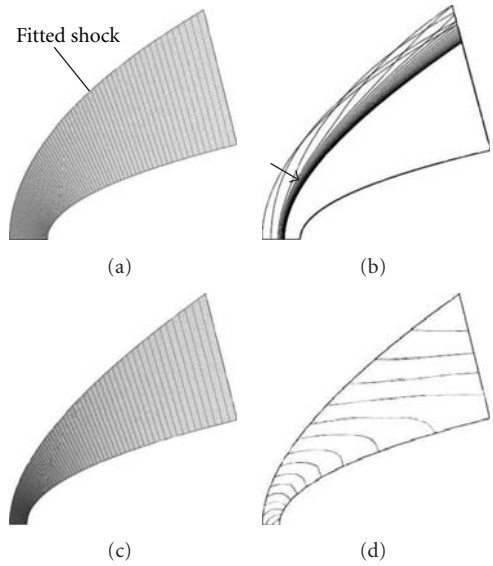

Figure 8: Boundary shock-fitting: (a) initial grid; (b) the grid deforms due to the shock displacement; (c) the fitted shock has settled to its final location; (d) computed flow field.

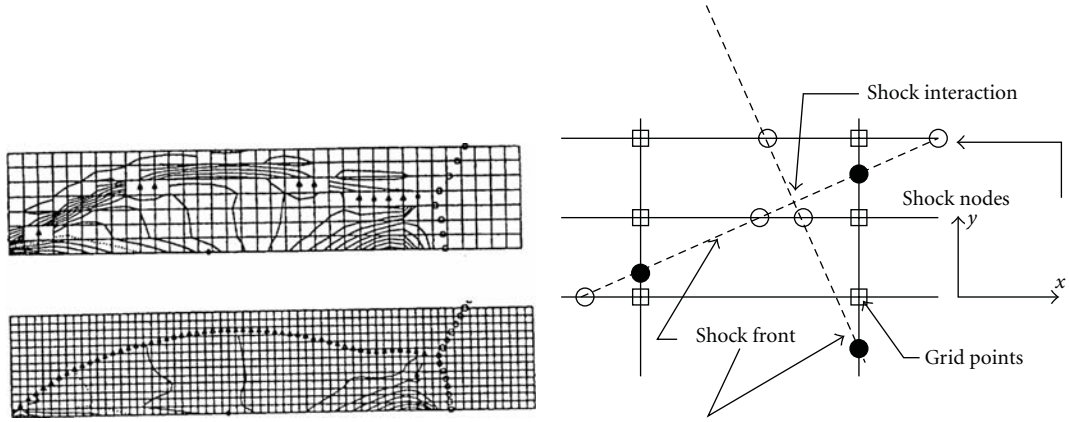

(a) Shock points floating over a background mesh: reprinted from [50]

(b) Shock points: ○: x-shock; ●: y-shock

Figure 9: Floating shock fitting.

3.1. Two-Dimensional, Unstructured Shock Fitting. The current capabilities of the two-dimensional version of the unstructured shock-fitting technique will be demonstrated by referring to the same test case already examined in Section 2.3. In two dimensions this technique is able not only to fit the shock waves, but also the contact discontinuities and the interaction points where various discontinuities meet. The shock fitting simulation uses the unadapted mesh shown in Figure 7(a) as the background triangulation. The fitted discontinuities are approximated by a set of linear splines (shown by the heavier solid lines in Figure 10) and their initial location is guessed using a preliminary shock-capturing calculation performed on the background grid. Starting from this initial solution, the shock-fitting calculation is advanced in time until steady state is reached: at each time step, the background triangulation is locally modified to accommodate the fitted discontinuities which are free to move at a speed which obeys the Ranking-Hugoniot jump relations. Local remeshing along the discontinuities requires a constrained Delaunay triangulation (CDT), a task which is carried out using the `triangle` code [56], a public domain software developed by Shewchuk [56] and based on Ruppert's algorithm [61]. At steady state, the speed of the discontinuities vanishes and the shock-fitting grid does not change any longer. Note that the converged shock-fitting grid, Figure 10, and the background one, Figure 7(a), only differ in the neighbourhood of the fitted discontinuities. Figure 7(a) shows the density isocontours computed by shock capturing on the same grid also used as background triangulation in the shock-fitting simulation; the shock-fitting result is shown in Figure 10. The superiority of the shock-fitting solution over a shock-capturing solution computed

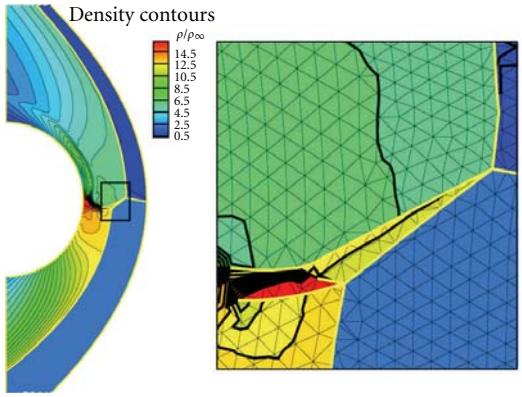

Figure 10: Type IV shock-shock interaction, $M_\infty = 10$: shock-fitting calculation.

on an unadapted mesh of comparable resolution is evident: the detailed view of the region of interaction, shown in the smaller frame of Figure 10, shows that the various discontinuities are clearly identifiable in the shock-fitting solution, whereas their features are completely lost in the shock-capturing calculation, shown in Figure 7(a). If we now compare the shock-fitting solution of Figure 10 with the shock-capturing solution on the anisotropically adapted mesh, shown in Figure 7(b), both calculations appear to be of comparable quality. In particular, both solutions feature smooth contours within the shock layer, even though small wavelength disturbances are visible in the proximity of the bow shock in the shock capturing solution. When comparing shock fitting with shock capturing computed on the anisotropically adapted mesh, it is worth underlining that the former technique requires roughly half the number of grid points and triangles than the latter. A more thorough comparison between shock fitting and shock capturing on anisotropically adapted meshes can be found in [24].

3.2. Three-Dimensional, Unstructured Shock Fitting. Although the three-dimensional version of the unstructured, shock-fitting methodology is conceptually the same as its two-dimensional version described in Section 3.1, the implementation of these ideas in 3D is very challenging and far from trivial. A three-dimensional shock-fitting calculation proceeds similarly to the two-dimensional case. A preliminary shock-capturing calculation on the background mesh provides the initial solution and the approximate shape and location of the fitted shock surface(s). The generation of the initial shock surface(s) proceeds as follows: a cloud of candidate shock points is extracted from the shock-capturing calculation using the algorithm by Ma et al. [62]; these shock points are then processed using various tools available in the `meshlab` [58] software and a preliminary, triangulated shock surface is obtained. The shock-fitting calculation is then advanced in time until steady state is reached. During its time evolution, the fitted shock surface is allowed to float over the background tetrahedral mesh using the shock speed computed within each of the grid points that belong to the shock surface. Volumetric remeshing in the neighbourhood of the shock surface requires a constrained Delaunay tetrahedralization (CDT). This complex operation is performed at each time step using `TetGen`, a public domain code recently developed by Si [57]. Differently from the two-dimensional case, the solution of a CDT problem in three dimensions may require the insertion of several additional mesh points (so-called Steiner points), a situation that needs to be properly handled by the shock-fitting algorithm. Moreover, since the shock surface may change its area and shape during its motion, it has to be periodically remeshed. Surface remeshing is required also to ensure that the local mesh size of the shock surface triangulation is comparable to that of the background tetrahedral mesh; the fulfilment of this criterion avoids the appearance of badly shaped tetrahedra in the neighbourhood of the shock front. Unfortunately, most of the available surface-meshing tools have been developed for computer graphics applications and are typically designed to optimise the distribution of triangles over the surface based upon geometrical features (e.g., the local curvature), rather than user-specified criteria. The solution to our specific surface meshing problem has therefore required a remarkable effort in the search and testing of appropriate software libraries. Among the various tools we have come across, `Yams`, a surface-meshing code developed by Frey [60], turned out to be the one that best suited our needs.

The three-dimensional version of the unstructured, shock-fitting technique has been applied to the calculation of hypersonic flows past geometrically simple bodies, such as the flow past a hemisphere, as well as rather complex ones, including the IXV vehicle described in Section 2.1. A detailed account of these efforts can be found in [26, 27]. The qualitative features of the three-dimensional version of the technique are here described by reference to the high speed flow past a blunt object which consists in a cylinder with a hemispherical nose and a conical flare forming an angle of 30° with respect to the cylinder's axis. The free-stream conditions are Mach number $M_\infty = 4.04$ and angle of attack equal to 20°. This flow configuration has been studied both experimentally and numerically by Houtman et al. [63]; it is characterised by a bow shock and an embedded shock which originates at the cylinder-cone junction. Figure 11(a) shows an experimental visualisation of the flow field, which highlights the type VI shock-shock interaction, as classified by Edney [46], which occurs along the windward side of the body.

A preliminary shock-capturing calculation has been performed using a grid which also served as background grid for the shock-fitting calculations. Two different shock-fitting solutions have also been computed: in the first only the bow shock has been fitted, whereas in the second also the embedded shock has been fitted; Figure 11(b) shows both fitted shock surfaces at steady state. It is worth underlining that the current three-dimensional version of the shock-fitting algorithm is able to fit more than a single shock surface, but the fitted shock surfaces are not allowed to mutually interact. The cause of this limitation is not related to modeling issues (the two-dimensional interaction models described in [24] can be extended to the three-dimensional

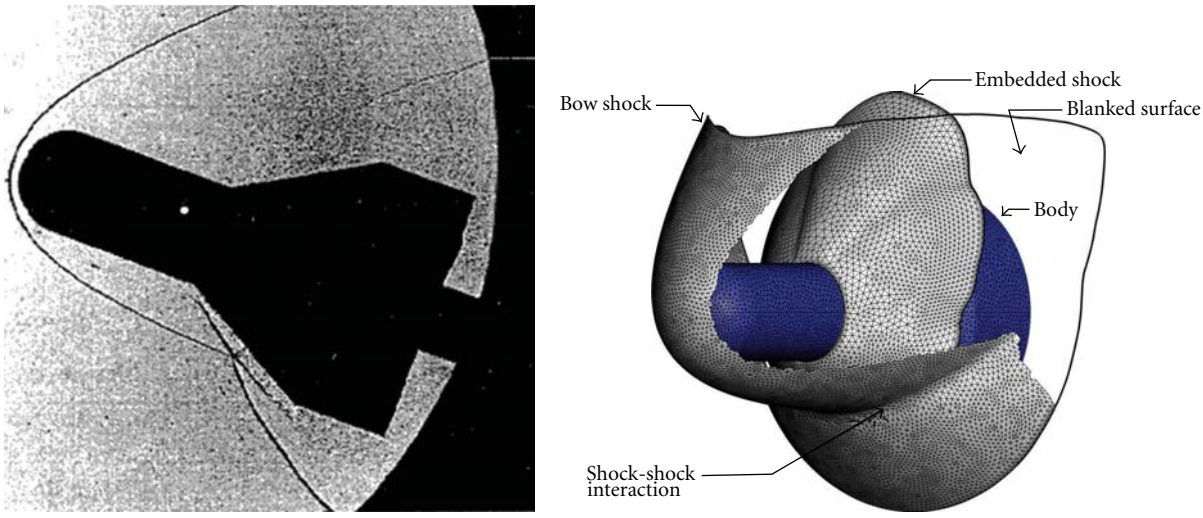

(a) Shadowgraph, reprinted from [63]

(b) Fitted shock surfaces

FIGURE 11: Supersonic ($M_\infty = 4.04$) flow past a cylinder with conical flare.

case without major problems), but it has to do with a specific mesh generation problem. Indeed, in the three-dimensional space, two shocks interact along a curve. This requires the capability to remesh different shock surfaces while prescribing the position of those shock points that are located along the curve where the shock surfaces meet. We are currently investigating this issue and we are confident that we shall be able to "fit" three-dimensional shock-shock interactions in the near future, as we already do in two space dimensions. For the time being, the interaction between different fitted shocks is handled by terminating the fitted surface of the embedded shock shortly before it reaches the bow shock and letting the shock-capturing code capture the shock-shock interaction. Although this is clearly suboptimal than a fully fitted interaction, it however provides improved resolution compared to the situation in which only the bow shock is fitted and the embedded one is captured. This point will be supported with examples in the remainder of this section; for further details the reader is referred to [25, 27]. Figure 12, which shows the normalised pressure distribution on the body surface and on the symmetry plane for all three numerical solutions, allows to pinpoint some significant details of the flow structure predicted by the shock-fitting and shock-capturing simulations. The shock-capturing solution is characterised by a large shock thickness, which has nearly the same width as the shock layer thickness in the stagnation region. In the neighbourhood of the stagnation point, the shock-fitting solutions are seen to be better defined and predict a pressure peak which is much closer to the theoretical stagnation value and higher than that predicted by the shock-capturing calculation.

The shock-shock interaction causes an abrupt change of the shock slope which is clearly visible in Figure 12. In all solutions, the shock-shock interaction is spread over a region of finite width. This is because in all three calculations the shock-shock interaction is captured by the shock-capturing solver, even when both the bow shock and the embedded shock are fitted. The pressure distribution on the body surface is characterised by a second peak which occurs in the proximity of the shock-shock interaction. This is an area where the three numerical simulations show relevant mutual differences. The pressure level which is reached at this second pressure peak in the shock-capturing solution is visibly lower than those predicted by the two shock-fitting solutions. Moreover, downstream of this second pressure peak, the shock-capturing calculation features smoother contour lines that those predicted by the shock-fitting calculations, which is an indication of the fact that the shock-shock interaction has been excessively smeared in the shock-capturing calculation. The relevant role played by the shock-shock interaction is clearly highlighted by the fact that also the two shock-fitting solutions display nonnegligible differences in the neighbourhood of the second pressure peak. This observation also points to the fact that the capability of fitting shock-shock interactions in three dimensions would be an important add-on to the current methodology.

4. Conclusions

Building upon the authors' experience in the field of the numerical simulation and of the development of numerical techniques, this paper highlights the strong relationship that exists between the development and application of mesh adaptation/refinement/generation techniques and the computation of high-quality solutions of flows featuring strong shocks.

The examples provided show that mesh adaptation/refinement/generation techniques that adapt the computational mesh to the shock front are a key ingredient to achieve accurate solutions for this kind of flow fields.

The application of these techniques in the framework of the shock-capturing approach allows to significantly reduce the numerical errors induced by the capture of the shock

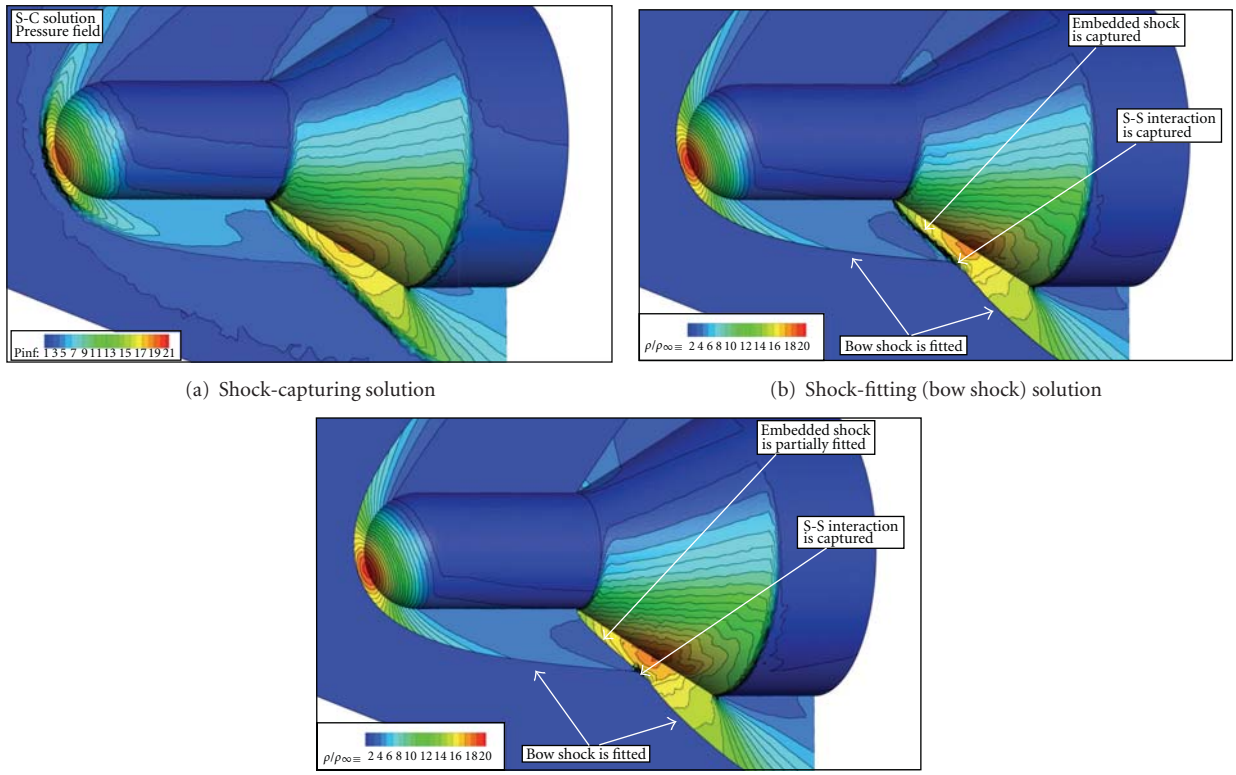

(a) Shock-capturing solution

(b) Shock-fitting (bow shock) solution

(c) Shock-fitting (bow shock and embedded shock) solution

FIGURE 12: Supersonic ($M_\infty = 4.04$) flow past a cylinder with conical flare: pressure isocontours predicted by the shock capturing and shock fitting calculations.

waves. Three different examples of mesh adaptation/ refinement/generation techniques, used in conjunction with three different shock-capturing solvers, have been discussed and analyzed. Specifically, the first two examples show how it is possible to improve the solution quality in the structured-grid framework by means of (i) a mesh adaptation technique that does not involve topological changes in the mesh, or (ii) an overlapping mesh technique whereby additional blocks are superimposed to a background computational mesh. Finally, the third example shows that the same target can be achieved, with greater flexibility, using an unstructured, anisotropic mesh adaptation technique.

The use of different shock-capturing codes, both commercial and in-house developed, structured, and unstructured, contributes towards making these observations of broad validity.

Nevertheless, more relevant and conclusive enhancements in terms of solution quality can be obtained by means of a shock-fitting technique for unstructured grids. Indeed, the use of this newly developed technique completely removes the capturing process that is the source of most of the problems that plague current shock-capturing schemes. The proposed shock-fitting technique heavily relies upon unstructured mesh adaptation/refinement/generation techniques and it is worth underlining that only the development of advanced algorithms and the availability of public domain tools for unstructured mesh generation have made the development of this novel shock-fitting technique possible.

All the analyses presented in this paper deal with steady flows and have been conducted using second-order accurate discretizations in space. We believe, however, that most of the conclusions that have been drawn are applicable to higher order discretizations and unsteady flows as well.

Very high-order methods on structured grids have been extensively used since almost two decades to perform LES or DNS of compressible turbulence, as reviewed in the two recent articles by Johnsen et al. [8] and Pirozzoli [64]. In this particular context, shock-capturing schemes are severely challenged by two conflicting requirements: on the one hand, the discretization scheme should be minimally dissipative in order to be able to adequately simulate all relevant turbulent scales; on the other hand, it must supply a sufficient amount of artificial dissipation around the shocks to avoid un-physical oscillations. This task can be accomplished using different discretization schemes, away and near the discontinuities, which are blended by means of a shock sensor. A number of variations of these hybrid shock-capturing techniques are described in the two aforementioned papers, along with their merits and limitations.

Although structured grid adaptation or refinement is hardly foreseeable in the context of LES or DNS, the advantages offered by shock-fitting, whenever the flow

topology makes it applicable, are clearly acknowledged by the "compressible" LES/DNS community [8, 64]. It is also true, however, as demonstrated using the test-cases presented in [8], that not only is the accurate treatment of the shock wave important to achieve accurate results in the entire domain, but also the properties of the numerical scheme used in smooth regions of the flowfield. It follows that the coupling between high-order schemes and improved shock modeling (such as the high-order shock-fitting technique presented in [53]) appears fully justified, at least in the context of LES/DNS.

The last two decades have also seen a growing interest in the development of high-order methods for unstructured grids [65]. These are expected to be more efficient than second-order accurate schemes, at least for selected applications requiring high accuracy. High-order methods on unstructured grids naturally lend themselves to the coupling with anisotropic mesh adaptation [66]. From the viewpoint of mesh generation/adaptation, high-order methods are less demanding than second-order accurate ones as they require coarser meshes than the latter to achieve the same error level. This is certainly true within boundary layers and wakes, but not around shocks, since also high-order methods need to locally downgrade their accuracy to first order around captured discontinuities. In this respect, the coupling between our newly developed unstructured shock-fitting algorithm and high-order unstructured grid schemes looks particularly promising.

References

[1] W. D. Hayes, *Gasdynamic Discontinuities*, Princeton University Press, 3rd edition, 1960.

[2] M. D. Salas, *A Shock-Fitting Primer*, CRC Applied Mathematics & Nonlinear Science, Chapman & Hall, 1st edition, 2009.

[3] R. Courant and K. O. Friedrichs, *Supersonic Flow and Shock Waves*, Interscience Publishers, 1948.

[4] G. Moretti, "Thirty-six years of schock fitting," *Computers and Fluids*, vol. 31, no. 4–7, pp. 719–723, 2002.

[5] J. von Neumann and R. D. Richtmyer, "A method for the numerical calculation of hydrodynamic shocks," *Journal of Applied Physics*, vol. 21, no. 3, pp. 232–237, 1950.

[6] M. H. Carpenter and J. H. Casper, "Accuracy of shock capturing in two spatial dimensions," *AIAA Journal*, vol. 37, no. 9, pp. 1072–1079, 1999.

[7] T. K. Lee and X. Zhong, "Spurious numerical oscillations in simulation of supersonic flows using shock-capturing schemes," *AIAA Journal*, vol. 37, no. 2-3, pp. 313–319, 1999.

[8] E. Johnsen, J. Larsson, A. V. Bhagatwala et al., "Assessment of high-resolution methods for numerical simulations of compressible turbulence with shock waves," *Journal of Computational Physics*, vol. 229, no. 4, pp. 1213–1237, 2010.

[9] D. L. Bonhaus, *A higher order accurate finite element method for viscous compressible flows*, Ph.D. thesis, Virginia Polytechnic Institute and State University, 1998.

[10] C. J. Roy, M. A. McWherter-Payne, and W. L. Oberkampf, "Verification and validation for laminar hypersonic flowfields, part 1: verification," *AIAA Journal*, vol. 41, no. 10, pp. 1934–1943, 2003.

[11] A. Suresh, "Interaction of a shock with a density disturbance via shock fitting," *Journal of Computational Physics*, vol. 206, no. 1, pp. 6–15, 2005.

[12] P. Gnoffo and J. A. White, "Computational aerothermodynamic simulation issues on unstructured grids," AIAA-2004-2371, 2004.

[13] G. V. Chandler, M. D. Barnhardt, T. W. Drayna, I. Nompelis, D. M. Peterson, and P. Subbareddy, "Unstructred grid approaches for accurate aeroheating simulations," in *Proceedings of the 18th AIAA Computational Fluid Dynamics Conference*, Miami, Fla, USA, June 2007.

[14] P. A. Gnoffo, "Simulation of stagnation region heating in hypersonic flow on tetrahedral grids," in *Proceedings of the 18th AIAA Computational Fluid Dynamics Conference*, vol. 1, pp. 581–599, Miami, Fla, USA, 2007.

[15] P. A. Gnoffo, "Multi-dimensional, inviscid flux reconstruction for simulation of hypersonic heating on tetrahedral grids," in *Proceedings of the 47th AIAA Aerospace Sciences Meeting*, Orlando, Fla, USA, 2009.

[16] P. A. Gnoffo, "Updates to multi-dimensional flux reconstruction for hypersonic simulations on tetrahedral grids," in *Proceedings of the 48th AIAA Aerospace Sciences Meeting*, Orlando, Fla, USA, 2010.

[17] J. C. Robinet, J. Gressier, G. Casalis, and J. M. Moschetta, "Shock wave instability and the carbuncle phenomenon: same intrinsic origin?" *Journal of Fluid Mechanics*, vol. 417, pp. 237–263, 2000.

[18] M. Pandolfi and D. D'Ambrosio, "Numerical instabilities in upwind methods: analysis and cures for the carbuncle phenomenon," *Journal of Computational Physics*, vol. 166, no. 2, pp. 271–301, 2001.

[19] P. Roe, H. Nishikawa, F. Ismail, and L. Scalabrin, "On carbuncles and other excrescences," in *Proceedings of the 17th AIAA Computational Fluid Dynamics Conference*, pp. 1–10, Ontario, Canada, June 2005.

[20] M. D. Salas, "A brief history of shock-fitting," in *Proceedings of the 6th International Conference on Computational Fluid Dynamics (ICCFD '11)*, A. Kuzmin, Ed., pp. 37–53, Springer, Saint-Petersburg, Russia, 2011.

[21] H. W. Emmons, "The numerical solution of compressible fluid flow problems," NACA-TN 932, NASA, 1944.

[22] H. W. Emmons, "Flow of a compressible fluid past a symmetrical airfoil in a wind tunnel and in free air," NACA-TN 1746, 1948.

[23] R. Paciorri and A. Bonfiglioli, "A shock-fitting technique for 2D unstructured grids," *Computers and Fluids*, vol. 38, no. 3, pp. 715–726, 2009.

[24] M. S. Ivanov, A. Bonfiglioli, R. Paciorri, and F. Sabetta, "Computation of weak steady shock reflections by means of an unstructured shock-fitting solver," *Shock Waves*, vol. 20, no. 4, pp. 271–284, 2010.

[25] R. Paciorri and A. Bonfiglioli, "Shock interaction computations on unstructured, two-dimensional grids using a shock-fitting technique," *Journal of Computational Physics*, vol. 230, no. 8, pp. 3155–3177, 2011.

[26] A. Bonfiglioli, M. Grottadaurea, R. Paciorri, and F. Sabetta, "An unstructured, three-dimensional, shock-fitting solver for hypersonic flows," in *Proceedings of the 40th AIAA Fluid Dynamics Conference*, July 2010.

[27] A. Bonfiglioli, M. Grottadaurea, R. Paciorri, F. Sabetta, D. Bianchi, and M. Onofri, "Numerical simulation of hypersonic flows past three dimensional blunt bodies through an unstructured shock-fitting solver," in *Proceedings of the 17th AIAA International Space Planes and Hypersonic Systems and Technology Conference*, 2011.

[28] G. Tumino, E. Angelino, F. Leleu, R. Angelini, P. Plotard, and J. Sommer, "The IXV project: the ESA reentry system and technolologies demonstrator paving the way to european autonomous space transportation and exploration endeavours," in *Proceedings of the 3rd Future Launchers Preparatory Programme (FLPP '08)*, Noordwijk, The Netherlands, October 2008.

[29] P. Roncioni, G. Ranuzzi, M. Marini, and E. Cosson, "Hypersonic CFD characterization of the IXV vehicle," in *Proceedings of the West-East High Speed Flow Field Conference*, Moscow, Russia, November 2007.

[30] Metacomp Technologies, CFD++, 2010.

[31] C. Park, "On convergence of computation of chemically reacting flows," in *Proceedings of the 23rd Aerospace Sciences Meeting*, 1985.

[32] R. N. Gupta, J. M. Yos, R. A. Thompson, and K.-P. Lee, "A review of reaction rates and thermodynamic and transport properties for an 11 species air model for chemical and thermal nonequilibrium calculations to 30000 K," NASA STI/Recon Technical Report 902, 1990.

[33] R. Paciorri, M. Onofri, D. Cardillo, E. Cosson, P. Binetti, and T. Walloschek, "Numerical assessment ofwall catalytic effects on the IXV surface," in *Proceedings of the 6th European Symposium Aerothermodynamics for Space Vehicles*, vol. 659, November 2008.

[34] E. A. Volkov, "A finite difference method for finite and infinite regions with piecewise smooth boundaries," in *Doklady*, vol. 168, pp. 744–747, 1966.

[35] E. A. Volkov, "The method of composite meshes for finite and infinite regions with piecewise smooth boundary," *Trudy Matematicheskogo Instituta im. V. A. Steklova*, vol. 96, pp. 117–148, 1968.

[36] J. A. Benek, J. L. Steger, and F. C. Dougherty, "A flexible grid embedding technique with application to the Euler equations," in *Proceedings of the 6th Computational Fluid Dynamics Conference*, pp. 373–382, Danvers, Mass, USA, 1983.

[37] G. Chesshire and W. D. Henshaw, "Composite overlapping meshes for the solution of partial differential equations," *Journal of Computational Physics*, vol. 90, no. 1, pp. 1–64, 1990.

[38] P. R. Spalart and S. R. Allmaras, "A one-equation turbulence model for aerodynamic flows," *Recherche Aerospatiale*, no. 1, pp. 5–21, 1994.

[39] R. Muscari, M. Felli, and A. Di Mascio, "Analysis ofthe flow past a fully appended hull with propellers by computationaland experimental fluid dynamics," *Journal of Fluids Engineering*, vol. 133, no. 6, Article ID 061104, 16 pages, 2011.

[40] A. Harten, B. Engquist, S. Osher, and S. R. Chakravarthy, "Uniformly high order accurate essentially non-oscillatory schemes, III," *Journal of Computational Physics*, vol. 71, no. 2, pp. 231–303, 1987.

[41] V. Dolejši, The ANGENER ver. 3.1 anisotropic mesh generator, http://www.karlin.mff.cuni.cz/~dolejsi/free.htm.

[42] V. Dolejši, "Anisotropic mesh adaptation for finite volume and finite element methods on triangular meshes," *Computing and Visualization in Science*, vol. 1, pp. 165–178, 1998.

[43] A. Bonfiglioli, "Fluctuation splitting schemes for the compressible and incompressible Euler and Navier-Stokes equations," *International Journal of Computational Fluid Dynamics*, vol. 14, no. 1, pp. 21–39, 2000.

[44] A. Bonfiglioli, M. S. Campobasso, and B. Carpentieri, "Parallel unstructured three-dimensional turbulent flow analyses using efficiently preconditioned Newton-Krylov solver," in *Proceedings of the 19th AIAA Computational Fluid Dynamics Conference*, June 2009.

[45] F. Grasso, C. Purpura, B. Chanetz, and J. Délery, "Type III and type IV shock/shock interferences: theoretical and experimental aspects," *Aerospace Science and Technology*, vol. 7, no. 2, pp. 93–106, 2003.

[46] B. Edney, *Anomalous Heat Transfer and Pressure Distributions on Blunt Bodies at Hypersonic Speeds in the Presence of an Impinging Shock*, Flygtekniska Forsoksanstalten, Stockholm, Sweden, 1968.

[47] J. D. Müller, The DELAUNDO mesh generator, http://www.cerfacs.fr/~muller/delaundo.html.

[48] J. D. Muller, P. L. Roe, and H. Deconinck, "A frontal approach for internal node generation in Delaunay triangulations," *International Journal for Numerical Methods in Fluids*, vol. 17, no. 3, pp. 241–225, 1993.

[49] G. Moretti, "Computation of flows with shocks," *Annual Review of Fluid Mechanics*, vol. 19, pp. 313–337, 1987.

[50] G. Moretti, "A general-purpose technique for two dimensional transonic flows," NASA-CR-194186, GMAF, Freeport, NY, USA, 1987, NASA Lewis Research Center under contract NAS3-24540.

[51] G. Moretti, "Numerical studies of 2-dimensional flows," NASA-CR-3930; NAS 1.26:3930, GMAF, Freeport, NY, USA, 1985, NASA Langley Research Center under contract NAS1-17263.

[52] M. D. Salas, "Shock-fitting method for complicated two-dimensional supersonic flows," *AIAA Journal*, vol. 14, no. 5, pp. 583–588, 1976.

[53] P. S. Rawat and X. Zhong, "On high-order shock-fitting and front-tracking schemes for numerical simulation of shock-disturbance interactions," *Journal of Computational Physics*, vol. 229, no. 19, pp. 6744–6780, 2010.

[54] F. Nasuti and M. Onofri, "Analysis of unsteady supersonic viscous flows by a shock-fitting technique," *AIAA Journal*, vol. 34, no. 7, pp. 1428–1434, 1996.

[55] F. Nasuti and M. Onofri, "Viscous and inviscid vortex generation during startup of rocket nozzles," *AIAA Journal*, vol. 36, no. 5, pp. 809–815, 1998.

[56] J. R. Shewchuk, "Triangle: engineering a 2D quality mesh generator and Delaunay triangulator," in *Applied Computational Geometry: Towards Geometric Engineering*, M. C. Lin and D. Manocha, Eds., vol. 1148 of *Lecture Notes in Computer Science*, pp. 203–222, Springer, 1996, From the *Proceedings of the 1st ACM Workshop on Applied Computational Geometry*.

[57] H. Si, *TetGen a Quality Tetrahedral Mesh Generator and a 3D Delaunay Triangulator*, 2011, http://tetgen.berlios.de/.

[58] M. Callieri, M. Corsini, M. Dellepiane, F. Ganovelli, N. Pietroni, and M. Tarini, *Meshlab*, 2011, http://meshlab.sourceforge.net/.

[59] C. Geuzaine and J. F. Remacle, "Gmsh: a 3-D finite element mesh generator with built-in pre- and post-processing facilities," *International Journal for Numerical Methods in Engineering*, vol. 79, no. 11, pp. 1309–1331, 2009.

[60] P. J. Frey, "Yams: a fully automatic adaptive isotropic surface remeshing procedure," Tech. Rep. 0252, Institut National de Recherche en Informatique et en Automatique (I.N.R.I.A.), INRIA Rocquencourt, Domaine de Voluceau, Rocquencourt, Cedex, France, 2001.

[61] J. Ruppert, "A Delaunay refinement algorithm for quality 2-dimensional mesh generation," *Journal of Algorithms*, vol. 18, no. 3, pp. 548–585, 1995.

[62] K.-L. Ma, J. Van Rosendale, and W. Vermeer, "3D shock wave visualization on unstructured grids," in *Proceedings of the*

Symposium on Volume Visualization, pp. 87–94, IEEE Press, San Francisco, Calif, USA, October 1996.

[63] E. M. Houtman, W. J. Bannink, and B. H. Timmerman, "Experimental and numerical investigation of the high-supersonic flow around an axisymmetric blunt-cylinder-flare model," in *Aerothermodynamics for Space Vehicles*, J. J. Hunt, Ed., vol. 367, pp. 517–522, ESA Special Publication, 1995.

[64] S. Pirozzoli, "Numerical methods for high-speed flows," *Annual Review of Fluid Mechanics*, vol. 43, no. 1, pp. 163–194, 2011.

[65] Z. J. Wang, "High-order methods for the Euler and Navier-Stokes equations on unstructured grids," *Progress in Aerospace Sciences*, vol. 43, no. 1–3, pp. 1–41, 2007.

[66] K. J. Fidkowski and D. L. Darmofal, "Review of output-based error estimation and mesh adaptation in computational fluid dynamics," *AIAA Journal*, vol. 49, no. 4, pp. 673–694, 2011.

Hindawi Publishing Corporation
Modelling and Simulation in Engineering
Volume 2012, Article ID 598479, 9 pages
doi:10.1155/2012/598479

Review Article

Computational Fluid Dynamics Modelling and Experimental Study on a Single Silica Gel Type B

John White

School of Mechanical Engineering, University of Birmingham, Birmingham B152TT, UK

Correspondence should be addressed to John White, jxw998@bham.ac.uk

Received 6 December 2011; Revised 23 January 2012; Accepted 24 January 2012

Academic Editor: Guan Heng Yeoh

The application of computational fluid dynamics (CFDs) in the area of porous media and adsorption cooling system is becoming more practical due to the significant improvement in computer power. The results from previous studies have shown that CFD can be useful tool for predicting the water vapour flow pattern, temperature, heat transfer and flow velocity and adsorption rate. This paper investigates the effect of silica gel granular size on the water adsorption rate using computational fluid dynamics and gravimetric experimental (TGA) method.

1. Introduction

The adsorption properties of silica gel have been studied for many years as silica gel is used in many industries including adsorption cooling systems. Past research has shown experimentally that the adsorpitivity of silica gel granules depends on their size. The purpose of this work was to study the effect of granule size on the adsorption properties of silica gel by using CFD and comparing the simulation results to those obtained experimentally. Computational fluid dynamics (CFD) is a field that has developed over the years because of the new development of computers and CFD simulation. CFD is also used a simulation tool in refrigeration and air conditioning industry. In this paper CFD simulation has been used for modelling of heat and mass transfer in an adsorption tube with silica. One of the questions in CFD modelling is can this type of technology be used as an alternative to experimental data gathering. For this hypothesis a confirmation of CFD data against experimental data is desired. In this paper a 3D silica gel and tube-structured model have been developed for this purpose. Data will be gathered from experimental study, an identical CFD model. This data will be compared to experimental and CFD results. The effects of silica gel size and properties have been studied using the porous media approaches by application of modified Navier-Stokes equations and the continuity equation. In this set of equations, an additional term is used describing the porosity distribution in order to take into account the porous media packing geometry. To design an efficient adsorber bed, flow and temperature information is essential. Studies of fluid dynamics and heat transfer in adsorber beds date back to the early twentieth century [1] The early investigation of flow in porous media packed beds provided mainly such bulk information as pressure drop correlations. For example, Ergun [2] suggested a pressure loss equation, in which parameters like porous media particle diameter and fluid physical properties were used to correlate the pressure drop. Similar correlations were proposed by Molerus [3].

These three empirical correlations rather well predict pressure loss for flow in adsorber beds but provide nothing more about local flow fields of our adsorption/desorption on porous media. On the other hand, of the many investigations of heat transfer in adsorber beds in the last several decades effective parameter methods were applied to predict temperature distribution [4, 5]. Computational fluid dynamics (CFDs) provide an innovative approach to model and analysing the local flow and the effect of silica gel size on adsorption performance of a packed bed. Numerical simulation of porous media local flow and heat transfer based on CFD technique has increasingly been reported in recent years in fields of packed bed flow and heat transfer

modelling [6]. In this work, a finite volume formulation based on the Chimera meshing technique is used to simulate the local flow and heat transfer in a silica gel packed bed, which contains 120 randomly packed spheres.

2. Experimental Apparatus Description

There are numerous methods used for measuring the adsorption uptake of an adsorbent, and the most widely reported procedures are the gravimetric method and the volumetric method. The experimental apparatus used in this paper is the gravimetric method (TGA) developed by Micromeritics instrument corporation; this system is designed to measure adsorption/desorption of porous media materials (see Figure 2 for a schematic layout of the system instruments).

2.1. Experimental Setup and Procedure. The thermogravimetric assembly (TGA) method is used for isotherm, kinetics adsorption experiments due to the high accuracy, ease of control of the pressure and temperature of the experiment. TGA gives a direct measurement of the quantity of adsorbate adsorbed throughout the uptake process. A microbalance device is used where the adsorbent mass is measured as a function of temperature and time. In the TGA, the sample container is suspended on an extension wire that is connected to the microbalance (see Figure 3).

The microbalance measures the weight of sample, and it can detect weight changes of the sample in a very short time. Its measurement ranges are between 0 and 150 mg with readability up to 0.1 μg. The control software screen shot displays control of the functions of the microfurnace, balance, and thermocouple; this runs on a computer connected to the TGA's thermal gas analysis station. During the experiment, time, weight, and temperature are recorded continuously at defined intervals and the data are stored on the computer.

Silica gel granules sample used in the experiment was Fuji type B size 3.5 mm mesh 10–40 (see Table 1 for thermophysical properties of this silica gel).

In Figure 4 you can see a single silica gel size 3 mm type B; the purpose of testing one silica gel adsorption/desorption was to generate experimental data to be used in a CFD module. The advantage of studying a single granule of silica gel is very useful when designing a 3D adsorption bed simulation prediction module.

3. GTA Experimental Results

The adsorption isotherms of the Fuji Davison silica gel water systems are known to exhibit zero hysteresis. Hence in the spirit of confirming the reliability of our analyzer, experiments are carried out from low vapour exposure to high vapour exposure (low-high process) and then from high coverage back to low exposure (high-low process). Figure 5 shows a typical adsorption isotherm plot for water vapour adsorption on the Fuji Davison type B size 3.5 mm silica gel (specific surface area is around 800 $m^2\,g^{-1}$). Figure 6 presents the water vapour adsorption uptake on the type B silica gel size 5 mm following the low-high process at 25°C. The adsorption temperature fluctuation is about 0.5°C which is controlled by the microcomputer controller (see Figure 1, pictorial view of the used TGA instrument).

Table 1: Thermophysical properties of this silica gel. A porous material had to be defined for the adsorbent used in the simulation. This data was taken from the experiment Type B data was created with a density of 730 kg/m^3, for type B and a density of 1000 kg/m^3 and a heat capacity of 0.921 (KJ/kg K) and a thermal conductivity of 0.174 (W/m K) (see Table 1).

	Type B
Specific surface area (m^2/g)	450
Porous volume (mL/g)	0.85
Average pore diameter (A)	22
Apparent density (kg/m^3)	730
pH value	5.0
Water content (wt.%)	<2.0
Specific heat capacity (kJ/kg K)	0.921
Thermal conductivity (W/m K)	0.174
Mesh size	10–40

Table 2: Thermophysical properties used in CFD simulation. The adsorption performance of silica gel is influenced by the physical properties such as surface area, pore size and pore volume and pore distribution, porosity, and density of the silica gel see Table 2.

Material	Water
Density, ρ (kg/m^3)	1000
Specific heat capacity, C_p (J/kg K)	4200
Thermal conductivity, k (W/mK)	0.61
Dynamic viscosity, μ (kg/ms) $\times$ 10^{-3}	0.96172

3.1. The Isotherm Plot for Silica Gel Size 3.5 mm. The adsorption/desorption Isotherm plot for silica gel size 3.5 mm for temperature 25°C in Figure 5 shows a typical water sorption result from a DVS experiment. The isotherm plot adsorption kinetic data shows the change in mass and humidity as over a function of time. From the kinetic results, the rate of water uptake and water diffusion coefficients can be determined. The equilibrium mass values at the end of each humidity step were used to calculate the sorption and desorption isotherms. The difference in water vapour uptake between the sorption and desorption isotherms is called the hysteresis.

3.2. The Isotherm Plot for Silica Gel Size 5 mm. In Figure 6 the Isotherm plot is for silica gel size 5 mm; the plot begins at water performance near zero and 1. The shape and location of the isotherm *hysteresis* give you information about the sorption method and sample porosity. Temperature of water vapour in the adsorbent sample chamber is at a constant 25°C silica gel size 5 mm. The isotherm plot will be used to assist in determining drying rates and optimal endpoints. The isotherm also shows whether the silica gel exhibits

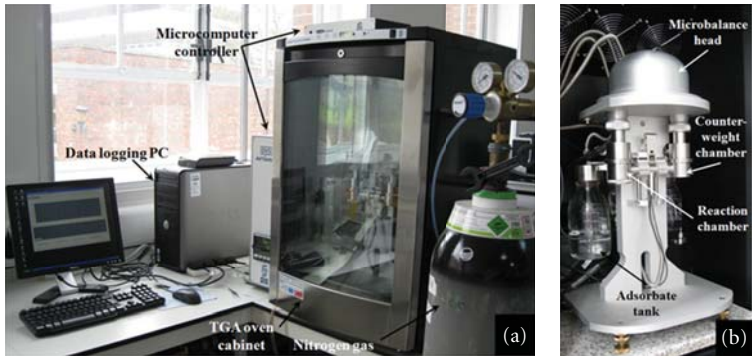

Figure 1: Pictorial view of the used TGA instrument; this system measures the change in weight of a silica gel sample as it is heated for desorption of water, cooled for the adsorption of water vapour, or held at a constant temperature.

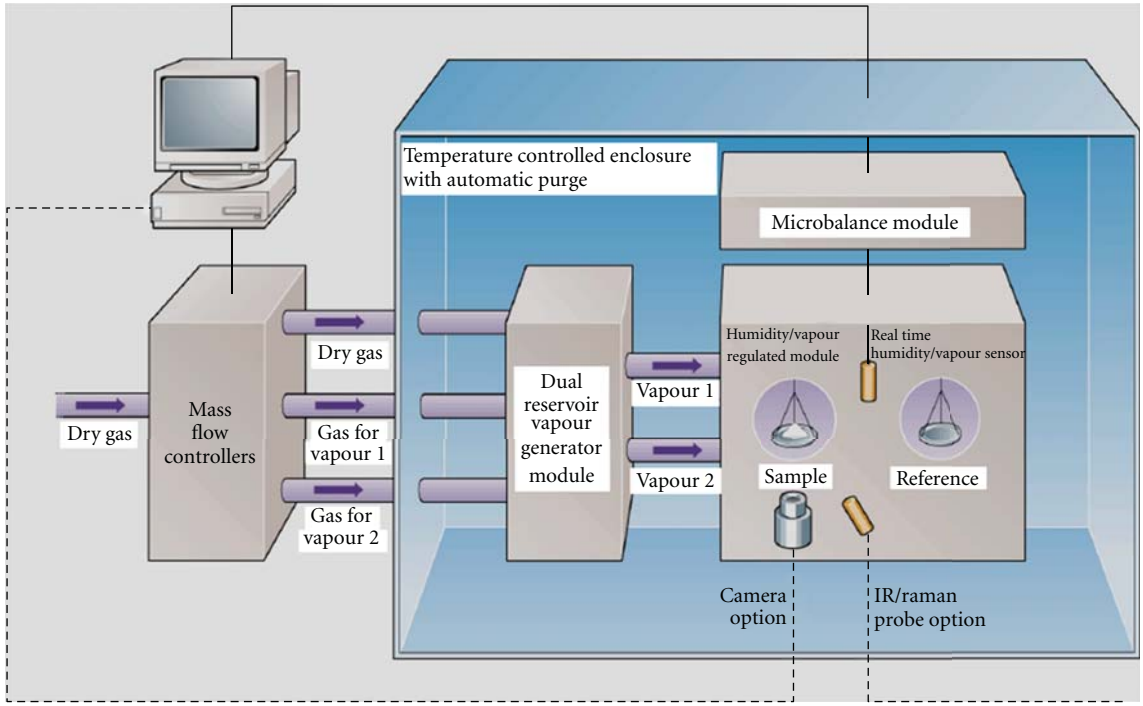

Figure 2: Schematic of the TGA instrument.

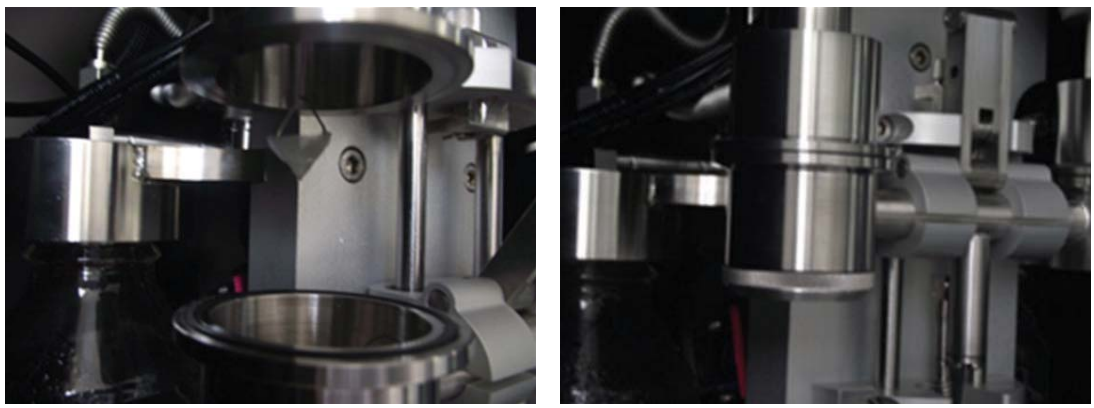

(a) (b)

Figure 3: Sample container suspended on an extension wire.

(a) (b)

Figure 4: One silica gel size 3 mm type B.

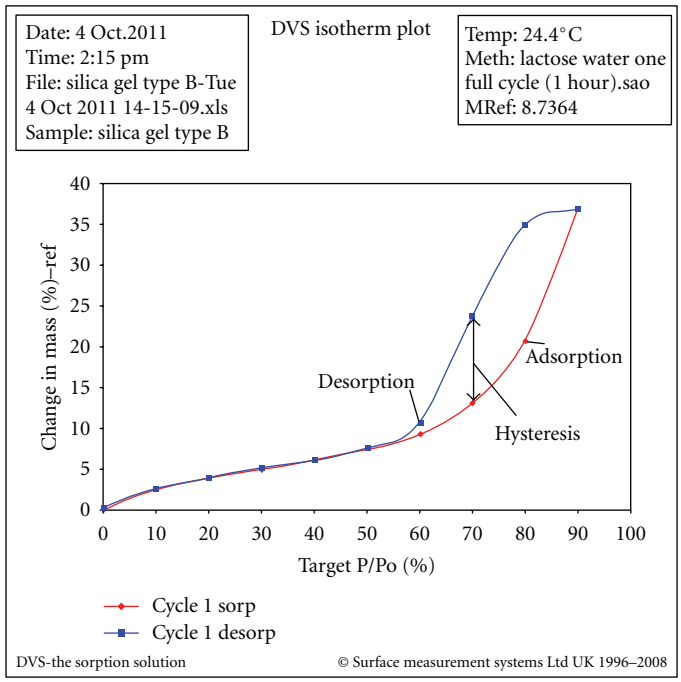

Figure 5: Moisture sorption behaviour of silica gel type B size 3.5 mm at 25°C 1-cycle experiment. Figure 5 shows two isotherms, one obtained by wetting a sample from a dry state and the other obtained by drying a sample from wet state. Water sorption (red) and desorption (blue) isotherms at 25°C measured on silica gel. The moisture content at each water activity is higher during desorption (drying from high moisture content) than adsorption (wetting from low moisture content).

hysteresis and what impact it will have on water activity after drying to a given moisture content drying curve for silica gel type size 5 mm. Figure 6 shows two isotherms, one obtained by wetting the silica gel sample from a dry state and the other obtained by drying the silica gel sample from wet state. The water sorption is shown (red) and desorption is shown (blue); isotherms temperature is at 25°C. In this Isotherm plot the moisture content at each water activity is higher during desorption (drying from high moisture content) than adsorption (wetting from low moisture content). The isotherm plot represents the limits or bounding isotherms since they begin at water performance near zero and one. The shape of the isotherm *hysteresis* gives you information about the sorption mechanism and sample porosity of the 5 mm silica gel.

The shape and location of the isotherm *hysteresis* for silica gel type B size 5 mm temperature of water vapour in the adsorbent sample chamber is at a constant 25°C silica gel size 5 mm.

3.3. Physical Properties. The adsorption performance of silica gel is influenced by the physical properties such as surface area, pore size and pore volume and pore distribution, porosity, and density.

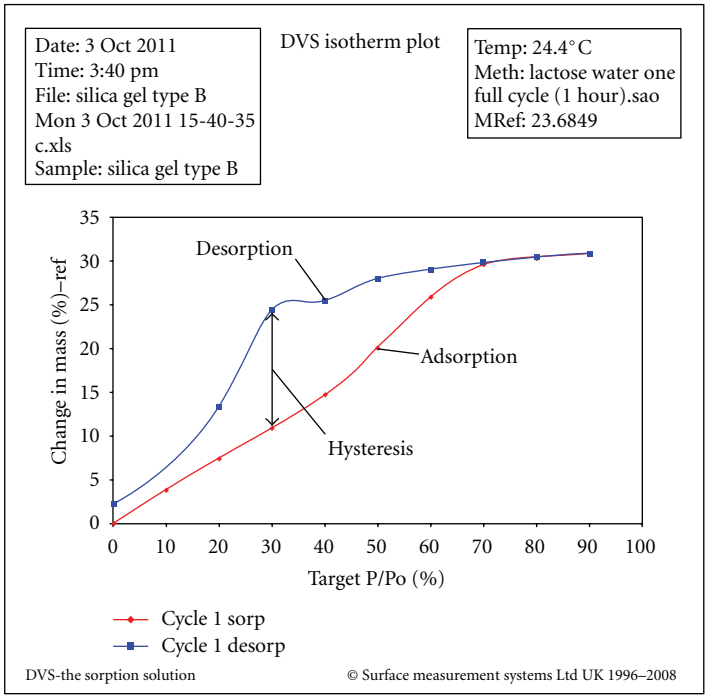

Figure 6: Moisture sorption behaviour of silica gel type B size 5 mm at 25°C 1-cycle experiment.

To help identify the desorption of different species, derivative curves were also produced; the results obtained from a sample of silica gel taken directly from the TGA instrument are shown in Figures 5 and 6.

4. Computational Fluid Dynamics

In this study an integrated CFD model was developed to simulate the adsorption dynamics of water vapour of silica gel granules in an adsorption tube by using the SolidWorks.

Flow Simulation module consisted of two modes of operation, the water vapour adsorption and the desorption mode. In each mode, the water vapour flow profile surrounding a single silica gel granules was determined by solving the Navier-Stokes equations, and the resulting velocity profile was regarded time invariant and stored for later use. Also, the time-dependent mass transfer both outside and inside the porous silica gel due to its adsorpitivity was simulated through a user defined function developed to solve the Brunauer, Emmett, and Teller (BET) equation [7] for both adsorption and desorption processes. The developed simulation model was used to determine the adsorption capacity of two different sizes of silica gel granules, namely, 3.5 mm and 5 mm as a function of time at different operating temperatures. The simulation results were compared with experimental data and found to agree.

4.1. Geometry and Analysis. Geometrical modelling was one of the most critical stages in the CFD simulation; correct definition of the geometry provides a more practical state for the simulation, and the technique used for constructing the geometry will ensure the feasibility of generating a mesh good enough to capture all of the phenomena involved in the problem.

4.2. Boundary Conditions. The boundary conditions determine the flow and thermal variables on the boundaries of the physical model. There are a number of classifications of boundary conditions:

(1) flow inlet and exit boundaries: pressure inlet, velocity inlet, pressure outlet,

(2) wall, repeating, and limit boundaries: wall, symmetry,

(3) internal fluid, solid,

(4) internal face boundaries: porous, wall, interior.

In our model we use a velocity inlet at the flow inlet of the adsorption bed; this boundary condition defines a flow velocity at the inlet of the bed. The flow exit boundary is defined as a pressure outlet; the outlet pressure is defined as atmospheric pressure. The bed and packing interior are defined as boundaries. The wall boundaries separate the fluid zone, vapour, in between the silica gel particles from the wall zones [5, 8–11]. With the determination of the boundary conditions, the physical model has been defined and a numerical solution was provided. It was then necessary to determine how the solution will be established. This was done by setting the iteration parameters. With all boundary conditions defined, a number of additional parameters and solving schemes where selected. An initial condition was assigned to the model and was used to help speed the convergence of the computation.

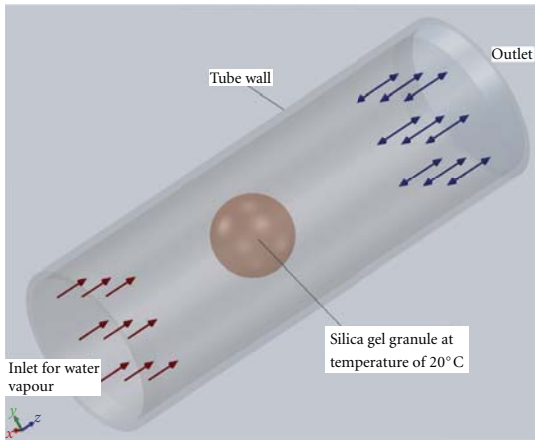

Figure 7: One silica gel in a tube geometry used for validation of CFD against experimental work.

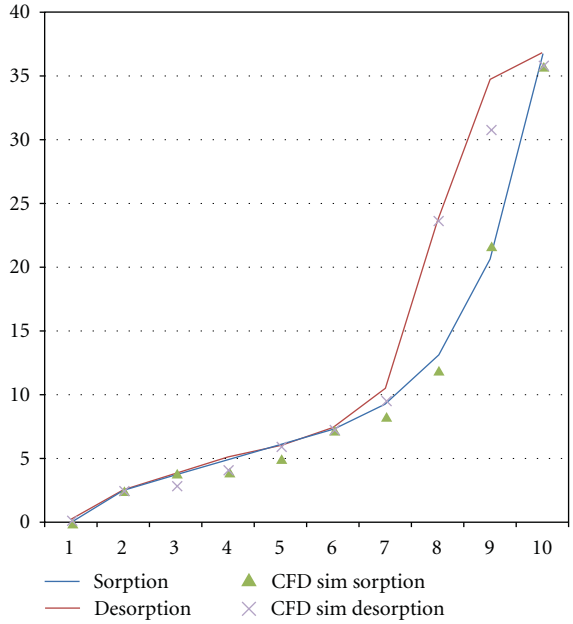

Figure 8: Adsorption and desorption curves for silica gel granules size 3.5 mm.

The computation is an iterative process that solves the governing equations for flow and energy in each simulated cell.

4.3. Modelling of Vapour Flow in a Single Silica Gel Particle. The diffusion equation in the silica gel particle is as a first introduction to CFD a simple model was created the model represented one silica granule in a tube as shown in Figure 7 the flow inlet and flow outlet.

4.4. Porous Media Simulations. A porous material had to be defined for the adsorbent used in the simulation. This data was taken from the experiment Type B; data was created with a density of 730 kg/m^3 for type B and a density of

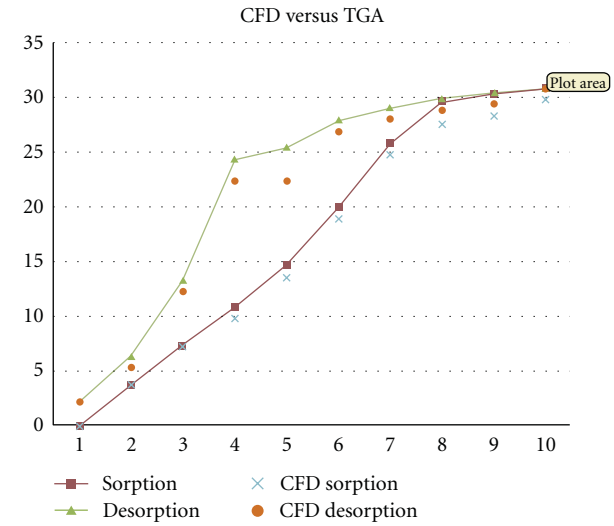

Figure 9: Adsorption and desorption curves for silica gel granules size 5 mm.

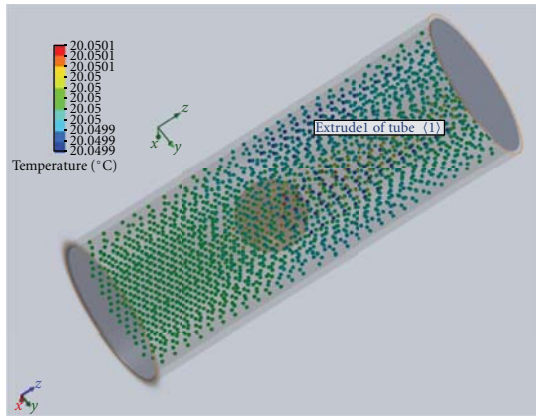

Figure 10: Simulation of water vapour adsorption on porous silica gel.

800 kg/m^3 and a heat capacity of 0.921 J/kg K and a thermal conductivity of 0.174 W/mK (see Table 1).

4.5. CFD Porous Medium Methodology. For the porous medium approach the CFD model has a mass of cells representing the fluid inlet. This is followed by the porous medium cells, which are used to model fluid flow through porous medium. Full flow field predictions are possible with the porous medium approach because the resistance of the porous medium to flow is described by the expression

$$\frac{\Delta P}{L} = -\alpha U_s^2 - \beta U_s, \tag{1}$$

where the permeability coefficient values α and β are assigned temperature-dependent values that describe the behaviour of a porous medium. High values of α and β preclude flow at right angles to the porous medium.

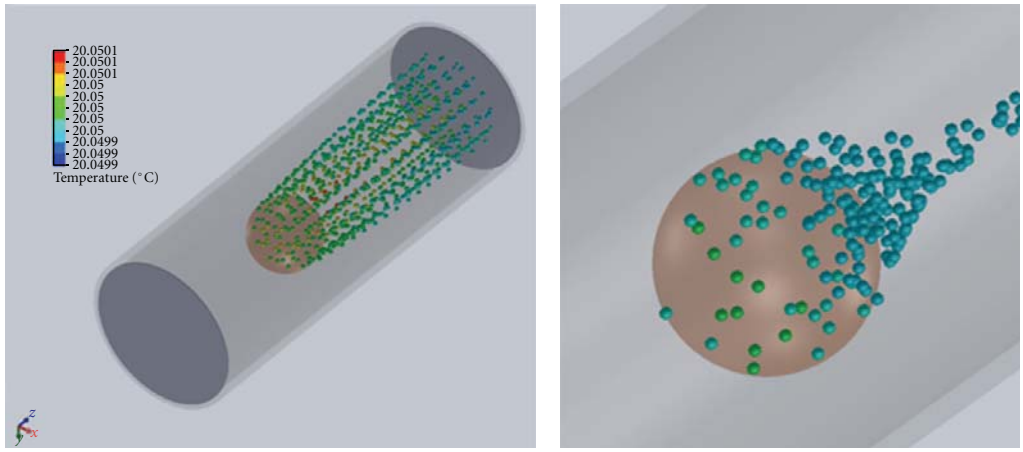

(a) (b)

Figure 11: simulation of water vapour desorption on porous silica gel. To simulate desorption of water vapour we created a function called desorption that could take several inputs (material, fluid, pressure, flow rate, and whatever factors that would affect silica gel desorption of water vapour (see Figure 11).

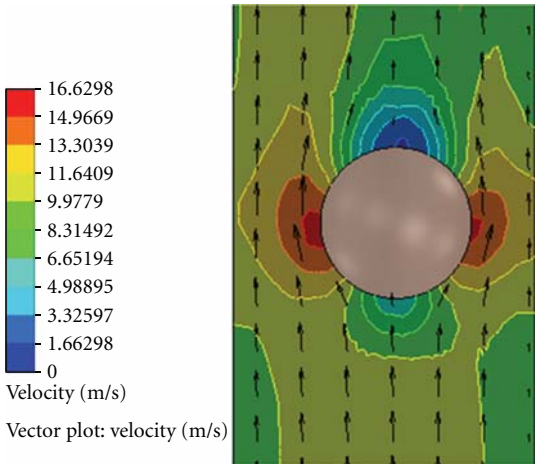

Figure 12: Velocity vectors profile vector plot of the water vapour velocity field around a single silica gel. The inlet velocity is 5 m/s and the velocity field plotted in the plane passing through the centre of the particle.

Upstream and downstream of the water vapour flow field are solved using the usual Reynolds averaged Navier-Stokes methodology.

4.6. Boundary Conditions Used in Simulation. The boundary conditions determine the flow and thermal variables on the boundaries of the physical model. There are a number of boundary conditions:

(i) flow inlet and exit boundaries: pressure inlet, velocity inlet, pressure outlet,

(ii) wall, repeating, and limit boundaries: wall, symmetry,

(iii) internal fluid, solid,

(iv) internal face boundaries: porous, wall, interior.

In our model we use a velocity inlet at the flow inlet of the adsorption bed, this boundary condition defines a flow velocity at the inlet of the bed; The flow exit boundary is defined as a pressure outlet; the outlet pressure is defined as atmospheric pressure. The bed and packing interior are defined as boundaries. The wall boundaries separate the fluid zone, vapour, in between the silica gel particles from the wall zones [5, 9–11].

With the determination of the boundary conditions, the physical model has been defined, and a numerical solution can be provided. It was then necessary to determine how the solution will be established. This was done by setting the iteration parameters. With all boundary conditions defined, a number of additional parameters and solving schemes were selected.

An initial condition was assigned to the model and was used to help speed the convergence of the computation. The computation is an iterative process that solves the governing equations for flow and energy in each simulated cell. Depending on the complexity of the model and the computer resources available, CFD simulation can take anywhere from minutes to days [12]. The results of the simulation can be viewed and manipulated with postprocessing software once the simulation has converted to a solution.

4.7. CFD Mesh Generation. One of the most important parts of this CFD simulation was the module mesh creation. The mesh establishes the accuracy of the simulation which has to be chosen with enough detail to describe the simulation processes accurately and with a degree of coarseness that enables solution within an acceptable amount of time. When an optimal density has been found refining this will increase the model size without displaying more flow details. When it is coarseneds the mesh will obscure, possibly essential, part of the flow detail. The mesh determines a large part of creating an acceptable simulation.

4.8. The CFD Mesh Density. For this study we focused mainly on maintaining a 3D simulation that described the physical model accurately and was able to handle the flow specifics of the silica gel geometry.

The mesh densities were varied to establish the optimal mesh density, describing the flow characteristics and limiting the calculation times.

The initial mesh was specified in the following stages.

(1) Specifying an automatic initial mesh, so all the following specifications consist in changing the default values of its parameters.

(2) Specifying a basic mesh consisting of nearly uniform cells.

(3) Refinement of the basic mesh to capture the relatively small silica gel porous features to resolve the small porous features in contact with fluid.

(4) Refinement of the basic mesh to resolve the solid/fluid interface as well as porous/solid, fluid/porous interfaces.

(5) Specifying other initial meshes in local regions (solid and/or fluid) to better resolve the model-specific geometry and/or flow (and/or heat transfer in solids) peculiarities in these regions.

4.9. Postprocessing the Simulation Data. When the simulation has converged, the last data set is stored as a final solution. This data set has a record of the status of all elements in the model, temperature, densities, pressures, flow aspects, and so forth. To be able to interpret the data, it needs to be ordered and reduced to comprehensible sizes [2]. This displaying of the data is called postprocessing and makes it possible to compare the different simulations with each other and with external data. There were as many ways of displaying the data as there were data points, so it was important to select the data representation that was required for the desired data comparison. Some of the standard options available are contour plots and velocity vector plots. Contour plots will give a plot in the defined data point collection; this can be a plane or a volume of contours of another variable. For example, a plane can be defined as a constant x coordinate plane (y-z plane); we can then make a contour plot showing temperature contours in this plane. In the same plane a velocity contour plot can be made showing absolute velocities of the fluid in the defined plane. Other variables that can be used for contour plots are magnitude of velocity components, turbulence components, pressure, and so forth. Velocity vector plots can be made to get an insight into the flow patterns in the overall geometry or details at specific locations [7, 12–14].

4.10. Fluid Flow Fundamentals. For iteration CFD solvers, use generalized fluid flow and energy balances based on the Navier Stokes equations. The balances are generalized so that the user can influence which elements are added in the balance and which are not. The number of balances to be solved is also user defined; it can be advantageous to not solve all balances initially. The generalized balances that are used by the Flow simulation commercial CFD package are the Navier Stokes equations for conservation of mass and momentum, when it is set to calculate laminar flow without heat transfer. Additional equations are solved for heat transfer, species mixing or reaction or κ and ε for turbulent cases [2, 4, 15].

5. CFD Results and Discussion

Figure 8 shows the adsorption curves for water adsorption on one granular size of silica gel; this curve was compared to Fuji data for smaller silica gel granules.

Figure 8 is an adsorption isotherm plot comparison between CFD simulation and the experimental results on silica gel size 3.5 mm.

Figure 9 is an adsorption isotherm plot comparison between CFD simulation and the experimental results on silica gel size 5 mm.

5.1. Water Vapour Adsorption CFD Simulation. The CFD simulation determines the distribution of water vapour molecules in the flow vapour phase and the adsorption of adsorbed vapour molecules on the silica gel surfaces. Figure 10 shows a silica gel porous media with a typical adsorption of water vapour molecules; this simulation was developed through a user-defined function developed to solve the Brunauer, Emmett, and Teller (BET) equation for both adsorption and desorption processes.

The developed model was used to determine the adsorption capacity of two different sizes of silica gel granules, namely, 3.5 mm and 5 mm as a function of time at different operating temperatures.

Figure 10 shows the water vapour being adsorbed onto the single silica gel. The porous media capabilities of CFD model determine the distribution of water vapour molecules in the flow vapour phase and the adsorption of adsorbed vapour molecules on the silica gel surfaces.

5.2. CFD Simulation of Desorption of Water Vapour from Silica Gel. When attempting to simulate the desorption of water vapour from silica gel, it was necessary to create a user-defined function (UDF). The major challenge in the use of CFD simulation of the desorption of water vapour from silica gel is the complex interconnected void space silica gel has. In traditional 2D mathematical approaches the engineers use to largely ignoring this fact. In CFD simulation this is not ignored; it is modeled into the 3D model of the porous media. In order to simulate desorption, we had to create a function called desorption that would take several inputs (material, fluid, pressure, flow rate, and whatever factors affecting the silica gel calculations; see Figure 12 where there is a simulation of the water vapor desorption).

5.3. Velocity Profiles. To study the velocity distribution in an adsorption silica gel packed bed section cuts were made along the packed bed to generate velocity vector plots. Velocity profiles were also observed in the *near-wall* region of the

modelled arrangements. As expected, in all of the cases analyzed, flow channelling took place near the wall and inside the bed, due to the presence of constrained flow areas. Strong radial flow from the middle to the wall was also noticeable. Due to the channelling of the flow (strong axial flow and reduced radial flow) at the wall, the local radial heat transfer rate decreases, causing the well-known.

6. Conclusions

A CFD model was developed for simulating the adsorpitivity of water vapour on silica gel granules and used to study the effect of granule sizes indicating that reducing the granule size increases the adsorpitivity. We used a thermogravimetric (TGA) to make some experimental data to be used in the CFD module; we compare our measurements with the CFD simulation. A good agreement was found with CFD and experimental data. In conclusion to this study, it is thought that using CFD could provide useful information for the design of adsorption cooling systems and better predict the system performance.

References

[1] K. E. Bertil Andersson, "Pressure drop in ideal fluidization," *Chemical Engineering Science*, vol. 15, no. 3-4, pp. 276–297, 1961.

[2] S. Ergun, "Fluid flow through packed columns," *Chemical Engineering Progress*, vol. 48, pp. 89–94, 1952.

[3] O. Molerus and J. Schweinzer, "Resistance of particle beds at Reynolds numbers up to Re ≈ 104," *Chemical Engineering Science*, vol. 44, no. 5, pp. 1071–1079, 1989.

[4] A. G. Dixon and D. L. Cresswell, "Effective heat transfer parameters for transient packed-bed models," *AIChE Journal*, vol. 32, no. 5, pp. 809–819, 1986.

[5] M. Rahimi and M. Mohseni, "CFD modeling of the effect of absorbent size on absorption performance of a packed bed column," *Korean Journal of Chemical Engineering*, vol. 25, no. 3, pp. 395–401, 2008.

[6] J. L. Steger and J. A. Benek, "On the use of composite grid schemes in computational aerodynamics," *Computer Methods in Applied Mechanics and Engineering*, vol. 64, no. 1-3, pp. 301–320, 1987.

[7] Akira Akahira, K. C. Amanul Alam, Yoshinori Hamamoto, Atsushi Akisawa, and Takao Kashiwagi, "Experimental investigation of mass recovery adsorption refrigeration cycle," *International Journal of Refrigeration*, vol. 28, no. 4, pp. 565–572, 2005.

[8] K. S. Chang, M. T. Chen, and T. W. Chung, "Effects of the thickness and particle size of silica gel on the heat and mass transfer performance of a silica gel-coated bed for air-conditioning adsorption systems," *Applied Thermal Engineering*, vol. 25, no. 14-15, pp. 2330–2340, 2005.

[9] K. S. Chang, M. T. Chen, and T. W. Chung, "Effects of the thickness and particle size of silica gel onthe heat and mass transfer performance of a silica gel-coated bed for air-conditioning adsorption systems," *Applied Thermal Engineering*, vol. 25, no. 14-15, pp. 2330–2340, 2005.

[10] May-Fun Liou, *A numerical study of transport phenomena in porous media*, Ph.D. thesis, Case Western Reserve University, 2005.

[11] G. E. Mueller, "Radial void fraction distributions in randomly packed fixed beds of uniformly sized spheres in cylindrical containers," *Powder Technology*, vol. 72, no. 3, pp. 269–275, 1992.

[12] A. Kopanidis and A. Theodorakakos, "Numerical simulation of fluid flow and heat transfer with direct modelling of microscale geometry," in *Proceedings of the 5th European Thermal-Sciences Conference*, The Netherlands, 2008.

[13] A. V. Anikeenko, N. N. Medvedev, M. K. Kovalev, and M. S. Melgunov, "Simulation of gas diffusion in porous layers of varying structure," *Journal of Structural Chemistry*, vol. 50, no. 3, pp. 403–410, 2009.

[14] D. C. Wang, J. Y. Wu, Z. Z. Xiaa, H. Zhaia, R. Z. Wanga, and W. D. Dou, "Study of a novel silica gel—water adsorption chiller. Part II. Experimental study," *International Journal of Refrigeration*, vol. 28, no. 7, pp. 1084–1091, 2005.

[15] F. Augier, C. Laroche, and E. Brehon, "Application of computational fluid dynamics to fixed bed adsorptioncalculations: effect of hydrodynamics at laboratory and industrial scale," *Separation and Purification Technology*, vol. 63, no. 2, pp. 466–474, 2008.

[16] F. Augier, C. Laroche, and E. Brehon, "Application of computational fluid dynamics to fixed bed adsorption calculations: effect of hydrodynamics at laboratory and industrial scale," *Separation and Purification Technology*, vol. 63, no. 2, pp. 466–474, 2008.

Hindawi Publishing Corporation
Modelling and Simulation in Engineering
Volume 2012, Article ID 567864, 8 pages
doi:10.1155/2012/567864

Research Article

Turbulent and Transitional Modeling of Drag on Oceanographic Measurement Devices

J. P. Abraham,[1] J. M. Gorman,[1] F. Reseghetti,[2] E. M. Sparrow,[3] and W. J. Minkowycz[4]

[1] *School of Engineering, University of St. Thomas, 2115 Summit Aveune, St. Paul, MN 55105-1079, USA*
[2] *ENEA, UTMAR-OSS, Forte S. Teresa, 19032 Pozzuolo di Lerici, Italy*
[3] *Department of Mechanical Engineering, University of Minnesota, 111 Church Street SE, Minneapolis, MN 55455-0111, USA*
[4] *Department of Mechanical and Industrial Engineering, University of Illinois at Chicago, Chicago, IL 60607, USA*

Correspondence should be addressed to J. P. Abraham, jpabraham@stthomas.edu

Received 3 October 2011; Accepted 11 January 2012

Academic Editor: Guan Heng Yeoh

Computational fluid dynamic techniques have been applied to the determination of drag on oceanographic devices (expendable bathythermographs). Such devices, which are used to monitor changes in ocean heat content, provide information that is dependent on their drag coefficient. Inaccuracies in drag calculations can impact the estimation of ocean heating associated with global warming. Traditionally, ocean-heating information was based on experimental correlations which related the depth of the device to the fall time. The relation of time-depth is provided by a fall-rate equation (FRE). It is known that FRE depths are reasonably accurate for ocean environments that match the experiments from which the correlations were developed. For other situations, use of the FRE may lead to depth errors that preclude XBTs as accurate oceanographic devices. Here, a CFD approach has been taken which provides drag coefficients that are used to predict depths independent of an FRE.

1. Introduction

Oceanography requires data samples of ocean information such as temperature and salinity at a sufficiently large number of locations and times to ensure proper characterization of ocean properties. The creation of such data sets is constrained by the number of measurements made around the globe. It is also constrained by the duration of measurement activities. For climate monitoring for instance, continuous measurements on the order of decades is required to extract a signal-to-noise ratio sufficient to make judgments about global warming [1].

One of the most commonly used devices for taking ocean temperature measurements is the expendable bathythermograph (XBT). Approximately six million XBT devices have been launched over the past few decades. XBT devices contain a temperature-sensing element housed within a streamlined object which is launched into the ocean. The XBT falls through the water at approximately 7 m/s. During its descent, a copper wire is unspooled maintaining an electrical connection with a data processing station onboard a ship. Temperature information is transmitted through the wire and is stored for processing.

There are multiple varieties of XBT devices, each with a unique label. They are broadly separated into two classes (T4/T6/T7/T10/DB which are most common, then the FD, T11, and the T5 class). The major difference between the two classes is the size of the XBT body. Additionally, there are two main XBT manufacturers (LM-Sippican and TSK). Slight differences in the manufacturing processes between these two suppliers and variations in the processes since the 1960s have introduced some variation in the fall rates of the respective devices [2–6].

Biases in XBT measurements have been known for approximately 40 years. These include biases in the estimated depth as well as biases in temperature. The biases have led to errors in ocean-heat estimations reported in [2, 7–9]. Numerous efforts have been completed to reduce these biases and thereby increase the accuracy of oceanographic measurements made by XBT devices. These efforts have typically focused on improving the depth-time correlation of the FRE [10–13].

Very rarely have researchers focused on developing a dynamic model of the XBT during its descent with an analysis of buoyant, drag, and weight forces. Perhaps the most significant effort in this regard was by Green [14] who developed a model utilizing approximate drag forces which were taken from literature corresponding to streamlined bodies.

Here, a new approach is adopted. A dynamic model is developed and drag-coefficient information is taken from a computational fluid dynamic study. To the best knowledge of the authors, the computational approach is the first of its kind for XBT devices. The authors will investigate the impact of laminar-to-turbulent transition in the boundary layer of the XBT. Specifically, a comparison of drag coefficients for fully turbulent and transitional models will be performed. The resulting drag information will be used to predict depths on recent XBT experiments. The predicted depths will be compared with both the industry-standard FRE and with collocated and contemporaneous experiments using CTD devices which are considered the gold standard in oceanography.

2. Fluid Dynamic Model

Two approaches are taken in handling the simulations of fluid flow in the vicinity of the probe. The first method is based on the popular Shear Stress Transport (SST) model developed by Menter [15]. This model combines the seminal κ-ε model of Launder and Spalding [16] in regions removed from the probe-water interface with the κ-ω model in the boundary layer [17, 18]. The SST smoothly transitions between the two models to take advantage of their respective strengths. The κ-ε typically provides more accurate results in the free stream and is less sensitive to the upstream flow conditions whereas the κ-ω method is more capable of handling the low-Re flow within the boundary layer.

The second method is a transitional model which was first exhibited by Menter et al. [19] and Menter et al. [20]. It was later developed by the present authors in a series of studies which extended its use to internal flows, flows with adverse pressure gradients in diffusers, and pulsating flows [21–30]. Both the SST method and the newly developed transitional method rely upon a control-volume solution method wherein conservation equations are developed at a multitude of elements which constitute the solution domain. Among the relevant equations are conservation of mass and momentum, which are expressed in tensor form as:

$$\frac{\partial u_i}{\partial x_i} = 0, \tag{1}$$

$$\rho\left(u_i \frac{\partial u_j}{\partial x_i}\right) = -\frac{\partial p}{\partial x_j} + \frac{\partial}{\partial x_i}\left((\mu + \mu_{\text{turb}})\frac{\partial u_j}{\partial x_i}\right), \quad j = 1, 2, 3. \tag{2}$$

Here, the term u is the local velocity, ρ is the fluid density, p is the pressure and μ represents the molecular viscosity. In (2), turbulent motion has been accounted for by the introduction of the eddy viscosity. It is the definition of the eddy viscosity which characterizes the turbulence model. When the SST approach is taken, the eddy viscosity is found from:

$$\mu_{\text{turb}} = \frac{a\rho\kappa}{\max(a\omega, SF_2)}, \tag{3}$$

where the terms κ and ω are found from two new transport equations for turbulent kinetic energy and the specific rate of turbulence dissipation:

$$\frac{\partial(\rho u_i \kappa)}{\partial x_i} = P_\kappa - \beta_1 \rho\kappa\omega + \frac{\partial}{\partial x_i}\left[\left(\mu + \frac{\mu_{\text{turb}}}{\sigma_\kappa}\right)\frac{\partial \kappa}{\partial x_i}\right], \tag{4}$$

$$\begin{aligned}\frac{\partial(\rho u_i \omega)}{\partial x_i} &= A\rho S^2 - \beta_2 \rho\omega^2 + \frac{\partial}{\partial x_i}\left[\left(\mu + \frac{\mu_{\text{turb}}}{\sigma_\omega}\right)\frac{\partial \omega}{\partial x_i}\right] \\ &\quad + 2(1 - F_1)\rho\frac{1}{\sigma_{\omega^2}\omega}\frac{\partial \kappa}{\partial x_i}\frac{\partial \omega}{\partial x_i}.\end{aligned} \tag{5}$$

The term P_κ represents the rate of production for the turbulent kinetic energy, κ. All of the σ terms are Prandtl-like numbers for the respective transported variables, indicated by a subscript. The F terms represent blending functions whose purpose is to allow the transition from the κ-ε model away from the wall to the κ-ω model near the wall. The S term refers to the magnitude of the shear strain rate. Taken together, (1)–(5) define the SST approach. This approach accounts for flow that is fully turbulent as it approaches the oceanographic probe.

The transitional model includes a slight variation to the SST method. The variation begins with a modified form of (4) which becomes

$$\frac{\partial(\rho u_i \kappa)}{\partial x_i} = \gamma \cdot P_\kappa - \beta_1 \rho\kappa\omega + \frac{\partial}{\partial x_i}\left[\left(\mu + \frac{\mu_{\text{turb}}}{\sigma_\kappa}\right)\frac{\partial \kappa}{\partial x_i}\right]. \tag{6}$$

There is seen to be a multiplier on the rate of turbulent production, P_κ. That multiplier is symbolized by γ, the intermittency. The term γ takes on values between 0 and 1. It serves to reduce the rate of turbulence production in regions that are not entirely turbulent. Local values of γ are found from two new transport equations which are

$$\frac{\partial(\rho u_i \gamma)}{\partial x_i} = P_{\gamma,1} - E_{\gamma,1} + P_{\gamma,2} - E_{\gamma,2} + \frac{\partial}{\partial x_i}\left[\left(\mu + \frac{\mu_{\text{turb}}}{\sigma_\gamma}\right)\frac{\partial \gamma}{\partial x_i}\right], \tag{7}$$

$$\frac{\partial(\rho u_i \Pi)}{\partial x_i} = P_{\Pi,t} + \frac{\partial}{\partial x_i}\left[\sigma_{\Pi,t}(\mu + \mu_{\text{turb}})\frac{\partial \Pi}{\partial x_i}\right]. \tag{8}$$

The collection of (1)–(3) and (5)–(8) is often termed the transitional SST model. The symbols P and E represent rates of production and destruction of the transported variables. The symbol Π is the turbulence adjunct function (sometimes called the transitional onset Reynolds number). The first equation, (7), provides values of the intermittency γ. As mentioned earlier, the intermittency takes on values between 0 and 1. Values of γ near zero represent laminar regions while values that approach 1 occur in turbulent zones. Intermediate values of γ are representative of flow that is partially laminar and partially turbulent. It should be noted

that this definition of the intermittency differs from that sometimes found in the literature. Often, the intermittency is used as a multiplier of the eddy viscosity so that the eddy viscosity is reduced in regions where flow is partially turbulent. In the present work, the intermittency is utilized as a multiplier of the rate of turbulent energy production.

With respect to the turbulent adjunct function, Π, it is correlated to the local Reynolds number where intermittency first begins to grow (the critical value of the momentum-thickness Reynolds number). So, solutions from (8) are utilized to calculate the value of the critical momentum thickness Reynolds number which, in turn, is used to modify (7) through the intermittency production terms P.

The output of the fluid dynamic model is the drag coefficient on the probe. This coefficient is a singular expression of the Reynolds number and will be employed in the following section.

Figure 1 has been prepared to illustrate some of the features of the computational mesh. The figure will convey the features common to the meshes employed on all of the XBT devices, although the mesh shown in the figure is meant to be illustrative. The image shows a probe with the mesh extending around the probe exterior as well as throughout the interior channel which houses the temperature sensor. Special boundary layer elements were employed at the surfaces of the probe. Two callouts are shown which illustrate the element deployment in those regions. It can be seen that the boundary-layer elements are thin prismatic elements aligned with the probe body. Those elements were carefully constructed so that the y^+ was less than 1.

For all investigated cases, a mesh-independence study was completed. This study involved the solution of the fluid flow problem with sequentially increasing element counts. The solutions were continued until the results were independent of mesh. For all probe shapes, the final mesh count was well over 1,000,000 elements. To provide some perspective on the mesh-refinement study, Table 1 has been prepared. That table lists the number of elements for two sequential simulations that were carried out on the T7 device. It can be seen that with a significant refinement of the mesh, the value of the drag coefficient has not changed appreciably. The results in Table 1, while shown for a single Reynolds number, are representative of findings carried out at all other Reynolds numbers.

The solutions to the fluid flow equations were found using the ANSYS CFX V13.0 software. In reality, the probes rotate during their descent. In the present simulations, rotation was ignored. It is expected that rotation may have a slight effect on the drag coefficient and may make it less sensitive to the Reynolds number. On the other hand, the present nonrotating results will be compared with experiments and the close agreement will be used to justify the present approach.

3. Probe Dynamic Model

With the drag coefficient of the probe available from the fluid dynamic simulations, it is possible to predict the probe fall rates through the ocean water. The first step in this stage is the development of a dynamic model that relates the drag force to the timewise variation in probe velocity. That relation begins with a balance of forces and momentum changes of the probe. Mathematically, this balance is expressed as

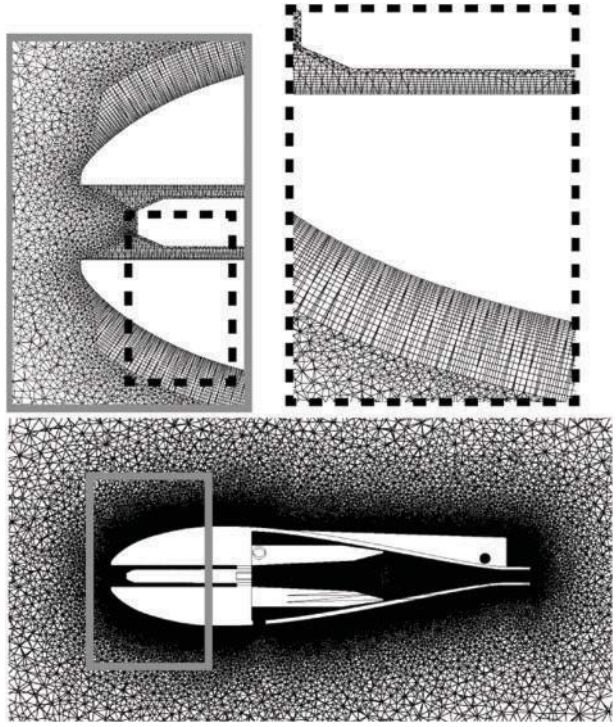

Figure 1: The computational mesh deployed in the fluid.

Table 1: Results of mesh-independence study, values of drag coefficient for the T7 device. Both calculations were completed for a Re = 950,000.

Number of elements	Drag coefficient
3,730,000	0.103
14,280,000	0.108

$$F_{\text{net}} = F_{\text{buoy}} - F_{\text{drag}} = \frac{d\left(m_p V\right)}{dt} = m_p \frac{dV}{dt} + V\frac{dm_p}{dt}. \quad (9)$$

Here, account is made for the change in mass of the probe as it descends through the water. It should be noted that the wire which is unspooled from the probe is not expected to exert any force on the probe. In addition, the unspooled wire has no velocity. When the drag and buoyancy forces are expressed in terms of the drag coefficient and the mass of the probe, the following expression is obtained:

$$\begin{aligned}\left(m_p - m_w\right)g - C_d\frac{1}{2}\rho V^2 A &= m_p\frac{dV}{dx}\frac{dx}{dt} + V\frac{dm_p}{dx}\frac{dx}{dt} \\ &= m_p V\frac{dV}{dx} + V^2\frac{dm_p}{dx}.\end{aligned} \quad (10)$$

Equation (10) can be written in a forward-stepping algorithm that allows the determination of velocity at a new time, provided information at the current time is known:

$$V^{\text{new}} = V + \frac{\Delta t}{m_p}\left[\left(m_p - m_w\right)g - C_d\frac{1}{2}\rho V^2 A - V^2\frac{dm_p}{dx}\right]. \tag{11}$$

It is (11) that will be employed to calculate the velocity at each timestep throughout the descent. It should be noted that this model is able to account for variations in the initial velocity of the probe (velocity of the probe when it enters the water) as well as variations in the linear mass of the wire, the diameter of the wire, and changes in the water temperature. This last issue deserves some detailed discussion. Historically, probe FREs are created by experimental correlation of XBT temperature values with more exact CTD results. Typically, XBT devices are dropped alongside CTD devices. Then, comparison of the temperatures between these devices allows construction of a FRE which takes the form

$$\text{Depth} = A + Bt + Ct^2. \tag{12}$$

For Class I probes (T4/T6/T7/DB), the recommended coefficients are $A = 0$, $B = -0.00225$, and $C = 6.691$ when depth is measured in meters and time is in seconds. For the Class II probes (T5), the constants are $A = 0$, $B = -0.00182$, and $C = 6.828$. However, the depth of a probe depends on local factors such as the specifics of the experiment (height of probe release above water), the details of the probe (size, mass, wire properties, etc.) and the local water temperature which affects the water viscosity. Consequently, when experiments are made under differing conditions, the FRE may no longer be valid. In particular, since most FREs are developed in tropical waters, their application to polar regions is questionable. The new method can account for variations in the water temperature and its impact on the viscosity. The variation is taken account of through the Reynolds-dependent drag coefficient. The definition of the Reynolds number used the probe length as the representative length.

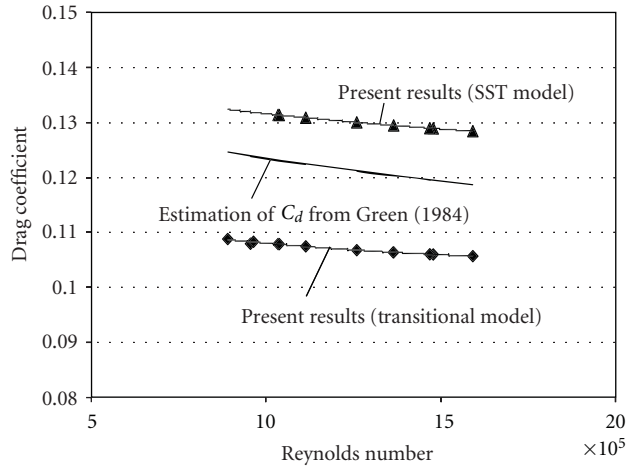

Figure 2: Drag coefficients for Class I probes, including SST model and transitional model results as well as drag coefficients from Green [14].

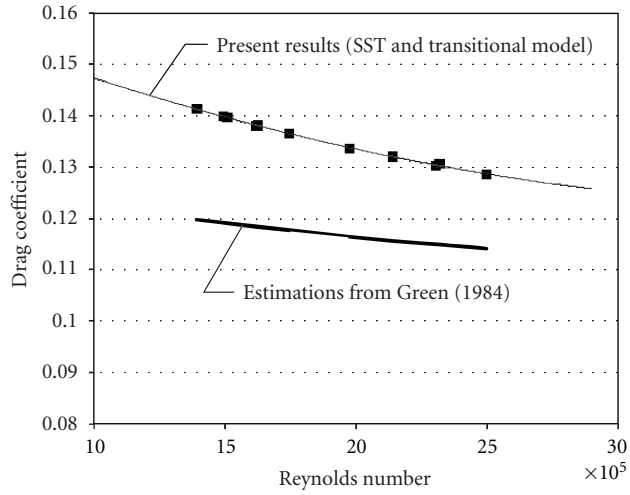

Figure 3: Drag coefficients for Class II probes, including SST model and transitional model results as well as drag coefficients from Green [14].

4. Results and Discussion

The first set of results will focus on the values of the drag coefficients which characterize two classes of probes (Class I = T4/T6/T7/DB and Class II = T5). Additionally, the impact of laminar-to-turbulent transition will be explored. First, Figure 2 has been prepared which shows the drag coefficients on the Class I probes. It can be seen that the two solution methods provide somewhat different drag coefficients; the SST model predicts higher drag than the transitional model. A more detailed discussion of this difference will be provided later. Also shown in the figure are values of the drag coefficient which are estimated from Green [14]. A corresponding figure for the Class II probes is presented in Figure 3. There, it can be seen that the differences between the transitional and SST models is very small however (not discernibly different), the two methods exhibit a significant difference compared to the values extracted from Green [14]. These results lead to the conclusion that for the T5 device, the effects of laminar-to-turbulent transition is negligible and that solutions with a fully turbulent model are sufficient to use in the present situation.

With respect to the model differences in the Class I devices, depths were calculated with both the transitional and the SST drag coefficients. It was found that the quality of XBT-CTD match was improved when the SST-based coefficient was employed. It is believed that for the Class I devices, which are shorter in length than their Class II counterparts, flow separation on the downstream faces plays a larger role in drag. The transitional model has difficulty in predicting the location of separation in adverse pressure gradient situations. Consequently, it was decided to utilize the drag coefficient obtained with the SST model.

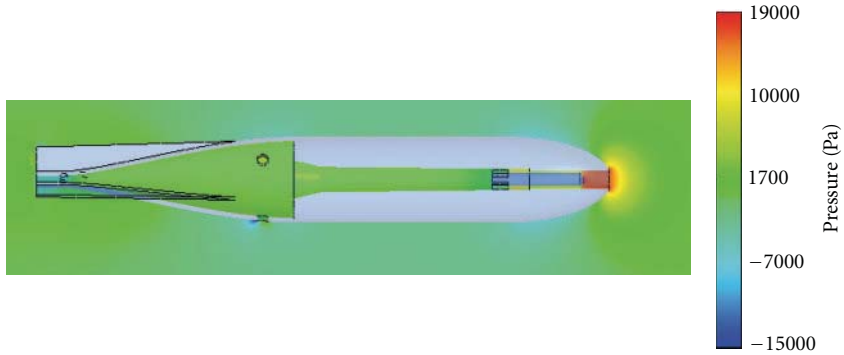

Figure 4: Pressure distribution in the fluid surrounding the probe (Class II probe).

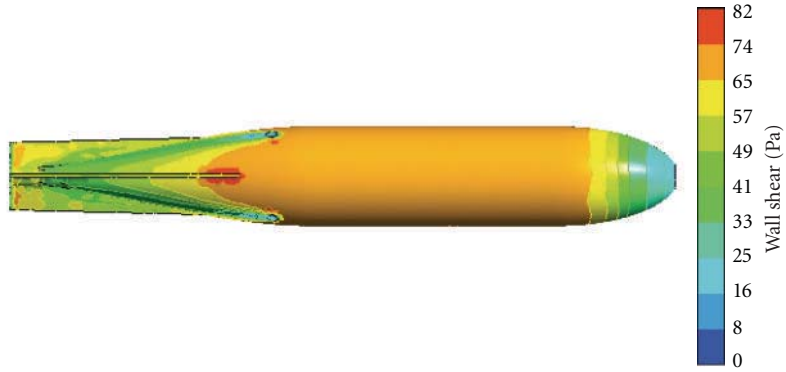

Figure 5: Distribution of surface shear stress (Class II probe).

For both classes of probes, the drag coefficients can be represented as functions of the Reynolds number. Those expressions are

$$C_d = 2.18 \times 10^{-15} \cdot \mathrm{Re}^2 - 1.10 \times 10^{-8} \cdot \mathrm{Re} + 0.140, \quad (13)$$

for Class I probes and

$$C_d = 2.74 \times 10^{-15} \cdot \mathrm{Re}^2 - 2.21 \times 10^{-8} \cdot \mathrm{Re} + 0.1668, \quad (14)$$

for Class II probes. The Reynolds number ranges are indicated by the figure axes.

Figure 4 has been prepared which shows the pressure distribution in the fluid near the XBT probe. In the figure, fluid is traveling from right to left. The figure shows that at the nose of the probe, there is a region of high pressure which decreases toward the upper and lower surfaces of the probe. Similarly, Figure 5 shows the variation of the shear stress on the surface of an XBT probe. It can be seen that the shear stress in the streamwise direction is low at the leading edge and trailing surfaces of the probe, as expected. The stress is more uniform along the length of the fuselage. The shear stress results presented in Figure 5 are representative of the results which can be extracted on any of the probe variants.

Next, displays of fluid flow patterns near the probe surface are shown in Figure 6. Here, representative images are exhibited which convey the basic features of the flow. It can be seen that the flow is channeled in the streamwise direction as it enters the center channel of the probe. The fluid in this channel washes over the temperature probe before passing through the body and emptying into a downstream chamber.

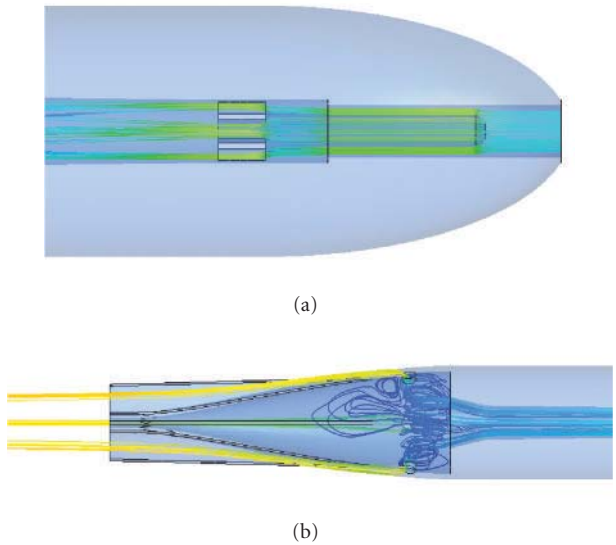

(a)

(b)

Figure 6: Streamline patterns through the center channel of a probe [31].

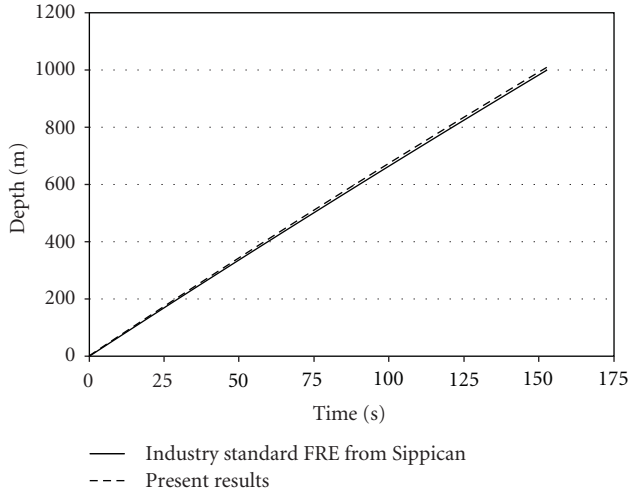

Figure 7: Comparison of depth calculated with the standard FRE and the new method.

In that chamber, there is flow recirculation and eddies which form before the fluid finally exits the probe interior.

In order to have confidence in the results presented here, it is necessary to make two comparisons. First, depth predictions will be compared with predictions obtained from the industry standard FRE. Second, comparisons between the new method and collocated CTD experiments will be made. An example of the first comparison is shown in Figure 7. The comparison from Figure 7 is taken from an experiment on Class II probes which was made in the Mediterranean Sea in May, 2011. It is seen that down to depths of 1000 m, the new method is nearly identical with the standard FRE technique. Comparisons with Class I probes reveal a similar level of agreement.

Next, experiments with coincident CTD/XBT devices are made. Typically, temperature and depth results from CTD probes are considered exact and are used to calibrate XBT devices. Two sample experiments are shown. The results of the experiments are shown in Figures 8 and 9. Each figure has two parts (a) and (b). The (a) part of the figure focuses on the near-surface region of the descent. The (b) part shows the temperature data down to the deepest parts of the descent. The images are separated into the parts to allow a magnification of temperature differences in the near-surface region.

Each part has three curves. Those curves represent the "exact" temperature information from the CTD devices, the temperatures from the new method, and temperatures which are obtained using the standard FRE. The display of results in Figures 7, 8, and 9 show that the new method is capable of calculating the depth of XBT devices throughout their entire descent with accuracy that is approximately equal to the industry standard FREs. In Stark et al. [31], it was shown that a quantitative comparison of a large number (seventeen) comparisons of CTD/XBT temperatures revealed that the temperature results from the new method and the accepted FRE agree to within the accuracy of the temperature sensing device. These findings were further reinforced in Abraham et al. [29]. This finding provides further evidence that the new technique has some merit in predicting XBT depths and in evaluating the ocean temperatures and ocean heat content.

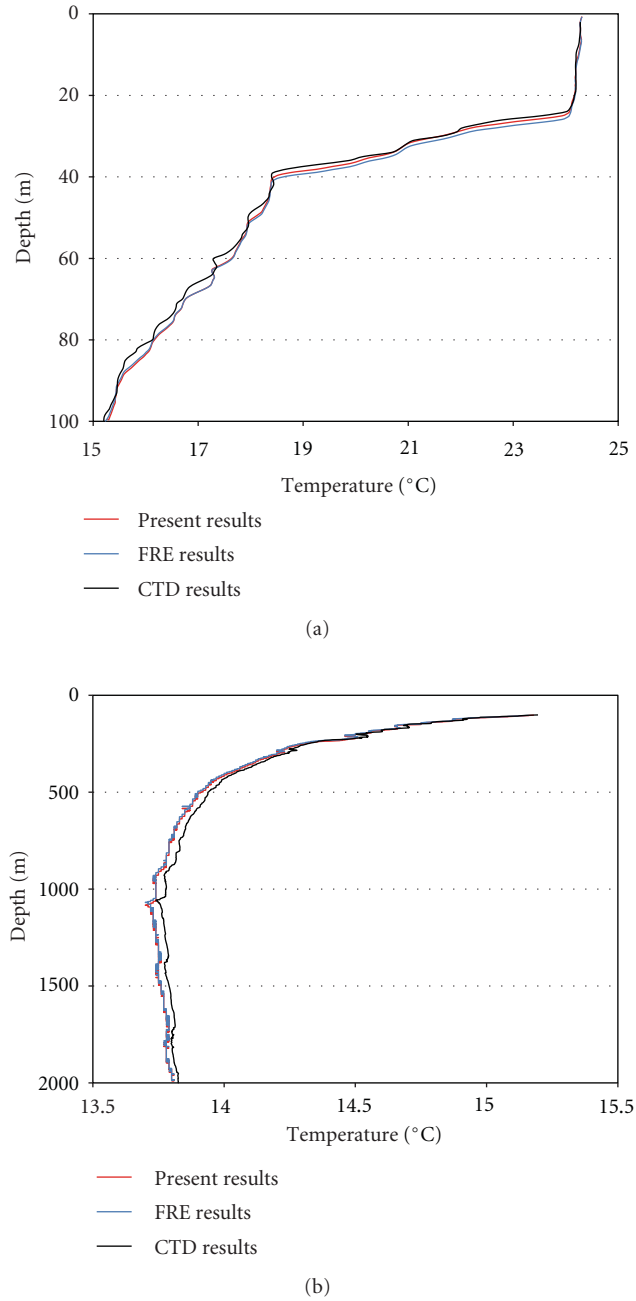

Figure 8: Comparison of the present method and the manufacturer FRE with a collocated CTD experiment.

As stated earlier, one significant advantage of the new method is that it is able to accommodate changes in the probe design or the launching method. For instance, the new method can incorporate different launch heights, probe shapes and sizes, initial probe mass, linear mass of the wire, diameter of the wire, and so forth.

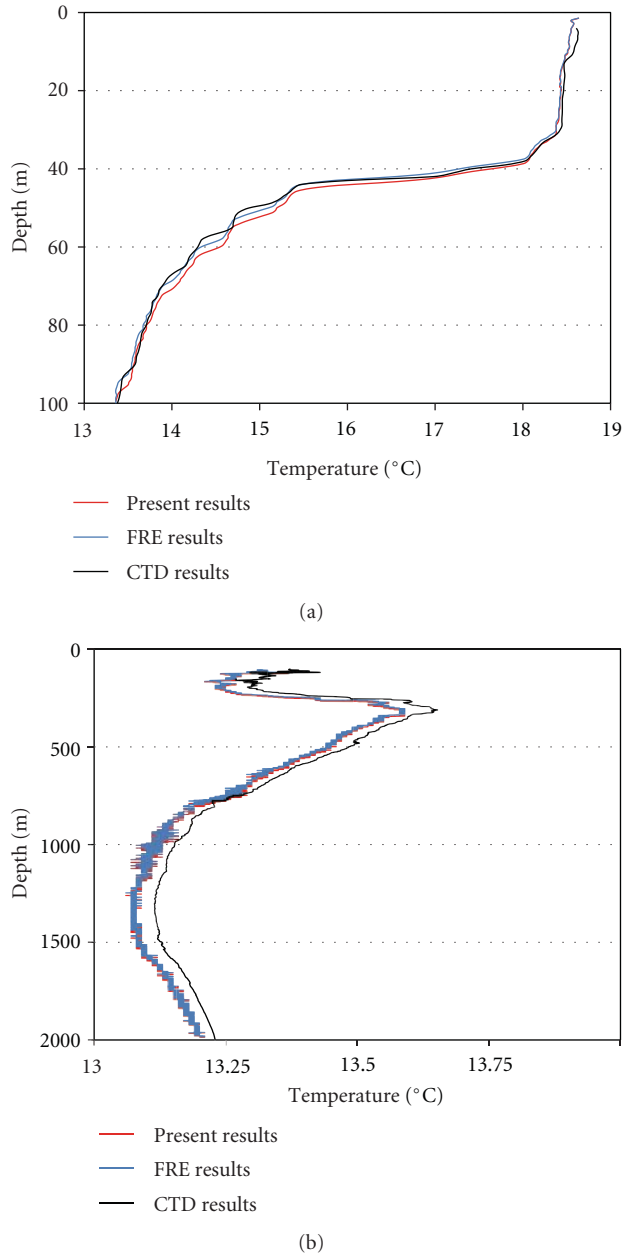

Figure 9: An additional comparison of the present method and the manufacturer FRE with a collocated CTD experiment.

5. Concluding Remarks

In this study, a new technique is presented to calculate depths of oceanographic temperature monitoring devices. Those devices, expendable bathythermographs, are launched into the ocean with high frequency each year. As the devices descend, they gather temperature information which, when combined with ocean depths, can provide ocean heat content assessments. XBT devices do not measure depth directly but rather determine depths from a correlative equation that is determined from experiment. This correlation, termed a Fall Rate Equation (FRE), is typically based on experiments carried out in tropical-water environments. FREs are incapable of handling variations in probe design, launch parameters, or water conditions. For instance, if the launch height or probe shape is changed, the FRE must be recalculated.

The new method, on the other hand, is based on a dynamic analysis of the probe which accounts for the forces exerted on the probe and the change in probe momentum. Necessary for the dynamic model is the drag coefficient on the probe. In this study, drag coefficients were determined on oceanographic devices for the first time (to the best knowledge of the authors). It was found that the drag coefficients were singular expressions with respect to the Reynolds number. With drag coefficients available, it was possible to calculate the depth of the XBT probes with accuracy that is comparable to the industry standard FRE.

It is hoped that this new method will be useful in re-evaluating the archive of oceanographic temperature data and can be used to improve the accuracy of ocean heat content, and consequently, the role of oceans in storing excess energy from the surrounding environment.

References

[1] B. D. Santer, C. Mears, C. Doutriaux et al., "Separating signal and noise in atmospheric temperature changes: the importance of timescale," *Journal of Geophysical Research D*, vol. 116, no. 22, Article ID D22105, 2011.

[2] S. E. Wijffels, J. Willis, C. M. Domingues et al., "Changing expendable bathythermograph fall rates and their impact on estimates of thermosteric sea level rise," *Journal of Climate*, vol. 21, no. 21, pp. 5657–5672, 2008.

[3] V. Gouretski and F. Reseghetti, "On depth and temperature biases in bathythermograph data: development of a new correction scheme based on analysis of a global ocean database," *Deep-Sea Research Part I: Oceanographic Research Papers*, vol. 57, no. 6, pp. 812–833, 2010.

[4] S. Kizu, C. Sukigara, and K. Hanawa, "Comparison of the fall rate and structure of recent T-7 XBT manufactured by Sippican and TSK," *Ocean Science Discussions*, vol. 7, no. 5, pp. 1811–1847, 2010.

[5] P. N. DiNezio and G. J. Goni, "Identifying and estimating biases between XBT and Argo observations using satellite altimetry," *Journal of Atmospheric and Oceanic Technology*, vol. 27, no. 1, pp. 226–240, 2010.

[6] F. Reseghetti, "Performance of XBT systems in Mediterranean Sea (2003–2010)," in *Proceedings of the XBT Bias and Fall Rate Workshop*, Hamburg, Germany, August 2010.

[7] V. Gouretski and K. P. Koltermann, "How much is the ocean really warming?" *Geophysical Research Letters*, vol. 34, no. 1, Article ID L01610, 2007.

[8] S. Levitus, J. Antonov, and T. Boyer, "Warming of the world ocean, 1955–2003," *Geophysical Research Letters*, vol. 32, no. 2, Article ID L02604, 2005.

[9] S. Levitus, J. I. Antonov, T. P. Boyer, R. A. Locarnini, H. E. Garcia, and A. V. Mishonov, "Global ocean heat content 1955–2008 in light of recently revealed instrumentation problems," *Geophysical Research Letters*, vol. 36, no. 7, Article ID L07608, 2009.

[10] J. D. Boyd and R. S. Linzell, "The temperature and depth accuracy of Sippican T-5 XBTs," *Journal of Atmospheric and Oceanic Technology*, vol. 10, no. 1, pp. 128–136, 1993.

[11] K. Hanawa, P. Rual, R. Bailey, A. Sy, and M. Szabados, "A new depth-time equation for Sippican or TSK T-7, T-6 and T-4 expendable bathythermographs (XBT)," *Deep-Sea Research*, vol. 42, no. 8, pp. 1423–1451, 1995.

[12] P. Thadathil, A. K. Saran, V. V. Gopalakrishna, P. Vethamony, N. Araligidad, and R. Bailey, "XBT fall rate in waters of extreme temperature: a case study in the Antarctic Ocean," *Journal of Atmospheric and Oceanic Technology*, vol. 19, no. 3, pp. 391–396, 2002.

[13] S. Kizu, H. Yoritaka, and K. Hanawa, "A new fall-rate equation for T-5 expendable bathythermograph (XBT) by TSK," *Journal of Oceanography*, vol. 61, no. 1, pp. 115–121, 2005.

[14] A. W. Green, "Bulk dynamics of the expendable bathythermograph (XBT)," *Deep Sea Research A*, vol. 31, no. 4, pp. 415–426, 1984.

[15] F. R. Menter, "Two-equation eddy-viscosity turbulence models for engineering applications," *AIAA Journal*, vol. 32, no. 8, pp. 1598–1605, 1994.

[16] B. E. Launder and D. B. Spalding, "The numerical computation of turbulent flows," *Computer Methods in Applied Mechanics and Engineering*, vol. 3, no. 2, pp. 269–289, 1974.

[17] D. C. Wilcox, "Reassessment of the scale-determining equation for advanced turbulence models," *AIAA Journal*, vol. 26, no. 11, pp. 1299–1310, 1988.

[18] D. C. Wilcox, "Comparison of two-equation turbulence models for boundary layers with pressure gradient," *AIAA journal*, vol. 31, no. 8, pp. 1414–1421, 1993.

[19] F. Menter, T. Esch, and S. Kubacki, "Transition modelling based on local variables," in *Proceedings of the 5th International Symposium on Engineering Turbulence Modeling and Measurements*, Mallorca, Spain, 2002.

[20] F. Menter, R. Langtry, S. Likki, Y. Suzen, P. Huang, and S. Volker, "A correlation-based transition model using local variables, part I: model formulation," in *Proceedings of ASME Turbo Expo Power for Land, Sea, and Air*, Vienna, Austria, June 2004.

[21] J. P. Abraham, E. M. Sparrow, and J. C. K. Tong, "Breakdown of laminar pipe flow into transitional intermittency and subsequent attainment of fully developed intermittent or turbulent flow," *Numerical Heat Transfer B*, vol. 54, no. 2, pp. 103–115, 2008.

[22] E. M. Sparrow, J. C. K. Tong, and J. P. Abraham, "Fluid flow in a system with separate laminar and turbulent zones," *Numerical Heat Transfer A*, vol. 53, no. 4, pp. 341–353, 2008.

[23] R. D. Lovik, J. P. Abraham, W. J. Minkowycz, and E. M. Sparrow, "Laminarization and turbulentization in a pulsatile pipe flow," *Numerical Heat Transfer A*, vol. 56, no. 11, pp. 861–879, 2009.

[24] J. P. Abraham and A. P. Thomas, "Induced co-flow and laminar-to-turbulent transition with synthetic jets," *Computers and Fluids*, vol. 38, no. 5, pp. 1011–1017, 2009.

[25] J. P. Abraham, E. M. Sparrow, and J. C. K. Tong, "Heat transfer in all pipe flow regimes: laminar, transitional/intermittent, and turbulent," *International Journal of Heat and Mass Transfer*, vol. 52, no. 3-4, pp. 557–563, 2009.

[26] J. P. Abraham, E. M. Sparrow, J. C. K. Tong, and D. W. Bettenhausen, "Internal flows which transist from turbulent through intermittent to laminar," *International Journal of Thermal Sciences*, vol. 49, no. 2, pp. 256–263, 2010.

[27] E. M. Sparrow, J. P. Abraham, and W. J. Minkowycz, "Flow separation in a diverging conical duct: effect of Reynolds number and divergence angle," *International Journal of Heat and Mass Transfer*, vol. 52, no. 13-14, pp. 3079–3083, 2009.

[28] A. P. Thomas and J. P. Abraham, "Sawtooth vortex generators for underwater propulsion," *The Open Mechanical Engineering Journal*, vol. 4, pp. 1–7, 2010.

[29] J. P. Abraham, E. M. Sparrow, J. C. K. Tong, and W. J. Minkowycz, *All Fluid-Flow-Regimes Simulation Model for Internal Flows*, Nova Science, Hauppauge, NY, USA, 2011.

[30] T. Gebreegziabher, E. M. Sparrow, J. P. Abraham, E. Ayorinde, and T. Singh, "High-frequency pulsatile pipe flows encompassing all flow regimes," *Numerical Heat Transfer A*, vol. 60, pp. 811–826, 2011.

[31] J. Stark, J. Gorman, M. Hennessey et al., "A computational method for determining XBT depths," *Ocean Science*, vol. 7, no. 6, pp. 733–743, 2011.